POROUS GAN PRODUCED BY CVD: PROGRESS IN DEVELOPMENT AND CHARACTERIZATION

Josué Mena Gómez

UNIVERSITAT ROVIRA i VIRGILI

Porous GaN produced by CVD: progress in development and characterization

JOSUÉ MENA GÓMEZ

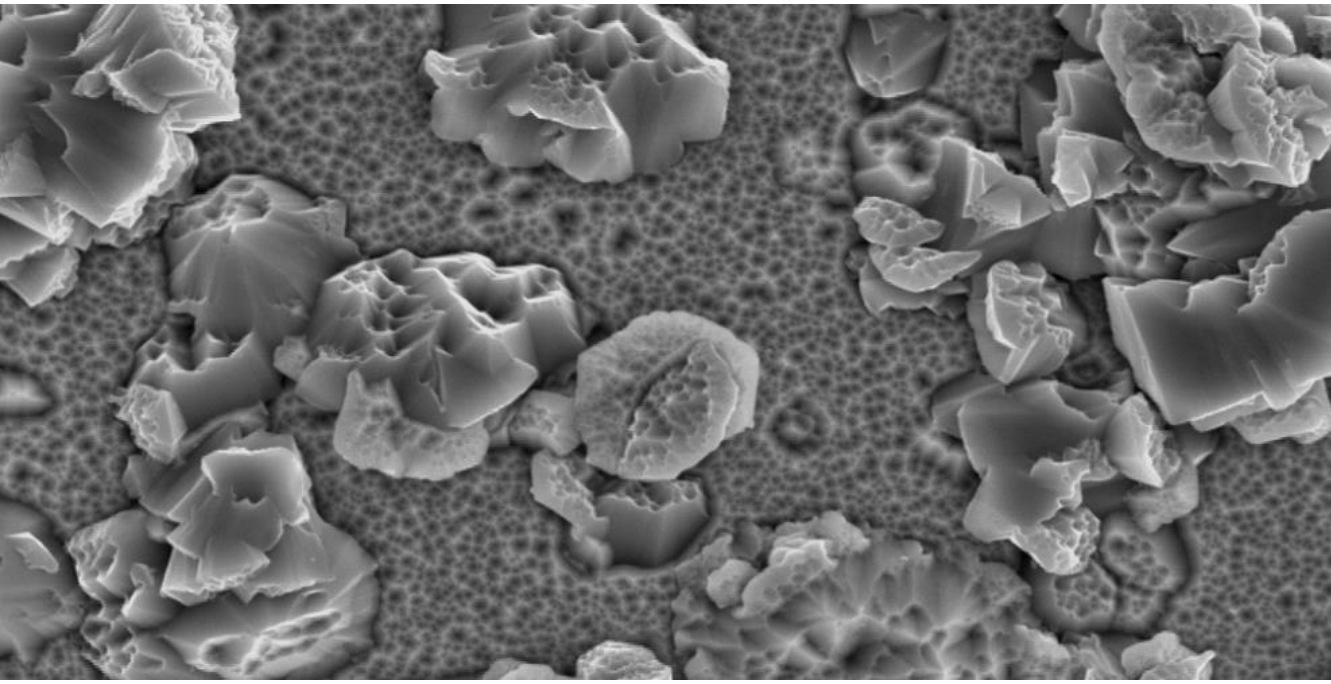

DOCTORAL THESIS
2017

UNIVERSITAT ROVIRA I VIRGILI
POROUS GAN PRODUCED BY CVD: PROGRESS IN DEVELOPMENT AND CHARACTERIZATION
Josué Mena Gómez

UNIVERSITAT ROVIRA I VIRGILI
POROUS GAN PRODUCED BY CVD: PROGRESS IN DEVELOPMENT AND CHARACTERIZATION
Josué Mena Gómez

Josué Mena Gómez

POROUS GaN PRODUCED BY CVD: PROGRESS IN DEVELOPMENT AND CHARACTERIZATION

Supervised by: Prof. Dr. Magdalena Aguiló

Dr. Joan J. Carvajal

Doctoral program in Nanoscience, materials and chemical engineering
Fisica i Cristalografia de Materials i Nanomaterials (FiCMA-FiCNA)
Departament de Química Física i Inorgànica

UNIVERSITAT ROVIRA i VIRGILI
Tarragona – 2017

UNIVERSITAT ROVIRA I VIRGILI
POROUS GAN PRODUCED BY CVD: PROGRESS IN DEVELOPMENT AND CHARACTERIZATION
Josué Mena Gómez

UNIVERSITAT
ROVIRA i VIRGILI

We STATE that the present study, entitled "Porous GaN produced by CVD: progress in development and characterization", presented by Mr. Josué Mena Gómez for the award of the degree of Doctor, has been carried out under our supervision at the Department of Physical and Inorganic Chemistry of this university, and that it fulfils all the requirements to be eligible for the International Doctorate Award.

Tarragona, 1st September 2017

Doctoral Thesis Supervisor/s

Dr. Joan Josep Carvajal

Prof. Dr. Magdalena Aguiló

UNIVERSITAT ROVIRA I VIRGILI
POROUS GAN PRODUCED BY CVD: PROGRESS IN DEVELOPMENT AND CHARACTERIZATION
Josué Mena Gómez

Acknowledgments

The elaboration of this thesis has been a long path with a lot of peaks and valleys together with some bifurcations from the original path; far away from a straight and flat, but not without puddles and brambles, path that one images to follow when the PhD starts.

In honour of the truth, it has to be said that through this tricky path, I have discovered a world of knowledge in science unknown to me after my graduation in Chemistry, and I have lived a lot of new experiences that I would have never imagined when I was in high school, such as giving a conference in English in front of an audience; being after four years in the same laboratory of physics when I started my bachelor, but this time playing the role of a teacher; living in Würzburg for a short period of time, city which now I consider my second home, and so many others.

The realization of this thesis would not have been possible without the support and guidance of my supervisors Dr. Joan J. Carvajal and Prof. Dr. Magdalena Aguiló. I am very grateful to my supervisors and Prof. Dr. Francesc Díaz to give me the chance to do my PhD thesis in their group and to contribute to their research. I want also to thank them the knowledge transferred through this long path called PhD thesis. I would like to specially thank Dr. Joan J. Carvajal for all the invested time in the corrections of the manuscripts and the discussions emerged from these corrections. Despite not being directly related to the elaboration of my thesis, I would also like to thank Dr. Mª Cinta Pujol for all the philosophical discussions about science, and why not, also to the more byzantine topics. Also, I want to mention here all the professors in the group: Jaume Masons, Airan Rodenas, Xavier Mateos and Rosa Solé for the help provided when needed during this period.

Four years of PhD studies is a lot of time, and it would not be a completely satisfactory without the human relationships emerged. In this paragraph I want to specially thank to the first people I met in the lab when I came as an undergraduate student, Nicolette Bakker and Agustí Montero for

the reception, which later would become more than work mates, sharing knowledge and sometimes similar, sometimes different, points of view. Of course I want to mention my close friends that have accompanied me during this time, Marc Medina, Irina Adell, Fran Martínez and Laura Abella for all the innumerable scares, laughs, bets, elaboration of hypothetical situations, philosophical discussions and so on we have made during this period.

I specially want to mention the help provided during my first steps in the synthesis and characterization of porous GaN by Dr. Oleksandr Bilousov to whom I have a special appreciation. I also want to thank to the old school collegues Jaume Cugat, Ali Butt, Oleksandr Savchuk, Usman Qadri, Carla Berrospe, Josep Mª Serres, Marc Isan, Javier Martinez, as well as to the new school Dat Nguyen, Eric Pedrol, Esrom A. Kifle for the laughs and time spent together and for the support given when needed.

Inside the URV I want to thank also to the technicians of the SRCiT that have helped me with the microscope techniques and Raman; Lukas Vojkuvka, Rita Marimon, Mariana Stefanova and Mercè Moncusí, as well as to Francesc Gispert who has helped me, not only with the structural characterization of my samples, but also with the deep understanding I have got through his patience always answering my questions about the fundamentals of XRD.

Also, I would like to thank my supervisor in Würzburg Anke Krüger and all my colleagues: Steffen Heyer, Peter and Rachel Buschmann, Andreas Muzha, and Sarah Schweeberg and specially to Benjamin Kiendl and Daniel Lang at Würzburg Unversitat that had really made a great experience of my time there, always ready to help me in everything, and to remind me my origins as a Chemist.

I also want to thank to the people of GdS in Valladolid Oscar Martinez and Juan Jimenez, not only for the opportunity of doing one of the

most important parts of my thesis, the luminescence characterization, but also for the plethora of things of semiconductors I have learnt from them.

Lastly and most important, thanks to my family, my mother Pilar, my father Antolin, and my sister Alba, who have done everything that has been in their hands to make me be where I am today, despite all the difficulties we have been through during this period. All this support is not directly shaped as a result or a number followed by units in this thesis but as an unpayable work done in the background. There is another family that is the family you choose, also known as friends, which have been there despite the tones of times I had to refuse a weekend plan or a succulent trip. Thank you for all “Topos”.

Tarragona, Spain

September 2017

Josué Mena

UNIVERSITAT ROVIRA I VIRGILI
POROUS GAN PRODUCED BY CVD: PROGRESS IN DEVELOPMENT AND CHARACTERIZATION
Josué Mena Gómez

“Keep an open mind, but not so open that your brain falls out”

Richard Feynman

UNIVERSITAT ROVIRA I VIRGILI
POROUS GAN PRODUCED BY CVD: PROGRESS IN DEVELOPMENT AND CHARACTERIZATION
Josué Mena Gómez

List of publications

Paper I

Bilousov, O. V.; Carvajal, J. J.; **Mena, Josué**; Martínez, O.; Jiménez, J.; Geaney, H.; Díaz, F.; Aguiló, M.; O'Dwyer, C. Epitaxial growth of (0001) oriented porous GaN layers by chemical vapour deposition. *CrystEngComm* **2014,** *16* (44), 10255-10261. DOI: 10.1039/c4ce01339e

Paper II

Carvajal, J.J.; **Mena, Josué**; Bilousov, O.V.; Martínez, O.; Jiménez, J.; Zubialevich, V.Z.; Parbrook, P.J.; Geaney, H.; O'Dwyer, C.; Díaz, F. and Aguiló, M. Fully porous GaN p-n junctions fabricated by chemical vapor deposition: a green technology towards more efficient LEDs. *ECS Trans.* **2015**, *66* (1), 163-176
DOI: 10.1149/06601.0163ecst

Paper III

Mena, Josué; Carvajal, J. J.; Martínez, O.; Jiménez, J.; Zubialevich, V. Z.; Parbrook, P. J.; Diaz, F.; Aguiló, M. Optical and Structural Characterization of Epitaxial Nanoporous GaN Grown by CVD. *Nanotechnology* **2017**, *28* (37), 375701
DOI: 10.1088/1361-6528/aa7e9d

Paper IV

Carvajal, J.J.; **Mena, Josué**; Aixart, J.; O'Dwyer, Colm; Díaz, F. and Aguilo, M. Rectifiers, MOS diodes and LEDs made of fully porous GaN produced by Chemical Vapor Deposition. *ECS Transactions* (Accepted)

Paper V

Carvajal, J.J.; **Mena, Josué**; Aixart, J.; O'Dwyer, Colm; Díaz, F. and Aguilo, M. Rectifiers, MOS diodes and LEDs made of fully porous GaN produced by Chemical Vapor Deposition. *ECS Journal of Solid State Science and Technology* (Accepted)

Paper VI

Mena, Josué; Carvajal, J. J.; Zubialevich, V. Z.; Parbrook, P. J.; Diaz, F. and Aguiló, M. Tailoring wettability properties of GaN through surface porosity induced during CVD deposition. *Applied Surface Science* (Submited)

Paper VII

Mena, Josué; Carvajal, J.J.; Bilousov, O.; Díaz, F. and Aguiló, M. Development of nanoporous GaN antireflective coatings on Si substrates. *Journal of Alloys and Compounds* (Submited)

UNIVERSITAT ROVIRA I VIRGILI
POROUS GAN PRODUCED BY CVD: PROGRESS IN DEVELOPMENT AND CHARACTERIZATION
Josué Mena Gómez

Porous GaN produced by CVD: progress in development and characterization

Josué Mena Gómez

2017

UNIVERSITAT ROVIRA I VIRGILI
POROUS GAN PRODUCED BY CVD: PROGRESS IN DEVELOPMENT AND CHARACTERIZATION
Josué Mena Gómez

Contents

Abstract

Gallium nitride (GaN) is a wide band gap semiconductor with important applications in white-light LEDs, which are an attractive alternative to conventional light sources due to its long operation lifetime, physical robustness, small-sized units, and minimal environmental impact, since it consumes 65% less energy than CFLs and reduces the mercury emissions by 50%. By replacing conventional light sources by LEDs a reduction of around 20% in the total electricity consumed would be expected. GaN, in its porous form, is expected to enhance the light extraction of these LEDs.

In the recent years GaN has also attracted the attention of the sensors world, and many prototypes have been fabricated using HEMT devices. Porous GaN based sensors are expected to enlarge the contact surface against which the analyte can interact, increasing the sensitivity of the devices. Moreover, making these sensors specific for a given target can be achieved by chemically functionalizating the surface of the device.

The main objective of this thesis is to optimize the growth conditions for the fabrication of porous GaN, as well as the growth of Mg- and Si-doped porous GaN and InGaN in order to be able to fabricate devices based on *p*-*n* junctions in the future. In this thesis, the study of the chemical functionalization with silanes and diazonium salts of the GaN surface in order to further fabricate efficient and selective sensors, has been also approached.

Nanoporous GaN particles and epitaxial layers were synthesized in a single step by chemical vapor deposition (CVD) through the direct reaction between gallium and ammonia. For the doping of the porous particles and layers magnesium acetylacetonate and silicon acetate were chosen as Mg and Si precursors, respectively, in order to generate the *p*- and *n*-type semiconductors, respectively. The obtained results show promising advances for the fabrication of porous *p*-*n* junction-based devices and the functionalization of GaN surfaces for sensing applications.

UNIVERSITAT ROVIRA I VIRGILI
POROUS GAN PRODUCED BY CVD: PROGRESS IN DEVELOPMENT AND CHARACTERIZATION
Josué Mena Gómez

1

Introduction

GaN became a semiconductor of especial interest in light-emitting diodes (LEDs) technology and a large number of potential applications, especially, after the demonstration of Nakamura in 1995 of the electrically pumped laser diode (LD) [1]. A well know example in which GaN injection LD is used in our daily life is for instance the Blu-ray storage, that can either write and read the disk [2]. Shorten the wavelength of the laser enhances the information areal packaging which is proportional to λ^{-2}, since the diameter of the laser spot is proportional to the wavelength of the laser and inversely proportionate to the numerical aperture (NA), laser spot diameter $\propto \lambda/NA$, by making the optical spot smaller, the disc area illuminated by the spot becomes smaller, and the bits written per unit area becomes greater. Hence, the size of the recorded bits can be reduced accordingly to increase the storage capacity [3]. Figure 1.1 shows the comparison of various optical storage media such as CD, DVD, HD DVD and Blu-ray, and the laser wavelength used to write the pits also known as “lands” which are the information containers.

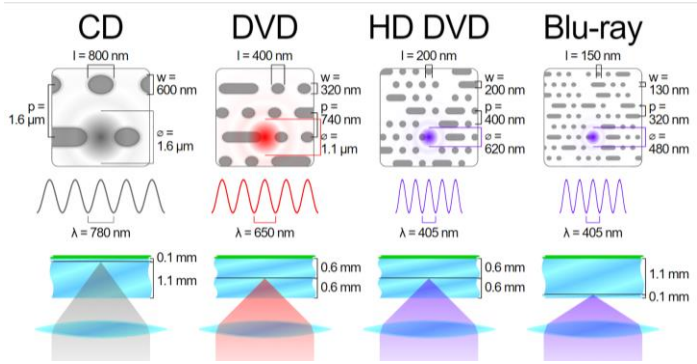

Figure 1.1. Comparison between the information packaging of various optical storage media; CD, DVD, HD DVD and a Blu-ray [4].

Also, white light GaN LEDs today have luminous efficacies in the same range as compact fluorescents (CFLs) [5]. However, LEDs compared with CFLs have the following advantages:

- Can have extremely long lifetimes, thus, reducing the replacement and therefore the quantity of waste,
- Have more physical robustness, reducing the decay of luminaries along time,
- Can be extremely small-sized units, that are adaptable to many form factors and designs without compromising the luminous flux,
- Provide a 41-50% reduction in mercury emissions [6].
- LEDs emit very little heat. In contrast, CFLs releases about 80% of the incoming energy as heat. This makes LEDs more energetically efficient, consuming about 65% less energy than CFLs [7].

Technology is improving very rapidly, and LEDs are becoming less expensive by improving the manufacturing processes [8] and more energy-efficient every year since prototypes of LEDs with a porous [9] or rough layer [10] have been already proved to improve the light extraction efficiency without the use of a polymer coating as a material with an intermediate refractive index between GaN and air.

Not so popular, but not less important, are the applications of GaN in high-temperature and high frequency devices like high-electron-mobility transistors (HEMT) [11], field-effect transistors (FETs) [12], Metal-oxide-semiconductor field-effect transistors (MOSFETs) [13] and *p*-type, intrinsic and *n*-type semiconductor diodes (PIN diodes) [14].

Most of the features described above would not be possible without a *p*-*n* junction, this means that the GaN needs to be doped with donors (*n*-type) and acceptors (*p*-type) to generate these junctions and develop the type of devices described above [15]. Not only to improve the electric properties of GaN it is important the incorporation of another atom in the GaN matrix, but also to tune the wavelength of the outgoing light from the device. Thus, it is necessary to find ways to synthesize ternary structures such as AlGaN and InGaN alloys that can generate emissions covering continuously all the UV-visible spectra, depending on the relative concentration of Al and In [16].

In the last decades GaN has also found a niche of applications in the world of sensors, in which the sensoring mechanism is based on different physical phenomena. Thus, sensor applications ranging from UV-photodetectors based on the generation of a photocurrent at wavelength below the band-gap of the semiconductor [17]; gas HEMT sensors based on changes in the source–drain current when the gas is adsorbed on the surface [18]; and prostate specific antigen (PSA) [19], breast cancer marker (c-erbB-2) [20], glucose [21], and DNA [22] detectors based on HEMT with a functionalized gate for a specific target changes in the source–drain current when the analyte interacts with the target, have already been demonstrated. As can be seen, most of the biosensors are based on HEMTs, the only difference between them is the receptor anchored to GaN via chemical functionalization of the surface. Thus, the chemical functionalization of the GaN surfaces is a central issue for the development of reliable and specific biosensors, since the receptor anchored to the GaN will determine the analyte to be sensed.

In this chapter we will describe the physical and chemical properties of GaN, and why these properties make GaN a good alternative to other

semiconductors for the fabrication of optoelectronic, electronic devices. Also, we will provide a discussion of the advantages, fabrication and applications of porous semiconductors relative to their bulk counterparts. Then, we will introduce a bit of history about GaN doping and the earlier problematic of the fabrication of *p*-type GaN. To follow, a brief introduction to the chemical functionalization of the GaN surfaces is given. Finally, we will present the objectives of this thesis.

1.1 GaN physical properties and its implications in electronics and optoelectronics

GaN is by far the most studied semiconductor of the III-nitrides group which includes also AlN and InN and their alloys $Al_xGa_yIn_{1-x-y}N$, ($0 \leq x,y \leq 1$ and $x+y=1$). The atomic bonds of the III-V compounds are mainly covalent with some degree of ionicity. Nonetheless, nitrogen, compared with the other V-elements, has the smaller atomic radius and the lowest number of electrons, which means that the outer electrons are not screened by the inner electrons, making the electrons to be tightly bound. This makes N the most electronegative atom of the V-elements, and this explains why the atomic bond in III-N compounds is highly ionic compared to the other III-V semiconductors. This higher ionic behavior of the bond between the III-elements and N leads to a stronger and shorter bond distance between the two elements which in turn make the III-N materials, like GaN, to have a significant hardness and chemical stability as will be discussed later.

The entire III-nitrides group share the same crystal structure: the wurtzite, zinc blende, and rocksalt structures, (see Figure 1.2) being the wurtzite structure the most stable structure. The other cubic metastable phases can only be obtained when a suitable cubic and lattice matched substrate is used to grow them [23]. The space group for the GaN wurtzite structure is $P6_3mc$ (C_{6v}^4) with lattice constants a=3.18 Å and c=5.16 Å [24], where the Ga and N atoms are tetrahedrally bonded to their neighbors. The fact that the wurtzite polytypes of GaN, AlN and InN are the most stable makes possible

the formation of a continuous alloy system with direct band-gaps ranging from 0.7 eV for InN [25] to 3.4 eV for GaN [26], and to 6.2 eV for AlN [26], by adjusting the quantity of In, Ga and Al in the compounds.

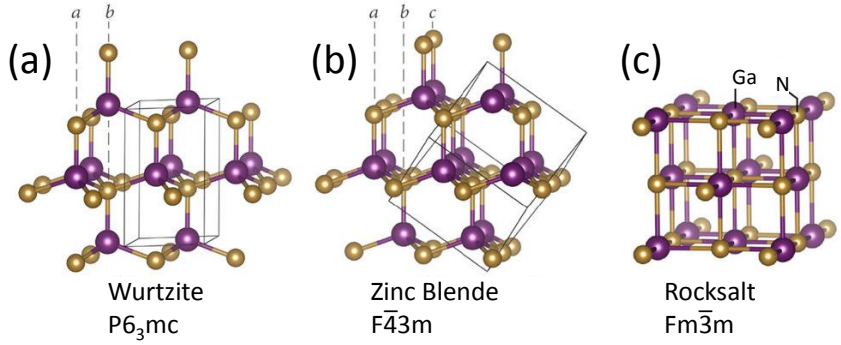

Figure 1.2. The crystal structures of GaN: (a) wurtizte, the most stable thermodynamically, and (b) zinc blende and (c) rocksalt, metastable structures. (image adapted from[27])

Besides offering great operation stability at high-temperatures due to its wide band-gap, GaN also exhibits a high chemical stability at elevated temperatures [26]. While the thermal stability of GaN allows freedom of high-temperature processing, its chemical stability presents a technological challenge. For instance, when etching of GaN is needed, the classical methods of wet-etching for semiconductors do not work with GaN. For example, GaN is insoluble in water, acids or bases at room temperature, but does dissolve in hot alkaline solutions at a very slow rate [28]. Hot KOH solutions are used to clean GaN deposited in the glassware after the reaction. However, NaOH for instance, when used with GaN, forms a passive layer of GaOH that avoids the etching of the underlying GaN [29]. Nevertheless, other chemical etchants are used in GaN to estimate its density of defects, like H_3PO_4 [30], H_2SO_4/H_3PO_4 mixtures [31], and NaOH [32].

Despite its great properties, the growth conditions used to obtain GaN determine the materials characteristics [2]. Because of this, a great variety of values for the same characteristics of GaN can be found in the literature, corresponding to GaN grown in different laboratories leading to inconsistent results. For instance, one example can be found in the thermal stability of

GaN that ranges from 1023 K to 1273 K, where no significant weight losses have been observed [2]. Also the thermal conductivity of GaN depends on the impurities and defects concentrations existing in the material, which is related with the growth method used to produce it [33].

GaN thermal conductivity (170 $W \cdot m^{-1} \cdot K^{-1}$) [34] is significantly lower than that of other wide band-gap semiconductors, like SiC (490 $W \cdot m^{-1} \cdot K^{-1}$) [35]. This property is especially important in high power and high temperature operations since the heat generated inside the electronic devices needs to be driven out as fast as possible to improve their reliability and prevent premature failure.

What makes III-nitrides, especially GaN, interesting in optoelectronics applications is their direct band-gap [36]. Direct band-gap semiconductors are very efficient electric to optical signal converters when a *p*-*n* junction is formed, that is why there was an important effort on producing *p*-type GaN, as will be discussed later. Direct band-gap semiconductors, like GaN, can produce an electron-hole pair quite easily, because the electron does not need to be given momentum because the minimum of the conduction band and the maximum of the valence band have the sample crystal momentum (*k*-vector). This makes III-nitrides good candidates for optoelectronic applications such as LEDs, injection LDs and photodetectors, apart that they can cover all the visible range of wavelengths and the UV as can be seen in Figure 1.3. One can notice from Figure 1.3 that there are many semiconductors from the II-VI and III-V groups that emit in the blue and UV part of the spectrum. Nonetheless, II-VI and III-V group semiconductors present short lifetimes and some of them are toxic to the environment, while III-nitrides are not. Thus, this makes III-nitrides good candidates for the fabrication of durable optoelectronic devices, and once the lifetime of the devices wears out, the residue generated is non-toxic to the environment.

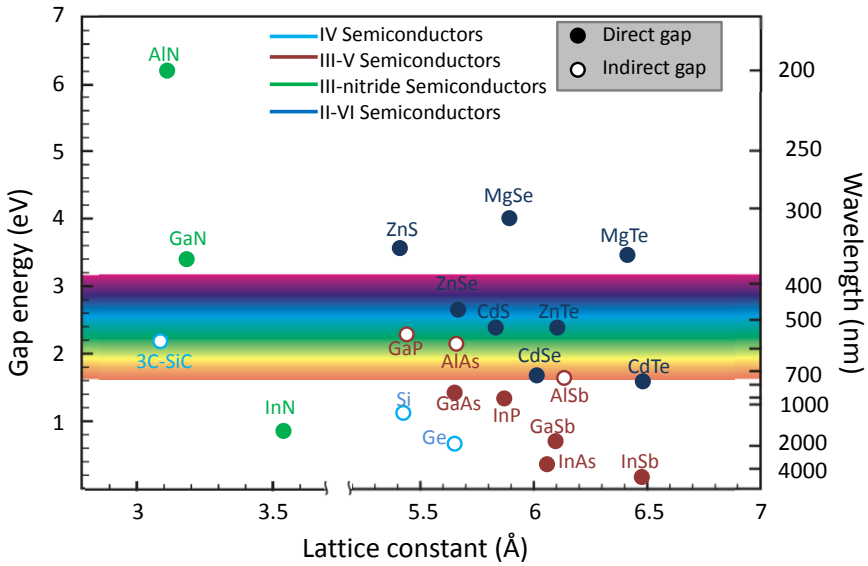

Figure 1.3. Bang gap plot against lattice constant of V, II-VI and III-V semiconductors.

Is its wide band-gap what makes GaN suitable for high temperature electronics applications, among other semiconductors as its competitor, 6H-SiC (E_g = 2.9 eV at RT) [37]. Wide band-gap semiconductors show superior material properties enabling higher potential power device operation at higher temperatures, voltages, and switching speeds than current Si (E_g = 1.1 eV at RT) [37] technology. GaN is particularly attractive for high-voltage, high-frequency, and high-temperature applications due to its wide band-gap, large critical electric field ($\sim 3 \cdot 10^3$ kV·cm^{-1}) [38], high electron mobility (1200-2000 cm^{2}V^{-1}s^{-1}) [39], and reasonably good thermal conductivity. In Figure 1.4 a comparison of electrical and thermal properties of Si, SiC and GaN is shown. One of the most interesting properties of GaN for high-power applications is the possibility to generate a two-dimensional electron gas (2DEG) in AlGaN/GaN heterostructures due to the large conduction band discontinuity between AlGaN and GaN and the presence of polarization fields [40]. They are well suited for high-power switching applications, with a projected performance advantage 100 times higher in the square breakdown voltage per specific on-resistance figure of merit over Si power devices [41], however, despite GaN-based devices are already commercially available in

the photonics area, its high-power applications are still in the first stages of development.

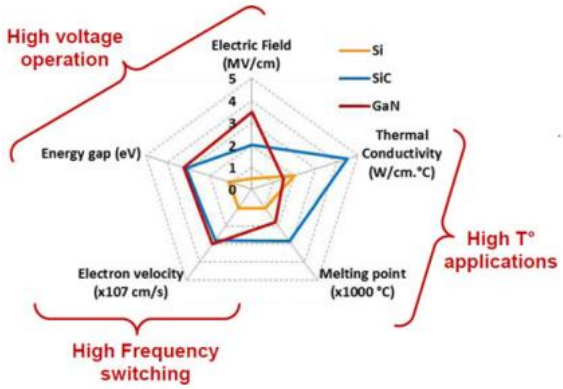

Figure 1.4. Radial graph of the relevant properties of Si, SiC and GaN for electronic high-power devices [41].

1.1.1 Electronic structure of GaN

Understanding the electronic band structure of GaN is fundamental to understand the optical transitions that are produced in this material, and take advantage of them, for instance, in the fabrication of quantum wells (QW). To determine the band structure of the material is a central issue knowing the Brillouin zone of the crystal and analyzing the points of high symmetry. Since GaN has a direct band gap, the fundamental transitions will occur near the Γ-point which is at the center of the Brillouin zone, at $k = 0$. The first Brillouin zone for wurtzite crystals is shown in Figure 1.5 (a).

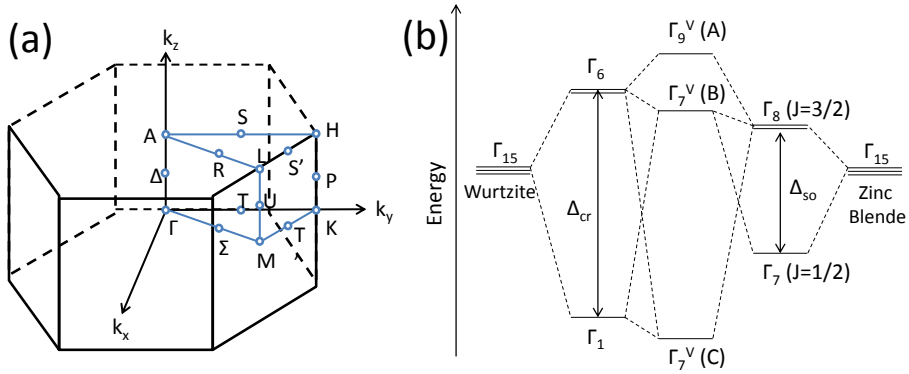

Figure 1.5. (a) First Brillouin zone of the wurtzite structure, note that the Γ point is at the center of the first Brillouin zone. (b) Band diagram showing the splitting of the top valence band of GaN by the crystal field and spin-orbit coupling (not scaled) (Image adapted from [42]).

In crystals with Zinc Blende structure, the valence band maximum has a Γ_{15} symmetry and it splits into two-fold and non-degenerate states under the influence of the crystal field, with a Γ_6 and Γ_1 symmetry, even in the lack of the spin-orbit interaction, being the Γ_6 state higher in energy than Γ_1 [26]. The energy splitting between these two levels is induced by the hexagonal symmetry of the wurtzite structure; therefore, this splitting is labeled as the crystal field splitting Δ_{cr}. The value of the Δ_{cr} and the position of the Γ_6 and Γ_1 depend on the kind of materials, the *c*/*a* lattice constant ratio and the internal parameter *u*, that describes the bond length parallel to the hexagonal axis and its value is $u = (a/c)^2$, for the ideal wurtzite structure this value is $u = 3/8$, thus the bond length parallel to the hexagonal axis is *u* times *c* (see Figure 1.6). Considering now the spin-orbit interaction, the two-fold degenerate Γ_6 state split into the Γ_9 and Γ_7 levels, and the non-degenerate Γ_1 state is labeled Γ_7 as well. Then, the Γ_7 levels are mixed by the spin-orbit interaction. The crystal field splitting and the spin-orbit coupling diagram is shown in Figure 1.5 (b) for clarity, in this image is also shown the approximation the other way round, starting from the spin orbit coupling in the Zinc Blende structure and then applying the crystal field splitting due to wurtzite structure. The energy splitting among these three levels by the spin-orbit interaction is called the

spin-orbit coupling Δ_{SO}. Due to the weak spin-orbit interaction of the nitrogen atom, the Δ_{SO} is lower than the Δ_{cr} in GaN and this behavior is also extended to the other III-nitrides.

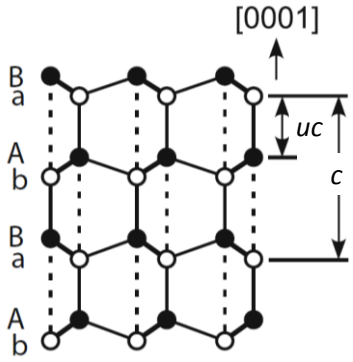

Figure 1.6. Atomic structure of the wurtzite structure indicating the bond length parallel to the hexagonal axis in terms of *uc*. Closed circle, open circle and thick solid line represent cation, anion, and projection of two bonds, respectively [43].

The effective masses of the holes of the three valence band levels are dependent on the *k*-vector, thus, the Γ_9^V (A), Γ_7^V (B) and Γ_7^V (C) levels are also labeled as heavy holes (HH), light holes (LH) and crystal-field split (CH), respectively, based on the feature in the k_x-k_y plane. The effective mass of the Γ_9^V (A) band is always heavy regardless of the *k* direction. The effective mass of the holes in the Γ_7^V (B) band is relatively light in the k_x-k_y plane but is heavy in the k_z direction. In the Γ_7^V (C) band the effective masses of the holes are light in the k_x-k_y plane and heavy along the k_z direction (see Figure 1.7 for clarity) [44].

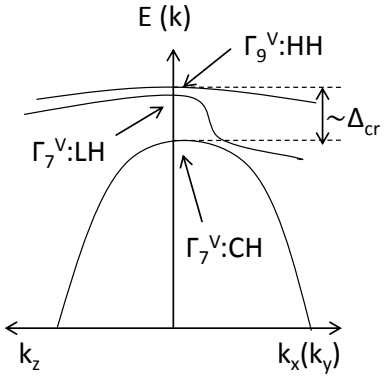

Figure 1.7. Valence-band structure of GaN in the k_z and k_x (k_y) directions. (Image adapted from [2]).

The energy position of the bands can be altered by the presence of a biaxial strain in the (0001) plane along the *x* and *y* axes, which is a very common effect in GaN since it is mostly grown on foreign substrates as sapphire, which causes a biaxial compressive strain, and 4H-SiC, which causes a biaxial tensile strain [45]. However, it was found that the energy dispersion between bands is almost unchanged, because due to the weak spin-orbit coupling the symmetry remains unchanged (C_{6v}^4), the hole effective mass remains heavy, and the density of states stays high. Only the crystal-field splitting energy becomes effectively large (small) under compressive (tensile) biaxial strain since the crystal still conserves the C_{6v}^4 symmetry (see Figure 1.8) [26].

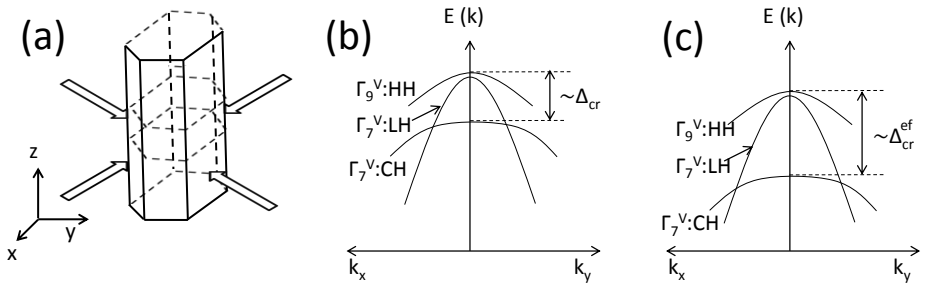

Figure 1.8. Scheme of the biaxial compression of the hexagonal structure of GaN with the arrows showing the direction of the strain, and the valence-band structure of GaN in the (0001) plane directions k_x and k_y (b) unstrained and (c) under compressive biaxial strain (Image adapted from [2]).

1.1.2 Optical transitions in GaN

The direct implication of the wide band gap of GaN is its associated luminescence, when the sample releases the excess of energy radiatively after being excited. The excess of energy is not always released radiatively, but it can also be released in a non-radiative way when the electrons and holes interact with phonons. During the radiative recombination process different scenarios can occur. One scenario is when the excited electron returns to the valence band with an energy E_g, this luminescence is called near band-edge (NBE) luminescence. The NBE luminescence of GaN consists in a set of lines associated to different recombination processes (see Figure 1.9). These lines are associated to free excitons (FX) -A, -B and -C, donor-bound excitons (DBX or DBE), acceptor-bound excitons (ABX or ABE), and a separated band at lower energies attributed to the donor-acceptor pair (DAP) or electron-acceptor transition (e-A) depending on the temperature.

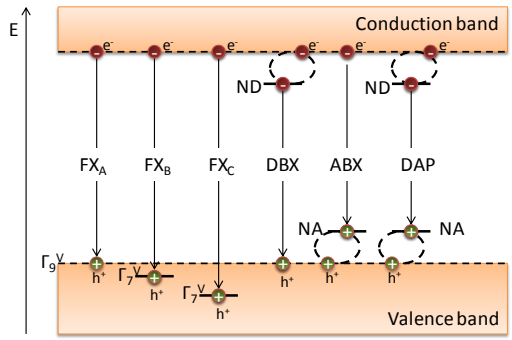

Figure 1.9. Optical transitions in GaN. e^- refers to the electron, h^+ to the hole, ND to a neutral donor, and NA to a neutral acceptor [46].

1.1.2.1 Free excitons (FX)

An exciton is an electrically neutral quasiparticle formed when an electron in the conduction band and a hole in the valence band separated in space are bound together by an electrostatic Coulomb attractive force, forming an electron-hole pair free to move through the crystal. However, the excitons are unstable having lifetimes of the order of 10^{-10} s, undergoing a

recombination of the electron and the hole. In GaN, three FX can be observed, labeled as FX_A, FX_B and FX_C corresponding to transitions from the bottom of the conduction band (Γ_7^C) to the three valence bands edges of GaN the Γ_9^V (A), Γ_7^V (B), and Γ_7^V (C), being the FX_A the most intense peak of the FX transitions (see Figure 1.10). As the temperature rises the FX peaks shift to lower energies and becomes dominant in the spectra. A typical spectra of the GaN NBE showing the FX_A and FX_B peaks (among others) is shown in Figure 1.10.

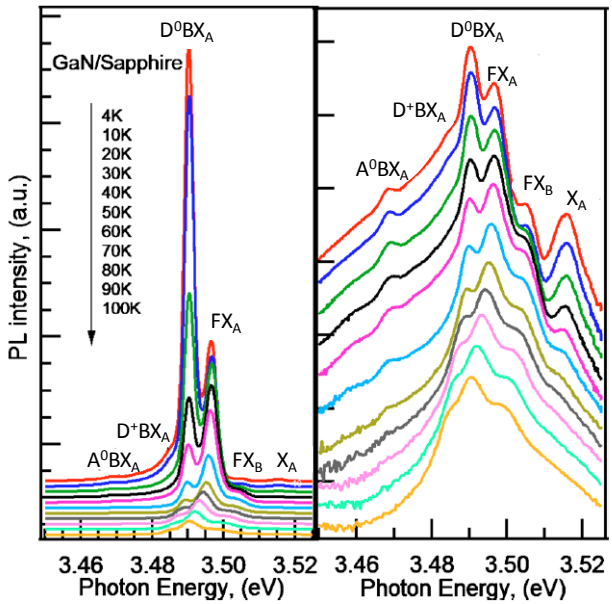

Figure 1.10. Temperature dependent photoluminescence (PL) spectra of GaN grown on sapphire in the temperature range from 4 K to 100 K showing the neutral DBX, FX_A and FX_B, among others (image adapted from [47]).

1.1.2.2 Bound excitons (BX)

Any impurity, e. g. dopants or defects, stacking faults and vacants introduce energy levels within the band-gap. They act as a small potential wells (traps), being able to trap free excitons. The free exciton loses part of its kinetic energy when trapped to the impurity, being then a bound exciton. The BX emission occurs at lower photon energies than the FX. Two kind of BX can be distinguished depending on the nature of the trap, acceptor bound

excitons (ABX) and donor bound excitons (DBX). Also BX can be classified on the electrical properties being neutral (A^0BX and D^0BX) or ionized (A^-BX and D^+BX) bound excitons. BX emissions are important in order to identify dopants in the crystal matrix, since they are an optical signature of the impurities. The PL spectra GaN at low temperatures is dominated by the BX, but as the temperature raises the BX peak decreases in favor of the FX_A peak. At 75 K the FX_A peak becomes dominant and above 100 K the BX thermally dissociates leaving the FX to dominate the spectrum (see Figure 1.9) [48].

1.1.2.3 Donor-acceptor pair (DAP)

When an electron from a donor level recombines radiatively with a hole from an acceptor level it is called a donor-acceptor pair (DAP) recombination. The atoms involved in the transition are neutral before, and become charged after the recombination. Usually de DAP band is centered at 3.26 eV (~380 nm) and followed by two longitudinal optical-phonon (LO-phonon) replicas separated ~91 meV between them (see Figure 1.11). Typically, the substitutional donors involved are Si atoms on Ga sites (Si_{Ga}) and O atoms on N sites (O_N), with activation energies of ~30 meV and ~33 meV, respectively. On the other side, the shallow acceptors for undoped GaN are usually attributed to Si atoms (Si_N) [49] on N sites and sometimes to Mg atoms on Ga sites (Mg_{Ga}) [50] if the reactor is contaminated with Mg. The activation energy of these impurities is around 220 meV. The DAP signal is only observed at low temperatures; above 150 K the signal is quenched. At temperatures above 50 K the free electrons from the shallow donor gain enough energy to jump to the conduction band leading to a transition from the conduction band to a shallow acceptor. This transition is called electron-acceptor transition (e-A). The temperatures higher than 150 K the electrons from the valence band can jump into the shallow acceptor levels suppressing the signal observed at 3.26 eV and the LO phonon replicas [51].

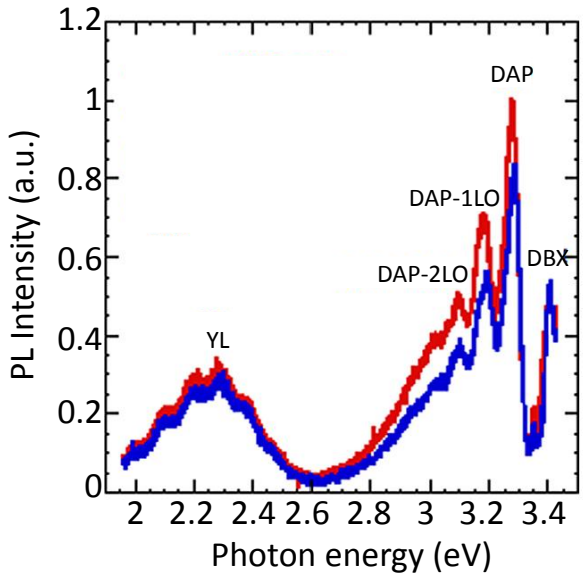

Figure 1.11. PL spectra of GaN showing the DBX, the DAP with the phonon replicas, and the YL (image adapted from [52]).

1.1.2.4 Yellow luminescence (YL)

YL is the most controversial signal in the GaN luminescence spectrum, since its origin is still unclear. The YL is usually observed in intentionally and unintentionally doped GaN. The YL band in GaN is a broad, nearly Gaussian band centered at ~2.2 eV (~560 nm) with a full width at half maximum (FWHM) of about 350–450 meV. The most accepted responsible for the YL seems to be gallium vacancies (V_{Ga}) or the recombination with oxygen on the N site (O_N), forming a vacancy impurity complex $V_{Ga}O_N$ [53] The formation of the vacancy impurity complex are driven by the Coulomb attraction force of the negatively charged V_{Ga} and the positively charged dopant, since at the deposition temperatures the isolated vacancies are mobile [54]. Another possibility described in the literature is the presence of carbon impurities [55]. However, the most accepted candidate to be responsible of the YL is the vacancy impurity complex $V_{Ga}O_N$. Figure 1.12 shows the YL of a *p*-i-*n* diode under different injection currents [56].

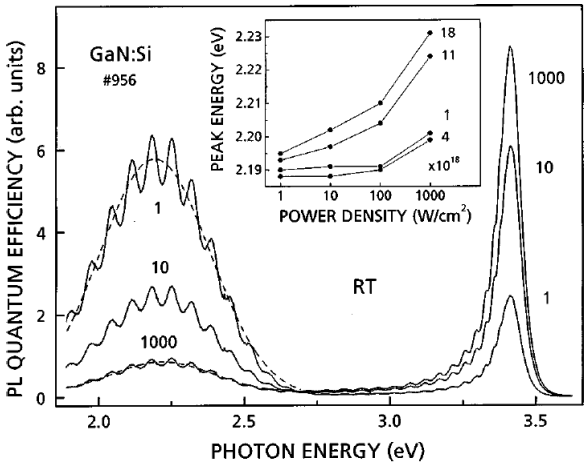

Figure 1.12. PL spectra of a Si-doped GaN sample excited at various power densities (PD) showing the YL at ~2.2 eV and the NBE. The dashed lines represent the Gaussian fitting of the YL . The inset shows the peak shift of the YL with increasing PD for different Si-doping concentrations [54].

1.1.2.5 Other luminescence bands

Apart from the already mentioned luminescent transitions, which are the most common ones, GaN also presents other luminescence bands that have to be briefly mentioned.

GaN grown by HVPE, produces a high quality film and the YL is not observed. Instead a green luminescence band (GL) appears centered at ~2.5 eV. Also GaN grown by MOCVD and MBE presents this GL under certain experimental conditions [57]. This band is attributed to a charged state of the defect-impurity complex $V_{Ga}O_N$ responsible for the YL band. The absence of GL on films of lower quality can be explained by the fact that the $V_{Ga}O_N$ complexes get bound to dislocations which may affect the charge state of the complex.

Another broad band observed in GaN samples grown by MOCVD and HVPE is the blue luminescence (BL) at about 2.9 eV. In Mg-doped and Zn-doped GaN samples the BL is attributed to a transition from a deep donor to the Mg shallow acceptor in the case of Mg-doped samples, and to a transition from a shallow donor or the conduction band to the Zn-related acceptor. Thus,

the BL of Mg- and Zn-doped GaN does not have the same origin. In the case of undoped GaN, the transitions look similar to the Zn-doped GaN, so, apparently the acceptor is the same [58].

Also, in undoped GaN grown by HVPE and MBE a red luminescence (RL) can be observed at around 1.8 eV. This luminescence band is attributed to defects and there are many that can play a role in this energy range. Despite the common luminescence energy position of the band, the different RL bands have different properties, since their origins are different [50]. For instance, in GaN grown by HVPE, the responsible of the RL is assumed to be a transition from a shallow donor at low temperatures to a deep-level defect at low temperatures, whereas in GaN grown by MBE, the proposed responsible for the RL are V_{Ga} trapped in different extended defects [59].

1.2 From thin GaN films to porous GaN films

GaN was first synthesized in 1932 by Johnson *et. al.*, by the direct reaction of ammonia gas on metallic gallium at high temperatures [60]. It was found that the reaction proceeded slowly at temperatures as low as 973 K (700° C), but it was necessary to heat the metal to 1173-1273 K (900-1000° C) for several hours in order to obtain an amount of the nitride sufficient for analysis and study, producing small platelets and needles. Later on, in 1938, Juza and Hahn synthesized also GaN passing ammonia over hot gallium to make a systematic study of inorganic compounds and investigated their crystal structure and lattice constants [61]. It was not until 1959 when Grimeiss et al. synthesized again GaN, using the same method as Juza, to measure and study its photoluminescence spectra [62]. Just a decade later, in 1969, Maruska and Tietjen [28] modified the standard method used at that time to produce GaN using a chloride vapor transport technique to produce a large-area of colorless GaN deposited on a sapphire substrate.

Bulk crystals of the III-nitrides cannot be grown by conventional crystal growth methods such as the Czochralski or Bridgman methods from

stoichiometric melts, since their melting temperatures and N pressures at melting are extremely high, 2723 K (2500 °C) and 456 MPa, respectively. Therefore, GaN dissociates rather than melts when heated at atmospheric pressures [63]. In order to put these numbers in context, the synthesis of diamond requires pressures of the same order 6079 MPa and temperatures about 1273 K (1000° C), less than those required for the crystal growth of GaN [64]. In the High Nitrogen Pressure (HNP) method, this decomposition is inhibited by using nitrogen under high pressure [65]. In this method, the growth of single crystals is performed in molten gallium and requires temperatures of about 1723 K (1500° C) and nitrogen pressures of the order of 1500-2000 MPa. However, only crystals of 2-3 mm could be obtained. It was not until the introduction, by Dwiliński *et al.* [66] in 2009, of the ammonothermal technique when truly bulk GaN substrates of 1 inch were produced, as shown in Figure 1.13.

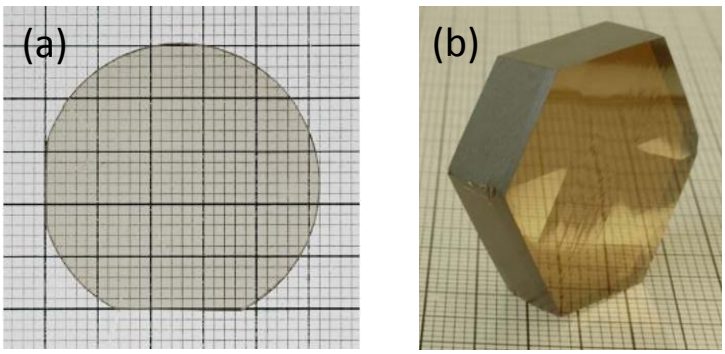

Figure 1.13. One-inch (a)-free-standing wafer [66] and (b) thick GaN [67] produced by the ammonothermal technique.

Parallely, while part of the research was focused on producing bulk GaN which could improve all the technology in which GaN relies by lessening the defect and dislocation concentrations generated due to the lattice mismatch between GaN and foreign substrates, efforts were done in producing porous GaN to be used as a buffer layer for heteroepitaxial growth on foreign lattice mismatched substrates, since the porous structure allows the relaxation of the structure.

The first method for producing porous GaN was reported by Mynbaeva *et al*. [68] in 1999 by anodizing, in aqueous solutions of HF under UV illumination, an epitaxial *n*-type GaN layer grown heteroepitaxially by hydride vapor-phase epitaxy (HVPE) on a 6H-SiC (0001) substrate. Since then, many groups have tried many other ways to induce porosity in GaN layers, all of them based on top-down approaches. Starting from the previous mentioned anodic etching technique, which is an electrochemical etching technique, to produce porous GaN, and followed by other techniques like photoelectrochemical wet etching [69], metal-assisted electroless etching [70] and alternating current photo-assisted electrochemical etching [71], the production of porous GaN has become wider in techniques in order to precisely control the optical and electrical properties of the resulting porous material.

Aside of using porous GaN as a buffer layer, the porous form of GaN has novel properties compared to bulk GaN. To number some of them:

- Strong photoresponse was found in anodized GaN layers grown on 6H-SiC in a aqueous solution of HF [72].
- If the width of the walls between pores is small enough a UV-shift of the bandgap due to quantum confinement is observed [73].
- PL intensity enhancement in the porous GaN [69].

One of the most interesting properties of porous materials for optoelectronic applications is its high luminescence extraction efficiency, which can be also obtained not only by porous materials but also by roughening the surface of the material (see Figure 1.14) [74]. The low extraction efficiency in conventional GaN is simply caused by the large difference in the refractive index between GaN (n_{GaN} = 2.5 at 460 nm) [75] and the external medium, air (n_{air} = 1). Most of the photons are trapped inside GaN by total internal reflection and converted to heat, which limits the external quantum efficiency of conventional LEDs based on GaN [75]. In fact, only photons emitter with an angle incident to the surface normal below

26° can escape the material. By roughening the surface, more photons are allowed to escape the material since more photons reach the surface with angles below the critical angle, thus, avoiding the total internal reflection (see the inset of Figure 1.14).

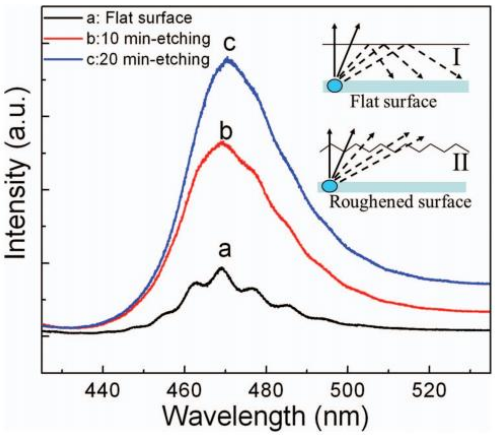

Figure 1.14. PL spectra at room temperature of a conventional LED wafer and nanoporous LED wafers after etching for 10 and 20 min through metal-assisted electroless etching. The inset shows the light traces for the planar (I) and roughened (II) surfaces [74].

Some of the techniques used for surface texturization in GaN are: maskless wet etching [76], electron-beam and nanoimprint lithography [77], self-assembled cluster of metal drops [78], inductively Coupled Plasma (ICP) etching [79], metal-assisted electroless fabrication [74] and electroless photochemical etching [10] to name a few. What all of these techniques have in common is that they are based on top-down approaches.

It was not since 2006 when Carvajal *et al.* [80] first reported the fabrication of porous GaN particles by the direct reaction between Ga and NH_3 in a chemical vapor deposition (CVD) during the growth process. The methodology was further improved since the obtaining of continuous porous GaN films on different foreign substrates like SiC (0001), AlN (0001), and GaN (0001) native substrates grown on sapphire wafers [81]. This methodology offers the possibility of obtaining porous films without any posterior etching treatment of the GaN previously grown. Also, one has to

take into account that the anodization processes previously used to generate the required porosity demand complex equipment for their control, and in general many of the electrolytes are highly toxic and/or corrosive [82]. Thus, by using the direct reaction method of GaN and NH_3 in a CVD system to obtain porous films we avoid the use of highly toxic and/or corrosive electrolytes, making this technique greener than the previous ones used.

1.3 The interest in doping GaN and the formation of GaN alloys

All the GaN produced from 1932 to 1969, described in the previous section, was *n*-type despite not being intentionally doped, with a typical carrier concentration on the order of 10^{19} - 10^{20} cm^{-3} [26]. This was the first bottle neck for the potential applications of GaN, since despite it had the suitable properties to develop optoelectronic devices, they could not be fabricated, since the form to produce *p*-type GaN was not trivial. This is a key point to produce LEDs, injection LDs, FET, HEMT and all the technology based on a *p*-*n* junction.

1.3.1 Attempts in compensating the *n*-type conduction background with Zn

A first attempt to compensate this *n*-type background was done by Pankove in 1971 producing the first insulating GaN by doping GaN with Zn [83]. This allowed him to produce the first blue LED made of GaN with a M-*i*-*n*-type structure (M:metal, *i*:insulator) [84]. The mechanism was the following: the electrons are injected from the metal to the insulator region (*i*-region) in forward bias, then, the electrons in the *i*-region, which is formed by Zn doping, drop to Zn centers, and finally the Zn centers give off blue light. However, the efficiency of the device was low, since the Zn centers are not efficient radiative recombination centers, despite the capacity of shifting the emission band from UV to blue. The blue emission is not a result of a shift to lower frequencies of the GaN NBE to the radiative transition from an electron

form the conduction band to the Zn acceptor as was discussed in sec 1.1.2.5. Despite the achievement of doping GaN with Zn, the obtainment of *p*-type GaN was still unachievable.

1.3.2 A brief history of the Mg-doped GaN

A previous step to obtain *p*-type GaN had to be done, and it was decreasing the large carrier concentration background. This was done by Akasaki *et al.* in 1985 when they developed the organometallic vapor-phase epitaxy (OMVPE) method for the production of III-nitrides using AlN buffer layers produced at low temperature (LT).

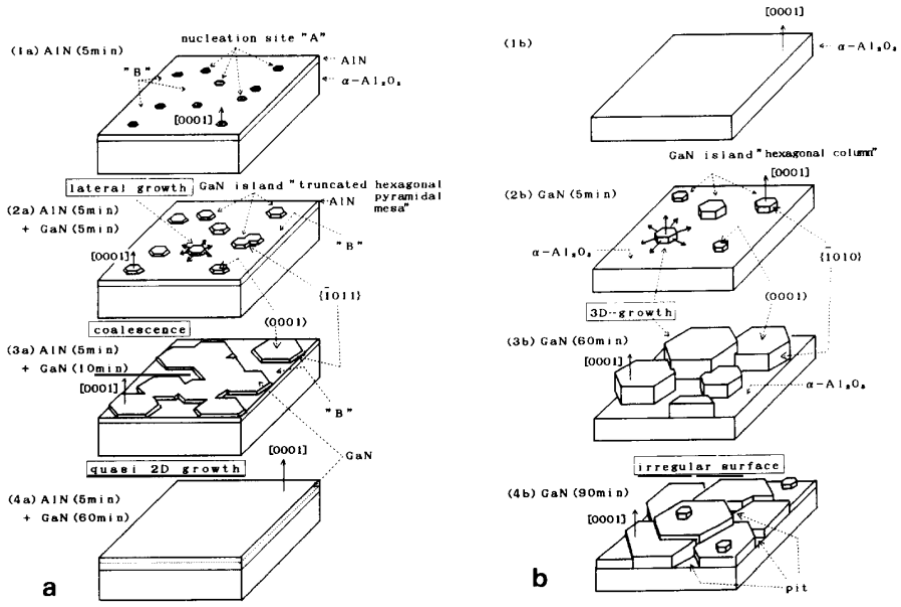

Figure 1.15. Growth model for GaN film on (0001) sapphire substrate (a) with and (b) without AlN buffer layer [85].

Later on, in 1989, Akasaki et al. observed that the AlN growth at LT is initially amorphous, and when the temperature is increased to the subsequent growth conditions of GaN, the AlN layer becomes a single crystal. Figure 1.15 shows a growth model for GaN with and without LT AlN buffer layer. Through the introduction of the buffer layers on the growth of GaN, the

background electron concentrations was lowered two orders of magnitude to 10^{17} cm^{-3}, this had two main effects: (i) improving the crystal quality of the epitaxial layers produced by reducing the concentration of dislocations and as a consequence the concentration of point defects, since extended defects can trap point defects [86] (see Figure 1.16); and (ii) set the stage for *p*-type doping since the doping with acceptors, like Mg, would not only compensate the donors, but also incorporate acceptor levels in GaN.

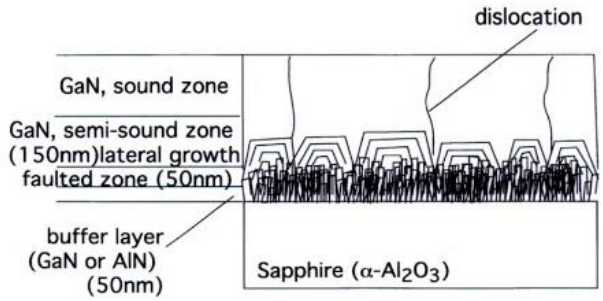

Figure 1.16. Scheme presenting depicts how the AlN buffer layer allows reducing the dislocations densities in the GaN growing film and increases the quality of GaN [87].

It was not until 4 years later, in 1989, when Akasaki and Amaro finally obtained a *p*-type GaN film by growning Mg-doped GaN on an AlN buffer layer. Mg was used as a dopant to obtain *p*-type GaN since it belongs to the II group and it might substitute Ga in the crystal structure giving a shallow acceptor with an ionization energy of ~240 meV [88]. It has to be said, that the obtainment of a conducting *p*-type GaN film was serendipity. The authors were observing the cathodoluminescence of a Mg doped GaN sample, and they realized that the brightness increased with further raster scanning. Thus, they decided to do a PL study of the sample before and after the irradiation of the sample with the electrons coming from the SEM, a process also known as low-energy electron-beam irradiation (LEEBI), and they found out that the sample exhibited two orders of magnitude higher luminescence efficiency after the LEEBI treatment [89]. The main point here was that prior to the LEEBI treatment Mg is complexed to a H atom, so the shallow acceptor behavior of the Mg is deactivated, and only after the LEEBI treatment the H

atom is released from the complex, leading to a Mg atom with a shallow acceptor behavior [90].

However, the mechanism of Mg activation was not completely understood until 1992, when Nakamura *et al.* obtained *p*-type GaN films through a rapid thermal annealing (RTA) process by annealing GaN films in a N_2-ambient at 1073 K (700° C) instead of the LEEBI treatment [91]. Figure 1.17 shows the activation mechanism of Mg under RTA. They also annealed low-resistivity *p*-type GaN films through RTA process in NH_3-ambient at 973 K (600° C) and they observed again that the resistivity was as high as the resistivity of untreated Mg-doped samples (10^6 Ω·cm). So, they proposed that a compensating complex Mg-H was formed due the presence of hydrogen [92] which comes from the nitrogen precursor (NH_3) during the MOCVD growth of GaN, and this process was confirmed by theoretical calculations in 1994 by Neugebauer and Van De Walle [93].

Nowadays, the most common technique to obtain low-resistivity *p*-type Mg-doped GaN is the RTA, and this is because the low-resistivity region of the Mg-doped GaN film depends on the penetration depth of the incident electron beam in the LEBBI treatment, whereas the RTA is a technique that produces uniform low-resistivity *p*-type GaN since the heat is distributed uniformly after the system reaches the equilibrium.

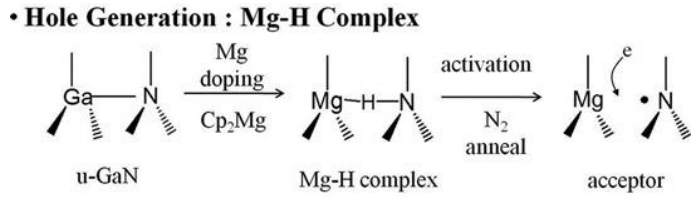

Figure 1.17. Mg doping of undoped GaN (u-GaN) using Bis(cyclopentadienyl)magnesium (Cp_2Mg) as Mg precursor, and Mg activation process of the Mg-H complex in Mg doped GaN through RTA under N_2 gas [94].

Thus, finally, after 20 years, the mystery of the production of *p*-type GaN was resolved. For all this work and efforts of doping GaN to obtain low resistivity *p*-type GaN, and the impact that it had in the development the *p-n*

junction technology, Nakamura, Akasaki and Amano won the Nobel Prize in Physics in 2014 [95].

Once the bases of Mg doping and activation were seated, the doping of GaN with Mg has still been improved. At present researchers are able to control the doping concentration, the holes concentration (which is not the same as the doping concentration, since the dopant can be compensated, thus reducing the holes concentration), and producing doping through many deposition techniques apart from the metal-organic chemical vapor deposition (MOCVD) [96], like ion implantation [97], reactive ion-beam molecular beam epitaxy (MBE) [98], plasma-assisted MBE [99], hydride vapor phase epitaxy (HVPE) [100], and CVD [101], among others.

1.3.3 A brief overview of Si-doped GaN

As discussed previously, GaN tends to grow unintentionally doped *n*-type, since the reactors of MOCVD are made of quartz which contains Si and O that can be incorporated as impurities giving the *n*-type character. When Si and O substitute Ga and N, respectively, they act as shallow donors with activation energies of 30 and 33 meV below the conduction band, respectively [102]. So, although the production of *p*-type GaN took a few decades to be understood (the mechanism of doping and activation of the holes), the production of *n*-type doping did not struggle the scientific community. However, after the introduction of LT AlN and LT GaN buffer layers that increased the crystalline quality of the epitaxial layers, making them suitable for long life and high efficiency LEDs and LDs, the carrier concentration of the unintentionally *n*-type doped GaN was decreased from $\sim 10^{19}$ [103] to values of $\sim 10^{16}$ cm^{-3} [104]. This is due to the fact that point defects (either impurities or vacancies) tend to be trapped in threading edge dislocations [105]. Therefore, at this point studies on how to produce *n*-type doped GaN were required to fabricate highly efficient emission devices.

In order to obtain high conductivity *n*-type GaN Se, Ge and Si are used as dopants. However, among these dopants Si has proved to be most suitable because the doping efficiency of Si is higher than that of Ge into GaN by one factor [106], also the solubility of Si in GaN is high, of the order of 10^{20} cm^{-3}, and free carrier concentrations in the range of 10^{17} to 10^{19} cm^{-3} have been reported [106], above these values the quality of the material starts to decrease very quickly due to tensile strain produced by the Si incorporation [107-108]. Thus, at present, *n*-type GaN is obtained using Si as a dopant, mostly using silane (SiH_4) as the Si precursor [109]. Nakamura *et al.* [106] and Li *et al.* [110] also observed that using SiH_4 as the Si precursor there was a good linearity between the carrier concentration and the flow rate of SiH_4, as can be seen in Figure 1.18. Si is the preferred dopant over Ge for group-III-nitrides in MOVPE and MOCVD due to its low cost and simple use [109].

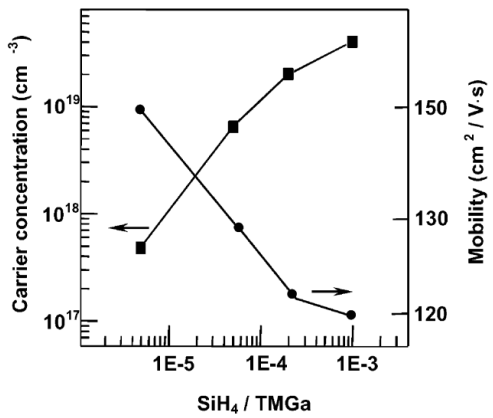

Figure 1.18. The electron carrier concentration and mobility in Si-doped GaN films as a function of the SiH_4/trimethylgallium ratio [110].

A curious phenomenon is the strain introduced by Si doping. Si is not expected to have any size effect in GaN, and first-principles calculations showed that Si incorporation does not produce any change in lattice constants of GaN. Nonetheless, the presence of tensile stress has been observed with increasing Si concentration. This can be related to the presence of tensile stress due to island coalescence [107]. Nix *et al.* [111] proposed that as the

crystallites are growing contacted each other at their bases, the side-walls zipped together until a balance was reached between the energy associated with eliminating surface area, creating a grain boundary and straining the film.

Other Si precursors have been used for *n*-type doping of GaN like SiH_2Cl_2 and Si_2H_6 for HVPE [112-113], t-$(C_4H_9)_2SiH_2$ for MOCVD [114], CH_3SiH_3 for MOVPE [115], and SiF_4 for ion implantation [116].

1.3.4 Introduction to ternary alloys of InGaN

Ternary alloys of InGaN with band gap energies ranging from 0.7 to 3.4 eV can be achieved varying the mole fraction of In in the alloy, covering the range of visible light, an essential requirement for visible light optoelectronics applications. Most of the optoelectronic devices consist on a double-heterostructure which consists on a structure where the material with the smaller band gap (active layer), in this case the InGaN alloy, is in the middle of two outer layers (or cladding) of a material with a bigger band gap, in this case GaN. Therefore, for the fabrication of a double-heterostructure, a GaN related layer (*p*-type or *n*-type) and an InGaN layer, as the active layer, is a central issue for the fabrication of high-efficient luminescence devices. Many efforts have been done to deposit InGaN active layers on GaN and AlGaN layers acting as cladding layers, despite the lattice mismatch between InGaN and AlGaN or GaN. The cladding layers are composed by a *n*-type layer at the bottom and a *p*-type layer on the top, which act as electrons and holes injectors, respectively, to the active layer. The active layer is where the recombination of electrons and holes takes place. The reason for choosing InGaN as the active emission layer was because its strong band to band luminescence and wavelength tunability with the molar fraction of In, which allowed to fabricate optoelectronic devices with the desired wavelength emission. Figure 1.19 plots the intensity vs. the emission wavelength of

$In_xGa_{1-x}N$ for different In molar fractions showing a shift towards lower energies when the In molar fraction increases.

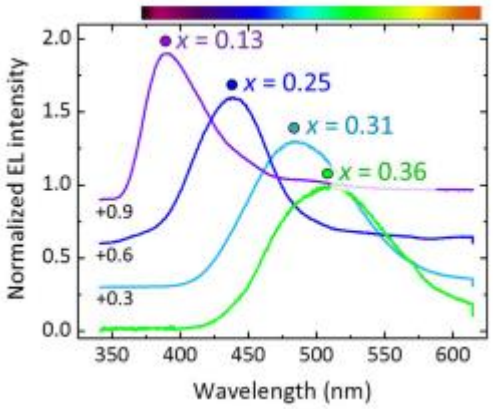

Figure 1.19. Evolution of the emission wavelength with the molar fraction of In in $In_xGa_{1-x}N$ [117].

Also, InGaN is useful for quantum-well (QW) structures and superlattices, in which a carrier energy state can be raised above the band-edge of the bulk semiconductor by confining carriers, which is of special interest for the development of LDs and LEDs [87]. Superlattices are structures of alternating layers of $In_xGa_{1-x}N/In_yGa_{1-y}N$ ($0 \leq y < x$). Multiquantum wells (MQWs) are heterostructures of alternating layers of thicknesses of the order of few nanometers (see Figure 1.20). The advantage of MQWs lasers, for instance, is that the incorporation of the MQW structures lowers the threshold current density compared with a LD without MQW. Thus, the incorporation of In in the GaN matrix is a central issue on developing tunable wavelength optical devices from the near infrared to the UV.

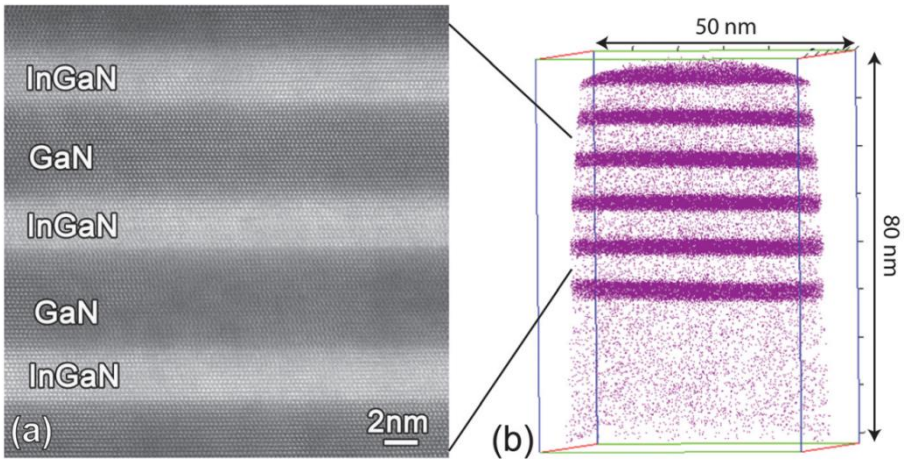

Figure 1.20. (a) High resolution high angle annular dark field scanning transmission electron microscope (HAADF STEM) image of $In_{0.2}Ga_{0.8}N$/GaN MQWs and (b) atom probe tomography (APT) reconstruction of the MQWs structure without a buffer layer. For visual clarity, only In atoms are displayed as purple dots in the reconstruction [118].

The beginnings of InGaN growth were a bit problematic. The very high equilibrium vapor pressure of nitrogen over InN only made possible the growth of InGaN with a composition control at temperatures around 923 K (650 °C). This low temperature growth for the InGaN on sapphire (0001) oriented substrates by means of MOCVD and MOVPE lead to a bad crystalline quality and no PL was reported arising from these layers [119]. In 1991, Yoshimoto et al. achieved the growth of InGaN on sapphire substrates at higher growth temperatures (1073 K) with a relatively high crystalline quality [120]. However, the crystal quality was not enough to produce long-life optoelectronic devices. It was not until the use of LT GaN (AlN) buffer layers for the growth of low defect GaN that InGaN was not grown on GaN which increased the crystal quality to the point to be used for optoelectronic applications [87].

1.4 GaN surface chemical functionalization for sensing applications

1.4.1 GaN based sensors

After the achievement of doping GaN with magnesium to obtain *p*-type GaN, and the doping with Si to obtain *n*-type GaN, it was possible the fabrication of devices based on *p*-*n* junctions like the blue LD [121], and LEDs; blue [122] first, and then white [123-125] based on InGaN technology as the main optoelectronic devices based on this material. Also the GaN *p*-*n* junctions let to the fabrication of the transistors: FET [12], HEMT [11], MOSFET [13], and metal-insulator-semiconductor (MIS) [126], and Schottky diodes [127] as the main electronic devices based on GaN.

In the mid-90s of the 20th century, GaN attracted the attention to develop sensing applications, since GaN typically is grown along the (0001) direction, and this is a polar axis, which makes that these materials have strong lattice polarization effects [18]. This allows using them as pyroelectric and piezoelectric [128] base materials for sensing applications [129].

Also, GaN, attracted the attention for gas sensing, especially hydrogen and hydrocarbons sensing [130-131], since high temperature operation and long term stability are important requirements for gas sensors at high temperatures, and GaN seems to fulfill this requirements, since GaN retain the semiconducting properties at high temperature. In 1999 it was developed the first Pt Schottky diode gas sensor based on GaN by Luther *et al.* [130] They developed a sensor made of a catalytic metal (Pt) deposited on *n*-type GaN. The catalytic metal acts dissociating the hydrogen or the hydrocarbon gas and leading the atoms to diffuse to the device interface. It is presumed that a dipole is formed, lowering the effective work function of the metal and changing the electrical characteristics of the devices. By measuring this change in the response of the Schottky diode one can correlate it with the presence of the gas under test.

However, the most suitable structure for sensors based on GaN is the AlGaN/GaN HEMT [132]. The high electron sheet carrier concentration in

AlGaN/GaN HEMTs is induced by the spontaneous piezoelectric polarization of the strained AlGaN layer, which is very large in wurtzite III-nitrides [133]. This provides an increased sensitivity when compared to that of simple Schottky diodes fabricated on GaN layers [134-135] [135]. In addition, the gate region can be functionalized chemically so that current changes can be detected for a variety of gases [136-138], liquids [139] and biomolecules [140]. Figure 1.21 shows an example of an AlGaN/GaN HEMT with the gate region chemically functionalized with aminopropyl triethoxysilane (APS) linked to biotin, able to immobilize proteins on the surface, producing a reduction of the drain-source current [141].

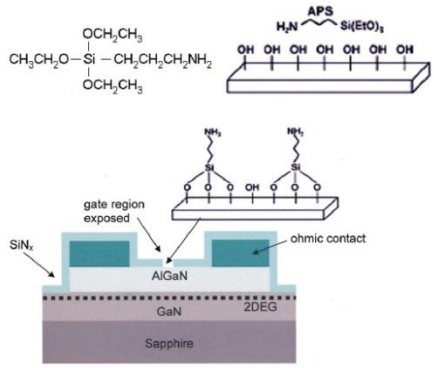

Figure 1.21. Scheme of a gateless AlGaN/GaN HEMT with the AlGaN surface chemically functiontionalized with APS [141].

Among the different FET-based transistors fabricated with GaN and derivates we can find: ion-selective field-effect transistors (ISFET) for the detection of biochemical reactions on the sensitive gate area [140], electrolyte gate field-effect transistor (EGFET) for the monitoring of electrical cell action potentials outside the cell by directly cultivation of the cells on the nonmetallized gate surface [142], HEMT functionalized with different molecular receptors or the specific antibody to sense proteins such as prostate specific antigen (PSA) [143], Streptavidin-a [141], and c-erbB-2 [20], among others, DNA [22], and glucose [144].

1.4.2 Brief review of the surface functionalization of GaN

From the information described above one can conclude that the crucial step for sensing any biological target is the proper chemical functionalization of the surface of the device to make it specific for a specific target.

Prior to the study of the chemical functionalization of GaN and its related alloys, another approach was explored to covalently bond GaN to organic molecules. In fact, the approach explored by Winter *et al*. [145] to link GaN to organic molecules was the other way round. The aim was to deposit a GaN layer on top of a previously chemically functionalized gold layer with a self-assembled monolayer (SAM) of 11-mercapto-1-undecanole with the thiol-groups facing the Au layer, getting the OH-groups at the end of the molecule free to react with the Ga precursor, in this case a galliumazide $Ga(N_3)NEt_3$ (see Figure 1.22). The growth of a GaN layer on the top of this functionalized gold layer consisted in: repeated cycles of dipping the GaN layer in a solution containing the galliumazide, rinsing then it with toluene, drying it in vacuum, and expose it to ammonia gas. They demonstrated, using spontaneous desorption time-of-flight mass spectrometry (SDMS), the bonding between the OH-terminated monolayer and the gallium azide units through a covalent gallium-oxygen bond.

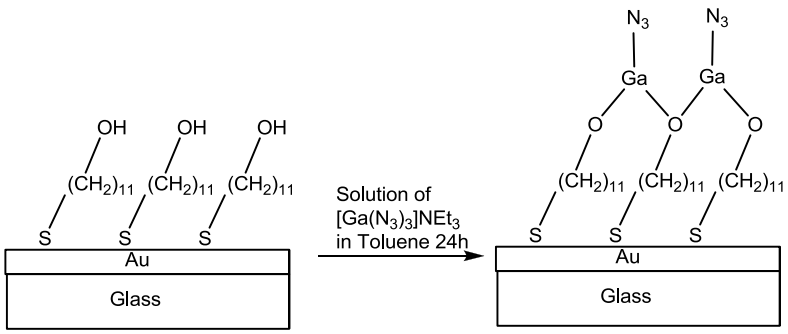

Figure 1.22. Chemical reaction to link gallium azide on top of the 11-mercapto-1-undecanole SAM [145].

Once the first antecedent was settled, other authors explored different strategies to deposit GaN on various functionalized surfaces and using different precursors like the method employed by Niesen *et al.* [146] for the growth of GaN on (001) Si and (0001) sapphire by using the assistance of functionalized surfaces with trichlorosilylhexadecane nitrile anchored SAMs with an amine terminal group, after the reduction of the nitrile-terminated group, and using as Ga precursor a Ga-containing carbodiimide-based polymer. For the deposition of GaN on the functionalized SAM on Si and sapphire the Ga-containing carbodiimide-based polymer was put in contact with the SAM-coated wafers for 7 days. After cleaning their surfaces the wafers were transferred into a tubular furnace and heated up to 1173 K (900 °C) under an ammonia flow. At that temperature the SAMs and the polymer are sacrificed and a layer of GaN is deposited on the wafers.

In parallel, studies of chemisorption with organic molecules were undertaken in 1997 to investigate the surface interactions of GaN with organic molecules to obtain deagglomerated GaN nanoparticles in polymer matrices [147]. However, this settled the precedent for other authors to begin the study of functionalization of GaN with organic molecules, first by chemisorption, and later on by covalent bonding.

It was not until 2002 when the first study on chemical functionalization of the GaN surface with organic molecules by chemisorption was reported completing a study of the absorption of ammonia (NH_3) [148], primary amines (R-NH_2) [149-150], and secondary amines (R_2-NH) [151] to the GaN(0001)-(1x1) surface. (1x1) reconstructed surfaces consist at least on a monolayer of Ga residing on top of the Ga-terminated bilayer. The amines investigated in these works were selected because GaN surfaces functionalized with aniline and 3-pyrroline might be suitable for subsequent chemical or photochemical reactions. Bermudez *et al.* [151] concluded that the bonding of aniline and 3-pyrroline occurs in the form of a phenyl-NH group via a Ga-N-Ga bridge (see Figure 1.23), analogous to the model proposed for the adsorption of NH_3 in the GaN surface. A year later, in 2003,

Bermudez *et al.* [152] again studied the chemistry of adsorption of thiols on the GaN (0001) surface. However the nature of the S-Ga chemical bond at the surface was not detailed.

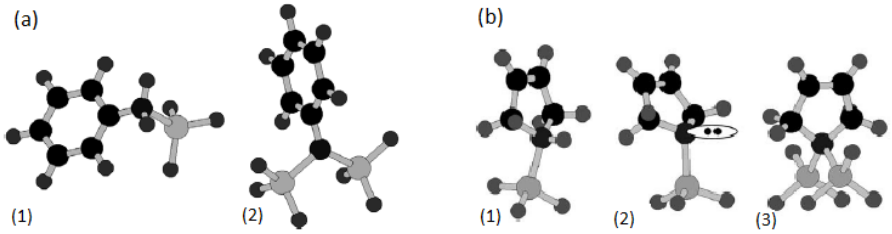

Figure 1.23. Schematic diagram of organometalic molecular models used in quantum-chemical analysis of the chemisorptions on GaN(0001)-(1 x 1). (a) Aniline bonded to (1) one GaH_3 and (2) to two GaH_3 groups. (b) 3-pyrroline bonded to (1) one GaH_3; (2) shows the non-bonded lonely pair (NBLP) of the N of 3-pyrroline, and (3) shows the bonding of the NBLP to a second GaH_3. The large, lightly shaded spheres, are Ga atoms and the two dots represent a pair of free electrons.[149, 151]

In 2005 appeared the first report by Kang *et al.* on the direct chemical functionalization of an AlGaN/GaN HEMT surface with silane molecules with an amine terminal group which was used to react with biotin [141]. Despite the good results in detection of Streptavidin-A protein, which indicated a strong binding with biotin and produced a decrease in the source-drain current when exposed to a streptavidin solution, no experimental evidence of the formation of a covalent bond was reported. Were Baur *et. al.* [153] who reported for the first time the covalent functionalization of hydroxilated GaN and AlN surfaces by means of X-ray photoelectron spectroscopy (XPS), confirming also the success of the previous work done by Kang *et al.* [141] of covalent bonding of silane molecules with GaN. For this purpose Baur *et al.* [153] functionalized the GaN and AlN surfaces with two different organic molecules: octadecyltrimethoxysilane (ODTMS) and (3-aminopropyl)triethoxysilane (APTES) by immersing the substrates into a solution of ODTMS or APTES under sonication. This demonstration offered a great flexibility since the possible applications of alkylsilane SAMs are determined only by their functional groups. In the case of the silane molecules

used by Bauer *et. al.*, the hydrophobic methyl groups of ODTMS could be used as a starting point for the deposition of polymer supported lipid membranes, whereas the reactive amino group of APTES were very suitable for the immobilization of biomolecules. Other chemical functionalization works with silane molecules on GaN (0001) surfaces and GaN nanowires (NW) included mercaptopropyl trimethoxysilane (MPTMS) [154-155], APTES [156-159], and octadecyltrichlorosilane (OTS) [160], corroborating in all cases the covalent bonding between silicon and the oxygen of the hydroxilated surface of GaN (see Figure 1.24).

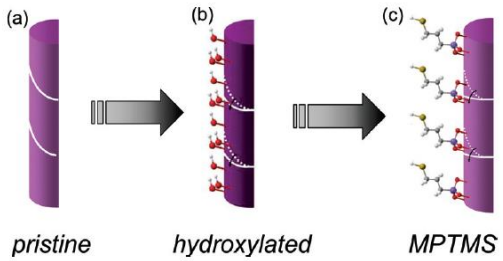

Figure 1.24. Study of the surface passivation of GaN NWs with the functionalization with MPTMS. Schematic illustration of the proposed surface band bending (white line) conditions of the GaN NWs with respect to different surface conditions to explain the observed results: (a) pristine GaN NWs, (b) OH-GaN NWs, and (c) MPTMS-GaN NWs. MPTMS is linked to GaN via the hydroxyl groups on the surface [155].

More detailed studies of the mechanism of silanization of the GaN surface were performed by Arranz *et al.* [156] studying the influence of the surface hydroxylation on different doped and undoped GaN substrates by means of angle-resolved XPS. They found that, depending on the conducting type of the GaN substrate, strong differences were observed on the APTES growth mode on the GaN surface. These differences were associated with the different characteristics of chemical hydroxylation in these surfaces that leads to important changes in the hydroxyl groups density on the GaN surface. This is an important assumption, since, depending on the density of surface hydroxyl groups, different mechanism of APTES attachment to the GaN were proposed, varying from a monolayer on *p*-type GaN to a multilayer-like on *n*-

type GaN. The monolayer-like growth is attributed to a high density of hydroxyl groups on the GaN surface whereas the multilayer-like growth is attributed to a low density of hydroxyl groups on the GaN surface.

Despite all the progress done in chemical functionalization of GaN surface with silane molecules, a study on the stability of silanized GaN surfaces in water revealed that after soaking in aqueous solutions for periods of hours to days, a loss of the SAMs on GaN was observed [160]. This was a setback to this functionalization strategy since it was conceived as a first step towards the fabrication of biosensors based on GaN. Since biosensing predominantly involves biological mediums that can be considered as aqueous environments, the lifetime of such a sensor is limited by the instability of the gallium oxide layer needed to react with the silicon of the silane molecule.

A different strategy for the chemical functionalization of the GaN surface was carried out by Guo *et al.* [161] on GaN NWs using $SiCl_4$. The $SiCl_4$ functionalization was used as an intermediate step for the posterior reaction with polietilenglicol (PEG)-biotin (see Figure 1.25).

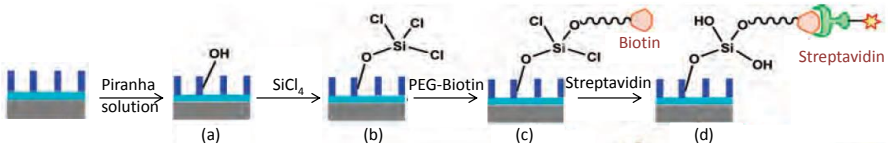

Figure 1.25. Schematic diagram of the (a) chemical activation of the GaN surface and (b) functionalization with $SiCl_4$ prior to the (c) linkage of PEG-biotin for the (d) detection of streptavidin. (Image adapted from [161])

Nevertheless, not all the chemical functionalization approaches of GaN surfaces via the hydroxilated GaN surface are based on the use of silane molecules. One additional approach to chemically functionalize the GaN surface is via phosphonic acid linkages [162-163]. Phosphonic acids are interesting for the chemical functionalization of GaN surfaces because, unlike silanization reactions, the covalent bonding does not occur only via the reaction with the –OH groups at the GaN surface, but it can also occur on the oxidized GaN layer. These results demonstrated that thermal grafting of

organophosphonic acids to oxidized GaN surfaces was successful; exhibiting also a great stability under aqueous conditions for one week compared with silane molecules that only lasted for a period of a few hours to a few days.

In order to avoid the grafting of organic molecules to the oxygen atoms present in oxidized and hydroxilated GaN surfaces Kim *et al.* proposed another approach to functionalize GaN based on generating hydrogen-terminated GaN surfaces and using UV light for the photochemical functionalization with 1-alkenes (see Figure 1.26) [164]. In this case, the 1-alkene used was 10-trifluoro-acetamide-1-decene (TFAAD), which, after the functionalization reaction, the trifluoracetic (TFA) protecting group was removed and the amine left at the end of the chain reacted with 4-(*N*-maleimidomethyl)cyclohexane-1-carboxylate (SSMCC), which was at the end linked to a DNA prove.

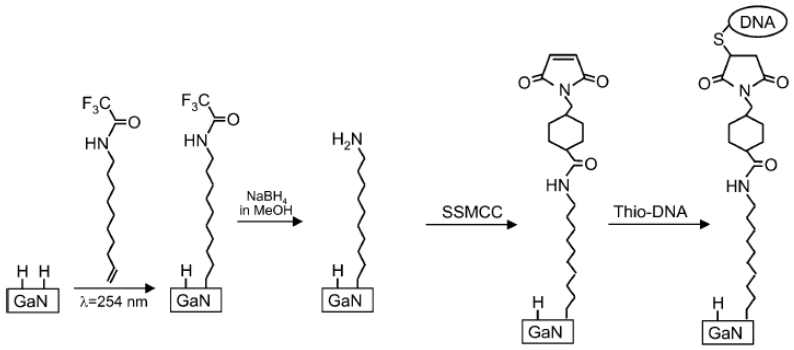

Figure 1.26. Reaction scheme of the photofunctionalization of GaN with an alkene, and the posterior chemical modifications to finally obtain a DNA strand linked to GaN [164].

A more recent publication based on previous photochemical functionalization of GaN with TFAAD [164] demonstrated also the thermal functionalization of GaN surfaces with 1-alkenes [165]. In that case, the 1-alkenes used for thermal and photochemical functionalization were TFAAD and 5-bromo-1-pentene (BP). XPS analyses demonstrated that the grafting of the alkene is not directly to the Ga atoms, but to the oxygen atoms on the surface of GaN via a Ga-O-C bond, since the previous step of hydrogenation of the surface was not performed in this experiment.

Formation of amine groups on the surface of GaN, which can then react directly with biomolecules [166], is another approach made by Stine *et al.* for the functionalization of GaN. The method proposed for the production of amine groups on the GaN surface was the exposure of GaN to a glow discharge plasma fed with humidified air. To test the reactivity of the primary amines formed on the surface, a covalent immobilization of a NeutrAvidin layer, a protein, was performed and demonstrated by FT-IR and by fluorescent biotin-binding assays.

The direct functionalization of organic molecules to the Ga atom of the outermost layer of GaN, creating a Ga-C bond, was also achieved with alkyl groups via sequential wet chemical chlorine activation, Grignard reaction process [167].

Finally, the functionalization of the GaN surface with amino acids [168], and peptides [169-170] has also been achieved via adsorption and the covalent linking to GaN. The responsible for the adsorption of peptides on GaN surface was found to be in the range of hydrophobic strengths. However, for more specificity, the whole sequence of peptide is needed; even so, a primordial role can be attributed to the hydrophobic domain of the peptide [169]. Studies on the functionalization of GaN surfaces with amino acids were performed by Ariaga *et al.* [168] They found that among the amino acids used, only cysteine was attached to GaN, due to the thiol group present in this aminoacid. Estephan *et al.* [169] designed a 12-mer (peptide of 12 amino acids) probe with a specific domain for the binding. The subtle interplay of mostly non-polar hydrophobic and some polar aminoacidic residues defined the high affinity adhesion properties of the peptide on the GaN surface.

As can be seen a lot of efforts have been done in the functionalization of GaN due to its excellent electrical properties and its real potential sensor applications.

Although there are reports on GaAs functionalization with aryldiazonium salts [171], so far to our knowledge there are no reports and evidence of GaN functionalization with aryldiazonium salts, which would

provide an interesting approach for chemical functionalization of GaN surfaces.

1.5 Aims of the thesis

The main objectives of this thesis are the synthesis and characterization of both, undoped and doped porous GaN particles and layers, and explore their surface chemical functionalization with silane molecules and aryldiazonium salts.

In this thesis all the porous GaN particles and layers have been growth in one single step by the direct reaction between metallic gallium and ammonia in a horizontal tubular CVD furnace, avoiding posterior treatments of the GaN samples to induce the porosity. The doping with Mg, Si and the ternary alloy formation with In, has been also done in the same CVD furnace with no posterior treatment of the sample more than the thermal annealing necessary for the activation of the acceptor behavior of Mg. The samples were characterized morphologically by scanning electron microscope (SEM), the structural characterization was carried out by X-ray diffraction (XRD) and Raman scattering, and the luminescence properties were investigated with the aim of photoluminescence and cathodoluminescence.

For the chemical functionalization of the surface of GaN the silane reagents were commercially available and all the aryldiazonium salts were synthesized and characterized in situ via nuclear magnetic resonance (NMR) and Fourier transform infrared spectroscopy (FT-IR). To assess the proper functionalization of the GaN surface a fluorescent dye was linked to the functionalized molecule and the presence of the dye was determined with the aim of a fluorescence microscope.

Chapter 2 is dedicated to describe the experimental techniques used in this work. In this chapter are described all the crystal growth/deposition techniques and the characterization techniques employed for the realization of this thesis, as well as some of the standard procedures used in organic

chemistry to dry, distillate and degas solvents needed for the synthesis of aryldiazonium salts.

In Chapter 3 are described some of the experimental parameters needed to full-fill a complete study of the influence of the reaction parameters on the growth of nanoporous GaN particles. The experimental parameters studied in this chapter are the effect of the shape of the gallium container, the quantity of Ga, the deposition time, the catalyst and the substrate. The morphology of the particles was observed by SEM, the luminescence properties were recorded by cathodoluminescence (CL) and reflectance measurements, and the structural analysis was characterized by XRD.

Chapter 4 continues the previous studies started in our group on the Mg-doping of GaN using magnesium acetylacetonate as a Mg precursor and also describes the experimental procedure for the doping of porous GaN particles with Si, and the deposition of InGaN ternary alloys. The doped GaN and InGaN ternary alloys where characterized morphologically by SEM, and the luminescence properties were characterized by CL. Also, the elemental composition of Mg-doped porous GaN layers deposited on GaN was characterized by electron probe microanalyzer (EPMA).

In Chapter 5 epitaxial layers of porous GaN grown on GaN/sapphire substrates are studied. We focused the study on the characterization of the porosity (porosity degree, pore size, pore height) and how it affects the wetting properties and also we studied the luminescence properties and the relationship with the structural defects. The study of the porosity of the porous GaN layers was carried out with atomic force microscope (AFM) and SEM, while the luminescence properties were analyzed by PL and CL, and the structural characterization was analyzed by resonant Raman scattering.

Chapter 6 is focused on the topic of surface chemical functionalization of GaN with silane molecules and diazonium salts. In this chapter are described all the chemical reactions and procedures for the synthesis of arydiazonium salts with the NMR and FT-IR spectra confirming the chemical structure of the desired molecule. Also the chemical

functionalization with silanes and diazonium salts procedure is explained as well as some discussion of the results obtained after the functionalization of GaN surfaces.

As a final section, the main conclusions of this thesis are presented.

References

[1] Shuji, N.; Masayuki, S.; Shin-ichi, N.; Naruhito, I.; Takao, Y.; Toshio, M.; Hiroyuki, K.; Yasunobu, S., Characteristics of InGaN multi-quantum-well-structure laser diodes. *Appl. Phys. Lett.* **1996,** *68* (23), 3269-3271.

[2] Morkoç, H., *Handbook of Nitride Semiconductors and Devices: GaN-Based Optical and Electronic Devices*. Wiley-VCH Verlag GmbH & Co.: 2009; Vol. 3.

[3] *White paper Blu-ray Disc™ format*. 3 ed.; Blu-ray Disc Association: 2012.

[4] https://en.wikipedia.org/wiki/Blu-ray (accessed 01/05/2017).

[5] http://www.popularmechanics.com/science/green-tech/a6040/will-led-light-bulbs-best-cfls-and-incandescents/ (accessed 05/05/2017).

[6] Principi, P.; Fioretti, R., A comparative life cycle assessment of luminaires for general lighting for the office – compact fluorescent (CFL) vs Light Emitting Diode (LED) – a case study. *Journal of Cleaner Production* **2014,** *83*, 96-107.

[7]

[8] http://www.ledsmagazine.com/articles/2012/02/sil-2012-led-cost-reduction-to-come-from-manufacturing.html (accessed 05/05/2017).

[9] Yang, C. C.; Lin, C. F.; Lin, C. M.; Chang, C. C.; Chen, K. T.; Chien, J. F.; Chang, C. Y., Improving light output power of InGaN-based light emitting diodes with pattern-nanoporous p-type GaN:Mg surfaces. *Appl. Phys. Lett.* **2008,** *93* (20), 203103.

[10] Fujii, T.; Gao, Y.; Sharma, R.; Hu, E. L.; DenBaars, S. P.; Nakamura, S., Increase in the extraction efficiency of GaN-based light-emitting diodes via surface roughening. *Appl. Phys. Lett.* **2004,** *84* (6), 855-857.

[11] Saito, W.; Takada, Y.; Kuraguchi, M.; Tsuda, K.; Omura, I., Recessed-gate structure approach toward normally off high-Voltage AlGaN/GaN HEMT for power electronics applications. *IEEE Trans. Electron Devices* **2006,** *53* (2), 356-362.

[12] Okamoto, Y.; Ando, Y.; Hataya, K.; Nakayama, T.; Miyamoto, H.; Inoue, T.; Senda, M.; Hirata, K.; Kosaki, M.; Shibata, N.; Kuzuhara, M., Improved power performance for a recessed-gate AlGaN-GaN heterojunction FET with a field-modulating plate. *IEEE Trans. Microwave Theory Tech.* **2004,** *52* (11), 2536-2540.

[13] Huang, W.; Chow, T. P.; Niiyama, Y.; Nomura, T.; Yoshida, S. In *Lateral Implanted RESURF GaN MOSFETs with BV up to 2.5 kV*, 2008 20th International Symposium on Power Semiconductor Devices and IC's, 18-22 May 2008; 2008; pp 291-294.

[14] Pearton, S. J.; Ren, F.; Zhang, A. P.; Lee, K. P., Fabrication and performance of GaN electronic devices. *Materials Science and Engineering: R: Reports* **2000,** *30* (3–6), 55-212.

[15] Li, S. S., *Semiconductor physical electronics*. 2 ed.; Springer-Verlag New York: 2006; p 697.

[16] Hong, Y. J.; Lee, C.-H.; Yoon, A.; Kim, M.; Seong, H.-K.; Chung, H. J.; Sone, C.; Park, Y. J.; Yi, G.-C., Visible-Color-Tunable Light-Emitting Diodes. *Adv. Mater.* **2011,** *23* (29), 3284-3288.

[17] Xu, G. Y.; Salvador, A.; Kim, W.; Fan, Z.; Lu, C.; Tang, H.; Morkoç, H.; Smith, G.; Estes, M.; Goldenberg, B.; Yang, W.; Krishnankutty, S., High speed, low noise ultraviolet photodetectors based on GaN p-i-n and AlGaN(p)-GaN(i)-GaN(n)structures. *Appl. Phys. Lett.* **1997,** *71* (15), 2154-2156.

[18] Anderson, T.; Ren, F.; Pearton, S.; Kang, B. S.; Wang, H.-T.; Chang, C.-Y.; Lin, J., Advances in Hydrogen, Carbon Dioxide, and Hydrocarbon Gas Sensor Technology Using GaN and ZnO-Based Devices. *Sensors* **2009,** *9* (6), 4669.

[19] Kang, B. S.; Wang, H. T.; Lele, T. P.; Tseng, Y.; Ren, F.; Pearton, S. J.; Johnson, J. W.; Rajagopal, P.; Roberts, J. C.; Piner, E. L.; Linthicum, K. J., Prostate specific antigen detection using AlGaN⁄GaN high electron mobility transistors. *Appl. Phys. Lett.* **2007,** *91* (11), 112106.

[20] Chen, K. H.; Kang, B. S.; Wang, H. T.; Lele, T. P.; Ren, F.; Wang, Y. L.; Chang, C. Y.; Pearton, S. J.; Dennis, D. M.; Johnson, J. W.; Rajagopal, P.; Roberts, J. C.; Piner, E. L.; Linthicum, K. J., c-erbB-2 sensing using AlGaN⁄GaN high electron mobility transistors for breast cancer detection. *Appl. Phys. Lett.* **2008,** *92* (19), 192103.

[21] Chu, B. H.; Kang, B. S.; Hung, S. C.; Chen, K. H.; Ren, F.; Sciullo, A.; Gila, B. P.; Pearton, S. J., Aluminum Gallium Nitride (GaN)/GaN High Electron Mobility Transistor-Based Sensors for Glucose Detection in Exhaled Breath Condensate. *Journal of Diabetes Science and Technology* **2010,** *4* (1), 171-179.

[22] Kang, B. S.; Pearton, S. J.; Chen, J. J.; Ren, F.; Johnson, J. W.; Therrien, R. J.; Rajagopal, P.; Roberts, J. C.; Piner, E. L.; Linthicum, K. J., Electrical detection of deoxyribonucleic acid hybridization with AlGaN⁄GaN high electron mobility transistors. *Appl. Phys. Lett.* **2006,** *89* (12), 122102.

[23] Powell, R. C.; Lee, N. E.; Kim, Y. W.; Greene, J. E., Heteroepitaxial wurtzite and zinc-blende structure GaN grown by reactive-ion molecular-beam epitaxy: Growth kinetics, microstructure, and properties. *J. Appl. Phys.* **1993,** *73* (1), 189-204.

[24] Leszczynski, M.; Teisseyre, H.; Suski, T.; Grzegory, I.; Bockowski, M.; Jun, J.; Porowski, S.; Pakula, K.; Baranowski, J. M.; Foxon, C. T.; Cheng, T. S., Lattice parameters of gallium nitride. *Appl. Phys. Lett.* **1996,** *69* (1), 73-75.

[25] Wu, J.; Walukiewicz, W.; Yu, K. M.; III, J. W. A.; Haller, E. E.; Lu, H.; Schaff, W. J.; Saito, Y.; Nanishi, Y., Unusual properties of the fundamental band gap of InN. *Appl. Phys. Lett.* **2002,** *80* (21), 3967-3969.

[26] Morkoç, H., *Nitride Semiconductors and Devices*. 1 ed.; Springer-Verlag Berlin Heidelberg: 1999.

[27] Balachandran, P. V.; Theiler, J.; Rondinelli, J. M.; Lookman, T., Materials Prediction via Classification Learning. *Scientific Reports* **2015,** *5*, 13285.

[28] Maruska, H. P.; Tietjen, J. J., The preparation and properties of vapor-deposited single-crystalline GaN. *Appl. Phys. Lett.* **1969,** *15* (10), 327-329.

[29] Pankove, J. I., Electrolytic Etching of GaN. *J. Electrochem. Soc.* **1972,** *119* (8), 1118-1119.

[30] Morimoto, Y., Few Characteristics of Epitaxial GaN — Etching and Thermal Decomposition. *J. Electrochem. Soc.* **1974,** *121* (10), 1383-1384.

[31] Weyher, J. L.; Brown, P. D.; Rouvière, J. L.; Wosinski, T.; Zauner, A. R. A.; Grzegory, I., Recent advances in defect-selective etching of GaN. *J. Cryst. Growth* **2000,** *210* (1–3), 151-156.

[32] Stocker, D. A.; Schubert, E. F.; Redwing, J. M., Crystallographic wet chemical etching of GaN. *Appl. Phys. Lett.* **1998,** *73* (18), 2654-2656.

[33] Shibata, H.; Waseda, Y.; Ohta, H.; Kiyomi, K.; Shimoyama, K.; Fujito, K.; Nagaoka, H.; Kagamitani, Y.; Simura, R.; Fukuda, T., High Thermal Conductivity of Gallium Nitride (GaN) Crystals Grown by HVPE Process. *MATERIALS TRANSACTIONS* **2007,** *48* (10), 2782-2786.

[34] Slack, G. A., Nonmetallic crystals with high thermal conductivity. *J. Phys. Chem. Solids* **1973,** *34* (2), 321-335.

[35] Weitzel, C. E.; Palmour, J. W.; Carter, C. H.; Moore, K.; Nordquist, K. K.; Allen, S.; Thero, C.; Bhatnagar, M., Silicon carbide high-power devices. *IEEE Trans. Electron Devices* **1996,** *43* (10), 1732-1741.

[36] Jain, S. C.; Willander, M.; Narayan, J.; Overstraeten, R. V., III–nitrides: Growth, characterization, and properties. *J. Appl. Phys.* **2000,** *87* (3), 965-1006.

[37] Morkoç, H.; Strite, S.; Gao, G. B.; Lin, M. E.; Sverdlov, B.; Burns, M., Large-band-gap SiC, III-V nitride, and II-VI ZnSe-based semiconductor device technologies. *J. Appl. Phys.* **1994,** *76* (3), 1363-1398.

[38] Dmitriev, V. A.; Irvine, K. G.; Jr., C. H. C.; Kuznetsov, N. I.; Kalinina, E. V., Electric breakdown in GaN p-n junctions. *Appl. Phys. Lett.* **1996,** *68* (2), 229-231.

[39] Mishra, U. K.; Shen, L.; Kazior, T. E.; Wu, Y. F., GaN-Based RF Power Devices and Amplifiers. *Proc. IEEE* **2008,** *96* (2), 287-305.

[40] Ambacher, O.; Foutz, B.; Smart, J.; Shealy, J. R.; Weimann, N. G.; Chu, K.; Murphy, M.; Sierakowski, A. J.; Schaff, W. J.; Eastman, L. F.; Dimitrov, R.; Mitchell, A.; Stutzmann, M., Two dimensional electron gases induced by spontaneous and piezoelectric polarization in undoped and doped AlGaN/GaN heterostructures. *J. Appl. Phys.* **2000,** *87* (1), 334-344.

[41] Millán, J.; Godignon, P.; Perpiñà, X.; Pérez-Tomás, A.; Rebollo, J., A Survey of Wide Bandgap Power Semiconductor Devices. *IEEE Transactions on Power Electronics* **2014,** *29* (5), 2155-2163.

[42] Nakamura, S.; Chichibu, S. F., *Introduction to Nitride Semiconductor Blue Lasers and Light Emitting Diodes*. CRC Press: 2000.

[43] Yao, T. H., Soon-Ku, *Oxide and Nitride Semiconductors. Processing, Properties, and Applications*. Springer Berlin Heidelberg: 2009.

[44] Pearton, S. J., *Optoelectronic properties of semiconductors and superlattices*. CRC Press: 2000; Vol. 7.

[45] Zhao, D. G.; Xu, S. J.; Xie, M. H.; Tong, S. Y.; Yang, H., Stress and its effect on optical properties of GaN epilayers grown on Si(111), 6H-SiC(0001), and c-plane sapphire. *Appl. Phys. Lett.* **2003,** *83* (4), 677-679.

[46] Cheng, K.; Degroote, S.; Leys, M.; Germain, M.; Borghs, G., Strain effects in GaN epilayers grown on different substrates by metal organic vapor phase epitaxy. *J. Appl. Phys.* **2010,** *108* (7), 073522.

[47] Zhang, L.-.; Cheng, K.; Degroote, S.; Leys, M.; Germain, M.; Borghs, G., Strain effects in GaN epilayers grown on different substrates by metal organic vapor phase epitaxy. *J. Appl. Phys.* **2010,** *108* (7), 073522.

[48] Manasreh, O., *III-Nitride Semiconductors: Electrical, Structural and Defects Properties*. Elsevier: Amsterdam, 2000; p 448.

[49] Glaser, E. R.; Freitas, J. A.; Shanabrook, B. V.; Koleske, D. D.; Lee, S. K.; Park, S. S.; Han, J. Y., Optically detected magnetic resonance of (effective-mass) shallow acceptors in Si-doped GaN homoepitaxial layers. *Phys. Rev. B* **2003,** *68* (19), 195201.

[50] Reshchikov, M. A.; Morkoç, H., Luminescence properties of defects in GaN. *J. Appl. Phys.* **2005,** *97*.

[51] Reshchikov, M. A.; Morkoç, H., Luminescence properties of defects in GaN. *Journal of Applied Physics* **2005,** *97* (6), 061301.

[52] Julkarnain, M.; Fukuda, T.; Kamata, N.; Arakawa, Y., A direct evidence of allocating yellow luminescence band in undoped GaN by two-wavelength excited photoluminescence. *Appl. Phys. Lett.* **2015,** *107* (21), 212102.

[53] Limpijumnong, S.; Van de Walle, C. G., Diffusivity of native defects in GaN. *Phys. Rev. B* **2004,** *69* (3), 035207.

[54] Kaufmann, U.; Kunzer, M.; Obloh, H.; Maier, M.; Manz, C.; Ramakrishnan, A.; Santic, B., Origin of defect-related photoluminescence bands in doped and nominally undoped GaN. *Phys. Rev. B* **1999,** *59* (8), 5561-5567.

[55] Lyons, J. L.; Janotti, A.; Walle, C. G. V. d., Carbon impurities and the yellow luminescence in GaN. *Appl. Phys. Lett.* **2010,** *97* (15), 152108.

[56] Kamyczek, P.; Placzek-Popko, E.; Kolkovsky, V.; Grzanka, S.; Czernecki, R., A deep acceptor defect responsible for the yellow luminescence in GaN and AlGaN. *J. Appl. Phys.* **2012,** *111* (11), 113105.

[57] Reshchikov, M. A.; Morkoç, H.; Park, S. S.; Lee, K. Y., Yellow and green luminescence in a freestanding GaN template. *Appl. Phys. Lett.* **2001,** *78* (20), 3041-3043.

[58] Reshchikov, M. A.; Morkoç, H.; Molnar, R. J.; Tsvetkov, D.; Dmitriev, V., Blue Luminescence in Undoped and Zn-doped GaN. *MRS Proceedings* **2011,** *743*.

[59] Reshchikov, M. A.; Morkoç, H.; Park, S. S.; Lee, K. Y., Photoluminescence study of deep-level defects in undoped GaN. *MRS Proceedings* **2011,** *693*.

[60] Johnson, W. C.; Parson, J. B.; Crew, M. C., Nitrogen Compounds of Gallium. III. *The Journal of Physical Chemistry* **1931,** *36* (10), 2651-2654.

[61] Juza, R.; Hahn, H., Über die Kristallstrukturen von Cu3N, GaN und InN Metallamide und Metallnitride. *Z. Anorg. Allg. Chem.* **1938,** *239* (3), 282-287.

[62] Grimmeiss, H. G.; Koelmans, H., Über die Kantenemission und andere Emissionen des GaN. *Zeitschrift für Naturforschung A* **1959,** *14* (3), 264-271.

[63] Utsumi, W.; Saitoh, H.; Kaneko, H.; Watanuki, T.; Aoki, K.; Shimomura, O., Congruent melting of gallium nitride at 6 GPa and its application to single-crystal growth. *Nat Mater* **2003,** *2* (11), 735-738.

[64] Izabella, G., High pressure growth of bulk GaN from solutions in gallium. *J. Phys.: Condens. Matter* **2001,** *13* (32), 6875.

[65] Grzegory, I.; Jun, J.; Boćkowski, M.; Krukowski, S. T.; Wróblewski, M.; Łucznik, B.; Porowski, S., III–V Nitrides—thermodynamics and crystal growth at high N2 pressure. *J. Phys. Chem. Solids* **1995,** *56* (3), 639-647.

[66] Dwiliński, R.; Doradziński, R.; Garczyński, J.; Sierzputowski, L. P.; Puchalski, A.; Kanbara, Y.; Yagi, K.; Minakuchi, H.; Hayashi, H., Bulk ammonothermal GaN. *J. Cryst. Growth* **2009,** *311* (10), 3015-3018.

[67] Kucharski, R.; Rudziński, M.; Zając, M.; Doradziński, R.; Garczyński, J.; Sierzputowski, L.; Kudrawiec, R.; Serafińczuk, J.; Strupiński, W.; Dwiliński, R., Nonpolar GaN substrates grown by ammonothermal method. *Appl. Phys. Lett.* **2009,** *95* (13), 131119.

[68] Mynbaeva, M.; Titkov, A.; Kryganovskii, A.; Ratnikov, V.; Mynbaev, K.; Huhtinen, H.; Laiho, R.; Dmitriev, V., Structural characterization and strain relaxation in porous GaN layers. *Appl. Phys. Lett.* **2000,** *76* (9), 1113-1115.

[69] Vajpeyi, A. P.; Chua, S. J.; Tripathy, S.; Fitzgerald, E. A.; Liu, W.; Chen, P.; Wang, L. S., High Optical Quality Nanoporous GaN Prepared by Photoelectrochemical Etching. *Electrochem. Solid-State Lett.* **2005,** *8* (4), G85-G88.

[70] Díaz, D. J.; Williamson, T. L.; Adesida, I.; Bohn, P. W.; Molnar, R. J., Morphology evolution and luminescence properties of porous GaN generated via Pt-assisted electroless etching of hydride vapor phase epitaxy GaN on sapphire. *J. Appl. Phys.* **2003,** *94* (12), 7526-7534.

[71] Mahmood, A.; Ahmed, N. M.; Yusof, Y.; Kwong, Y. F.; Siang, C. L.; Abd, H. R.; Hassan, Z., A Novel AC Technique for High Quality Porous GaN. *International Journal of Electrochemical Science* **2013,** *8*, 5801-5809.

[72] Mynbaeva, M.; Bazhenov, N.; Mynbaev, K.; Evstropov, V.; Saddow, S. E.; Koshka, Y.; Melnik, Y., Photoconductivity in Porous GaN Layers. *Physica Status Solidi (B)* **2001,** *228* (2), 589-592.

[73] Li, X.; Kim, Y.-W.; Bohn, P. W.; Adesida, I., In-plane bandgap control in porous GaN through electroless wet chemical etching. *Appl. Phys. Lett.* **2002,** *80* (6), 980-982.

[74] Wang, R.; Liu, D.; Zuo, Z.; Yu, Q.; Feng, Z.; Xu, X., Metal-assisted electroless fabrication of nanoporous p-GaN for increasing the light extraction efficiency of light emitting diodes. *AIP Advances* **2012,** *2* (1), 012109.

[75] Schubert, E. F., *Light-Emitting Diodes*. 2 ed.; Cambridge University Press: 2006; p 422.

[76] Seok-In, N.; Ga-Young, H.; Dae-Seob, H.; Seok-Soon, K.; Ja-Yeon, K.; Jae-Hong, L.; Dong-Joon, K.; Kyeong-Ik, M.; Seong-Ju, P., Selective wet etching of p-GaN for efficient GaN-based light-emitting diodes. *IEEE Photonics Technology Letters* **2006,** *18* (14), 1512-1514.

[77] David, A.; Fujii, T.; Moran, B.; Nakamura, S.; DenBaars, S. P.; Weisbuch, C.; Benisty, H., Photonic crystal laser lift-off GaN light-emitting diodes. *Appl. Phys. Lett.* **2006,** *88* (13), 133514.

[78] Kang, E.-J.; Huh, C.; Lee, S.-H.; Jung, J.-J.; Lee, S.-J.; Park, S.-J., Improvement in Light-Output Power of InGaN/GaN LED by Formation of Nanosize Cavities on p -GaN Surface. *Electrochem. Solid-State Lett.* **2005,** *8* (12), G327-G329.

[79] Wei, T.; Kong, Q.; Wang, J.; Li, J.; Zeng, Y.; Wang, G.; Li, J.; Liao, Y.; Yi, F., Improving light extraction of InGaN-based light emitting diodes with a roughened p-GaN surface using CsCl nano-islands. *Opt. Express* **2011,** *19* (2), 1065-1071.

[80] Carvajal, J. J.; Gomez, N.; Bai, J.; Dudley, M.; Rojo, J. C., Synthesis of nanoporous GaN crystalline particles by chemical vapor deposition. *SPIE Proceedings* **2006,** *6121*, 61210E.

[81] Bilousov, O. V.; Carvajal, J. J.; Mena, J.; Martínez, O.; Jiménez, J.; Geaney, H.; Díaz, F.; Aguiló, M.; O'Dwyer, C., Epitaxial growth of (0001) oriented porous GaN layers by chemical vapour deposition. *CrystEngComm* **2014,** *16* (44), 10255-10261.

[82] Carvajal, J. J.; Bilousov, O. V.; Drouin, D.; Aguiló, M.; Díaz, F.; Rojo, J. C., Chemical Vapor Deposition of Porous GaN Particles on Silicon. *Microsc. Microanal.* **2012,** *18* (4), 905-911.

[83] Pankove, J. I.; Miller, E. A.; Richman, D.; Berkeyheiser, J. E., Electroluminescence in GaN. *J. Lumin.* **1971,** *4* (1), 63-66.

[84] Pankove, J. I.; Miller, E. A.; Berkeyheiser, J. E., GaN blue light-emitting diodes. *J. Lumin.* **1972,** *5* (1), 84-86.

[85] Akasaki, I.; Amano, H.; Koide, Y.; Hiramatsu, K.; Sawaki, N., Effects of AlN buffer layer on crystallographic structure and on electrical and optical properties of GaN and Ga1−xAlxN (0 < x ≦ 0.4) films grown on sapphire substrate by MOVPE. *J. Cryst. Growth* **1989,** *98* (1), 209-219.

[86] Neugebauer, J.; Walle, C. G. V. d., Gallium vacancies and the yellow luminescence in GaN. *Appl. Phys. Lett.* **1996,** *69* (4), 503-505.

[87] Nakamura, S.; Pearton, S.; Fasol, G., *The Blue Laser Diode. The Complete Story*. 2 ed.; Springer-Verlag Berlin Heidelberg: 2000.

[88] Brochen, S.; Brault, J.; Chenot, S.; Dussaigne, A.; Leroux, M.; Damilano, B., Dependence of the Mg-related acceptor ionization energy with the acceptor concentration in p-type GaN layers grown by molecular beam epitaxy. *Appl. Phys. Lett.* **2013,** *103* (3), 032102.

[89] Hiroshi, A.; Masahiro, K.; Kazumasa, H.; Isamu, A., P-Type Conduction in Mg-Doped GaN Treated with Low-Energy Electron Beam Irradiation (LEEBI). *Jpn. J. Appl. Phys.* **1989,** *28* (12A), L2112.

[90] Neugebauer, J.; Walle, C. G. V. d., Role of hydrogen in doping of GaN. *Appl. Phys. Lett.* **1996,** *68* (13), 1829-1831.

[91] Shuji, N.; Takashi, M.; Masayuki, S.; Naruhito, I., Thermal Annealing Effects on P-Type Mg-Doped GaN Films. *Jpn. J. Appl. Phys.* **1992,** *31* (2B), L139.

[92] Shuji, N.; Naruhito, I.; Masayuki, S.; Takashi, M., Hole Compensation Mechanism of P-Type GaN Films. *Jpn. J. Appl. Phys.* **1992,** *31* (5R), 1258.

[93] Neugebauer, J.; Van de Walle, C. G., Atomic geometry and electronic structure of native defects in GaN. *Phys. Rev. B* **1994,** *50* (11), 8067-8070.

[94] Lee, J. K.; Hyeon, G. Y.; Tawfik, W. Z.; Choi, H. S.; Ryu, S.-W.; Jeong, T.; Jung, E.; Kim, H., Electrochemical removal of hydrogen atoms in Mg-doped GaN epitaxial layers. *J. Appl. Phys.* **2015,** *117* (18), 185702.

[95] https://www.nobelprize.org/nobel_prizes/physics/laureates/2014/press.html (accessed 16/05/2017).

[96] Kozodoy, P.; Xing, H.; DenBaars, S. P.; Mishra, U. K.; Saxler, A.; Perrin, R.; Elhamri, S.; Mitchel, W. C., Heavy doping effects in Mg-doped GaN. *J. Appl. Phys.* **2000,** *87* (4), 1832-1835.

[97] Pearton, S. J.; Vartuli, C. B.; Zolper, J. C.; Yuan, C.; Stall, R. A., Ion implantation doping and isolation of GaN. *Appl. Phys. Lett.* **1995,** *67* (10), 1435-1437.

[98] Rubin, M.; Newman, N.; Chan, J. S.; Fu, T. C.; Ross, J. T., p-type gallium nitride by reactive ion-beam molecular beam epitaxy with ion implantation, diffusion, or coevaporation of Mg. *Appl. Phys. Lett.* **1994,** *64* (1), 64-66.

[99] Lieten, R. R.; Motsnyi, V.; Zhang, L.; Cheng, K.; Leys, M.; Degroote, S.; Buchowicz, G.; Dubon, O.; Borghs, G., Mg doping of GaN by molecular beam epitaxy. *J. Phys. D: Appl. Phys.* **2011,** *44* (13), 135406.

[100] Usikov, A.; Kovalenkov, O.; Soukhoveev, V.; Ivantsov, V.; Syrkin, A.; Dmitriev, V.; Nikiforov, A. Y.; Sundaresan, S. G.; Jeliazkov, S. J.; Davydov, A. V., Electrical and optical properties of thick highly doped p-type GaN layers grown by HVPE. *physica status solidi (c)* **2008,** *5* (6), 1829-1831.

[101] Bilousov, O. V.; Geaney, H.; Carvajal, J. J.; Zubialevich, V. Z.; Parbrook, P. J.; Giguère, A.; Drouin, D.; Díaz, F.; Aguiló, M.; O'Dwyer, C., Fabrication of p-type porous GaN on silicon and epitaxial GaN. *Appl. Phys. Lett.* **2013,** *103* (11), 112103.

[102] Moore, W. J.; Freitas, J. A.; Lee, S. K.; Park, S. S.; Han, J. Y., Magneto-optical studies of free-standing hydride-vapor-phase epitaxial GaN. *Phys. Rev. B* **2002,** *65* (8), 081201.

[103] Cunningham, R. D.; Brander, R. W.; Knee, N. D.; Wickenden, D. K., Variation of photoluminescence with carrier concentration in GaN. *J. Lumin.* **1972,** *5* (1), 21-31.

[104] Nakamura, S., GaN Growth Using GaN Buffer Layer. *Jpn. J. Appl. Phys.* **1991,** *30* (10A), L1705.

[105] Jones, R.; Elsner, J.; Haugk, M.; Gutierrez, R.; Frauenheim, T.; Heggie, M. I.; Öberg, S.; Briddon, P. R., Interaction of Oxygen with Threading Dislocations in GaN. *physica status solidi (a)* **1999,** *171* (1), 167-173.

[106] Nakamura, S.; Mukai, T.; Senoh, M., Si- and Ge-Doped GaN Films Grown with GaN Buffer Layers. *Jpn. J. Appl. Phys.* **1992,** *31* (9R), 2883.

[107] Romano, L. T.; Walle, C. G. V. d.; III, J. W. A.; Götz, W.; Kern, R. S., Effect of Si doping on strain, cracking, and microstructure in GaN thin films grown by metalorganic chemical vapor deposition. *J. Appl. Phys.* **2000,** *87* (11), 7745-7752.

[108] Pampili, P.; Parbrook, P. J., Doping of III-nitride materials. *Mater. Sci. Semicond. Process.* **2017,** *62*, 180-191.

[109] Fritze, S.; Dadgar, A.; Witte, H.; Bügler, M.; Rohrbeck, A.; Bläsing, J.; Hoffmann, A.; Krost, A., High Si and Ge n-type doping of GaN doping - Limits and impact on stress. *Appl. Phys. Lett.* **2012,** *100* (12), 122104.

[110] Li, S.; Mo, C.; Wang, L.; Xiong, C.; Peng, X.; Jiang, F.; Deng, Z.; Gong, D., The influence of Si-doping to the growth rate and yellow luminescence of GaN grown by MOCVD. *J. Lumin.* **2001,** *93* (4), 321-326.

[111] Nix, W. D.; Clemens, B. M., Crystallite coalescence: A mechanism for intrinsic tensile stresses in thin films. *J. Mater. Res.* **2011,** *14* (8), 3467-3473.

[112] Richter, E.; Stoica, T.; Zeimer, U.; Netzel, C.; Weyers, M.; Tränkle, G., Si Doping of GaN in Hydride Vapor-Phase Epitaxy. *J. Electron. Mater.* **2013,** *42* (5), 820-825.

[113] Sheu, J. K.; Chi, G. C., The doping process and dopant characteristics of GaN. *J. Phys.: Condens. Matter* **2002,** *14* (22), R657.

[114] Fong, W. K.; Leung, K. K.; Surya, C., Si doping of metal-organic chemical vapor deposition grown gallium nitride using ditertiarybutyl silane metal-organic source. *J. Cryst. Growth* **2007,** *298*, 239-242.

[115] Kida, Y.; Iishiga, A.; Shibata, T.; Naoi, H.; Miyake, H.; Hiramatsu, K.; Tanaka, M., MOVPE growth and n-type conductivity control of high-quality Si-doped Al0.5Ga0.5N using epitaxial AlN as an underlying layer. *physica status solidi (c)* **2003,** *0* (7), 2128-2131.

[116] Nakano, Y.; Jimbo, T., Co-implantation of Si+N into GaN for n-type doping. *J. Appl. Phys.* **2002,** *92* (7), 3815-3819.

[117] Hong, Y. J.; Lee, C.-H.; Yoo, J.; Kim, Y.-J.; Jeong, J.; Kim, M.; Yi, G.-C., Emission color-tuned light-emitting diode microarrays of nonpolar InxGa1–xN/GaN multishell nanotube heterostructures. *Scientific Reports* **2015,** *5*, 18020.

[118] Liu, F.; Huang, L.; Davis, R. F.; Porter, L. M.; Schreiber, D. K.; Kuchibatla, S. V. N. T.; Shutthanandan, V.; Thevuthasan, S.; Preble, E. A.; Paskova, T.; Evans, K. R., Composition and interface analysis of InGaN/GaN multiquantum-wells on GaN substrates using atom probe tomography. *Journal of Vacuum Science & Technology B, Nanotechnology and Microelectronics: Materials, Processing, Measurement, and Phenomena* **2014,** *32* (5), 051209.

[119] Nagatomo, T.; Kuboyama, T.; Minamino, H.; Omoto, O., Properties of Ga 1- x In x N Films Prepared by MOVPE. *Jpn. J. Appl. Phys.* **1989,** *28* (8A), L1334.

[120] Yoshimoto, N.; Matsuoka, T.; Sasaki, T.; Katsui, A., Photoluminescence of InGaN films grown at high temperature by metalorganic vapor phase epitaxy. *Appl. Phys. Lett.* **1991,** *59* (18), 2251-2253.

[121] Nakamura, S.; Senoh, M.; Nagahama, S. i.; Iwasa, N.; Yamada, T.; Matsushita, T.; Kiyoku, H.; Sugimoto, Y., Characteristics of InGaN multi-quantum-well-structure laser diodes. *Appl. Phys. Lett.* **1996,** *68* (23), 3269-3271.

[122] Nakamura, S.; Mukai, T.; Senoh, M., Candela-class high-brightness InGaN/AlGaN double-heterostructure blue-light-emitting diodes. *Appl. Phys. Lett.* **1994,** *64* (13), 1687-1689.

[123] Guo, W.; Banerjee, A.; Bhattacharya, P.; Ooi, B. S., InGaN/GaN disk-in-nanowire white light emitting diodes on (001) silicon. *Appl. Phys. Lett.* **2011,** *98* (19), 193102.

[124] InGaN/GaN nanorod array white light-emitting diode. *Appl. Phys. Lett.* **2010,** *97* (7), 073101.

[125] Nguyen, H. P. T.; Zhang, S.; Connie, A. T.; Kibria, M. G.; Wang, Q.; Shih, I.; Mi, Z., Breaking the Carrier Injection Bottleneck of Phosphor-Free Nanowire White Light-Emitting Diodes. *Nano Lett.* **2013,** *13* (11), 5437-5442.

[126] Tsai, T.-H.; Huang, J.-R.; Lin, K.-W.; Hsu, W.-C.; Chen, H.-I.; Liu, W.-C., Improved hydrogen sensing characteristics of a Pt/SiO2/GaN Schottky diode. *Sensors and Actuators B: Chemical* **2008,** *129* (1), 292-302.

[127] Hacke, P.; Detchprohm, T.; Hiramatsu, K.; Sawaki, N., Schottky barrier on n-type GaN grown by hydride vapor phase epitaxy. *Appl. Phys. Lett.* **1993,** *63* (19), 2676-2678.

[128] Edwards, M. J.; Le Boulbar, E. D.; Vittoz, S.; Vanko, G.; Brinkfeldt, K.; Rufer, L.; Johander, P.; Lalinský, T.; Bowen, C. R.; Allsopp, D. W. E., Pressure and temperature dependence of GaN/AlGaN high electron mobility transistor based sensors on a sapphire membrane. *physica status solidi (c)* **2012,** *9* (3-4), 960-963.

[129] Shur, M. S.; Gaska, R.; Bykhovski, A., GaN-based electronic devices. *Solid·State Electron.* **1999,** *43* (8), 1451-1458.

[130] Luther, B. P.; Wolter, S. D.; Mohney, S. E., High temperature Pt Schottky diode gas sensors on n-type GaN. *Sensors and Actuators B: Chemical* **1999,** *56* (1–2), 164-168.

[131] Schalwig, J.; Müller, G.; Ambacher, O.; Stutzmann, M., Group-III-Nitride Based Gas Sensing Devices. *physica status solidi (a)* **2001,** *185* (1), 39-45.

[132] Stutzmann, M.; Steinhoff, G.; Eickhoff, M.; Ambacher, O.; Nebel, C. E.; Schalwig, J.; Neuberger, R.; Müller, G., GaN-based heterostructures for sensor applications. *Diamond Relat. Mater.* **2002,** *11* (3–6), 886-891.

[133] Ambacher, O.; Smart, J.; Shealy, J. R.; Weimann, N. G.; Chu, K.; Murphy, M.; Schaff, W. J.; Eastman, L. F.; Dimitrov, R.; Wittmer, L.; Stutzmann, M.; Rieger, W.; Hilsenbeck, J., Two-dimensional electron gases induced by spontaneous and piezoelectric polarization charges in N- and Ga-face AlGaN/GaN heterostructures. *J. Appl. Phys.* **1999,** *85* (6), 3222-3233.

[134] Kang, B. S.; Ren, F.; Gila, B. P.; Abernathy, C. R.; Pearton, S. J., AlGaN/GaN-based metal–oxide–semiconductor diode-based hydrogen gas sensor. *Appl. Phys. Lett.* **2004,** *84* (7), 1123-1125.

[135] Wang, H.-T.; Kang, B. S.; Ren, F.; Fitch, R. C.; Gillespie, J. K.; Moser, N.; Jessen, G.; Jenkins, T.; Dettmer, R.; Via, D.; Crespo, A.; Gila, B. P.; Abernathy, C. R.; Pearton, S. J., Comparison of gate and drain current detection of hydrogen at room temperature with AlGaN⁄GaN high electron mobility transistors. *Appl. Phys. Lett.* **2005,** *87* (17), 172105.

[136] Kang, B. S.; Mehandru, R.; Kim, S.; Ren, F.; Fitch, R. C.; Gillespie, J. K.; Moser, N.; Jessen, G.; Jenkins, T.; Dettmer, R.; Via, D.; Crespo, A.; Gila, B. P.; Abernathy, C. R.; Pearton, S. J., Hydrogen-induced reversible changes in drain current in Sc2O3/AlGaN/GaN high electron mobility transistors. *Appl. Phys. Lett.* **2004,** *84* (23), 4635-4637.

[137] Eickhoff, M.; Schalwig, J.; Steinhoff, G.; Weidemann, O.; Görgens, L.; Neuberger, R.; Hermann, M.; Baur, B.; Müller, G.; Ambacher, O.; Stutzmann, M., Electronics and sensors based on pyroelectric AlGaN/GaN heterostructures – Part B: Sensor applications. *physica status solidi (c)* **2003,** *0* (6), 1908-1918.

[138] Schalwig, J.; Müller, G.; Eickhoff, M.; Ambacher, O.; Stutzmann, M., Gas sensitive GaN/AlGaN-heterostructures. *Sensors and Actuators B: Chemical* **2002,** *87* (3), 425-430.

[139] Mehandru, R.; Luo, B.; Kang, B. S.; Kim, J.; Ren, F.; Pearton, S. J.; Pan, C. C.; Chen, G. T.; Chyi, J. I., AlGaN/GaN HEMT based liquid sensors. *Solid·State Electron.* **2004,** *48* (2), 351-353.

[140] Steinhoff, G.; Purrucker, O.; Tanaka, M.; Stutzmann, M.; Eickhoff, M., AlxGa1–xN—A New Material System for Biosensors. *Adv. Funct. Mater.* **2003,** *13* (11), 841-846.

[141] Kang, B. S.; Ren, F.; Wang, L.; Lofton, C.; Tan, W. W.; Pearton, S. J.; Dabiran, A.; Osinsky, A.; Chow, P. P., Electrical detection of immobilized proteins with ungated AlGaN⁄GaN high-electron-mobility Transistors. *Appl. Phys. Lett.* **2005,** *87* (2), 023508.

[142] Steinhoff, G.; Baur, B.; Wrobel, G.; Ingebrandt, S.; Offenhäusser, A.; Dadgar, A.; Krost, A.; Stutzmann, M.; Eickhoff, M., Recording of cell action potentials with AlGaN⁄GaN field-effect transistors. *Appl. Phys. Lett.* **2005,** *86* (3), 033901.

[143] Li, J.-d.; Cheng, J.-j.; Miao, B.; Wei, X.-w.; Xie, J.; Zhang, J.-c.; Zhang, Z.-q.; Wu, D.-m., Detection of prostate-specific antigen with biomolecule-gated AlGaN/GaN high electron mobility transistors. *Journal of Micromechanics and Microengineering* **2014,** *24* (7), 075023.

[144] Kang, B. S.; Wang, H. T.; Ren, F.; Pearton, S. J.; Morey, T. E.; Dennis, D. M.; Johnson, J. W.; Rajagopal, P.; Roberts, J. C.; Piner, E. L.; Linthicum, K. J., Enzymatic glucose detection using ZnO nanorods on the gate region of AlGaN⁄GaN high electron mobility transistors. *Appl. Phys. Lett.* **2007,** *91* (25), 252103.

[145] Winter, C.; Kashammer, J.; Mittler-Neher, S.; Fischer, R. A., A new pathway to GaN: deposition of GaN-clusters on functionalized thiol-SAMs on gold. *Opt. Mater.* **1998,** *9* (1), 352-355.

[146] Niesen, T. P.; Puchinger, M.; Gerstel, P.; Rodewald, D.; Wolff, J.; Wagner, T.; Bill, J.; Aldinger, F., Chemical liquid deposition of gallium nitride thin films on siloxane-anchored self-assembled monolayers. *Mater. Chem. Phys.* **2002,** *73* (2–3), 301-305.

[147] Baraton, M.-I.; Carlson, G.; Gonsalves, K. E., DRIFTS characterization of a nanostructured gallium nitride powder and its interactions with organic molecules. *Materials Science and Engineering: B* **1997,** *50* (1–3), 42-45.

[148] Bermudez, V. M., Chemisorption of NH3 on GaN(0001)-(1×1). *Chem. Phys. Lett.* **2000,** *317* (3–5), 290-295.

[149] Bermudez, V. M., Functionalizing the GaN(0 0 0 1)-(1×1) surface I. The chemisorption of aniline. *Surf Sci.* **2002,** *499* (2–3), 109-123.

[150] Bermudez, V. M., Adsorption and photodissociation of 4-haloanilines on GaN(0 0 0 1). *Surf Sci.* **2002,** *519* (3), 173-184.

[151] Bermudez, V. M., Functionalizing the GaN(0 0 0 1)-(1×1) surface II. Chemisorption of 3-pyrroline. *Surf Sci.* **2002,** *499* (2–3), 124-134.

[152] Bermudez, V. M., Adsorption of 1-Octanethiol on the GaN(0001) Surface. *Langmuir* **2003,** *19* (17), 6813-6819.

[153] Baur, B.; Steinhoff, G.; Hernando, J.; Purrucker, O.; Tanaka, M.; Nickel, B.; Stutzmann, M.; Eickhoff, M., Chemical functionalization of GaN and AlN surfaces. *Appl. Phys. Lett.* **2005,** *87* (26), 263901.

[154] Petoral, R. M.; Yazdi, G. R.; Spetz, A. L.; Yakimova, R.; Uvdal, K., Organosilane-functionalized wide band gap semiconductor surfaces. *Appl. Phys. Lett.* **2007,** *90* (22), 223904.

[155] Hsu, C.-W.; Ganguly, A.; Chen, C.-P.; Kuo, C.-C.; Paskov, P. P.; Holtz, P. O.; Chen, L.-C.; Chen, K.-H., Optical properties of functionalized GaN nanowires. *J. Appl. Phys.* **2011,** *109* (5), 053523.

[156] Arranz, A.; Palacio, C.; García-Fresnadillo, D.; Orellana, G.; Navarro, A.; Muñoz, E., Influence of Surface Hydroxylation on 3-Aminopropyltriethoxysilane Growth Mode during Chemical Functionalization of GaN Surfaces: An Angle-Resolved X-ray Photoelectron Spectroscopy Study. *Langmuir* **2008,** *24* (16), 8667-8671.

[157] Williams, E. H.; Davydov, A. V.; Oleshko, V. P.; Steffens, K. L.; Levin, I.; Lin, N. J.; Bertness, K. A.; Manocchi, A. K.; Schreifels, J. A.; Rao, M. V., Solution-based functionalization of gallium nitride nanowires for protein sensor development. *Surf Sci.* **2014,** *627*, 23-28.

[158] López-Gejo, J.; Navarro-Tobar, Á.; Arranz, A.; Palacio, C.; Muñoz, E.; Orellana, G., Direct Grafting of Long-Lived Luminescent Indicator Dyes to GaN Light-Emitting Diodes for Chemical Microsensor Development. *ACS Appl. Mater. Interfaces* **2011,** *3* (10), 3846-3854.

[159] Baur, B.; Howgate, J.; Ribbeck, H.-G. v.; Gawlina, Y.; Bandalo, V.; Steinhoff, G.; Stutzmann, M.; Eickhoff, M., Catalytic activity of enzymes immobilized on AlGaN/GaN solution gate field-effect transistors. *Appl. Phys. Lett.* **2006,** *89* (18), 183901.

[160] Arisio, C.; Cassou, C. A.; Lieberman, M., Loss of Siloxane Monolayers from GaN Surfaces in Water. *Langmuir* **2013,** *29* (17), 5145-5149.

[161] Guo, D. J.; Abdulagatov, A. I.; Rourke, D. M.; Bertness, K. A.; George, S. M.; Lee, Y. C.; Tan, W., GaN Nanowire Functionalized with Atomic Layer Deposition Techniques for Enhanced Immobilization of Biomolecules. *Langmuir* **2010,** *26* (23), 18382-18391.

[162] Ito, T.; Forman, S. M.; Cao, C.; Li, F.; Eddy, C. R.; Mastro, M. A.; Holm, R. T.; Henry, R. L.; Hohn, K. L.; Edgar, J. H., Self-Assembled Monolayers of Alkylphosphonic Acid on GaN Substrates. *Langmuir* **2008,** *24* (13), 6630-6635.

[163] Kim, H.; Colavita, P. E.; Paoprasert, P.; Gopalan, P.; Kuech, T. F.; Hamers, R. J., Grafting of molecular layers to oxidized gallium nitride surfaces via phosphonic acid linkages. *Surf Sci.* **2008,** *602* (14), 2382-2388.

[164] Kim, H.; Colavita, P. E.; Metz, K. M.; Nichols, B. M.; Sun, B.; Uhlrich, J.; Wang, X.; Kuech, T. F.; Hamers, R. J., Photochemical Functionalization of Gallium Nitride Thin Films with Molecular and Biomolecular Layers. *Langmuir* **2006,** *22* (19), 8121-8126.

[165] Schwarz, S. U.; Cimalla, V.; Eichapfel, G.; Himmerlich, M.; Krischok, S.; Ambacher, O., Thermal Functionalization of GaN Surfaces with 1-Alkenes. *Langmuir* **2013,** *29* (21), 6296-6301.

[166] Stine, R.; Simpkins, B. S.; Mulvaney, S. P.; Whitman, L. J.; Tamanaha, C. R., Formation of amine groups on the surface of GaN: A method for direct biofunctionalization. *Appl. Surf. Sci.* **2010,** *256* (13), 4171-4175.

[167] Mukherjee, J.; Peczonczyk, S.; Maldonado, S., Wet Chemical Functionalization of III−V Semiconductor Surfaces: Alkylation of Gallium Phosphide Using a Grignard Reaction Sequence. *Langmuir* **2010,** *26* (13), 10890-10896.

[168] Arízaga, G. G. C.; Oviedo, M. J.; López, O. E. C., Electrical properties of polycrystalline GaN films functionalized with cysteine and stabilization of GaN nanoparticles in aqueous media. *Colloids and Surfaces B: Biointerfaces* **2012,** *98*, 63-71.

[169] Estephan, E.; Larroque, C.; Cuisinier, F. J. G.; Bálint, Z.; Gergely, C., Tailoring GaN Semiconductor Surfaces with Biomolecules. *The Journal of Physical Chemistry B* **2008,** *112* (29), 8799-8805.

[170] Foster, C. M.; Collazo, R.; Sitar, Z.; Ivanisevic, A., Cell Behavior on Gallium Nitride Surfaces: Peptide Affinity Attachment versus Covalent Functionalization. *Langmuir* **2013,** *29* (26), 8377-8384.

[171] Stewart, M. P.; Maya, F.; Kosynkin, D. V.; Dirk, S. M.; Stapleton, J. J.; McGuiness, C. L.; Allara, D. L.; Tour, J. M., Direct Covalent Grafting of Conjugated Molecules onto Si, GaAs, and Pd Surfaces from Aryldiazonium Salts. *J. Am. Chem. Soc.* **2004,** *126* (1), 370-378.

UNIVERSITAT ROVIRA I VIRGILI
POROUS GAN PRODUCED BY CVD: PROGRESS IN DEVELOPMENT AND CHARACTERIZATION
Josué Mena Gómez

2

Experimental techniques

This chapter is focused on describing the experimental techniques used for the development of this thesis. The first part of this chapter is devoted to the synthesis technique of porous GaN by the chemical vapor deposition (CVD) technique, deposition of metallic thin films used as catalyst by sputtering in the clean room and the synthesis of organic compounds for the functionalization of the GaN surfaces. In the second part, the imaging techniques used to characterize the porous GaN structures are described. In this section we included the microscopy techniques employed, such as scanning electron microscopy (SEM), environmental scanning electron microscopy (ESEM), atomic force microscopy (AFM)) and fluorescence microscopy. Another section is dedicated to the structural analysis techniques such as the crystallographic orientation performed by X-ray diffraction (XRD) with a subsection dedicated to the analysis of rocking curves (RC) and resonant Raman scattering (RRS). The optical characterization of GaN is presented in another section of the chapter describing the four techniques used for this purpose: cathodoluminescence (CL), photoluminescence (PL) and reflectance measurements. The technique employed for the electrical characterization of GaN, done by two-prove measurements, is also described in this chapter. The last section is devoted to the molecular characterization of the compounds used to functionalize the surface of GaN, in which we described the fundaments of techniques such as nuclear magnetic resonance (NMR) and Fourier transform infrared (FT-IR) spectroscopy that allowed a continuous track of the synthesis pathway.

2.1 Deposition techniques

2.1.1 Crystal growth by chemical vapor deposition (CVD)

The term chemical vapor deposition (CVD) refers to all the processes for solid film deposition on a given substrate where the reagents enter into the system in vapor phase, and after a chemical reaction, the solid film is deposited. In contrast with physical vapor deposition (PVD), in which a solid metal is evaporated under ultra-high vacuum conditions and high temperature, in CVD a chemical reaction is involved, being more versatile for film deposition than PVD, due to the huge combination of chemical reactions that can be involved in the vapor phase [1]. Usually, the gases delivered into the CVD chamber are called precursor gases, which many times are carried by an inert gas. CVD has been used in a wide range of applications starting from the first to be developed which was metal purification; also it had a huge impact on microelectronics manufacturing over the past 40 years in the synthesis of metal-oxide-semiconductors (MOS), semiconductors, conductive interconnect materials and insulating materials, for instance. In recent years a huge variety of applications for CVD have emerged, such as the fabrication of devices for the communication industry [2], optoelectronics with a special impact in the fabrication of light emitting diodes (LEDs) [3], nanotechnology [4], coatings [5], high temperature superconductors such as YBaCuO [6], etc.

A CVD process consists in various physical and chemical processes, summarized as follows and depicted in Figure 2.1 [7]:

1. Mass transport of the precursor gases in the desired concentration to the vicinity of the substrate.
2. Diffusion of the reactant species through the boundary layer to the substrate surface and/or homogenous chemical reactions to form intermediates usually by thermal cracking.
3. Adsorption of reactant species or intermediates on the heated substrate surface.

4. Surface migration; this process also includes: heterogeneous reaction, inclusion of coating atoms into the growing surface, and formation of by-product species.
5. Desorption of by-product species on the surface reaction.
6. Diffusion of by-product species to the bulk gas.
7. Transport of by-product gaseous species away from the substrate.

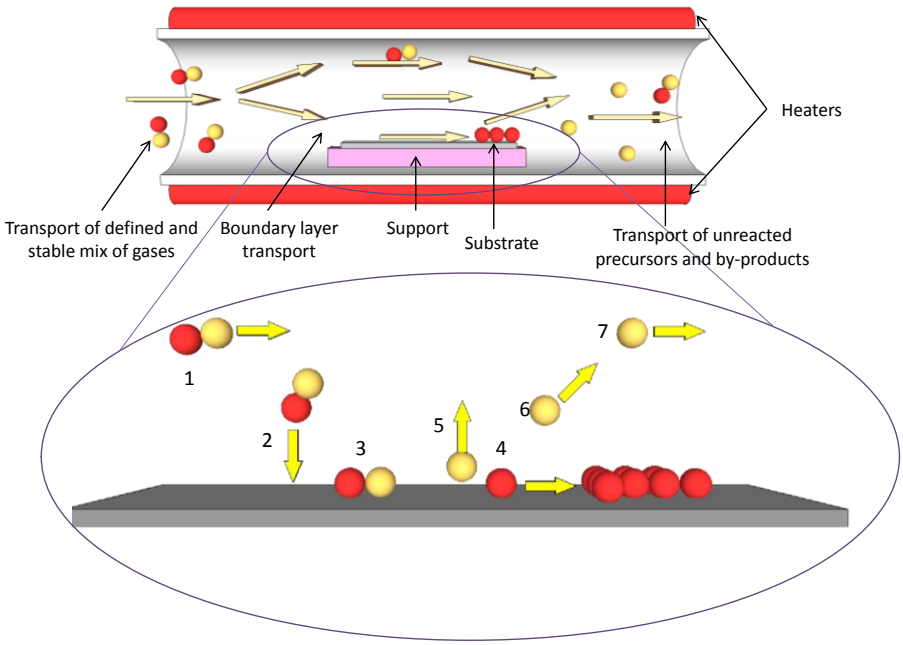

Figure 2.1. Scheme of the processes that typically occurs in a CVD system.

Despite all the variations of CVD techniques, generally a CVD equipment consist basically on a gas supplier controlled with a gas flow meter at one end of the setup, a CVD reactor with a heating system, and at the other end of the CVD setup a vacuum pump coupled to the CVD reactor in order to either remove the by-products and control the pressure of the system [7]. In order to obtain the desired film coatings a variety of parameters have to be controlled such as the precursors and carrier gas flow rates, temperature, pressure and time, among others. Other parameters have to be controlled for

specific CVD-assisted techniques like plasma, microwaves, lasers and so on [8].

As a method for deposition of thin-film layers onto a substrate, CVD has a number of advantages[7]:

- CVD has a great flexibility for using a large library of gas precursors such as halides, hydrides, organo-metallic compounds, and so forth, which enable the deposition of a large variety of materials such as metals, carbides, polymers, oxides, III-V and II-VI compounds, to name a few.
- Compared to other deposition techniques like PVD, CVD is a non-line-of-sight process, which means that the source of atoms is not located at a fixed point, this leads to a good and quite uniform deposition of conformal layers into complex surfaces such as steps, deep recesses, holes and other types of complex 3D features, even containing inner surfaces.
- This technique requires low deposition temperatures compared to PVD, in which melting or sublimation temperatures are required.
- An accurate control of the deposition parameters, which can be easily controlled in CVD, leads to a control on the crystal structure, stoichiometry, surface morphology and orientation of the deposited layer. Also multilayer deposition can be achieved only by switching on and off the inlet of precursor gases.
- One of the greatest advantages of CVD, compared with PVD techniques is that CVD equipment does not explicitly require ultra-high vacuum environment, but the equipment generally can be adapted to many process variations, from atmospheric pressure to ultra high vacuum pressures regarding on the chemical reaction of the process.

However, CVD has some disadvantages as follows [7]:

- The use of highly toxic, corrosive, flammable and explosive precursor gases even at low concentrations. Not only the

precursors, but the by-products, can be also highly toxic, corrosive, flammable and explosive. Also some of the precursor gases like metal-organic precursors are quite expensive. Therefore, proper security measures have to be taken.

- Numerous tests have to be done in order to determine the suitable parameters for film deposition due to the complexity of the process, relying in the multiple gaseous species involved in the reactions and the intermediates produced, the difficulty of identifying the reaction mechanism due to the impossibility of identifying the by-products in most cases, and the fact that CVD implies a sequence of chemical reactions before the film is deposited, when compared to physical deposition methods.

In this work for the synthesis of porous GaN and its doped analogous, a horizontal CVD system has been used with metallic gallium (Alfa Aesar 99.999%) as the gallium source, and ammonia gas (NH_3) (Carburos Metálicos >99.98%) as the nitrogen source. The general reaction of the GaN synthesis is the following:

$$2Ga + 2NH_3 \longrightarrow 2GaN + 3H_2$$

The CVD system used for the deposition of porous GaN has a particularity compared with other common CVD systems, and is the fact that the gallium is introduced into the horizontal CVD system in liquid form just beneath the substrate, and that the deposition of GaN is produced on the side of the substrate facing the gallium source. When the temperature of the system reaches the deposition temperature gallium starts to evaporate having a line-of-sight process only for gallium, while NH_3 enters into the system throw the gas flow-meter following the typical path of a gas in a CVD system. Also, at the reaction temperature some NH_3 cracks into N and H radicals among other species such as NH_x,[9] described in the following equation:

$$yNH_3 \longrightarrow (y-z)NH_x + zN^{\cdot} + [3y-(y-z)x]H^{\cdot}$$

but it is not the preferential source of N for GaN. Alternatively, heterogeneously decomposition of NH_3 adsorbed on gallium is the preferential path to create nitrogen atoms for GaN growth. Since NH_3 is a polar molecule, it will be preferentially adsorbed in an electron acceptor (gallium atom) and cracked afterwards giving H_2 as a by-product [9].

The CVD reaction was performed in a horizontal tubular CVD furnace Thermolyne 79300, Thermo Fisher Scientific Inc., USA with a built-in temperature controller. The deposition of GaN undergoes inside a quartz tube. The inlet of the quartz tube is connected to a Sierra INC. Smart-Trak gas flowmeter, through which the ammonia is introduced. The inlet of the quartz tube is connected to a vacuum pump from Oerlikon Leybold Vacuum that allows controlling the intensity of gas extraction, through a butterfly valve for the control of the pressure after monitoring the pressure inside the reactor through a CMOVE 1250 Oerlikon Leybold Vacuum digital pressuremeter located in vertical position to avoid contamination by the deposition of by-products and to manually monitor the pressure inside the reactor. All the items described are shown in Figure 2.2.

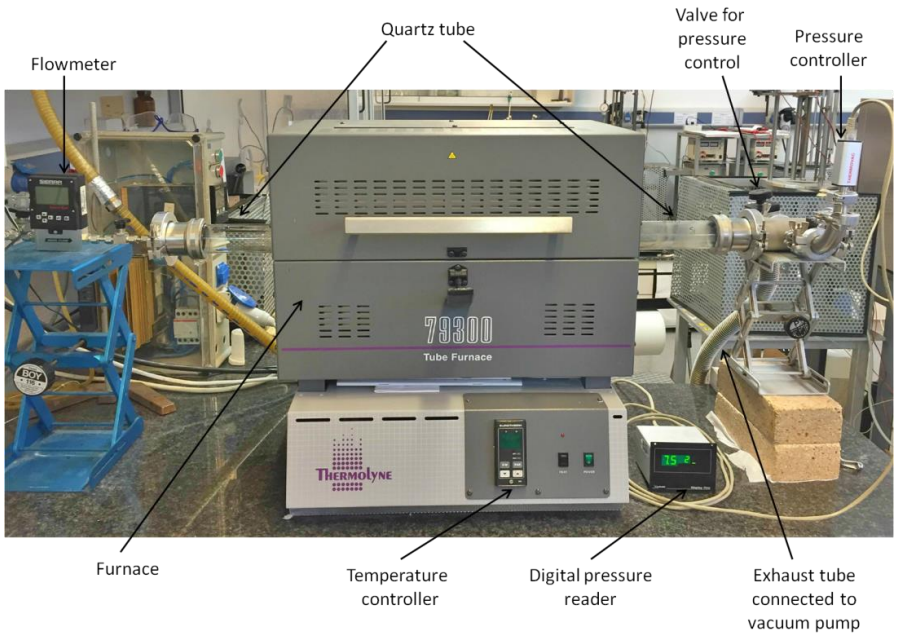

Figure 2.2. CVD set up used for the synthesis of porous GaN.

The thermal characterization inside the quartz tube of the CVD furnace was performed in order to know the temperature distribution inside it, and correlate the real temperature inside the furnace with the one set in the controller. For this a Pt-Rh thermocouple was placed inside the furnace when the desired temperature was reached. After the temperature signal was stabilized the thermocouple has moved 1 cm away from the center, and the process was repeated until a temperature profile was obtained from the center of the furnace to 15 cm away from it. Figure 2.3 plots the two temperatures used in GaN deposition versus the distance inside the furnace corresponding to this thermal characterization. The temperature measured with the thermocouple only differs from the temperature given by the controller by 2.5 K at a temperature of 1203 K and 7.5 K at a temperature of 1173 K. In the zone between the center of the furnace and 4 cm away from the center at a settled temperature of 1203 K, the temperature is quite stable, with a thermal gradient of only 5 K. For this reason, and assuming a symmetric behavior of the temperature profile, the substrate and Ga droplet were placed just in the middle of the furnace, coinciding with the point with the highest temperature and taking advantage of the thermal stability in the surrounding area.

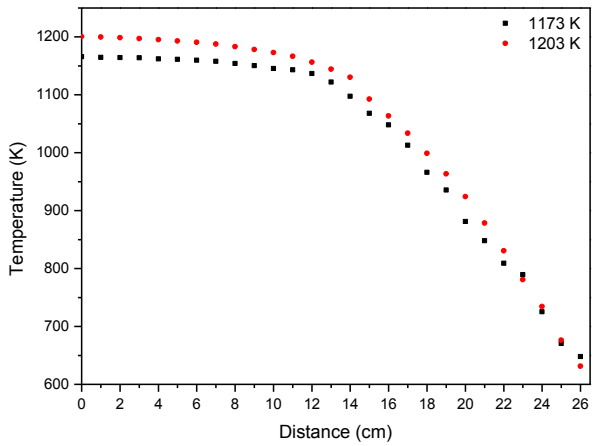

Figure 2.3. Temperature profile inside the horizontal tubular furnace when the temperature was set at 1203 K and 1173 K, respectively.

The gallium source was placed in a hand-made quartz crucible. The quartz crucibles or gallium holders were made in three different shapes: flat plate (the spreading of the gallium drop on the surface of the crucible was not limited), half of a cylindrical tube (spreading of gallium was limited from two sides) and concave crucible (the spreading of gallium is limited from all sides).

Since gallium tends to passivate in air forming a thin oxide film on its surface it was mandatory to manipulate the gallium inside a controlled atmosphere. The one used in this work was a Precise Controlled Atmosphere Glove Box 5220120 CA from Labconco filled with nitrogen. The gallium was weighted inside the globe box, with an amount that was varied from 0.2 to 0.6 g depending on the experiment. The crucible with the metallic gallium was placed into a quartz liner which was used to easily place the gallium and the substrate inside the quartz tube of the furnace and prevent it to be dirty due to gallium spreading. An additional reason to use a cylindrical liner was to allow us to place the support with the substrate at a given distance respect to the gallium source keeping it constant. A hand-made boron nitride (BN) plate was used as support for the substrate with a window of approximately 0.7 x 0.7 cm^2 so that the substrate was placed above that window facing the gallium droplet, which was placed just below the window of the BN support at a vertical distance of approximately 2 cm. The decision of using BN as a material for the support of the substrate is due to its high thermal conductivity (~740 W/(m·K)) [10], which allows a homogeneous distribution of the temperature in the substrate placed above. Also, another property to consider is that BN ceramic plates are easy to machine, allowing us to fabricate the desired shape for our supports. BN aside from its good physical properties has also a good chemical stability at high temperatures and under corrosive atmosphere [11] such the one used in our experiments. A scheme of the experimental set up used is shown in Figure 2.4.

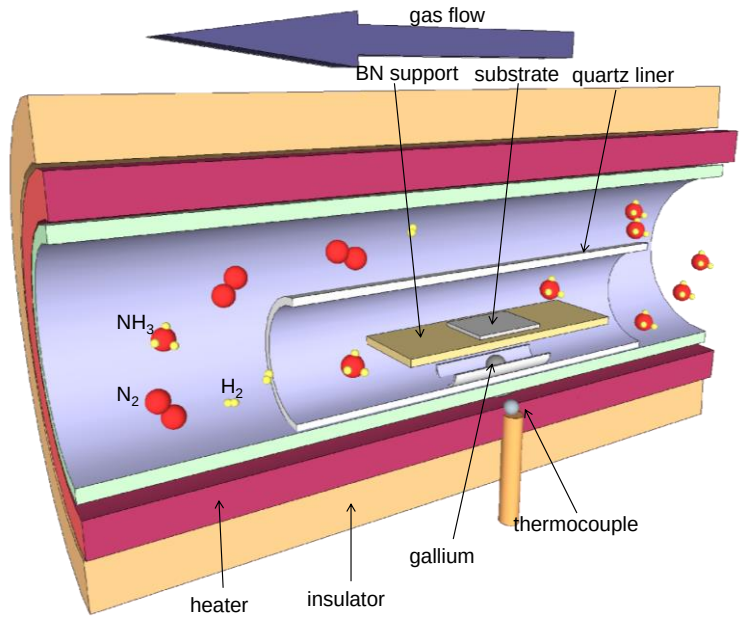

Figure 2.4. Scheme of the horizontal tubular CVD set up used for the synthesis of porous GaN.

After the introduction of the liner with the gallium and the substrate into the quartz tube at the center of the furnace the system was closed and purged under nitrogen flow for 5 minutes. Afterwards, the system was degassed until a pressure of $<10^{-2}$ Torr was reached for 5 more minutes. Then, the ammonia flow was introduced into the system controlled by the flowmeter at a constant flow rate of 75 sccm, at the same time the heating system was turned on. No additional carrier gas was used for these experiments. The heating rate was set to 60 K/min from room temperature to the reaction temperature, set between 850 and 930 K. The system was kept at the constant NH_3 flow rate of 75 sccm, a pressure of 15 Torr and at the desired reaction temperature to allow the chemical reaction occurs during the desired deposition time. The deposition time was varied between 15 and 120 min, depending on the experiment, as it will be discussed later. To stop the deposition of GaN the incoming of one of the two precursors used, in this case NH_3, was stopped since gallium was already inside the furnace, and the heating of the furnace was stopped as well. The furnace was let to cool down to room temperature under vacuum at a pressure $<10^{-2}$ Torr. When the furnace

was cooled down, the cylindrical liner was taken out of it, and the sample was wrapped in optical paper and stored in a box.

Due to the gallium spreading along the cylindrical liner, it had to be cleaned we used two methods to clean the cylindrical liner depending on the residue deposited on the liner. The first one was removing the GaN deposited on the liner, and consisted on submerging the liner in a hot solution of concentrated KOH. The second cleaning procedure was removing the remaining unreacted metallic gallium spread along the liner and it consisted on submerging the liner in an *aqua regia* solution (1:3 HNO_3:HCl). Once the liners were apparently clean they were rinsed with deionized water and ethanol and kept in an oven with the temperature set at 80 °C.

2.1.2 Sputtering

When silicon wafers were used as substrates for the synthesis of porous GaN particles, a metallic catalyst was needed to favor the deposition. For this purpose a thin film of metallic catalyst was deposited on silicon by sputtering.

Sputtering is cataloged as one of the main PVD techniques, followed by thermal evaporation [10]. In contrast with thermal evaporation, where the substrate is heated to high temperatures in a high-vacuum system with pressures below 10^{-6} Torr to favor the evaporation of the solid, when a thin film is deposited by sputtering the material we want to deposit, called target, is bombarded with energetic particles such as accelerated ions, so the surface atoms of the solid target are scattered backwards, due to collisions between the surface atoms and the energetic particles. In that way the neutral particles sputtered ballistically travel form the target to the substrate. Sometimes sputtering can also be referred as cathode sputtering, cathode disintegration, and impact evaporation [12].

Several sputtering methods are proposed for the deposition of thin film of materials, including direct current (DC) diode, radio frequency (RF)

diode, and magnetron, among others [10]. Among these sputtering systems the simplest model is the DC diode sputtering system. This system is composed by two planar electrodes. One of the electrodes is a cold cathode, where the target is placed, and the other electrode acts as an anode, where the substrate is placed (see Figure 2.5). The sputtering chamber is filled with the sputtering gas, typically argon at $4 \cdot 10^{-2}$ Torr, which later is ionized to produce plasma. The glow discharge is maintained under the application of a DC voltage between the electrodes. The Ar^+ plasma generated is accelerated to the cathode, where the target is placed, producing the sputtering of the target atoms, resulting in the deposition of the material of the target onto the substrate placed in the anode. In a DC sputtering system, the target must be a metal since the glow discharge is maintained between the metallic electrodes.

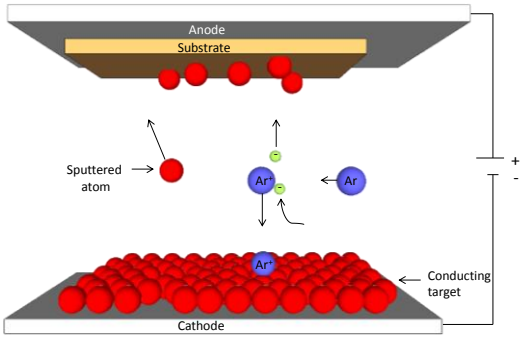

Figure 2.5. Scheme of the physical process occurring inside a sputtering chamber in DC mode.

When the target is an insulator the DC sputtering system cannot be used because of the immediate buildup of a surface charge of positive ions on the front side of the insulator. Thus, to sustain the glow discharge with the insulator target, a RF voltage is supplied to the target (see Figure 2.6). In a RF-sputtering system, the thin films of the insulator are sputtered directly from the insulator target [12].

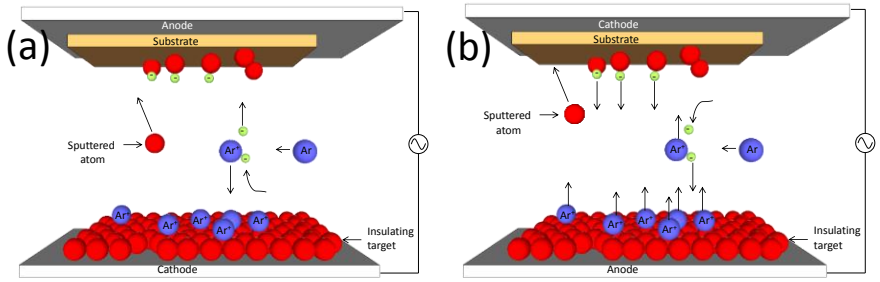

Figure 2.6. Scheme of the physical process occurring inside a sputtering chamber in RF mode, (a) depicts de situation when the plasma cations (argon) are covering the insulating target due to the inability of electrons to flow through the target to neutralize the plasma cations and (b) depicts an inversion of the polarity which makes the plasma cations moving opposite to the target.

In magnetron sputtering, a magnetic field is superposed on the cathode and glow discharge, aligned parallel to the cathode surface. In that way, electrons in the glow discharge show a cycloidal motion, and the center of the orbit drifts in the direction of the cross product between the electric field and the magnetic field, **E** x **B**. This electron-trapping effect increases the collision rate between the electrons and the sputtering gas molecules. This enables one to lower the pressure of the system up to 10^{-5} Torr if desired [13]. In the magnetron sputtering system, the magnetic field increases the plasma density which leads to an increase of the current density at the cathode target. Due to the low gas pressure, this enhances the probability of target atoms to reach the substrate without colliding with the plasma or gas species, resulting in a high deposition rate [12].

For the deposition of metallic catalyst onto silicon substrates magnetron sputtering was performed by an ATC Orion 8-HV AJA International system and both RF and DC modes where used indistinctly for Au, Pt and Ni deposition while only the RF mode was used for Ti deposition since the surface of the Ti target is passivated with an oxide layer blocking the conductivity of Ti. The flow rate of Ar used for all the depositions was 20 sccm and the pressure of the system was kept at $3 \cdot 10^{-3}$ Torr. When the sputtering was performed on the DC mode, a power of 200 W was used, while

it was reduced to 150 W in the case of RF sputtering. The magnetron sputtering system is encompassed in a set of instrumental techniques in the clean room located in the Servei de Recursos Científics i Tècnics, Universitat Rovira i Virgili, Tarragona.

2.2 Organic synthesis

In this subsection we describe some common techniques used in organic synthesis. The global procedures for each reaction are explained in more detail in Appendix 2.

2.2.1 Drying of organic solvents

In this work dried toluene was needed for the silanization of GaN. The first step for drying the toluene is the addition of metallic sodium into sheets in the flask containing the toluene. The flask is then connected to the column and placed on a heater connected to a thermocouple to display the temperature. On the top of the column there is a Dimroth condenser (see Figure 2.7) on which the top of it is connected to a nitrogen entrance. Once the toluene is boiling it travels up the side arm of the condenser and condenses, with the aid of the condenser, and it drops in the reservoir. If the collecting valve is open it will be refluxing, if it is closed the solvent will be collected in the reservoir. We left it under reflux for 1h approximately and then we closed the collection valve and wait until the column was filled with the desired volume of toluene.

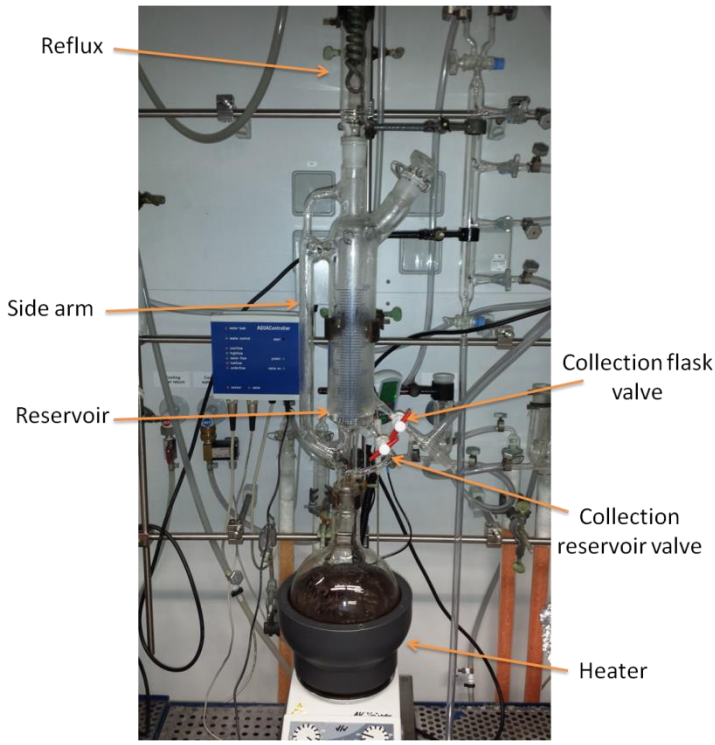

Figure 2.7. Experimental setup to obtain dry solvents

Previous to collect the toluene into the flask we have to purge the flask, for that, we connected the flask into the Schlenk line and made vacuum (see Figure 2.8). In order to make sure that no moiety remained in the flask we heated it up with a heating gun for 2 min. Once this time has elapsed we introduced nitrogen, and we made two additional purges (now without heating it up with the heating gun). Once the purge has finished we filled the flask with nitrogen and kept it closed. The purged flask was then connected to the nitrogen entrance, near the dry toluene column set up, and we left it under nitrogen. Then, we connected the flask into the column and finally we collected the desired amount of dried toluene.

Figure 2.8. Experimental setup of the Schlenk line for drying and removing oxygen from the reaction flasks.

2.2.2 Destilation of organic solvents

In order to use the commercial organic solvents in synthesis, they have to be cleaned previously. The standard procedure for cleaning solvents was the following. First, we filled a flask with the organic solvent, and then connected it to the rotavap and set it to the recommended pressure for the solvent we wanted to clean. When few ml of the solvent were collected in the collection flask, we stopped the vacuum and we filled the condenser with air, and we got rid of the collected solvent. This was done in order to get rid of possible traces of other solvents in the collection flask. We connected again the collection flask to the condenser column and let the flask fill with clean solvent. The clean solvent was stored in glass bottles.

2.2.3 Degassing of organic solvents (freeze pump)

In this thesis the use of the freeze pump procedure has been used for the Sonogashira coupling, for which we need a free oxygen solution prior to the addition of trimethylsilylacetylene.

The first step prior to the use of the freeze pump was the removal of air inside the Schlenk flask, for this we followed the same procedure described in Section 2.1.3.1 for air removal in a flask. Afterwards, with the flask under positive pressure of nitrogen, we added the solvent (and the reagents). Still with the flask under positive pressure of nitrogen, we cooled the flask with liquid nitrogen to freeze the solvent (or solution). Once the solvent (or the solution) was freezed we made vacuum inside the flask for 10 min. After that, we removed the liquid nitrogen and we let the solution reach room temperature (RT) under positive pressure of nitrogen. For a complete degassing we repeated this cycle for three times.

2.3 Morphological characterization techniques

2.3.1 Scanning electron microscopy (SEM)

A scanning electron microscope (SEM) is a microscope that uses a focused beam of high-energy electrons on the surface of solid specimens instead of light. The interaction between the incident electron beam and the surface to analyze generates a variety of signals including backscattered electrons, secondary electrons, X-rays, Auger electrons and visible photons, giving information about the sample's topography and composition [10]. The fact that SEM uses electrons in lieu of light, allows us to have images of much higher resolution, thus, so closely spaced specimens can be magnified at much higher levels. For that purpose SEM uses electromagnets rather than lenses, this allows to have much more control in the degree of magnification. With SEM we can achieve magnifications of the order of 300.000X greater than modern optical microscopes which can reach a maximum magnification of 1000X, due to the diffraction limit imposed by the visible light [14].

The electron beam is produced at the top of the column of the SEM by the electron gun made of a tungsten wire with a V shape that acts as the cathode, and it is accelerated down to the sample (anode). The electron beam passes through a combination of condenser lenses and apertures to produce a focused beam of electrons which hits the surface of the sample. The position of the beam is controlled by scan coils situated above the objective lens. These coils allow the beam to be scanned over the surface of the sample. This beam scanning, as the name of the microscope suggests, enables to get information about a defined area on the sample. In order to obtain information of any region of the analyzed sample, the sample is mounted on a stage in the chamber area, and as well as the column, the chamber is under high vacuum conditions with the aid of a combination of vacuum pumps. SEM requires vacuum conditions, because a gas atmosphere rapidly spreads and attenuates electron beams. A schematic diagram of a SEM is shown in Figure 2.9.

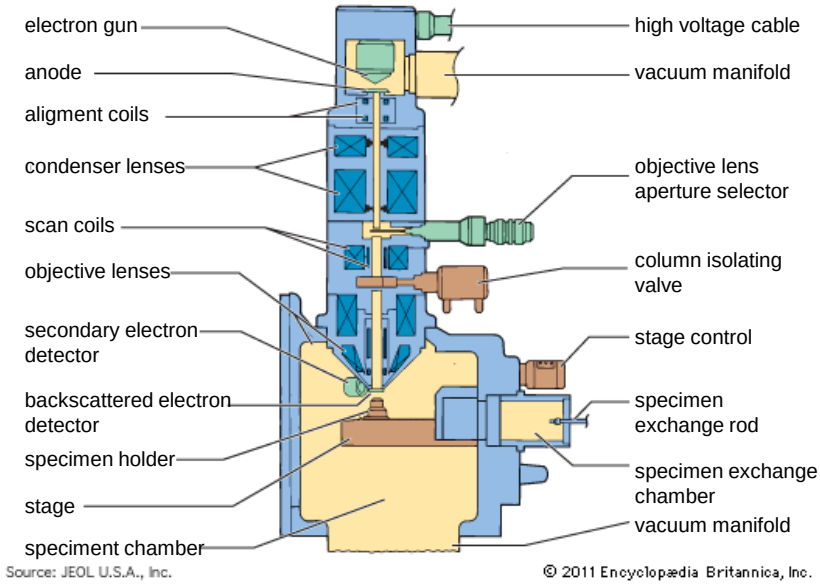

Figure 2.9. Schematic diagram of a conventional SEM set-up [14].

The electron beam interacts after hitting the sample in different ways, producing different signals which provide useful information (see Figure

2.10). The backscattered electrons are produced when the incident electrons are scattered backwards by the presence of the atomic nucleus of the sample specimen and give us information of the atomic composition of the sample. The atoms with higher atomic number appear much brighter than the lighter ones, since the backscattered electrons are directly proportional to the atomic number. When the electrons pass near the atoms of the specimen and collide with its electrons, they suffer a slight energy loss and path change and produce the ionization of the electrons in the atom. The ionized electrons leave the atom with a very low kinetic energy, of the order of few eV (~50 eV). These are called secondary electrons, and that is why only the superficial atoms of the specimen can produce secondary electrons that will reach the detector. For that reason secondary electrons are related to the topography of the sample. Also Auger electrons arising from 1-5 nm below the surface can be analyzed providing information of the surface composition, and since they are related with electronic states of the material they allow distinguishing between, for instance, Si, SiO_2, Si_3N_4 and SiO species. This is because the Auger effect is a process by which electrons with characteristic energies are ejected from atoms in response to a downward transition by another electron in the atom. This means that the energy released by the downward transition is given to one of the outer electrons instead of to a photon, and this electron is then ejected from the atom with an energy equal to the energy lost by the electron which made the downward transition minus the binding energy of the electron that is ejected from the atom. Since the binding energy of the ejected electron takes part of the equation, one can distinguish between different species despite having the same atom (e.g. Si, SiO_2, Si_3N_4 and SiO). Characteristic X-rays are produced when an energetic beam of charged particles, such as electrons, impacts with an atom and the incident beam ejects an electron from the inner shell of the atom. Thus, the X-rays emitted by the atom are characteristic of each atom and are used for elemental analysis of the sample. Finally cathodoluminescence provides the

luminescence spectra of the analyzed sample or a luminescence image of the sample.

One requirement for samples to be analyzed by SEM is to be conductive so the incident electrons are evacuated away from the sample. A lack of conductivity in the sample will induce the charge up of the surface which leads to bad quality imaging. In nonconductive samples, a thin film of gold can be deposited onto the surface of the sample.

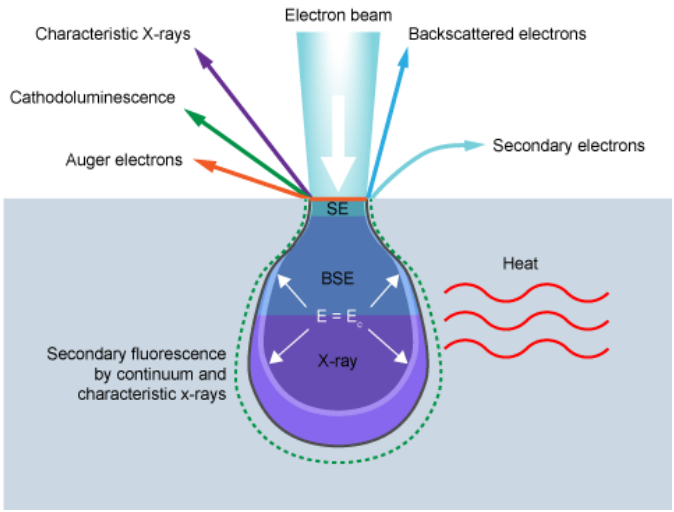

Figure 2.10. Electron beam – sample interaction and generated signal scheme [14].

In this thesis a Jeol JSM 6400 SEM was used. When needed, a thin film of gold was sputtered on the sample's surface with a Bal-Tec SCD004 sputterer. This microscope and sputtering system are available at the Serveis de Recursos Científics i Técnincs of the Universitat Rovira i Virgili.

2.3.2 Environmental scanning electron microscope (ESEM)

Environmental SEM has the same characteristics of a conventional SEM, but with the additional advantage that a high vacuum is not required for the visualization of the samples. Thus, it allows varying the sample environment through a range of pressures, temperatures and gas compositions [15]. This allows the imaging of non-conductive samples without previous

sample preparation. Thus, original characteristics of the sample may be preserved for further testing or manipulation.

In ESEM after the sample is bombarded with an electron beam the secondary electrons arising from the sample strike the gas molecules, producing secondary electrons themselves, which in turn produce secondary electrons from adjacent water vapor molecules [16]. The secondary electrons generated signal is collected at the gaseous secondary electron detector (GSED) which is strongly positively charged. In a conventional SEM, non-conductive samples cannot get rid of the superficial electrons since they cannot be shed to an electrical ground. Instead, in ESEM, since the gas molecules struck by secondary electrons are now positively charged, they are accelerated from the positively charged GSED to the negatively charged sample, neutralizing the charged surface of the sample.

In this thesis a FEI Quanta 600 ESEM coupled to an Oxford Inca 3.0 microanalysis was used, available at the Serveis de Recursos Científics i Técnics of the Universitat Rovira i Virgili.

2.3.3 Atomic force microscope (AFM)

An atomic force microscope is a mechanical-optical instrument of particular interest due to its ability to detect forces of the order of nanoNewtons (nN) [17]. The AFM is a type of scanning probe microscope (SPM) which scans the sample continuously with a pyramidal tip which is coupled to a cantilever. The continuous scan of the sample can provide topography images with a spatial resolution on the order of fraction of nanometers when using a relatively small tip radius of the AFM cantilever [18], and vertical resolution of 0.1 nm independently of the cantilever radius [19]. Besides imaging, AFM can also measure forces useful to determine elastic properties of the material like the elastic modulus [20], and also, it can be used for atom manipulation [21].

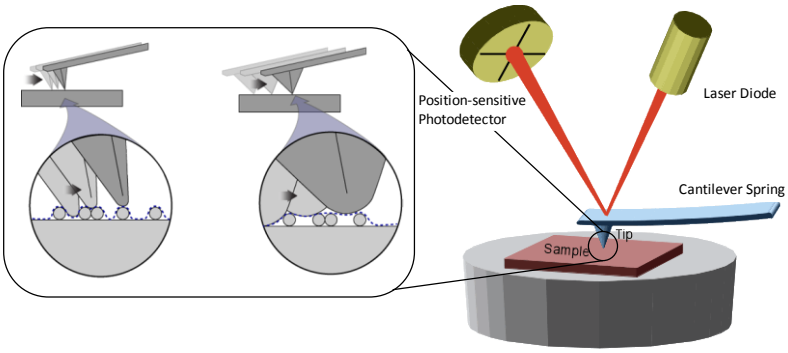

Figure 2.11. Scheme operation of an AFM and its main components. The inset shows the effect of the tip on the AFM spatial resolution. [22]

An AFM, despite other microscopes like the optic microscope or the SEM, in which light and electrons beams are used, respectively, to produce the image, uses a cantilever with a very sharp tip to scan over the surface of the sample (see Figure 2.12). This probe is connected to a piezoelectric material that enables the scan over the surface. When the tip is close enough to the surface, attractive forces between the surface and the tip cause the cantilever to deflect towards the surface. However, as the cantilever is brought closer to the surface, this produces an increasing of the repulsive forces causing the cantilever deflection away from the surface. In order to detect this deflection of the cantilever a laser beam is used. The reflection of the incident beam off the flat top of the cantilever is detected by a position-sensitive photodiode which is used to track the changes in the cantilever position. Thus, if an AFM tip passes over a raised surface feature, the resulting cantilever deflection (and the subsequent change in direction of the reflected beam) is recorded by the photodiode detector. This system amplifies a very small cantilever deflection, such that the longer the cantilever-detector beam path, the more amplification is provided at the detector level. The sensitivity of such a system is 0.1 nm. The photodetector converts this change in an electrical signal and sends it to a computer, where a map of topography is generated [23].

The AFM scanners are made from piezoelectric material, which expands/contracts proportionally to an applied voltage. The scanner itself is constructed by stacking three independent piezoelectric crystals, each of them being responsible for movements on one axis (x, y or z).

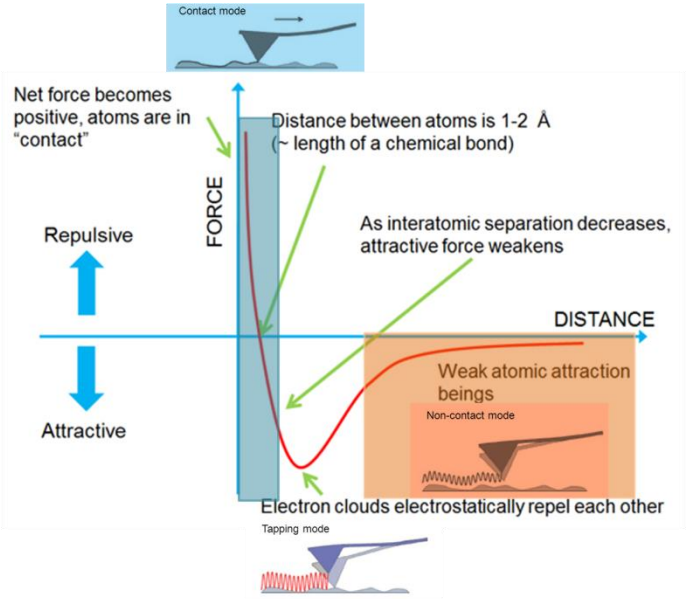

Figure 2.12. Plot of force as a function of probe distance to the sample and the three different scanning modes associated to each regime. (Image composed by [22])

Since AFM is based in weak interactions between the tip and the sample surface, such as van der Waals forces, there are three different operation modes: contact mode, taping mode and non-contact mode (see Figure 2.11). In contact mode the scan is done with the tip in continuous contact with the surface of the sample. In such situation, the probe cantilever is deflected by topographical changes in the z-direction and the scanner adjusts the probe position to restore the original cantilever deflection. This change in the z axis corresponds with the topographical height of the sample at each given point. By adjusting the pre-set force accordingly, the image contrast can be varied and the damage to the sample can be minimized. This operation mode is thus used to obtain a topographical map. The inconvenient with this operation mode is that soft samples can be damaged or scratched

after the scan in contact mode. In tapping mode, the cantilever vibrates at its resonant frequency under an external electrical excitation. While scanning the sample along x-y directions, the AFM tip briefly touches the sample at the bottom of each swing, producing a decrease in the oscillation amplitude. Similar to the pre-set constant force in contact mode, the feedback loop keep this decrease in oscillation amplitude at a constant value by moving the piezoelectric element, and a height image can be recorded. Also, a *phase* image can be recorded in tapping mode. In this mode, when the tip touches the sample at the bottom of its swing, the phase of oscillation is disturbed, inducing a phase difference between the tip and the electrical oscillator that is driving it. The contrast of a phase image is directly dependent on the elastic properties of the sample. Finally, in non-contact mode the probe tip does not contact the sample surface, but oscillates above the surface during scanning. This mode extends probe lifetime applying very low forces on the sample surface, but generally has a lower resolution.

In this thesis, the surface of porous GaN films were visualized by an Agilent 5500 microscope operating in the tapping mode with Si tips with a diameter of 10 nm and oscillating at a resonance frequency of 75 kHz. This equipment is available at the Servei de Recursors Científics i Técnics of the Universitat Rovira i Vigili.

2.4 Structural characterization techniques

2.4.1 X-ray diffraction (XRD)

X-ray diffraction (XRD) is a non-destructive technique that provides information about the structure of crystalline materials [14]. This is due to the fact that X-rays are electromagnetic radiation with wavelengths in the range of 0.5-2.5 Å, of the same order of magnitude as the interatomic distance in solids. The basic set-up for an X-ray diffractometer consists on an X-ray source, a goniometer where the stage to hold the sample is, and a X-ray detector. The X-rays are generated by a cathode ray tube, where high energy

electrons collide with a metallic target (anode) and electrons from the inner shell of the metal are ejected. The generated electron vacancy is filled with an electron from a higher energy state, emitting an X-ray photon. The generated X-rays are filtered to produce monochromatic radiation and collimated to concentrate the beam before being directed towards the sample.

When a beam of X-rays interacts with an ordered array of atoms, called crystal structure, part of the beam is transmitted, absorbed and scattered, and part is reflected. The conditions for diffraction (constructive interference of the reflected light) are easily derived from the simple geometrical picture for the scattering of an X-ray beam by planes of atoms in a crystal, shown in Figure 2.13, described by the Bragg's law:

$$n\lambda = 2d\cos\theta \qquad \textbf{(Eq. 2.1)}$$

where n is an integer of the wavelength λ known as the diffraction order, θ is the angle of the incident X-ray beam that coincides with the reflexion angle, and d is the spacing between the crystallographic planes in the crystalline structure. From Bragg's law, d-spacings can be easily calculated using the X-ray wavelength (K_α of Cu in our case corresponding to a wavelength of 1.54056 Å) [14] and the θ angles measured by the diffractometer. The intensity of the X-rays that reaches the detector is plotted versus the θ angle resulting in a diffraction pattern. The characteristic X-ray diffraction pattern provides a unique "fingerprint" of the crystalline structures present in the sample. When properly interpreted, by comparison with standard reference patterns, this fingerprint allows the identification of the crystalline form. Also other crystal parameters can be obtained apart from the d-spacings, such as their crystalline structure, lattice parameters, concentration of defects, and structural strain of the sample [24].

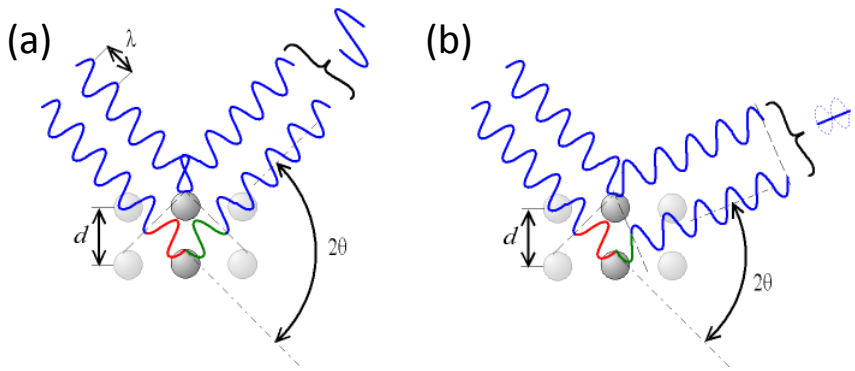

Figure 2.13. Schematic representation of (a) constructive and (b) destructive interference of X-rays diffracted by a crystalline structure [25].

In this thesis, X-ray diffraction (XRD) patterns of porous GaN samples were recorded using Cu K_α radiation in a Bruker-AXS D8-Discover diffractometer equipped with a parallel incident beam (Göbel mirror), a vertical θ-θ goniometer, an XYZ motorized stage, and a General Area Diffraction Detection System (GADDS) HI-STAR detector with a multiwire proportional counter of 30 x 30 cm^2 area and 1024 x 1024 pixel density. Samples were placed on the sample holder fixed with wax, and the area of interest was selected with the aid of a video-laser focusing system. An X-ray collimator system allows the analysis of an area of 500 μm^2 on the sample. The X-ray diffractometer was operated at 40 kV and 40 mA. We collected 2D XRD patterns covering a range of 2θ between 20 and 85° corresponding to 3 frames of the GADDS detector, located at 15 cm from the sample. The exposure time was 120 s per frame. The identification of the crystalline phases was achieved by comparing the XRD pattern with the Joint Committee on Powder Diffraction Standards (JCPDS) database using the DIFFRACplus Evaluation software from Bruker [26].

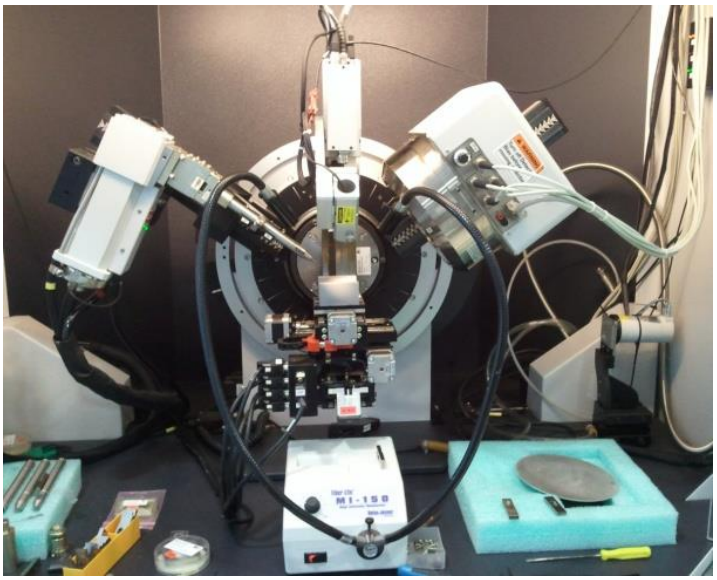

Figure 2.14. Bruker-AXS D8-Discover diffractometer used in this thesis.

2.4.1.1 Analysis of the rocking curves (RC)

Another type of X-ray analysis scanning is the analysis of the rocking curves (RC). From RC measurements it is possible to determine the mean spread in orientation of the different crystalline domains of a non-perfect crystal [27]. This is a powerful technique to analyze the orientation of thin films and epitaxial layers. In a rocking curve scan, the relative positions of the X-ray source and the detector are maintained at 2θ but the angle ω respect to the sample is being varied (see Figure 2.15). This is why it is also known as ω-scan. For $\Delta\omega = 0$ the sample and the detector are at the exact positions for constructive interference, so a peak will be observed. When we move the ω angle so that $\Delta\omega \neq 0$ signal can be observed and the width of this peak analyzed as the full width at half-maximum (FWHM) will be determined by several factors, being the most interesting the spread in crystalline orientation between the different domains to the chosen Bragg reflection [28]. Defects like dislocations create disruptions in the perfect parallelism of atomic planes and this is observed as a broadening of the peak. Also, with the peak position

of the RC the lattice constants can be obtained, which give us information about the expansion or compression of the crystalline cell.

To record the RC the same diffractometer was employed. In that case the X-ray source and the X-ray detector position were settled at the desired Bragg angle. The X-ray diffractometer was operated at 40 kV and 20 mA, and 120 frames where taken at integration time of 1 s every 0.05° in ω. Note that the current and the recording time were reduced in order not to saturate the detector. The ω-scan was set to start at an ω angle of 3° below the desired Bragg angle corresponding to a particular reflection of interest for the case being analyzed, and finishes 3° above that Bragg angle. The envelope function of the collection of 120 frames was then plotted, and corresponds to the RC.

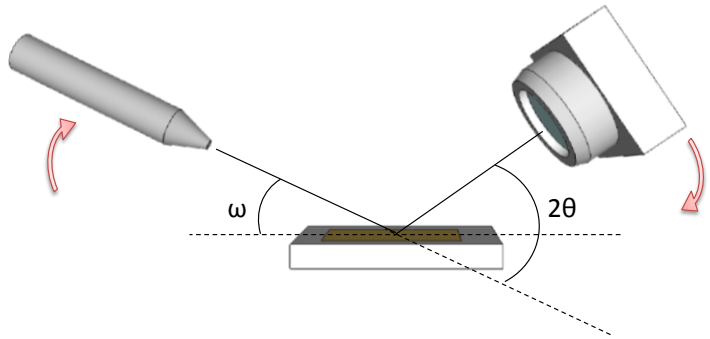

Figure 2.15. Schematic representation of the relative movement of the X-ray source and detector in a Rocking Curve scan.

In the present case we analyzed the (0004) and ($10\bar{1}2$) reflections of the hexagonal GaN. The (0004) reflection gives information about the in plane structural strain, while the ($10\bar{1}2$) reflection gives information about the structural strain out of plane.

For the identification of the ($10\bar{1}2$) peak either a χ-scan and a φ-scan were done to find the exact diffraction conditions. The χ position is fixed when the scattering vector $\vec{K}$ (the scattering vector $\vec{K}$ is the substracting of the incident wave vector $\vec{k}_I$ and the scattered wave vector $\vec{k}_O$) is perpendicular to the (*hkil*) plane, in this case the ($10\bar{1}2$) plane. The χ angle is defined using the

stereographic projection and measuring the angle between the $(10\bar{1}2)$ and (0001) planes. Then, a φ-scan must be done to find the location of the $\vec{a}$ (or $\vec{b}$) crystallographic axis. A φ-scan consists on the rotation of the platform where the sample is placed once the χ angle is fixed, and the position of the X-ray source and the detector are also fixed to accomplish Bragg diffraction conditions (see Figure 2.16). This procedure allows indentifying peaks that are out of the plane of the sample when the thin film is parallel to the ground platform. For this, the X-ray source and the detector were placed at a defined θ Bragg angle, and then, the sample was rotated every 5° for 36 times with an integration time of 5 seconds, covering 180° of the sample. Once a φ angle is identified, at which the diffraction intensity was higher, a second φ-scan was done to refine its value, at which the diffraction intensity was at its most. For this, a scan of 1 degree was performed 5 times with an integration time of 5 seconds.

Once the φ and the χ angles are defined the RC can start. For the RC scan for the $(10\bar{1}2)$ reflection with θ = 24.19°, the initial ω_1 and final ω_2 angles were set at 21.19° and 27.19° respectively. In the case of the (0004) reflection with a θ = 36.44°, ω_1 and ω_2 angles were set at 33.44° and 39.44°, respectively.

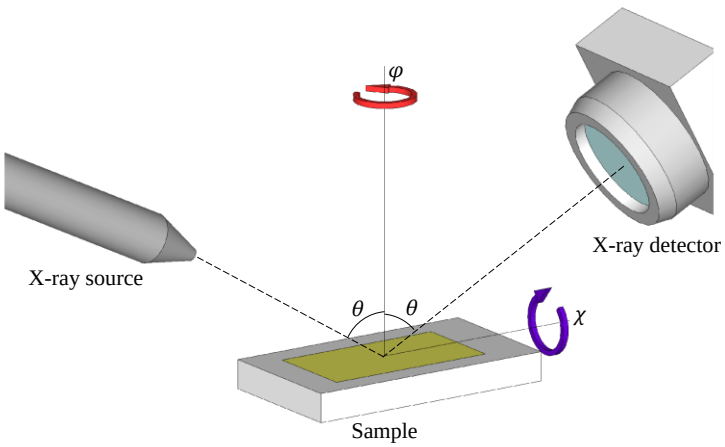

Figure 2.16. Schematic representation of the φ and χ rotations with respect to the sample platform and the X-ray source and detector, that are located at fixed positions.

2.4.2 Resonant Raman scattering (RRS)

Raman scattering is a standard spectroscopic technique used to study various aspects of solids such as lattice properties, electronic properties, and magnetic properties. The Raman spectrum, or the so called Raman shift, is characteristic from a material, thus Raman scattering can be used to identify the material as well. Raman scattering is a non-destructive analysis technique, is contactless, and requires no special sample preparation. Raman scattering occurs essentially as a result of modulation of the electronic polarizability, which is determined by the electron cloud's ability to interact with an electric field, induced by various elementary excitations in solids such as phonons and plasmons. In the case of Raman scattering by phonons, the scattering efficiency is higher in covalent crystals than in ionic crystals, because the valence electrons are less localized and larger fluctuations of the polarizability can be induced by lattice vibration [29].

The term Raman scattering is historically associated with the scattering of light by optical phonons in solids and molecular vibrations. But lately the term refers to inelastic scattering by most elementary excitations associated with degrees of freedom of ions and electrons in crystalline and amorphous solids [30]. Inelastic processes are two-photon events that involve the simultaneous annihilation of an incident photon and the creation of a scattered photon (see Figure 2.17). If the frequency of the latter, ω_s is smaller than that of the former, ω_L , a quantum of energy $\hbar(\omega_L-\omega_S)$ is added to the scattering medium and the event is referred to as a Stokes process (here, we use ω_L to designate the incident photon frequency, since the incident beam is invariably generated by a laser source). If, instead $\omega_S > \omega_L$, we have an anti-Stokes process, where an elementary excitation of the medium is annihilated. The difference between the laser source wavenumber and that of the emitted photon is called Raman shift. We have an identical energy spectrum at the left and right sides of the zero phonon line provided by the laser, with different intensities, being the more intense the Stokes lines. For systems in thermal

equilibrium, the anti-Stokes intensity depends strongly on temperature, since these processes can occur only when the medium is not in its ground state [31]. The dominant form of Raman scattering, first-order scattering, involves a single quantum of excitation in the medium. However, it is not uncommon for materials to show strong higher-order processes leading to the creation or annihilation of two or more quanta [30].

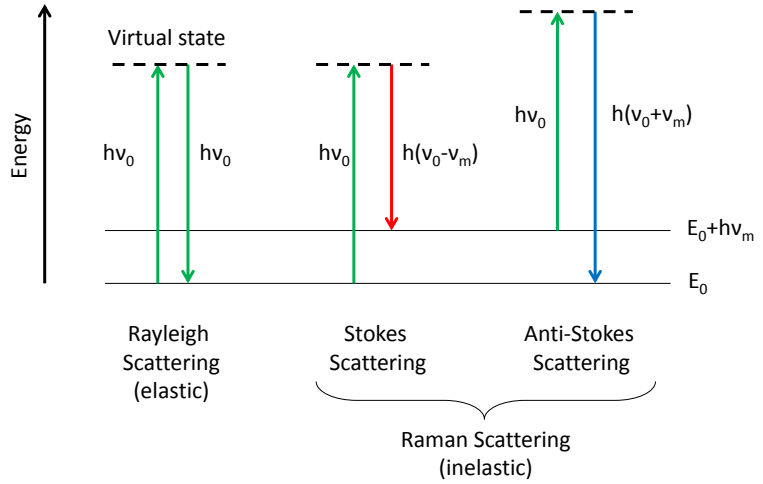

Figure 2.17. Energy diagram of the three possibilities of light scattering: Rayleigh scattering (there is no exchange of energy), Stokes Raman scattering (molecule absorbs energy: scattered photon has less energy than the incident photon) and anti-Stokes Raman scattering (molecule loses energy: scattered photon has more energy than the incident photon).

The strongest inelastic light scattering processes are due to the coupling of light to the electric moments of the scattering medium [31]. At relatively high frequency of light, the dominant contributions to electric moments are due to the excitation of electrons across energy bandgaps. The coupling of incident and scattered light to the medium may be understood as the modulation of the electric susceptibility by elementary excitations. It is well known that coupling of light to optical transitions of the scattering medium is enhanced when ω_L and ω_S are close to interband gaps. Such optical resonances result in large enhancements of Raman scattering cross-sections and intensities. Events involving light at frequencies when ω_L and ω_S are close to interband transition energies are referred to as RRS processes [30]. The

process is described by the Feynman diagram in Figure 2.18. The study of resonant effects is of great interest because enhanced cross-sections (intensity) enable Raman scattering observations of otherwise weak processes, especially in the spectra of optical phonons. In these conditions, light scattering might occur within ultrathin layers of thickness that in some cases might be 10 nm thick or even thinner.

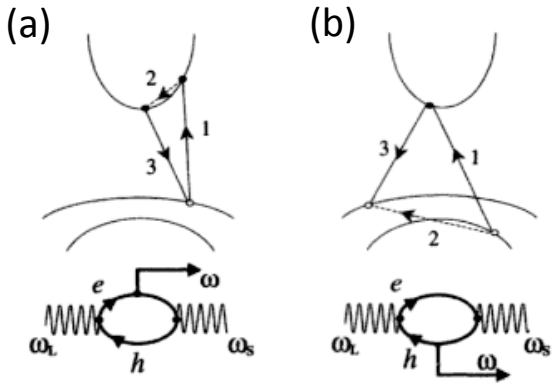

Figure 2.18. Electronic energy band diagrams and associated Feynman diagrams for light scattering process due to (a) electrons (*e*) and (b) holes (*h*). The numbers indicate the order of the electronic transitions. In the Feynamn diagrams the wavy lines represent incoming (ω_L) and outcoming (ω_S) photons, the solid line corresponds to the emitted (upper line) or absorbed photon (lower line) (ω) and the loop called fermion loop corresponds to the intermediate state where an electron (*e*) and a hole (*h*) pair is generated.[31]

For this aim, resonant micro-Raman (μ-Raman) spectra were obtained at room temperature with a Labram HR800UV Raman spectrometer from Horiba-Jobin-Yvon attached to a metallographic microscope, and equipped with a LN2-cooled CCD detector. The excitation was carried out with a UV laser at 325 nm using 40X UV or 15X UV microscope objectives. The scattered light was collected by the same objective in a backscattering configuration. This system is available at the Departamento de Física de la Materia Condensada, Universidad de Valladolid, Valladolid (Spain).

2.5 Luminescent characterization techniques

2.5.1 Photoluminescence

Photoluminescence is the spontaneous emission of light from a material under optical excitation [32]. PL analysis is a nondestructive analysis method of the electronic structure. Indeed, the technique requires very little sample manipulation or environmental control. The excitation energy and intensity are chosen to probe different regions and excitation concentrations in the sample, since the excitation of the materials depend on the photon energy and the excitation intensity controls the density of photoexcited electrons and holes, which governs the behavior of these carriers. Features of the emission spectrum can be used to identify surface, interface, and impurity levels and to gauge alloy disorder and interface roughness as well as residual stress in epitaxial layers [33]. In PL, when light of sufficient energy is incident on a semiconductor material, photons are absorbed and electronic excitations between bands occur. Eventually, these excited electrons relax to the ground state. If the relaxation is radiative, the emitted light is called photoluminescence. The emitted light by the material is then collected by lenses and passes through an optical monochromator or spectrometer onto a photodetector (see Figure 2.19). The resultant PL spectrum provides the transition energies, which can be used to determine the electronic energy levels.

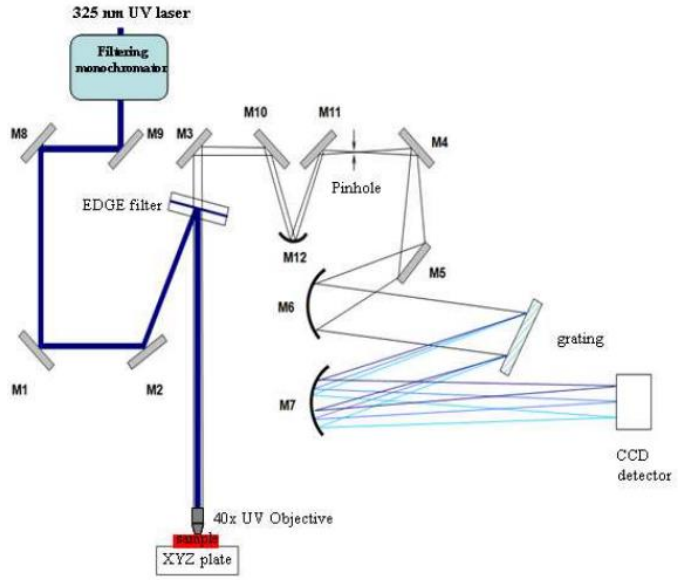

Figure 2.19. General scheme of PL spectrometer. M1 to M12 a mirrors used to guide the laser beam and luminescence signal. The EDGE filter is used to reject the 325 nm excitation from the luminescence signal. The grating and CCD detector defines the spectrometer resolution [34].

The micro-photoluminescence (μ-PL) spectra of the GaN porous films were obtained at room temperature and 80 K with a Labram HR800UV Raman spectrometer from Horiba-Jobin-Yvon attached to a metallographic microscope, and equipped with a LN2-cooled CCD detector. The excitation was carried out with a UV laser at 325 nm using 40X UV or 15X UV microscope objectives. The PL setup was available at the Departamento de Física de la Materia Condensada, Universidad de Valladolid, Valladolid (Spain).

2.5.2 Cathodoluminescence

Cathodoluminescence is the optical signal obtained when a high energetic beam of electrons hits a luminescent material [35]. As mentioned previously in section 2.2.1, cathodoluminescence is one of the multiple signals coming out of the sample due to the interaction of the material with an

incident electron beam. The cathodoluminescence process in semiconductors results when an electron in the conduction band, previously excited with the electron beam, recombines with a hole in the valence band. This relaxation process results in a release of energy which is delivered in the form of a photon when the process is radiative [36]. The excitation process is not the result of the direct interaction with primary electrons, too energetic, but with the secondary electrons generated by these primary electrons. These secondary electrons can excite valence electrons into the conduction band when they have a kinetic energy about three times that of the band gap energy of the material ($E_c \approx 3E_g$) [37].

CL is a common technique used in geology, mineralogy, materials science and semiconductor engineering in order to get information of the composition of a particular sample, including the presence of dopants and impurities, visualized by the presence of additional emission bands apart from the corresponding to the Near Band Edge (NBE). Other information that can be obtained from the CL signal is the residual structural stress which causes a shift in the positioning of the NBE emission band, apart from the information on the quality of the material such presence of defects like dislocations seen as a non-radiative recombination centers in panchromatic CL images.[38] The great advantage of CL set-ups is that usually they are coupled to a SEM, so the sample can be analyzed morphologically and optically in the same equipment. To do that a parabolic mirror is coupled to the system, located above the sample in order to collect the light generated in it and send it to a monochromator, and to a detector (see Figure 2.20). A CL set-up also allows obtaining the spectra of single points in the sample visualized via secondary electrons in the SEM.

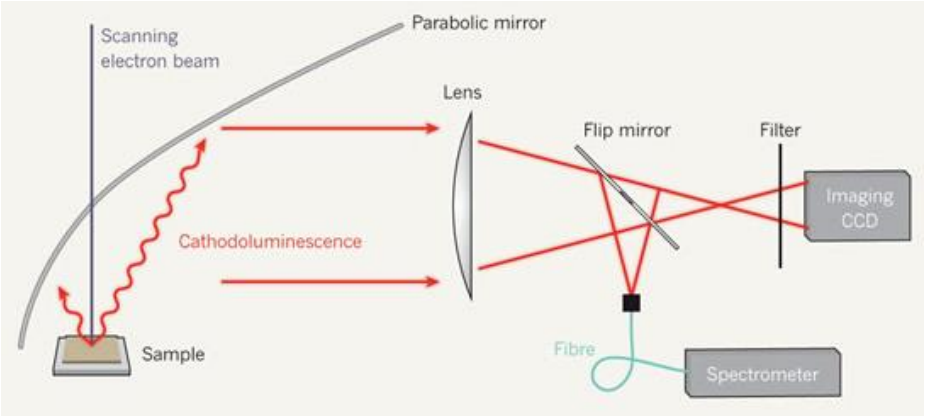

Figure 2.20. Schematic representation of the cathodoluminescence signal pathway and the equipment required to couple this system to a SEM in order to process the signal [39].

In this thesis CL measurements were carried out at 80 K with a XiXLOne Mono-CL2 system from Gatan attached to a field emission scanning electron microsocope (Carl Zeiss-LEO 1500). The acceleration voltage of the electron beam was varied between 5 and 10 keV. The CL spectra were acquired using a Peltier cooled charge-coupled-device (CCD) as detector. The equipment was available at the Departamento de Física de la Materia Condensada, Grupo de Semiconductores, Universidad de Valladolid, Valladolid (Spain).

2.5.3 Reflectance measurements

The reflectance of a material's surface is the fraction of the incident electromagnetic radiation that is reflected at an interface [40]. In a typical reflectance spectrum the fraction of reflectance on a given surface is plotted against the wavelength.

Reflection consists of two components: specular and diffuse reflection, described in Figure 2.21 [41]. Specular reflectance is the mirror-like reflection off a sample surface. Polished materials or glasses, are also called specular surfaces because the reflectance will be nearly zero at all angles except at the appropriate reflected angle, this means when the incident angle with respect to the normal is equal to the angle of the outgoing photon.

Diffuse reflectance occurs when radiation is reflected in all angles equally or near-equally, giving to the surface a matt appearance. This process of reflectance is typical from rough or unpolished surfaces. Diffuse surfaces are also called Lambertian surfaces. Traditionally, the accessory used to measure diffuse reflectance is the integrating sphere [41]. Among the applications of characterization in which reflectance measurements are involved include characterization of solar-cell materials, color measurement and characterization, collecting the reflectance spectra of painted surfaces, and the analysis of the optical properties of substrates like the transparency window, and is a standard technique in the determination of the absorption properties of materials. The determination of the band gap energy from the measurement of the diffuse reflectance of a powder sample is also a standard technique by using integrating spheres [42].

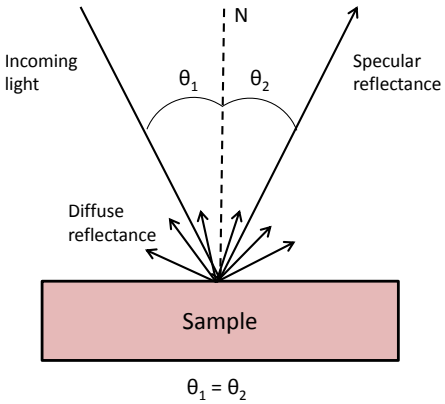

Figure 2.21. The two components of reflection of a surface: specular and diffuse reflection. N represents the surface normal (image adapted from [43]).

The diffusive reflectance measurements in this thesis were performed using an Agilent Cary 5000 UV-Vis-NIR spectrophotometer equipped with an internal diffuse reflectance accessory (DRA) which consists on a 110 mm diameter integrating sphere. The internal coating of the integrating sphere is made of polytetrafluoroethylene (PTFE), which exhibits a superior NIR performance when compared to traditional coatings, whilst maintaining a

good UV-Vis performance. In our case, the GaN substrates are specular surfaces while the porous GaN samples behave like Lambertian surfaces. The results obtained in both cases have to be comparable. For that reason, the sample was placed in the 'S' position and not in 'D' position in the integrating sphere (see Figure 2.22) which means that the angle between the incident beam and the sample is fixed at 3° and 20 min so that the specular reflection is trapped also into the integrating sphere and does not go back to the incident beam entrance. The reflection process is schematically shown in Figure 2.21. Prior to the reflectance measurements of the sample under study a baseline scan with a 100% reflectance reference sample has to be done, using a protruding PTFE reference plate. Also a second baseline with a 0% reflectance sample, recorded without any sample in the integrating sphere, must be done.

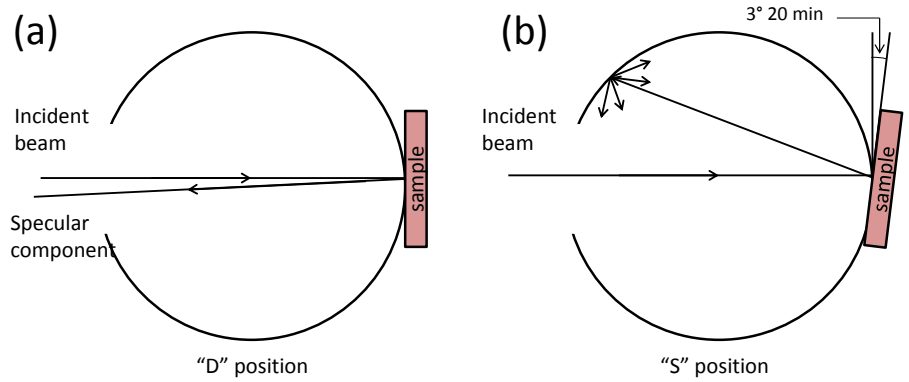

Figure 2.22. Scheme of the light path inside an integrating sphere with the sample located in (a) position 'D', which measures diffuse reflectance only, and in (b) position 'S' where the total reflectance is measured, including also the specular component (image adapted from [43]).

2.6 Electrical characterization techniques

2.6.1 Two-probe measurements

The two-probe electrical measurements technique is often used to record the I-V curves of a device under test (DUT). In two-point probe

methods, each contact serves as a current and as a voltage probe. The two probes are connected at a fixed spacing distance on the sample surface. Current is sent through one probe and exits through the second one. The voltage drop is measured between the two probes. The measured resistance in two-probe measurements is not the resistance of the device under test (R_{DUT}), so in order to determine the resistance of the DUT we have to isolate the value from the total resistance, R_T, given by:

$$R_T = {}^{V}/_{I} = 2R_W + 2R_C + R_{DUT} \quad \textbf{(Eq.2.2)}$$

where R_w is the wire probe resistance, R_C the contact resistance, and R_{DUT} the resistance of the device under test (see Figure 2.23).

The drawback of this methodology to determine the R_{DUT} is that the voltage measured across the resistance also includes the resistance of the probes (R_w) and the contacts (R_C). It is only possible to obtain the value of the resistance of the DUT with quite good accuracy when the values of resistance of the probe and the contacts are negligibly small.

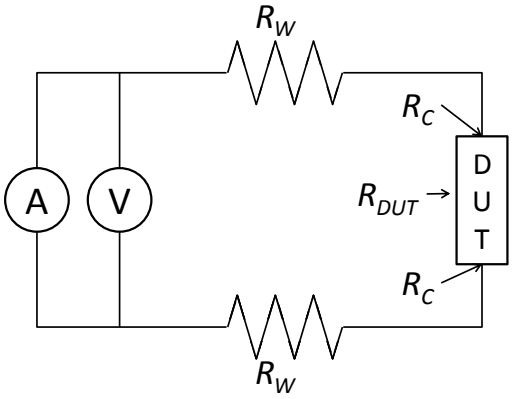

Figure 2.23. Scheme of the principle of work of the two-probe measurements.

In this thesis two-probe electrical measurements of GaN films were conducted using a Keithely 2400 sourcemeter able to source and measure voltage/current with a single-channel. The I-V curve was monitored and recorded using the Labtracer 2.9 SourceMeter ® Integration Software from Keithley Instruments, Inc. The contacts are needles made of tungsten.

2.7 Molecular characterization

2.7.1 Nuclear magnetic resonance (NMR)

Nuclear magnetic resonance (NMR) is a nuclear specific spectroscopy that has applications throughout the physical sciences and industry [44]. NMR uses a large magnet to probe the intrinsic spin properties of atomic nuclei. Like all spectroscopy techniques, NMR uses a component of electromagnetic radiation, in this case radio frequency waves, to promote transitions between nuclear energy levels, which are based in two spin states that have the same energy when the external magnetic field is zero, but diverge as the external magnetic field increases [45]. In chemistry, the use of NMR is widely used for structure determination of molecules. Among all the spectroscopic methods, it is the only one for which a complete analysis and interpretation of the entire spectrum is normally expected.

The nuclei of many elemental isotopes have a characteristic spin (I). Some nuclei have integral spins (e.g. I = 1, 2, 3 ....), some have fractional spins (e.g. I = 1/2, 3/2, 5/2 ....), and a few have no spin, I = 0 (e.g. ^{12}C, ^{16}O, ^{32}S, ...). Isotopes of particular interest and used by organic chemists are ^{1}H, ^{13}C, ^{19}F and ^{31}P, all of which have I = ½ [45].

In order to split the degenerate energy levels of the nucleus spin, strong magnetic fields are necessary. Modern NMR spectrometers use powerful magnets having fields from 1 to 20 T. Even with these high magnetic fields, the energy difference between the two spin states are less than 0.1 cal/mol. This small energy difference is usually given as a frequency ranging from 20 to 900 MHz, in the microwaves frequency, depending on the magnetic field strength and the specific nucleus being studied. Irradiation of a sample with radio frequency energy corresponding exactly with the spin state separation of a specific set of nuclei will cause excitation of these nuclei in the +1/2 state to the higher energy -1/2 spin state.

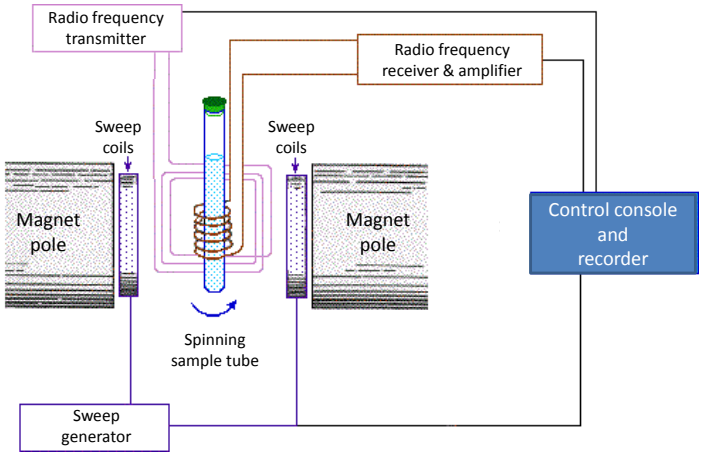

Figure 2.24. A typical NMR CW-spectrometer setup diagram (adapted from [45]).

The principal components of a typical continuous wave (CW) NMR spectrometer are shown schematically in Figure 2.24. A solution of the sample under analysis dissolved with the proper deuterated solvent is added in a uniform 5 mm glass tube. The tube is oriented between the poles of a powerful magnet, and is spun in order to average any magnetic field variations, as well as tube imperfections. A receiver coil surrounds the sample tube (labeled as radio frequency (RF) receiver and amplifier in Fig. 2.24), and the emission generated from the absorbed RF energy (generated by the RF transmitter) is monitored by a computer. An NMR spectrum is acquired by sweeping the magnetic field over a small range while observing the RF signal emitted from the sample. An equally effective technique is to vary the frequency of the RF radiation while holding the external field constant.

Since protons all have the same magnetic moment, we might expect all hydrogen atoms to give resonance signals at the same field/frequency values. However, since the surrounding electrons are charged particles, they move in response to the external magnetic field (B_0) so as to generate a secondary field that opposes the much stronger applied field. This secondary field shields the nucleus from the applied field, so B_0 must be increased in order to achieve resonance (absorption of RF energy), for more clarity see Figure 2.25.

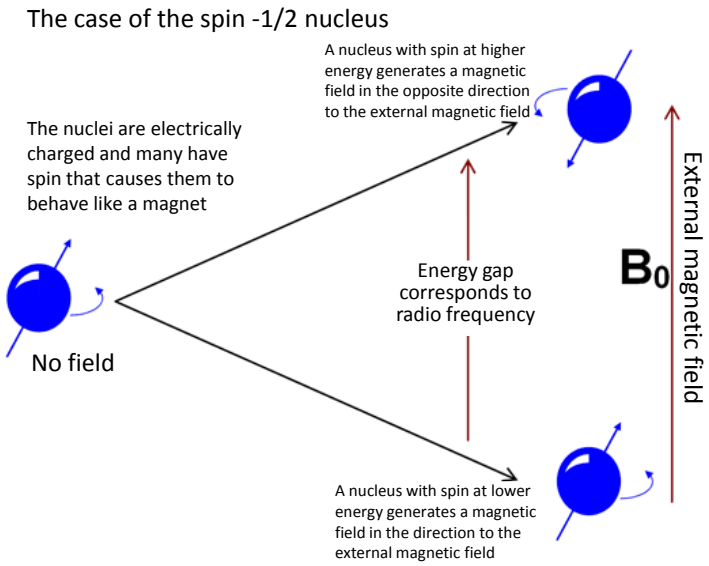

Figure 2.25. Scheme of the interactions of the nucleis with spin ½ when an external magnetic field B_0 is applied, the transition between spin states gives the NMR line.

Unlike infrared and UV-visible spectroscopy, where absorption peaks are uniquely located by frequency or wavelength, the location of different NMR resonance signals is dependent on both the external magnetic field strength and the RF. Since two magnets will not have exactly the same field, resonance frequencies will vary accordingly and an alternative method for characterizing and specifying the location of NMR signals is needed. One method of solving this problem is to report the location of an NMR signal in a spectrum relative to a reference signal from a standard compound added to the sample, where ν_{sample} is the absolute resonance frequency of the sample and ν_{ref} is the absolute resonance frequency of a standard reference compound. Since the separation (or dispersion) of NMR signals depend on the magnetic field, one additional step must be taken in order to provide an unambiguous location unit. To correct these frequency differences for their field dependence, we divide them by the spectrometer frequency. The resulting number would be very small, since we are dividing Hz by MHz, so it is multiplied by a million, and this locator number is called the chemical shift,

having units of parts-per-million (ppm), and designated by the symbol δ, the full equation is shown in Eq.3 [46].

$$\delta\ (\text{ppm}) = \frac{\nu_{\text{sample}} - \nu_{\text{ref}}\ (\text{HZ})}{spectrometer\ frequency\ (\text{MHz})} \qquad \textbf{(Eq.2.3)}$$

In an NMR spectrum we plot the intensity versus the chemical shift. The intensity in NMR is proportional to the molar concentration of the sample, so it gives us additional information of the proportion of each signal in the molecule under analysis. It allows us to build up the molecule structure under analysis from the relative intensities obtained in the spectra, together with the previously noted chemical shift correlations.

The NMR equipment used in this thesis is a Bruker Avance III HD 400 available at the Fakultät für Chemie und Pharmazie of Universität Würzburg, Würzburg (Germany).

2.7.2 Fourier transform infrared (FT-IR) spectroscopy

Infrared spectroscopy is a technique for compounds and material analysis, since each compound produce a unique spectrum that acts as a fingerprint, in which each peak corresponds to the frequency vibrations of bonds between atoms in the molecule or material under analysis [47]. Therefore, IR spectroscopy is a tool ideal to identify qualitatively any material or molecule.

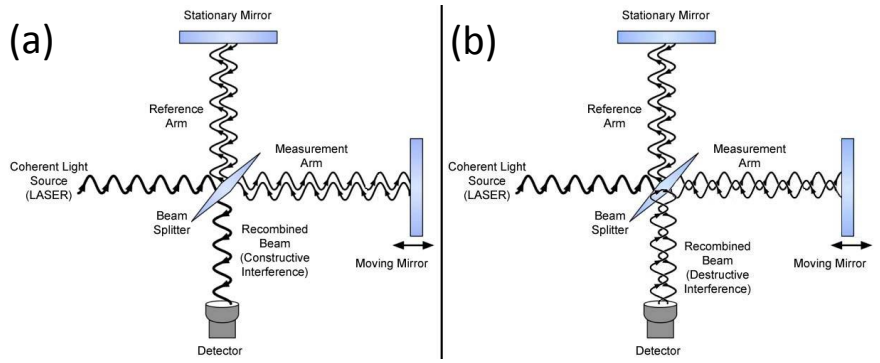

Figure 2.26. Scheme of an FT-IR interferometer where the two extreme scenarios are shown: (a) when the light reflected by the moving mirror is coherent, producing a constructive interference, and (b) when the light reflected by the moving mirror is incoherent, thus, leading to a destructive interference [48].

Fourier transform infrared (FT-IR) spectrometry was designed to measure all the infrared frequencies simultaneously with the aid of an interferometer (see Figure 2.26). The interferometer consists in a laser which acts a source of coherent light, a beam splitter which is partially reflective, splitting the light into two beams, the reflected beam is directed towards the stationary mirror and the transmitted beam is directed towards the moving mirror. The reflected light from the stationary and moving mirrors recombine again in the beam splitter to produce an interference pattern incident on the detector. Finally the interferogram is generated by making measurements of the signal at many discrete positions of the moving mirror. This allows obtaining IR spectrums very quickly (in the order of a few seconds rather than several minutes). The resulting signal is called an interferogram which has the property that every data point which makes the signal (a function of the moving mirror position) has information about every infrared frequency which comes from the source. But, for us this spectrum does not give the proper information, and a conversion to a frequency spectrum is needed. This is accomplished via the Fourier transformation where the spectra are collected based on measurements of the coherence of a radiative source, using time-domain or space-domain measurements of the electromagnetic radiation or other type of radiation. This transformation is performed by the computer

which presents the user with the desired spectral in which the percentage of transmittance (%T) is plotted against the wavenumber (cm^{-1}).

The FT-IR equipment used in this thesis is a JASCO FT/IR-430 available at the Fakultät für Chemie und Pharmazie of Universität Würzburg, Würzburg (Germany).

2.7.3 Inverted Fluorescence Microscopy

Fluorescence microscopy is an optical imaging technique that uses the fluorescence of the substances under study instead of reflection and absorption of light, and thereby, it is capable of imaging the distribution of single molecular species based solely on the properties of fluorescence emission [49]. Thus, using fluorescence microscopy, the precise location of fluorescent components can be monitored in functionalized surfaces for instance.

The simplest fluorescence microscope configurations featured an optical train that focused the excitation light generated by a Mercury arc lamp and that passed through a filter, on the sample, using a dichroic mirror and an objective. The fluorescence emission generated by the sample was gathered by the objective, along with a significant amount of the excitation illumination, which was partially blocked by the dichroic mirror and was projected through a second filter, which blocked the non-fluorescent light, so only the fluorescent signal generated the resultant image. The light that passed the fluorescent filter was splitted into two beams: one was addressed to the digital detector, which allow us to have a digital image in the computer, and the other one was addressed into the eyepiece to form the intermediate image, which allow us to monitor optically the image directly from the microscope setup, for more clarity see Figure 2.27.

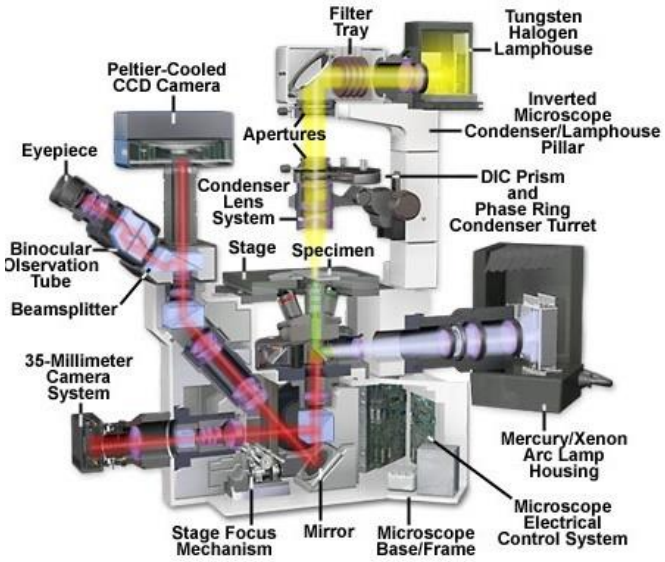

Figure 2.27. Principal components of an inverted fluorescence microscope and the light pathway from the mercury arc lamp to the camera where the fluorescent image is recorded [50].

In this thesis a Nikon Eclipse TE2000 Inverted Microscope is used to evaluate the functionalization of GaN surfaces with a fluorescent dye. The microscope is equipped with three different fluorescence filter cubes: one for fluorescent samples under blue excitation (Excitation (Ex) 465-495 / Dichroic mirror (DM) 505 / Barrier filter (BA) 515-555), another for green excitation (Ex 540-625 / DM 565 / BA 605-655), and another for red excitation (Ex 640-660 / DM 660 / BA 700-775). The microscope is equipped with 4 Plan Fluor Nikon objectives of 10X (maginification) / numerical aperture (NA) 0.3 / work distance (WD) 16.0 mm, 20x / NA 0.45 / WD 2.1 mm, 20x / NA 0.75 Multi-immersion (MI) / WD 0.35 mm, 20x / NA 0.75 MI / WD 0.35 mm, 40x / NA 1.3 oil (the NA correspons to the NA when immersing the lenses in oil) / WD 0.2 and two Plan Apo Nikon objectives of 60x / NA 1.40 oil / WD 0.21 mm and 100x / NA 1.40 oil / WD 0.13 mm. Finally, the image is recorded by a HAMAMATSU Digital Camera C8484 and send to the computer. The microscope described above is available at the Serveis de Recursos Científics i Técnics of the Universitat Rovira i Virgili.

2.7.4 X-ray photoelectron spectroscopy (XPS)

X-ray photoelectron spectroscopy (XPS) is a characterization technique based on the photoelectric effect and the posterior analysis of the kinetic energy distribution of the emitted electrons to study the composition and electronic state of the surface region of a sample.

XPS is highly interesting for surface analysis since the average depth of analysis for an XPS measurement is approximately 5 nm.

For this reason X-ray photoelectron spectroscopy has become one of the standard tools for surface characterization.

XPS spectra are obtained by irradiating a solid surface with a beam of X-rays, typically mono-energetic Al K_α X-rays, while simultaneously measuring the kinetic energy and electrons that are emitted from the top 1-10 nm of the material being analyzed with a raster scanned electron gun (see Figure 2.28). A photoelectron spectrum is recorded by counting ejected electrons over a range of electron kinetic energies. Peaks appear in the spectrum from atoms emitting electrons of a particular characteristic energy. The energies and intensities of the photoelectron peaks enable identification and quantification of all surface elements (except hydrogen). From the binding energy and intensity of a photoelectron peak, the elemental identity, as well as the chemical state, and quantity of a detected element can be determined [51] [52].

When an atom or molecule absorbs an X-ray photon, an electron can be ejected. The kinetic energy of the electron (E_K) is equal to the photon energy (hv) minus the binding energy of the electron (BE) (i.e., the energy required to remove the electron from the surface) [52].

By measuring the kinetic energy of the emitted electrons, it is possible to determine which elements are near a material's surface, their chemical states and the binding energy of the electron. The binding energy depends upon a number of factors, including the following:

- The element from which the electron is emitted.

- The orbital from which the electron is ejected
- The chemical environment of the atom from which the electron was emitted.

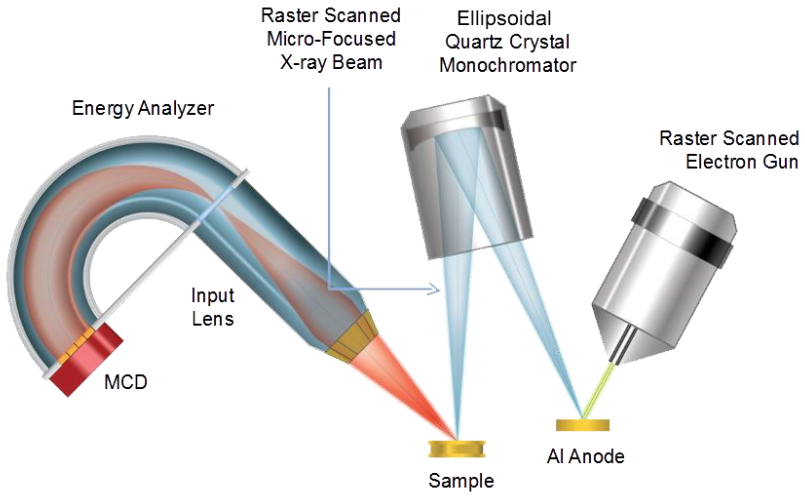

Figure 2.28. Scheme of the basic components of an XPS set-up [51].

The XPS measurements were carried out with a hemispherical analyzer PHOIBOS 150 (SPECS) with 2D-DLD detector; energy resolution: 0.1 eV; acceptance area (field of view on the sample): ~2 mm. X-ray source: non monochromated Mg K_α ($h\nu$ = 1253.6 eV) and Al ($h\nu$ = 1486.61 eV) 200 W, 12 kV. XPS spectra quantification: CasaXPS software, peak fitting: Shirly'type background and mixed Gaussian/Lorenzian peak shapes. The XPS measurments were carried out at the CIC energigune, Alava Technology Park, Miñano-Alava (Spain).

References

[1] Chapter 1 Overview of Chemical Vapour Deposition. In *Chemical Vapour Deposition: Precursors, Processes and Applications*, Jones, A. C.; Hitchman, M. L., Eds. The Royal Society of Chemistry: 2009; pp 1-36.

[2] Roblin, P.; Rohdin, H., *High-speed heterostrucutre devices. From device concepts to circuit modeling*. 1 ed.; Cambridge University Press: 2002; p 726.

[3] Nakamura, S.; Pearton, S.; Fasol, G., *The Blue Laser Diode. The Complete Story*. 2 ed.; Springer-Verlag Berlin Heidelberg: 2000.

[4] Shafa, M.; Akbar, S.; Gao, L.; Fakhar-e-Alam, M.; Wang, Z. M., Indium Antimonide Nanowires: Synthesis and Properties. *Nanoscale Res. Lett.* **2016,** *11* (1), 164.

[5] Lee, H.; Song, M. Y.; Jurng, J.; Park, Y.-K., The synthesis and coating process of TiO2 nanoparticles using CVD process. *Powder Technol.* **2011,** *214* (1), 64-68.

[6] Kim, Y.-S.; Park, H.-H.; Kim, Y.-S.; Shin, H.-S., Preparation of $Y_{1-x}Yb_xBa_2Cu_3O_{7-y}$ superconducting films by chemical vapor deposition. *Korean J. Chem. Eng.* **2000,** *17* (4), 473-476.

[7] Yan, X.-T. X., Yongdong, *Chemical Vapour Deposition. An integrate engineering design for advanced materials*. Springer-Verlag: London, 2010; p 342.

[8] Yan, X.-T.; Xu, Y., *Chemical Vapor Deposition. An Integrated Engineering Design for Advanced Materials*. 1 ed.; Springer-Verlag London: 2010; p 342.

[9] Sato, M., Nitrogen radical densities during GaN growth by molecular beam epitaxy, plasma-assisted metalorganic chemical vapor deposition, and conventional metalorganic chemical vapor deposition. *Solid·State Electron.* **1997,** *41* (2), 223-226.

[10] http://www.ioffe.ru/SVA/NSM/Semicond/BN/thermal.html (accessed 2017-08-03).

[11] Kostoglou, N.; Polychronopoulou, K.; Rebholz, C., Thermal and chemical stability of hexagonal boron nitride (h-BN) nanoplatelets. *Vacuum* **2015,** *112*, 42-45.

[12] Wasa, K.; Kitabatake, M.; Adachi, H., Thin Film Materials Technology. Sputtering of Compound Materials. William Andrew Publishing: Norwich, NY, 2004; p 518.

[13] Gill, W. D.; Kay, E., Efficient Low Pressure Sputtering in a Large Inverted Magnetron Suitable for Film Synthesis. *Rev. Sci. Instrum.* **1965,** *36* (3), 277-282.

[14] http://www.ammrf.org.au/myscope/sem/background/concepts/interactions.php#detail (accessed 2017-08-04).

[15] Donald, A. M., The use of environmental scanning electron microscopy for imaging wet and insulating materials. *Nat Mater* **2003,** *2* (8), 511-516.

[16] Environmental Scanning Electron Microscopy. An introduction to ESEM. http://www2.unibas.it/cigas/amministrazione/editor/uploads/files/estutor1.pdf (accessed 2017-08-04).

[17] Microscopio de fuerza atómica. https://es.wikipedia.org/wiki/Microscopio_de_fuerza_at%C3%B3mica (accessed 2017-08-04).

[18] http://www.asylumresearch.com/applications/surfaceroughness/surfaceroughness.shtml (accessed 14/05/2017).

[19] http://www.nanoscience.gatech.edu/zlwang/research/afm.html (accessed 15/05/2017).

[20] Ludwig, T.; Kirmse, R.; Poole, K.; Schwarz, U. S., Probing cellular microenvironments and tissue remodeling by atomic force microscopy. *Pflügers Archiv - European Journal of Physiology* **2008,** *456* (1), 29-49.

[21] Custance, O.; Perez, R.; Morita, S., Atomic force microscopy as a tool for atom manipulation. *Nat Nano* **2009,** *4* (12), 803-810.

[22] http://slideplayer.com/slide/9702681/31/images/9/Modes+of+operation.+There+are+3+modes+of+AFM+operation+Contact+mode.jpg.

[23] https://medicine.tamhsc.edu/afm/principles.php (accessed 13/05/2017).

[24] Ayers, J. E., The measurement of threading dislocation densities in semiconductor crystals by X-ray diffraction. *J. Cryst. Growth* **1994,** *135* (1), 71-77.

[25] https://commons.wikimedia.org/wiki/File:Loi_de_bragg.png (accessed 2017-07-29).

[26] http://diffrac-plus-evaluation-release.software.informer.com/ (accessed 10/05/2017).

[27] Owens, A., Detector Fabrication. In *Compound Semiconductor Radiation Detectors*, Taylor & Francis: 2012; pp 119-206.

[28] https://fys.kuleuven.be/iks/nvsf/experimental-facilities/x-ray-diffraction-2013-bruker-d8-discover (accessed 2017-08-10).

[29] Hiroshi, H., Properties of GaN and related compounds studied by means of Raman scattering. *J. Phys.: Condens. Matter* **2002,** *14* (38), R967.

[30] Merlin, R.; Pinczuk, A.; Weber, W. H., Overview of Phonon Raman Scattering in Solids. In *Raman Scattering in Materials Science*, Weber, W. H.; Merlin, R., Eds. Springer Berlin Heidelberg: Berlin, Heidelberg, 2000; pp 1-29.

[31] Weber, W. H.; Merlin, R., *Raman scattering in materials science*. 1 ed.; Springer-Verlag Berlin Heidelberg: 2000; p 494.

[32] Islam, M. M., Photoluminescence in Analysis of Surface and Interfaces of Semiconductor Nanostructures. *International Letters of Chemistry, Physics and Astronomy* **2015,** *57*, 102-113.

[33] Gfroerer, T. H., Photoluminescence in Analysis of Surfaces and Interfaces. In *Encyclopedia of Analytical Chemistry*, John Wiley & Sons, Ltd: 2006.

[34] Fournier, J.; Néauport, J.; Grua, P.; Fargin, E.; Jubera, V.; Talaga, D.; Jouannigot, S., Evidence of a green luminescence band related to surface flaws in high purity silica glass. *Opt. Express* **2010,** *18* (21), 21557-21566.

[35] Saha, A., *Optoelectronics and Optical Communitation*. USP/Laxmi Publications: New Delhi, p 563.

[36] Tadashi, M.; Takashi, S.; Daisuke, F.; Nobuyuki, K., Comparison between Electron Beam and Near-Field Light on the Luminescence Excitation of GaAs/AlGaAs Semiconductor Quantum Dots. *Jpn. J. Appl. Phys.* **2005,** *44* (4R), 1820.

[37] Klein, C. A., Bandgap Dependence and Related Features of Radiation Ionization Energies in Semiconductors. *J. Appl. Phys.* **1968,** *39* (4), 2029-2038.

[38] Lei, H.; Leipner, H. S.; Schreiber, J.; Weyher, J. L.; Wosiński, T.; Grzegory, I., Raman and cathodoluminescence study of dislocations in GaN. *J. Appl. Phys.* **2002,** *92* (11), 6666-6670.

[39] Reich, E. S., Electron beams set nanostructures aglow. *Nature* **2013,** *493*, 143.

[40] https://en.wikipedia.org/wiki/Reflectance (accessed 2017-07-25).

[41] AGILENT Diffuse Reflectance Accessories (DRAs). https://www.agilent.com/cs/library/flyers/Public/5991-1717EN_PromoFlyer_UV_DRA.pdf (accessed 2017-07-24).

[42] Murphy, A. B., Band-gap determination from diffuse reflectance measurements of semiconductor films, and application to photoelectrochemical water-splitting. *Sol. Energy Mater. Sol. Cells* **2007,** *91* (14), 1326-1337.

[43] Diffuse Reflectance Accessory (external) Manual. http://mmrc.caltech.edu/Cary%20UV-Vis%20Int.Sphere/manuals/Cary%20manuals/4000_5000_6000i_external_dra.pdf (accessed 2017-07-20).

[44] https://chem.libretexts.org/Core/Physical_and_Theoretical_Chemistry/Spectroscopy/Magnetic_

Resonance_Spectroscopies/Nuclear_Magnetic_Resonance/Nuclear_Magnetic_Resonance_II (accessed 2017-07-28).

[45] https://www2.chemistry.msu.edu/faculty/reusch/virttxtjml/spectrpy/nmr/nmr1.htm (accessed 2017-07-30).

[46] Carey, F. A.; Giuliano, R. M., *Química orgánica (9a. ed.)*. 2014.

[47] https://chem.libretexts.org/Textbook_Maps/Organic_Chemistry_Textbook_Maps/Map%3A_Organic_Chemistry_with_a_Biological_Emphasis_(Soderberg)/Chapter_04%3A_Structure_Determination_I/4.3%3A__Infrared_spectroscopy (accessed 2017-08-02).

[48] http://www.muelaner.com/wp-content/uploads/2013/07/Interferometer.jpg (accessed 2017-08-01).

[49] https://www.microscopyu.com/techniques/fluorescence/introduction-to-fluorescence-microscopy (accessed 2017-08-06).

[50] http://www.olympusmicro.com/primer/techniques/fluorescence/ix70fluorescence.html (accessed 2017-08-05).

[51] https://www.phi.com/surface-analysis-techniques/xps-esca.html (accessed 21/07/2017).

[52] http://xpssimplified.com/whatisxps.php (accessed 20/07/2017).

3

Deposition and characterization of porous GaN particles

In this chapter we present the results obtained on the systematic study of the optimization of the deposition parameters of unintentionally *n*-type doped porous GaN by the direct reaction of metallic gallium and NH_3 in a CVD system. The parameters under study were the effect of the shape of the

gallium container, the catalyst, the amount of gallium, the deposition time and the substrate used.

3.1 Effect of the shape of the gallium container

A set of experiments with several containers for gallium with different shapes were carried out to analyse how the shape of the container affected the spreading of the Gallium droplet, and how this affected to the final shape and porosity of the particles obtained. The election of the containers shape was based on the freedom of gallium to spread along the container. We choose a flat, a half cylindrical and a concave container. Thus, in the flat container the gallium is allowed to spread along the in-plane directions, while in the half cylindrical container the gallium is free to spread along the longitudinal direction, and finally, in the concave container the spreading is restricted in the in-plane direction. In the containers with a vertical component, the half cylindrical and the concave container, the gallium is able spread out of the container as it wets the walls, as will be discussed later.

Figure 3.2 shows the evolution of the spreading of the Gallium droplet as the temperature increases for the different Gallium holders analysed. Through the optical window, located at one end of the CVD reactor, we recorded the evolution of the Gallium droplet during the growth process with a CCD camera to which we coupled a telescope.

Figures 3.2 (a) to 3.2 (f) show the evolution of the gallium droplet on the flat plate holder. Up to 1177 K the GaN droplet remained unaffected. From that moment some cracks appeared at the bottom part of the gallium droplet, the part in contact with the gallium holder, marked with green arrows in Figure 3.2 (b). These cracks are most likely to be a thin layer of GaN deposited on the drop due to the constant flow of ammonia over the gallium surface. In order to corroborate this assumption, a droplet of gallium was heated under NH_3 flow until the formation of the covering layer, always below 1203 K, at this point the NH_3 flow and the furnace were stopped at the same time while the vacuum pump remained on. The obtained droplet with a

covering layer was analysed by XRD. Figure 3.1 shows the X-ray pattern of the material that covers the gallium droplet. Despite the broad bands observed due to the liquid gallium beneath the covering layer, some peaks corresponding to GaN can be observed, indicated with arrows in the figure. This would confirm the formation of a very thin layer of GaN on the gallium drop.

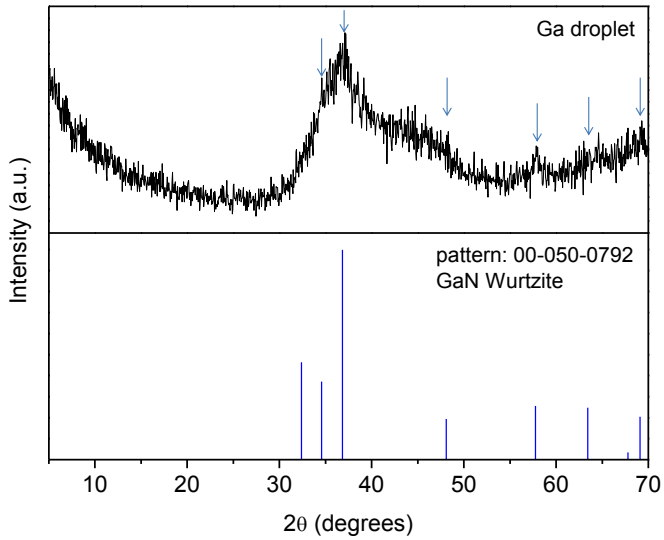

Figure 3.1. X-ray diffraction patterns of the gallium droplet covered with a thin layer of GaN. The X-ray diffraction pattern of GaN from the JCPDS database is included for comparison.

Two min after the formation of the cracks the furnace reached a temperature of 1203 K, and the gallium droplet totally spread. Despite the high surface tension of the liquid gallium (695 mN/m at room temperature [1]), at 1203 K there is enough energy to increase the surface of the liquid, resulting on the spreading of gallium along the container. Finally, at around 30 min after the furnace reached 1203 K we observed a layer covering the container, identified later as GaN by XRD.

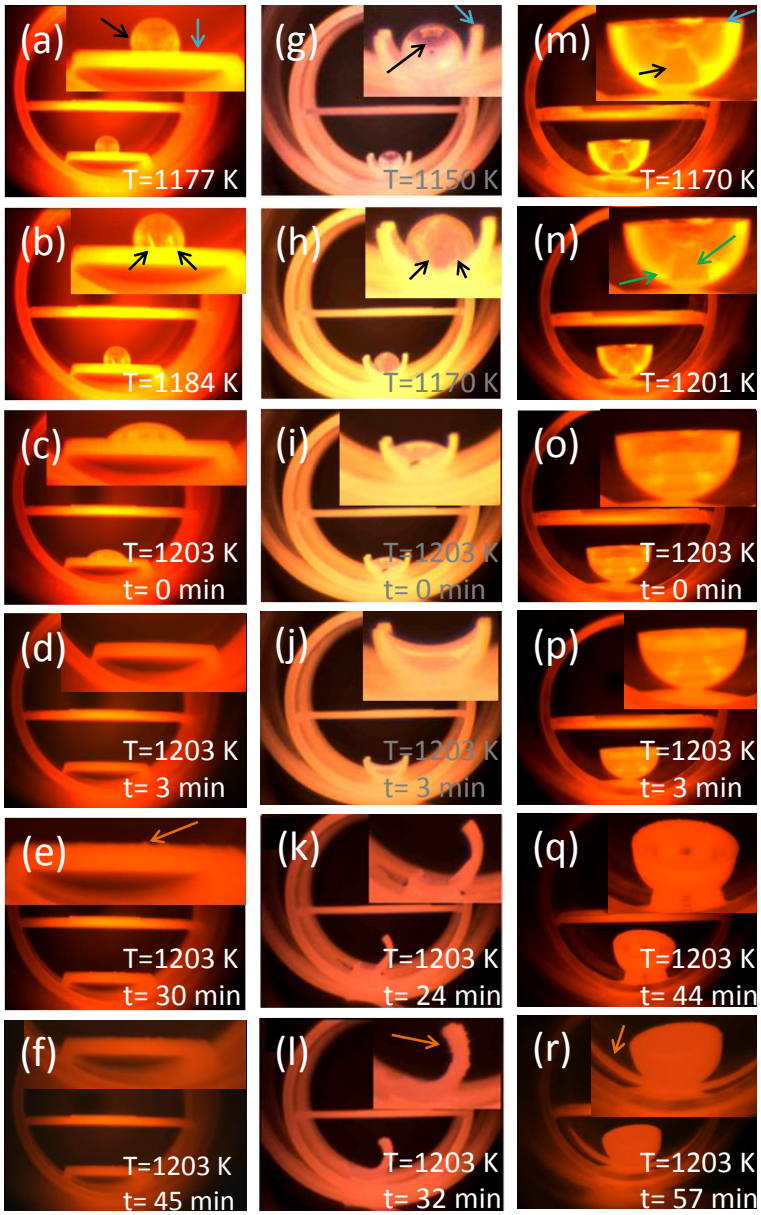

Figure 3.2. Optical images, in a front-side view, recorded inside the horizontal tube furnace showing the evolution (cracks are pointed with a green arrow) of the gallium droplet (pointed with a black arrow in the first row of images) with the different gallium holders used (pointed with a blue arrow) in these experiments: (a-f) flat plate, (g-l) half cylindrical tube and (m-r) concave container. The orange arrows indicate the GaN layer grown on the gallium holder.

Figure 3.2 (g-l) shows the evolution of the gallium droplet on the half of a cylindrical tube holder, the results are similar to those observed in the flat plate holder. However, the temperatures at which each step of the spreading out process of the gallium droplet happened were different. The cracks at the bottom of the gallium droplet started to appear at 1170 K, earlier than when the flat holder was used. After 3 min the furnace reached 1203 K, the meniscus of the gallium droplet passed from a convex shape towards a concave shape, indicating that the gallium is wetting the container. From that moment, the liquid gallium started to wet the holder walls and spread also on the quartz liner tube. This caused the leaning of the gallium holder around 30 min after the furnace reached 1203 K. Finally, the covering of the container with GaN occurred around 45 min after the furnace reached 1203 K, later than in the previous case.

When using the concave holder (see Figure 3.2 (m-r)), the gallium droplet followed a similar behaviour as in the previous cases. However, it was more challenging to see clearly what was happening inside the concave holder. However, we can roughly see that at 1201 K the two cracks appear at the bottom part of the droplet just before the spreading of the gallium droplet. What we could clearly see was that when the gallium droplet reached a temperature of 1203 K it started to wet the walls of the holder until it spread over the quartz liner. In this case the lean of the gallium holder occurred later, 44 min after the furnace reached the deposition temperature of 1203 K. Also the appearance of the GaN layer covering the areas were the liquid gallium was spread was observed later, 57 min after the furnace reached 1203 K.

It can be seen that the more the freedom of gallium to spread along the container is restricted, the later occurs the consumption of liquid gallium transformed into GaN on the container, and more gallium can thus be evaporated onto the substrate. It can be said that the deposition of GaN onto the substrate is limited by the conversion of the liquid gallium, which is the source of gallium atoms, into a layer of GaN, thus, interrupting the contribution of gallium atoms to the substrate. This is because when low

restriction (flat) containers are used, a larger area of liquid gallium is exposed to ammonia favouring the formation of the layer of GaN. The opposite occurs when the container restricts the freedom of the liquid to spread (half cylindrical and concave).

SEM pictures of the porous GaN particles deposited on Si (100) substrates covered with an ethanol solution of $Ni(NO_3)_2$ using different gallium containers are shown in Figure 3.3 In all cases, the temperature of reaction was chosen to ensure the total spread out of the gallium droplet, generating the maximum extension of the surface of metallic gallium to favour the evaporation of this precursor. The GaN particles obtained when using a flat plate or a half cylindrical tube as gallium holders were similar, with sizes between 2-3 μm, and a similar degree of porosity (see Figures 3.3 (a) and 3.3 (b)). The particles obtained using the concave container (see Figure 3.3 (c)) show bigger sizes (around 4 μm), and the pores seem to be smaller in diameter, giving a more rough aspect to the surface of the particles.

The increase of the average particle size of the porous GaN particles grown using the concave gallium holder is attributed to the longer deposition time. Despite in all cases the furnace was kept at 1203 K for 60 min, the conversion of the liquid gallium onto GaN on the gallium holder occurs later when using a concave gallium holder than when using a flat or a half cylindrical gallium holder.

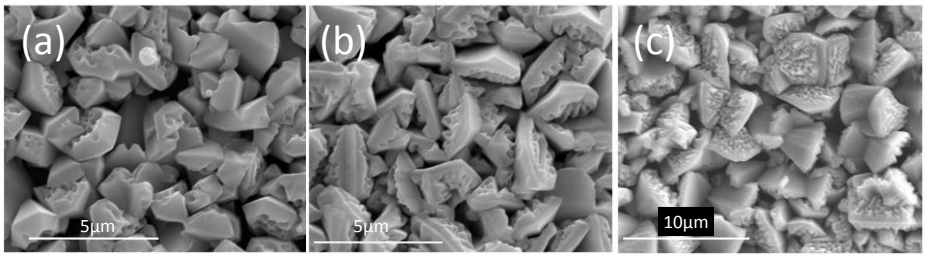

Figure 3.3. SEM pictures of the porous GaN particles obtained using different gallium holders: (a) flat plate, (b) half cylindrical tube, and (c) concave container.

3.2 Effect of the gallium quantity

Three sets of experiments varying the initial amount of gallium were carried out to analyse its effect on the coverage of the substrate with porous GaN particles, while keeping constant the other reaction parameters. The gallium quantities used were 0.2 g (N/Ga: 70.04), 0.4 g (N/Ga: 53.02) and 0.6 g (N/Ga: 23.35). The N/Ga is the atomic ratio between the NH_3 introduced into the CVD system along the deposition time and the gallium quantity used for the GaN deposition. The N/Ga atomic ratio it is an orientative value, since the gallium precursor, in this case metallic gallium, does not enter into the furnace as a vapour phase. Here, only a fraction of the initial metallic gallium evaporates, is this reduced amount who has the probability to reach the substrate surface and contribute to the GaN growth. The rest of the gallium will react with ammonia to form GaN in the same gallium holder, stopping the gallium supply for the growth process of GaN onto the substrate.

Figure 3.4 shows SEM pictures of the GaN particles grown using the different amounts of gallium. In the three cases hexagonal porous particles were obtained with different particle sizes, but more importantly, with different substrate coverages.

When 0.2 g of gallium were used (see Figure 3.4(a)) a low degree of coverage on the substrate could be observed. This was attributed to the low gallium evaporation and deposition on the substrate forming a small number of nucleuses along the substrate. This was confirmed by the fact that particles are bigger in size than in the other cases, around 5-6 μm. A higher coverage of the substrate with porous GaN particles could be seen when 0.4 g of gallium were used (see Figure 3.4 (b)). In contrast with the previous case, the particle size was smaller, of around 2 μm. This was attributed to the higher evaporation of gallium and the formation of a higher number of Ga-metallic catalyst nucleuses which lead to a higher coverage of the substrate with smaller porous GaN particles. Finally, in Figure 3.4 (c) we can see a SEM image of the GaN particles grown using 0.6 g of gallium. A similar particles

density and size was observed when compared to the experiment using 0.4 g of gallium. This would indicate the existence of a quantity of gallium above which no more GaN particles are formed, probably related to the Ga/N ratio used. However, in this latter case, the coverage on the surface of the substrate seems to be more homogenous.

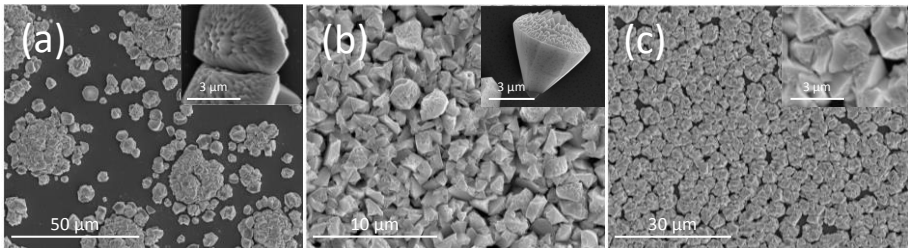

Figure 3.4. SEM pictures of the porous GaN particles obtained using different gallium quantities at the beginning of the experiment: (a) 0.2 g, (b) 0.4 g, and (c) 0.6 g.

3.3 Effect of the deposition time

We performed additional experiments to analyse the influence of the deposition time in the shape and porosity of the GaN particles and the substrate coverage. The deposition times selected were 30, 45, 60 and 120 min. The first two times (30 and 45 min) were chosen because we observed two particular moments during the development of the growth process, highlighted in Figure 3.2. The first one is related to the leaning of the container when a half cylindrical tube was used, due to the wetting of both, the container and the liner because of the spreading of gallium. The second one is the time when we observed the appearance of a material covering the container, identified later as GaN by X-ray diffraction. We also decided to explore one additional deposition time above 60 min, which is the time used up to now to produce these porous GaN particles, to analyze if the chemical reaction continued after we observed the conversion of liquid gallium to GaN on the container.

The deposition time has an important effect on the coverage of the substrate with porous GaN particles, as can be seen in Figure 3.5, while the particle size is more or less constant. In Figure 3.5 it can also be seen that the

density of GaN particles on the surface of the substrate increases with increasing the deposition time until 60 min. From there, it seems that no additional particles nucleate and the particles density remains constant. Hexagonal pyramidal porous particles were obtained in all cases; however, as we increased the deposition time, the morphology of the particles seems to fade away. Also, at long deposition times, smaller particles can be seen in the background covering the substrate, which might be formed by decomposition and further nucleation at expenses of the big particles, which would explain the deformation observed. This hypothesis would be confirmed by the reduction of the thickness of the sample at long deposition times, due to the high temperature and low pressure at which the sample is exposed during the growth experiment. Particles follow the same porous pattern observed up to now: pores located only on the (0001) face, with wider holes in the central part of the particles. It seems that the particles obtained after 30 min reaction time (see Figure 3.5 (a)) have a larger amount of pores, and those seem to be more superficial. These particles tend to show a smaller number of ridges. This would mean that ridges are formed by the coalescence of the neighbouring pores at deposition times long enough, since these ridges are more apparent at the central part of the particles as the deposition time is extended. Also, the bigger contrast observed in the SEM images for the pores, would indicate that the particles obtained at longer times develop deeper pores. When the deposition time is 120 min the porosity is less evident (see Figure 3.5 (d)), which would corroborate the evaporation of the material to form the smaller particles observed in the background. This effect be more pronounced at the rough faces, i.e. those that contain the pores.

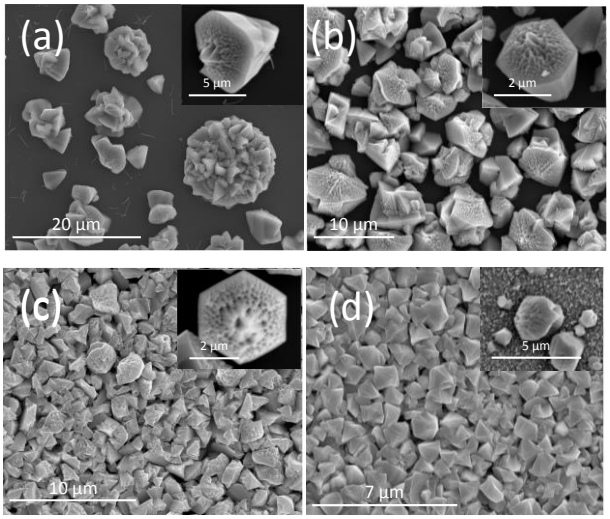

Figure 3.5. SEM pictures of the particles obtained at (a) 30 min, (b) 45, (c) 60, and (d) 120 min deposition times.

3.4 Effect of the catalyst

To synthesize porous GaN on Si substrates, it is necessary to coat the substrate with a metallic catalyst [2]. Here, we tested different metallic catalysts with which we coated Si (100) and Si (111) substrates: Ni, introduced as $Ni(NO_3)_2$ dissolved in ethanol, and 20 nm thick films of Ni, Au, Pt, W and Ti deposited by RF sputtering.

3.4.1 Si (100) substrates

SEM pictures of as-grown GaN on Si (100) substrates shown in Figure 3.6 demonstrate that by using all catalysts, GaN appears in the form of micron-sized porous particles. The bigger particles were obtained using $Ni(NO_3)_2$ as catalyst, while using Pt and Au thin films we obtained smaller particles more homogenous in size. The highest level of porosity was obtained, however, in the GaN particles synthesized using $Ni(NO_3)_2$. It is curious to notice that Ni, introduced as $Ni(NO_3)_2$ or directly as metallic Ni has a different effect on the morphology and porosity degree of the particles, despite $Ni(NO_3)_2$ is reduced to Ni under the reaction conditions. This different

effect might be attributed to the distribution of the catalyst on the surface of the substrate. We obtained agglomerated of big particles with high porosity using $Ni(NO_3)_2$, as can be seen in Figure 3.6 (a). However, as can be seen in Figure 3.6 (b), the particles grown on a continuous Ni film have an irregular shape and a lower degree of porosity. Porous GaN layers grown using Pt and Au catalysts show a uniform coverage of the substrate with GaN particles (see Figure 3.6 (c) and 3.6 (d)). These polycrystalline films show an interesting dual porosity since they present interparticle and intraparticle pororosity, defined in a previous publication [3]. The level of intraparticle porosity is higher when Pt is used (see inset in Figure 3.6 (c)). Porous GaN particles grown on Ti thin films have a totally different morphology, remembering the shape of a sea star with a high level of porosity. In this case it seems that GaN starts growing as an epitaxial layer on the substrate with a further growth of porous GaN particles on the top of it (see Figures 3.6 (e-f)).

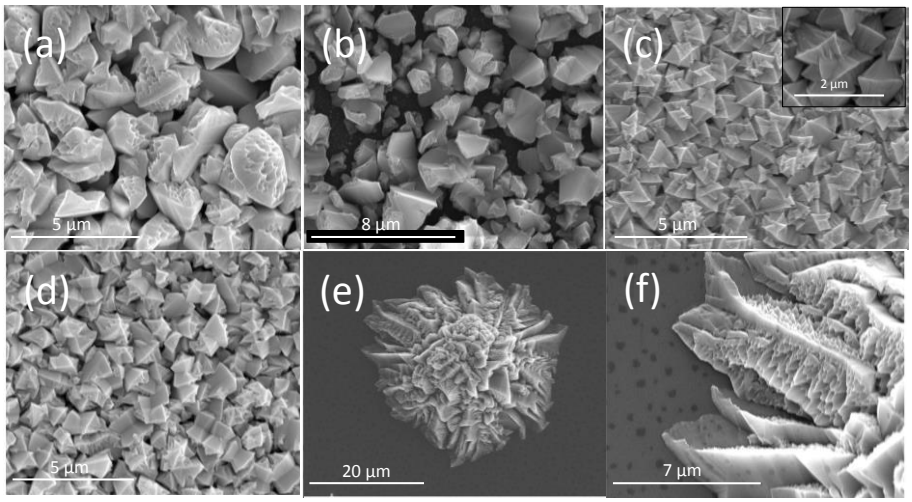

Figure 3.6. SEM pictures of porous GaN grown on Si (100) substrates with the use of different catalysts: (a) $Ni(NO_3)_2$, (b) Ni, (c) Au, (d) Pt, (e) and (f) Ti. The inset in figure (c) show a magnified image of the interparticle porosity.

To know the crystal structure of the porous GaN particles, XRD analysis of the grown samples deposited on Si (100) using different catalysts was performed. XRD patterns for the porous GaN samples synthesized using

$Ni(NO_3)_2$ dissolved in ethanol, Ni, Au, Pt and Ti continuous films are shown in Figure 3.7.

The peaks of the XRD pattern of the porous GaN particles grown using $Ni(NO_3)_2$ dissolved in ethanol as catalyst, matched with the hexagonal wurtzite GaN reference pattern (JCPDS database, pattern 00-050-0792) included in the figure for comparison. The sharp diffraction peaks are an indicator or a good crystalline quality. By contrast, when the Ni catalyst is deposited as a continuous film rather than in solution, the intensity ratio of the peaks differs from that of the wurtzite GaN reference pattern, showing an important decrease of the (0002) diffraction peak. These results are consistent with the SEM image which shows a preferential orientation of the particles with the (0001) plane perpendicular to the substrate. Also another crystalline phase corresponding to α-Si_3N_4 (JCPDS database, pattern 01-0071-0570) was identified.

The XRD pattern of the GaN obtained on Si (100) substrates coated with Au (see Figure 3.7 (c)) shows a change in the intensity ratio of the diffraction peaks compared with the reference pattern. The main peak differing from the reference pattern is the (0002) peak, which has lower intensity than expected, as in the previous case, associated to a preferential orientation of porous GaN particles. Two new crystalline structures were also identified: the α-Si_3N_4 and a metallic alloy (Ga_2Au) (JCPDS database, pattern 03-065-7583). The Ga_2Au intermetallic alloy it is the responsible to lower the resistance of the contacts due to its lower workfunction, thus, lowering the Schottky barriers, allowing the ohmic electron transport to the GaN particles [3].

The XRD pattern of GaN obtained on Si (100) substrates coated with Pt (see Figure 3.7 (d)) shows the peaks corresponding to wurtzite GaN with the same intensity as in the reference pattern. Again another crystalline structure is detected, corresponding to α-Si_3N_4. The presence of a crystalline α-Si_3N_4 layer in some cases was favoured by the presence of metallic Ni, Pt

and Au layers which could as catalyst between the Si substrate and the ammonia used for the GaN growth [4].

Finally, the XRD pattern of the GaN sample grown using Ti continuous film as catalyst confirms a texturing of the porous GaN particles, induced by the catalyst as it was observed previously by SEM.

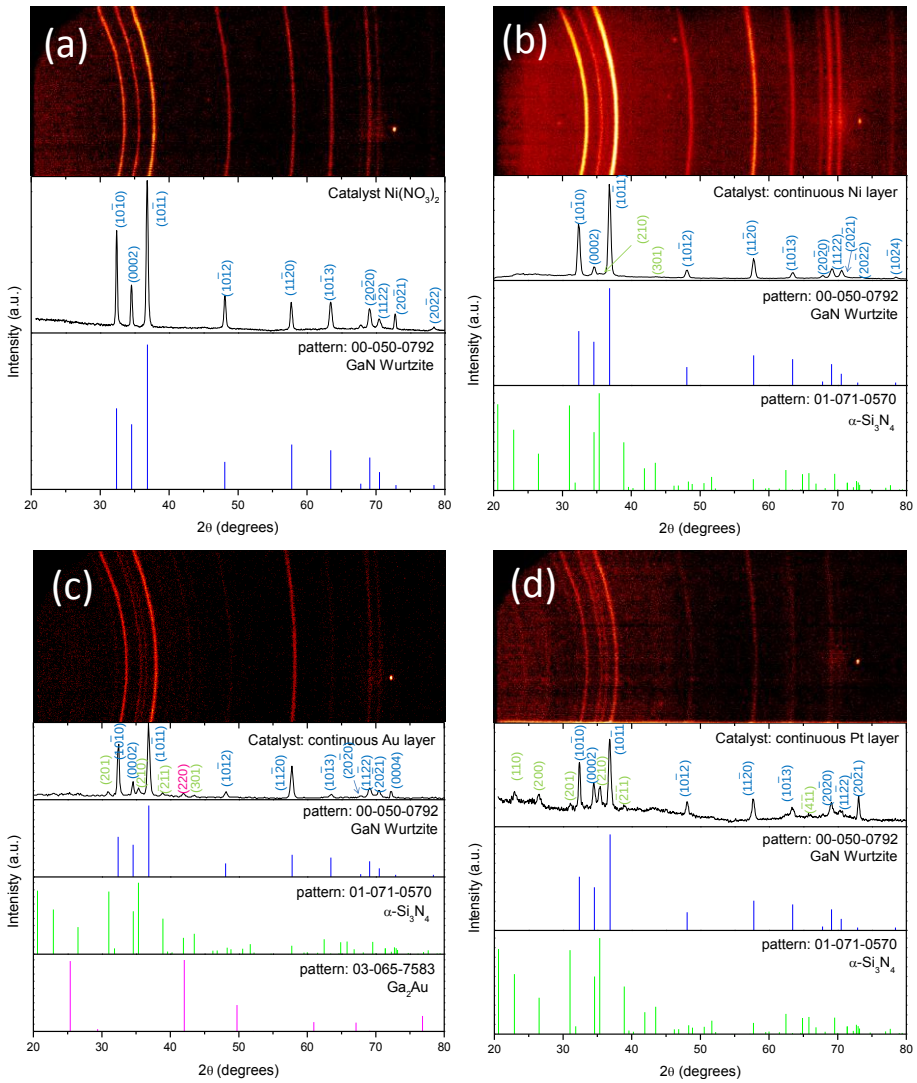

Figure 3.7. X-ray diffraction patterns, with the corresponding 2D diffraction images of porous GaN obtained on Si (100) substrates coated (a) $Ni(NO_3)_2$ dissolved in ethanol, (b) 10 nm of Ni, (c) 20 nm of Au and (d) 20 nm of Pt. The reference X-ray diffraction patterns of GaN, Ga_2Au and Si_3N_4 from the JCPDS database are included for comparison.

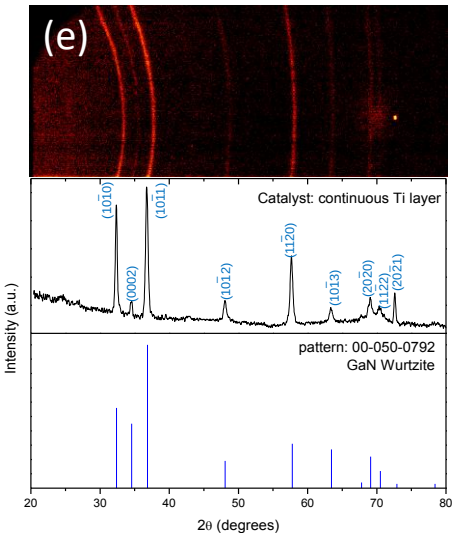

Figure 3.7. (continuation). X-ray diffraction patterns, with the corresponding 2D diffraction images of porous GaN obtained on Si (100) substrates coated with (e) 20 nm of Ti. The reference X-ray diffraction pattern of GaN is included for comparison.

The non-uniform distribution of intensity in the Debye rings observed with the GADDS detector (see Figure 3.7(e)) and the different intensity ratio of the diffraction peaks when compared to the reference pattern for GaN, reveal a texturing of the sample, although it is not trivial to establish which is the preferential orientation of the particles, from the data obtained. This is more evident when we compare this XRD pattern with any of those recorded for the porous GaN particles obtained using other catalysts, corresponding to porous GaN particles obtained using $Ni(NO_3)_2$ as catalyst, that can be seen in Figures 3.7 (a).

Based on the morphological data obtained by SEM and the crystallographic data obtained by XRD, a simulation of the external morphology of the porous GaN particles was done with Shape V7.4. Figure 3.8 (a) shows a SEM image of a porous GaN particle grown on a Si (100) substrate using a $Ni(NO_3)_2$ ethanolic solution as catalyst. The chosen particle has hourglass shape morphology, a very common morphology in the as-grown porous GaN particles. This shape is possibly due to a reflection

twinning along the *c* crystallographic direction. That produces particles with two opposite crystal domains.

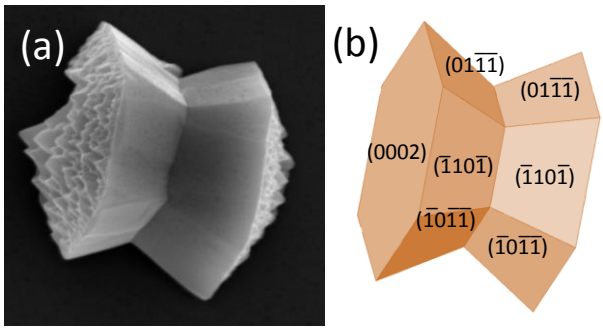

Figure 3.8. (a) SEM image of a porous GaN particle obtained on a Si (100) substrate using $Ni(NO_3)_2$ catalyst showing an hourglass morphology, and (b) simulation of the morphology obtained with Shape V7.4. indicating the possible crystal faces. The background of the particle represents the substrate.

Once the crystal domain is known, the next step could be to understand the main particle orientation on the substrates where the XRD patterns showed a clear texturing of the sample, indicating a preferential orientation of the particle distribution. We will represent the simulated particles with the substrate in the background and with a view of 10 degrees to the left from the centre of the particle, as it is depicted in Figure 3.9, in order to visualize this preferential orientation of the particle texturation. This visualization is only for the simulated GaN particles in Figure 3.10.

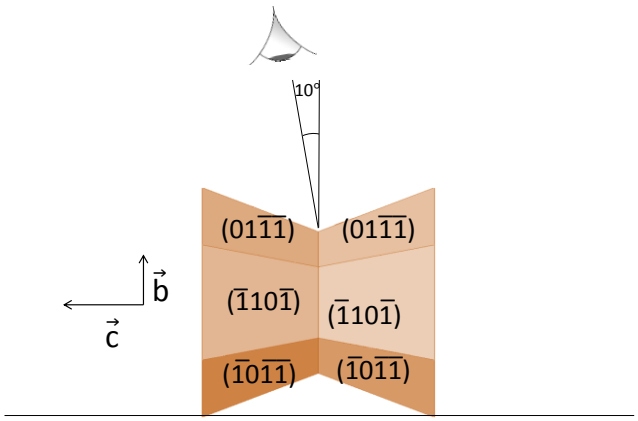

Figure 3.9. Instructions for the viewing of the morphology of the simulated GaN particles to identify their preferential crystallographic orientation.

The XRD patterns of the porous GaN particles grown on Si (100) substrates using a continuous layer of Ni, Au and Ti as catalyst show an increase in intensity of the $(10\bar{1}0)$ and $(11\bar{2}0)$ diffraction peaks. This would mean that the particles are tilted with the *c* crystallographic direction parallel to the substrate as can be seen in Figure 3.10, showing these two possible orientations of the porous GaN particles.

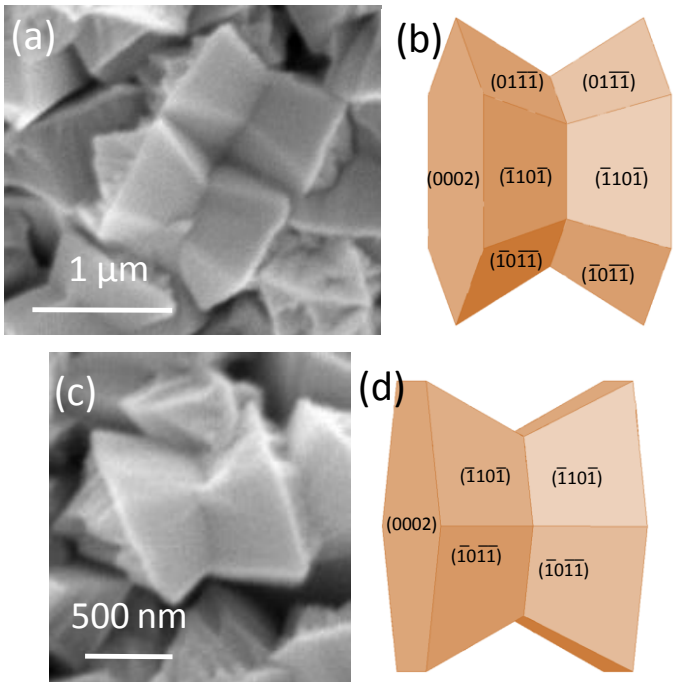

Figure 3.10. SEM image of porous particles grown on Si (100) using Pt as catalyst and the corresponding simulation of the morphology of GaN particles with (a,b) one plane of the $\{01\bar{1}0\}$ family planes and (c,d) $\{11\bar{2}0\}$ family planes parallel to the substrate using a view 10 degrees to the left from the centre of the particle. The background of the simulated particle corresponds to the substrate.

This representation is consistent with the SEM images of the porous GaN particles grown on Si (100) substrate using a continuous layer of Ni, Au and Ti as catalyst.

Luminescence properties of the porous GaN particles grown on Si (100) substrates using a layer of 20 nm thick of Pt and Au as catalysts were analyzed by cathodoluminescence (CL) at 80 K.

CL spectra are shown in Figure 3.11. The peak observed in the spectra corresponds to the near band edge emission (NBE), which is the name for the optical transitions that occurs between the edges of the conduction band and the valence band (for further information go to section 1.1.2 Optical transitions in GaN). The NBE peak consists of a predominant peak centred at 3.43 eV (362 nm) and a second peak of lower intensity at higher photon energies that appears as a shoulder of the main peak. The main peak can be attributed to a donor bound exciton D^0X whereas the shoulder at higher photon energies can be attributed to the free exciton FX. The lack of high resolution makes difficult the resolution of these peaks. Observe that the CL of the porous GaN particles grown on a Si (100) substrate coated with a layer of Pt 20 nm thick, the broad signal at the right side of the NBE peak can be attributed to the DAP recombination and its phonon replicas. The FWHM of the NBE peak is 87 meV for the sample grown using Au as catalyst and 99 meV for the sample grown using Pt as catalyst. Note that no YL (~2.2 eV), which is attributed to V_{Ga} complexes, was observed in any case.

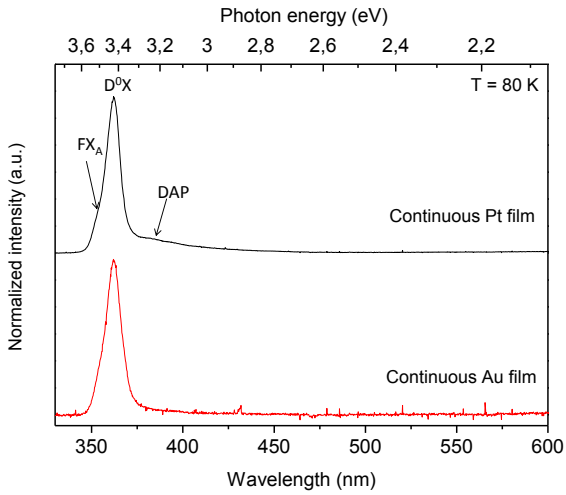

Figure 3.11. CL spectra recorded at 80 K of the porous GaN samples grown on Si (100) coated with Au and Pt thin layers as catalysts.

Figure 3.12 shows the reflectance spectra of the nanoporous GaN particles grown on Si substrates coated with layers of Au and Pt 20 nm thick. The reflectivity of Si is about 40% in the wavelength range of 400-800 nm, which is consistent with previous reports [5] whereas the Au covered Si substrates have a reflectivity value between 50-70% in the wavelength range of 500-800 nm, and Pt has an almost invariable reflectivity from 400 to 800 nm at around ~65%. However, nanoporous GaN particles grown on Si (100) substrates covered with Au and Pt layers 20nm thick decrease the reflectivity down to values around 10%. The decrease in the reflectivity of the nanoporous GaN layer can be attributed to the large surface-volume ratio of the particles [6]. This decrease in the reflectivity of Si layers covered with nanoporous GaN particles especially at wavelengths below the band gap (~365 nm), makes nanoporous GaN particles interesting for antireflecting coatings for solar cells, since the coating reduces the optical reflection, making the solar cells more efficient.

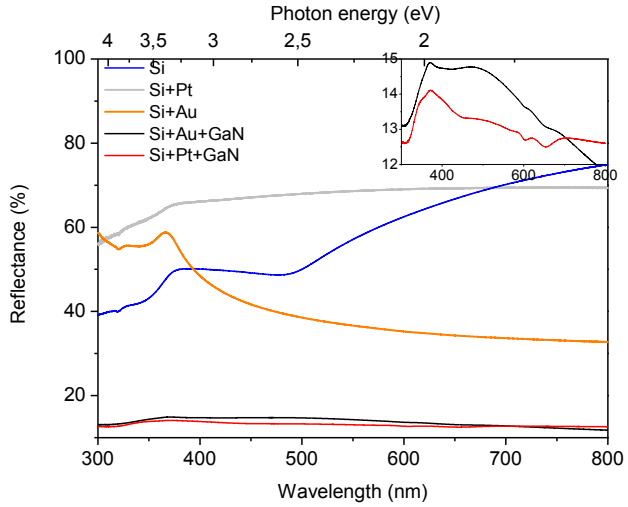

Figure 3.12 Reflectance spectra of (black) Si substrate, (red) Si substrate coated with a layer of Au 20 nm thick, and (blue) nanoporous GaN particles grown on Si substrates coated with a layer of Au 20 nm thick.

3.4.2 Si (111) substrates

When GaN is grown on Si (111) substrates coated with different metallic catalysts it appears in the form of micron-sized porous particles with a mean size of 2-5 μm (see Figures 3.13 (a-d)). If we compare the particles obtained on Si (100) and Si (111) substrates coated with the same catalyst, we observe that the GaN particles obtained on Si (111) substrates tend to be more irregular in shape. According to these images, it seems that the combination of the substrate and the catalyst play a big role in the morphology of the particles. In most of the cases, nanowires were also observed together with the porous particles, especially when Au and Pt where used as catalyst (see insets of Figures 3.13 (c-d)) and with the exception of using $Ni(NO_3)_2$ and metallic Ni as catalyst.

Figure 3.13 (a) shows the SEM images of the porous GaN particles grown on Si (111) substrates covered with an ethanolic solution of $Ni(NO_3)_2$ as catalyst. The morphological analysis of the images reveals, in average, particles grown with a wide basal plane and short in the *c*-crystallographic direction. The pores located on the basal plane are apparently wider when compared to those obtained on Si (100) substrates using the same catalyst.

The morphological analysis reveals a high irregularity in the shape of the GaN particles grown using a continuous layer of Ni as catalyst on Si (111) substrates, despite having a well defined shape (see Figure 3.13 (b)).

Figure 3.13 (c) shows the SEM images of the porous GaN particles grown using Au as catalyst. The morphological analysis show isolated and twined porous GaN particles.

The morphological analysis of the porous GaN particles grown using Pt as catalyst, reveals as well as when $Ni(NO_3)_2$ is used as catalyst, particles short in the *c* crystallographic direction.

When Ti is used as catalyst, the particles tend to grown with the *c*-crystallographic direction nearly parallel to the substrate, and it is possible to observe at the edges of the sample, which corresponds to the earlier stages

of growth, an incipient epitaxial growth that fades away towards the centre of the sample (see inset of Figure 3.13 (e)).

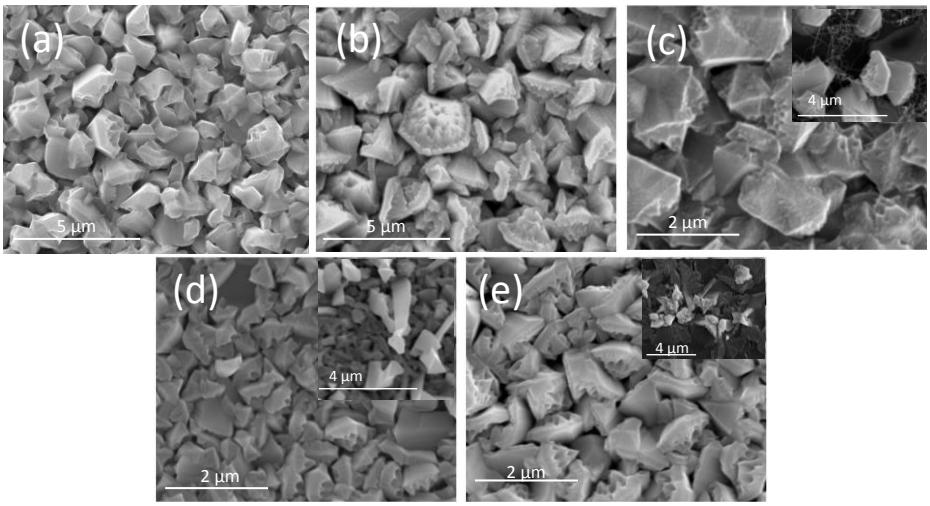

Figure 3.13. SEM images of the porous GaN particles grown on Si (111) substrates coated with different catalysts: (a) an ethanolic solution of $Ni(NO_3)_2$, and continuous films of (b) Ni, (c) Au, (d) Pt and (e) Ti.

The crystal structure of the porous GaN particles deposited on Si (111) substrates using different catalyst was studied by XRD analysis. Figure 3.14 (a) shows the XRD pattern for the porous GaN particles grown on Si (111) using an ethanolic solution of $Ni(NO_3)_2$ as catalyst. The peaks of the XRD pattern recorded for this sample correspond to wurtzite GaN. Also, the intensity ratio of the peaks matches the intensities listed in the XRD reference pattern for wurtzite GaN, indicating the absence of any texture in the sample.

The XRD pattern and the 2D diffraction image for the porous GaN particles grown on Si (111) covered with 20 nm of Ni as catalyst are shown in Figure 3.14 (b). The peaks matched those of the wurtzite GaN structure reference pattern from the JCPDS database. However, the intensity ratio does not match, exhibiting an increase of the peak corresponding to the (0002) plane relative to the diffraction peak corresponding to the $(10\bar{1}0)$ plane. Thus, a slightly texturing of the sample seems to be possible in this case. It can be also seen the presence of a small intensity peak corresponding to a metallic

alloy formed between the catalyst and Ga, $GaNi_3$. The observed peak of the $GaNi_3$ alloy corresponds to its highest intensity peak, the (111) peak. Its low intensity indicate that its concentration in the sample seems to be small, and it can be attributed to the need of three atoms of Ni per each atom of Ga to form the alloy, and the low amount of Ni available in a 20 nm thick film.

The XRD pattern of the porous GaN particles grown on Si (111) substrates coated with a continuous film of Au 20 nm thick not only reveals the peaks corresponding to the wurtzite GaN but also to the α-Si_3N_4 and Ga_2Au interalloys, as can be seen in Figure 3.14 (c). The crystalline quality of the porous GaN particles is difficult to assess due to the background noise that make the diffraction peaks to appear wider indicating also some amorphication of the sample. Also, it is difficult to assess if there is any preferential orientation of the porous GaN particles. In contradiction to the sample grown on Si (100) substrates, in this case the metallic alloy formed between Ga and the catalyst, Ga_2Au, is highly oriented, appearing as bright spots rather than Debye rings in the 2D diffraction image above the XRD pattern, indicating that Ga_2Au appears as a monocrystalline phase.

Figure 3.14 (d) shows the XRD pattern of the porous GaN particles grown on Si (111) substrates coated with a layer of Pt 20 nm thick. The XRD pattern shows the presence of two crystalline structures, GaN and α-Si_3N_4. Notice that the intensity ratio of the GaN formed does not match that of the reference one, being similar to that of the porous GaN particles grown on Si (111) coated with Ni, with the (0002) peak exhibiting a higher intensity than the $(10\bar{1}0)$ peak. Also, the Debye rings show that the intensity of the $(10\bar{1}1)$ peak is more concentrated in the centre of the ring, indicating a possible texturing of the sample.

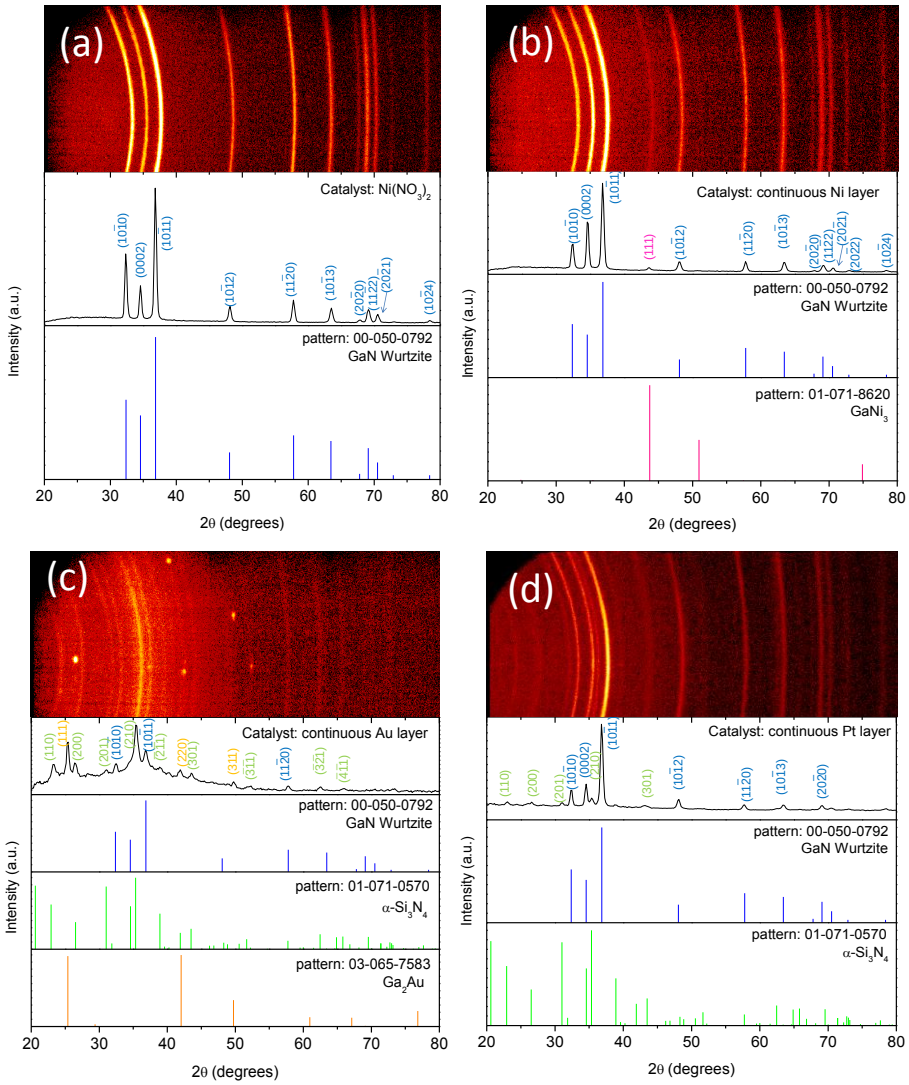

Figure 3.14. X-ray diffraction patterns, with the corresponding 2D diffraction images of porous GaN obtained on Si (111) substrates coated with (a) $Ni(NO_3)_2$ dissolved in ethanol, and 20 nm thick layer of (b) Ni, (c) Au and (d) Pt. The reference X-ray diffraction patterns of GaN, Ga_2Au and Si_3N_4 from the JCPDS database are included for comparison.

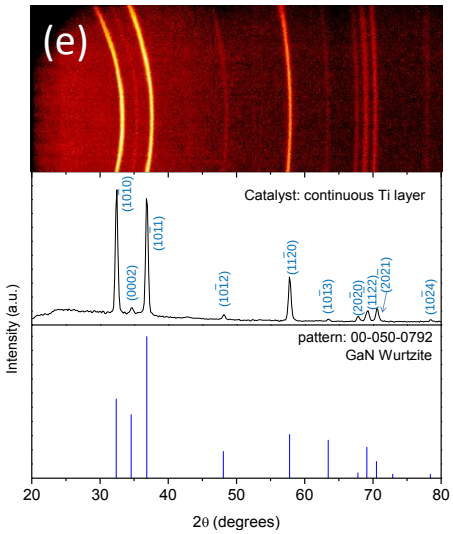

Figure 3.14 (continuation). X-ray diffraction patterns, with the corresponding 2D diffraction images of porous GaN obtained on Si (111) substrates coated with (e) Ti. The reference X-ray diffraction pattern of GaN is included for comparison.

Finally, in the XRD pattern corresponding to the porous GaN particles grown on Si (111) substrates coated with a layer of Ti 20 nm thick, shown in Figure 3.14 (e), only the peaks corresponding to wurtzite GaN were observed. Nevertheless, in this case, the texturing is evident and follows the same behaviour as the sample grown on Si (100) using the same catalyst. It would confirm the observations made by SEM, according to which a great amount of the particles are tilted with the (0002) face, perpendicular to the substrate plane. This would also explain the important decrease of the intensity of the (0002) diffraction peak, and a simultaneous increase of the intensity of the (10$\bar{1}$0) and the (11$\bar{2}$0) diffraction peaks.

The anomaly in the ratio intensity of the (10$\bar{1}$0) and (10$\bar{1}$1) diffraction peaks of the porous GaN particles grown on Si (111) substrates coated with Ni and Pt might correspond to a preferential orientation of the porous GaN particles, with the (10$\bar{1}$1) plane parallel to the substrate rather than the (10$\bar{1}$0) plane. A simulated particle oriented with the (10$\bar{1}$1) plane parallel to the substrate is depicted in Figure 3.15.

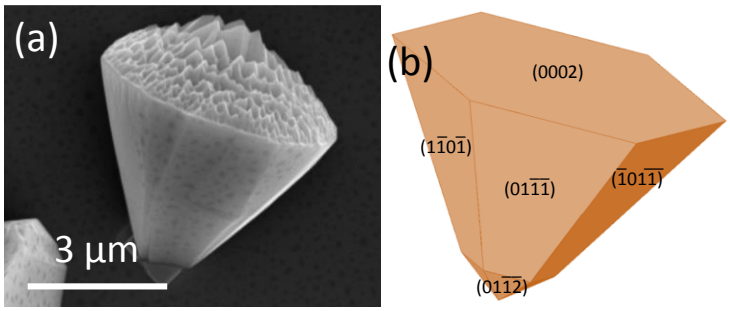

Figure 3.15. (a) SEM image of a porous GaN particle and (b) simulation of the morphology of the GaN particle with a plane of the $\{01\bar{1}1\}$ family of planes parallel to the substrate.

The orientation of the porous GaN particles obtained on Si (111) substrates coated with Ti would correspond to that depicted in Figure 3.10 and Figure 3.15.

The luminescence properties of porous GaN particles grown on Si (111) substrates coated with Pt, Au and Ti were also analysed by CL at 80 K (see Figure 3.16). The NBE peak observed consists again in two peaks not resolved, corresponding to a more intense D^0X and a lower in intensity FX_A peak. We also observed that the position of the NBE peak depends on the catalyst. The NBE peak of the porous GaN particles grown on Si (111) substrates coated with Pt, Ti and Au is centred at 366.3, 362.7 and 360.1 nm, with a FWHM of 9.7, 5.9 and 6.8 nm, respectively. The CL spectrum of the porous GaN particles grown on Si (111) substrate coated with Pt shows additionally a weak and broad band at the right side of the NBE peak that would correspond to the DAP and its phonon replicas. Note again that no YL, is observed in any case.

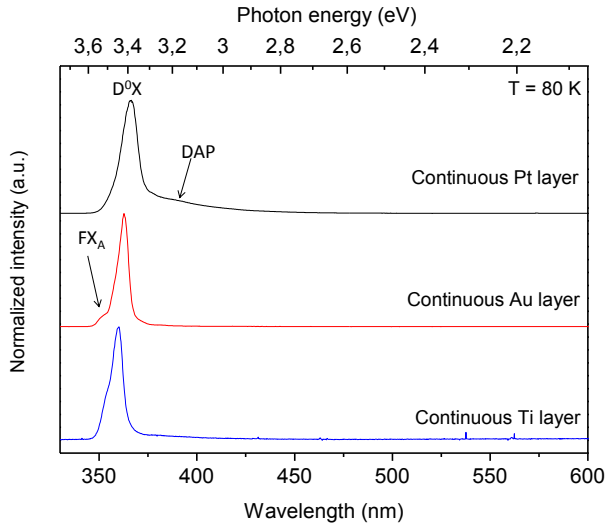

Figure 3.16. CL sprectra recorded at 80 K for the porous GaN samples grown on Si (111) coated with layers of Pt, Au and Ti 20 nm thick as catalysts.

3.5 Attempts to grow oriented porous GaN particles on silicon substrates driven by using a thin layer of titanium catalyst

After studying the effect of different metallic catalysts for the growth of porous GaN particles on silicon substrates, it seems that when a thin layer of Ti is deposited on Si substrates the porous GaN particles obtained tended to exhibit a preferential crystallographic orientation. This preferential orientation effect can be seen in Figures 3.6 (e-f) and Figure 3.12 (e), and was also corroborated by the XRD characterization, as can be seen in Figure 3.7 (e) and Figure 3.14 (e). Thus, we wanted to explore the possibilities of deposition of oriented porous GaN particles on Si (111) substrates driven by a continuous film of Ti as catalyst that would act as a pre-orienting layer for the heteroepitaxial growth of porous GaN.

Choi *et al.* [7] already explored the deposition of GaN on a continuos layer of Ti, used as a pre-orienting layer on glass substrates for LEDs applications. They took advantage of the same hexagonal crystal lattice structure of Ti ($P6_3/mmc$) than wurzite GaN with a relative small lattice mismatch ($\Delta a/a$=-7,4%). To act as a pre-orienting layer Ti has to be oriented

with its *c*-axis paralel to the *z*-direction. When Ti is deposited using sputtering, often forms columnar grains with the *c*-axis paralel to the *z*-direction, notwithstanding the grains are randomly oriented in the in-plane direction [7]. This preferential orientation is explained by thermodinamics, which states that the facet with the lowest total free energy, which is the sume of the surface energy and the strain energy, will form the preferential growth plane [7]. It has been reported, using *Ab initio* density functional calculations [8] and analytical equations [9], that the (0001) face of Ti has the lowest surface energy, thus, becoming the preferential growth plane.

3.5.1 Crystal growth of porous GaN particles on Si (111) varying the titanium layer thickness.

In addition to the porous GaN particles grown on Si (111) coated with a continuous film of Ti 20 nm thick, another set of experiments was performed in order to study the effect of the catalyst layer thickness on the possible orientation of the porous GaN particles. For this purpose Ti films 100, 150 and 200 nm thick were sputtered on Si (111) substrates.

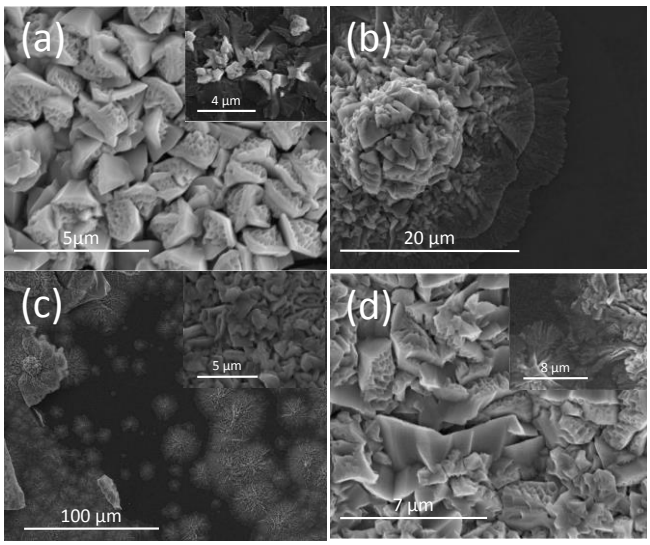

Figure 3.17. SEM images of the porous GaN particles grown on Si (111) with different Ti layer thickness (a) 20 nm, (b) 100 nm, (c) 150 nm, and (d) 200 nm.

SEM images of the porous GaN particles grown on these substrates are shown in Figure 3.17. In all cases porous particles were obtained, however, the morphology of the particles is very irregular and depends on the area of the substrate in which it has been deposited. Also, we observed that the deposition is not uniform, with the growth process starting in isolated islands, eventually coalesce. The isolated islands are shown in the insets of Figure 3.17 (a, d) and Figures 3.16 (b, c)).

The best results in terms of orienting the porous GaN particles along the *c*-axis seem to be obtained when a 150 nm thick layer of Ti was used. The inset in Figure 3.17 (c) shows an underlying layer of mostly oriented porous GaN particles with the *c*-direction perpendicular to the substrate. However, the adhesion of Ti on the Si (111) substrates seems to be an issue and we observed, by naked eye, the peeling off of the grown GaN layer in several areas of the substrate, as can be seen in Figure 3.18.

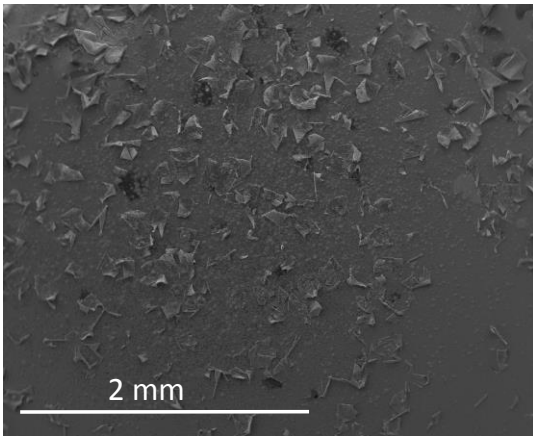

Figure 3.18. SEM image of the porous GaN particles deposited on a Si (111) coated with a Ti film, showing the peeling off of the GaN layer.

XRD analysis of the porous GaN particles grown on Si (111) substrates coated with Ti layers of different thicknesses was performed to analyze their crystal structure and orientation, and to observe the presence of additional crystalline structures, if any. Figure 3.19 shows the XRD patterns of the porous GaN particles obtained.

Figure 3.19 (a) corresponds to the XRD diffraction pattern of the porous GaN particles grown on a Si (111) substrate coated with a layer of Ti, 20 nm thick, shown previously on Figure 3.12 (e), is included here for a better comparison. Figure 3.19 (b) shows the XRD pattern of the sample grown on a Ti layer 100 nm thick. The presence of wurtzite GaN is confirmed, with the intensity ratio of the difraction peaks following the same patern observed previously for the sample grown on a Ti layer 20 nm thick. However, a new crystalline phase was observed present corresponding to the formation of an alloy between the catalyst and the substrate, the Si_2Ti. The XRD pattern for the sample grown on a Ti layer 150 nm thick is depicted in Figure 3.19 (c). Again, two crystalline structures are observed: wurtzite GaN and Si_2Ti, with a preferential orientation of the porous GaN particles on the (0002) plane, as can be seen by the enhancement of the intensity of the diffraction peak corresponding to that plane. Also, the Debye ring corresponding to this peak shows a non-uniformity intensity distribution, being the center of the ring more intense than the edges, which would corroborate the presence of this preferential orientation of the GaN particles. Finally, when the thickness of the Ti layer was increased to 200 nm, a new crystalline phase, corresponding to TiO_2 in its rutile form, was also observed, aside from wurtzite GaN and Si_2Ti. The diffraction peaks corresponding to the Si_2Ti phase appear with a higher intensity, when compared to the sample grown on a Ti layer 150 nm thick, indicating that it is present with a higher concentration, probably related to the increase of Ti quantity in the last case. Also, it has to be noticed that this metallic alloy is highly oriented, as can be seen in the Debye rings in Figure 3.19 (d), with an increase of the intensity corresponding to the (313) diffraction peak.

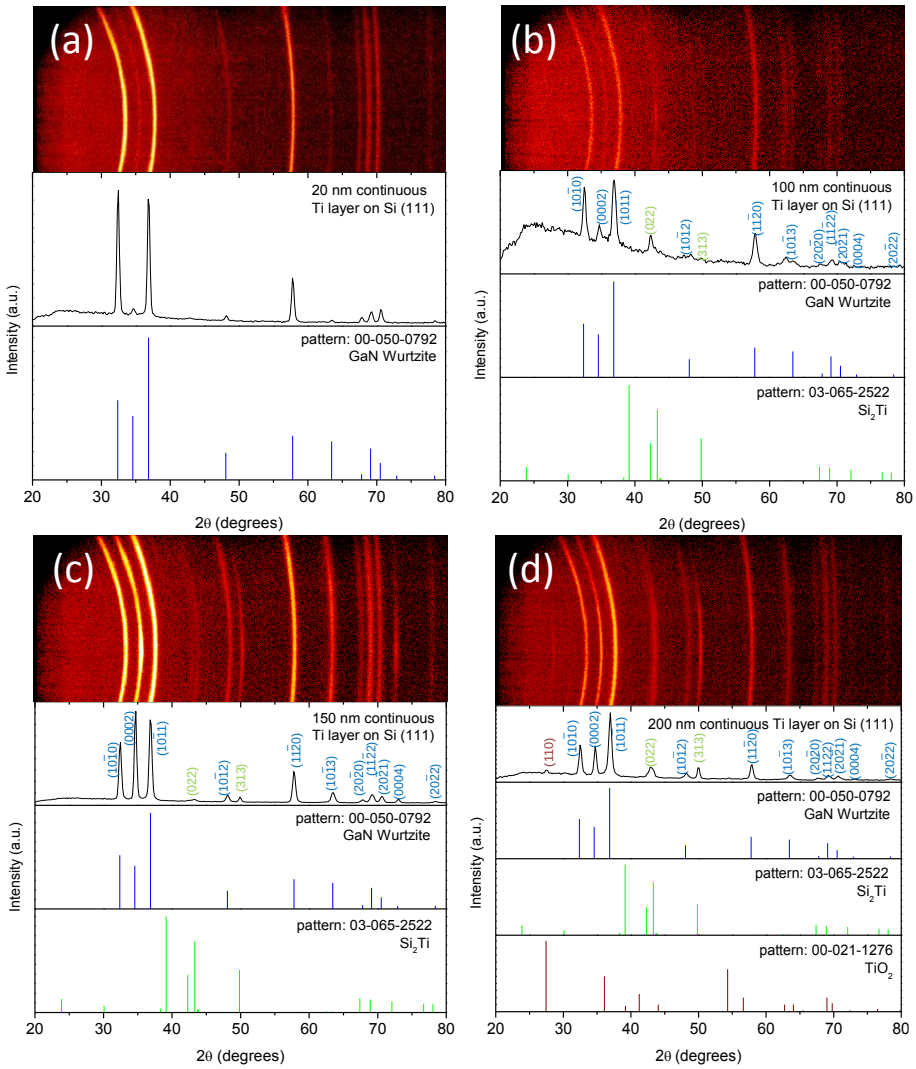

Figure 3.19. X-ray diffraction patterns with the corresponding Debye rings of porous GaN obtained on (111) Si substrates coated with (a) 20 nm, (b) 100 nm, (c) 150 nm, and (d) 200 nm of Ti. The reference X-ray diffraction patterns of GaN, Si_2Ti and TiO_2 from the JCPDS database are included for comparison.

These results seem to indicate that it is not possible to deposit a fully oriented porous GaN layer on top of a Ti layer. To understand why this is not possible, we designed a set of experiments to know what is happening with the Ti layer after sputtering and after being exposed to the experimental

conditions used in the deposition process to obtain porous GaN. The results of these experiments are summarized in the following section.

3.5.2 Crystallographic orientation of the sputtered titanium on silicon substrates

A closer analysis of the Si (111) substrates coated with a thin Ti layer is done to analyze the crystallographic orientation of the sputtered Ti layer and identify the presence of other crystalline phases, if any, that might be formed during deposition process of GaN.

A first analysis was done on Si (111) substrates coated with Ti layers 150 and 200 nm thick by magnetron sputtering. As can be seen in Figure 3.20, only the XRD peak corresponding to the (002) plane of Ti appears, which means that the deposition of Ti by sputtering on Si (111) occurs with its *c*-axis paralel to the *z*-direction (perpendicular to the substrate). In fact Si (111) was selected as substrate, because, despite crystallizing in the cubic system (space group $Fd\bar{3}m$) it shows a hexagonal distribution of the atoms in this plane similar to the atomic distribution of Ti in the (0001) basal plane. The signal corresponding to the (111) peak of Si appears as a single spot, which means that the substrate is monocrystalline, whereas the (0002) peak corresponding to Ti appears as a ring, indicating that Ti grows with grains randomly oriented along the *x* and *y* directions. The results are identical for the two different thicknesses of Ti films analyzed, as can be seen in Figures 3.19 (a) and (b).

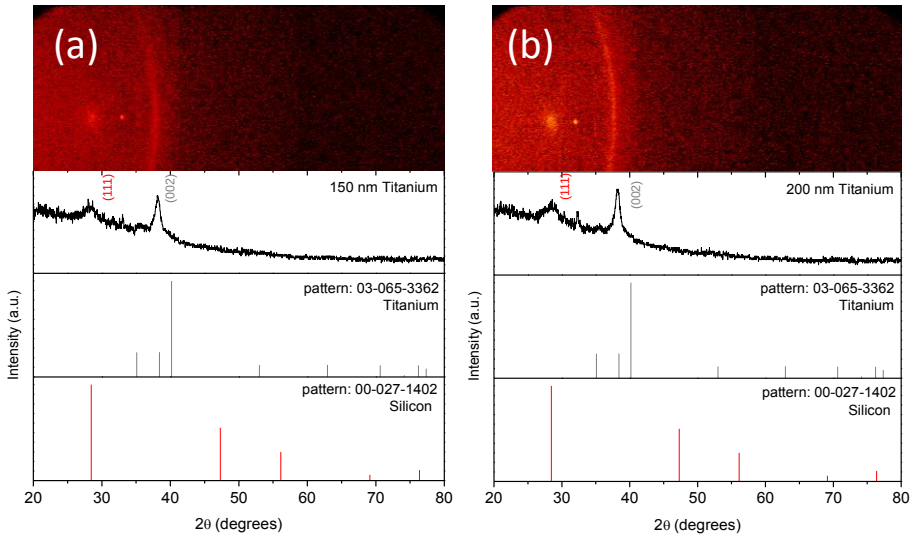

Figure 3.20. X-ray diffraction patterns with the corresponding Debye rings of Si (111) substrates coated with a continuous film of Ti (a) 150 nm and (b) 200 nm thick. The reference X-ray diffraction patterns of Ti and Si from the JCPDS database are included for comparison.

These two samples where heated at 1203 K, the usual reaction temperature we used for the deposition of GaN, under vacuum conditions. The samples were after analyzed again by XRD (see Figure 3.21). We could see the formation of two new phases corresponding to TiO_2 in the rutile form, (space group $P4_2/mnm$) and an alloy of the catalyst with the substrate (Si_2Ti, space group Fddd). The Debye rings show that the Si_2Ti phase is textured, with a preferential orientation of the plane (313). These results were reproducible. Two possible explanations for the appearance of the TiO_2 layer would be the inherent limitations of the CVD reactor we used, or a possible silicon oxide passivating layer covering the Si (111) substrate.

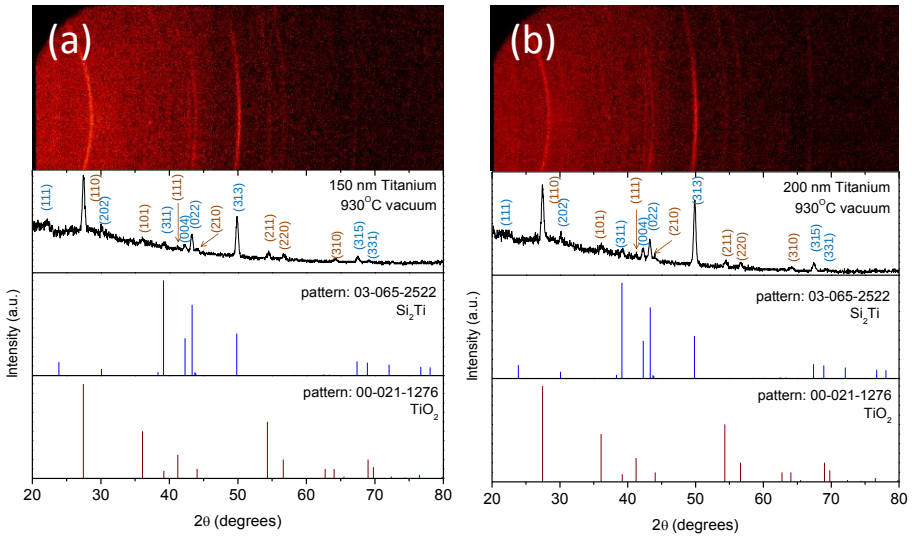

Figure 3.21. X-ray diffraction patterns with the corresponding Debye rings of Si (111) substrates coated with a continuous film of Ti (a) 150 nm and (b) 200 nm thick after being heated to 1203 K for 60 min under vacuum. The reference X-ray diffraction patterns of Si_2Ti and rutile TiO_2 from the JCPDS database are included for comparison.

Still, we explored the effect of a continuous NH_3 flow of 75 sccm at 1203 K on freshly Ti sputtered layers 150 and 200 nm thick on Si (111) substrates. XRD results confirm again the presence of TiO_2 and Si_2Ti (see Figure 3.22), but not metallic Ti in this case. For thicker Ti layers a preferential orientation of the (313) face could be observed for the Si_2Ti alloy phase.

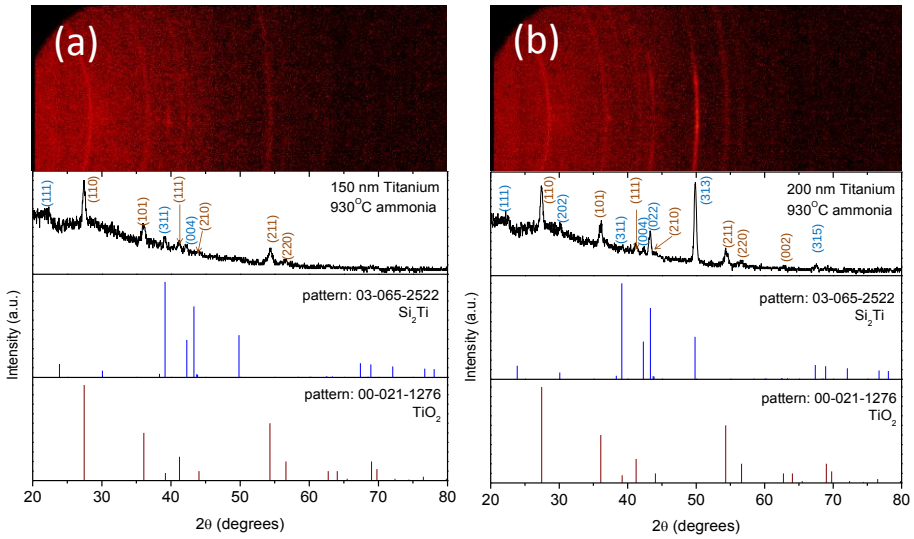

Figure 3.22. X-ray diffraction patterns with the corresponding Debye rings of Si (111) substrates coated with continuous films of Ti, (a) 150 nm and (b) 200 nm thick heated to 1203 K for 60 min under an ammonia flow of 75 sccm. The reference X-ray diffraction patterns of Si_2Ti and TiO_2 from the JCPDS database are included for comparison.

To prevent the diffusion of oxygen from the passivating SiO_2 layer covering the Si (111) substrate, those were cleaned with HF prior to being and coated with the Ti layers. However, XRD patterns (see Figure 3.23) indicate still the formation of TiO_2. It has also been noticed that when a layer 200 nm thick of Ti is used a preferential orientation of the (313), (022) and (315) planes of the Si_2Ti phase was observed. This effect was not observed when the Ti layer was only 150 nm thick.

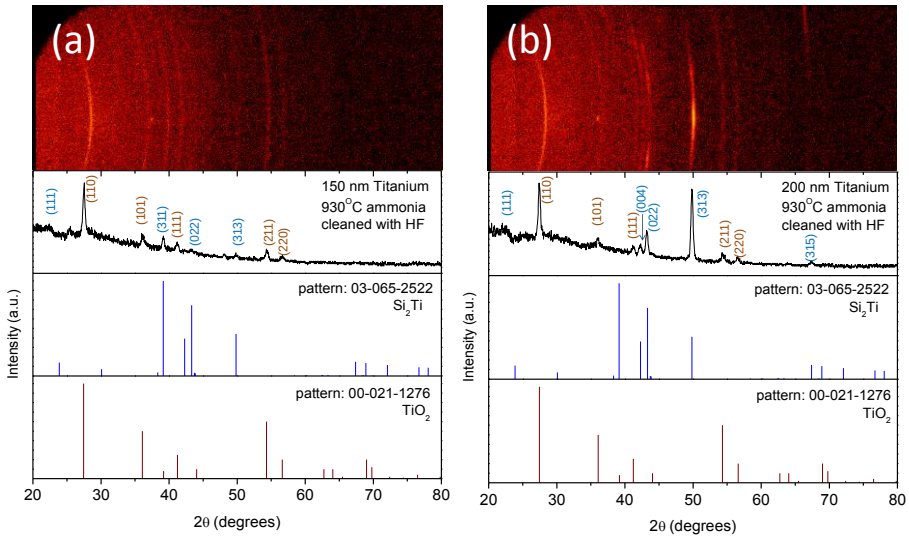

Figure 3.23. X-ray diffraction patterns with the corresponding Debye rings of Si (111) substrates cleaned with HF and coated with a continuous film of Ti (a) 150 nm and (b) 200 nm thick heated to 930°C for 60 min under an ammonia flow of 75 sccm. The reference X-ray diffraction patterns of Si_2Ti and TiO_2 from the JCPDS database are included for comparison.

These data show that the thickness of the Ti layer seems to play an important role in the formation of an oriented intermetallic allow layer between the catalyst and the substrate. It seems also possible that the presence of oxigen in the system that allows forming the TiO_2 phase would not attributed be to the diffusion of the oxygen present on the pasive layer of Si the substrates, but to the intrinsic limitations of the CVD system. This incorporation of oxygen in the CVD system would also be responsable for the unintentionally *n*-type doping of GaN we observed [10]. Thus, these results would explain why it was not possible to deposit an oriented GaN layer on the tope of the Ti layers.

3.6 Effect of the substrate

We have tested different substrates to ascertain if it might play a role in the crystallographic orientation of the GaN particles. For this purpose we used amorphous SiO_2 (fused silica), tungsten wire (W), pyrolytic boron nitride (p-BN) and sapphire as substrates for the deposition of porous GaN particles.

We have chosen these substrates with the criterion of using an amorphous substrate (fused silica), a cubic substrate different than Si with any particular crystallographic orientation (W wire), a substrate with hexagonal structure (p-BN) and the most common substrate for heteroepitaxial growth of GaN, sapphire (0001). If GaN follows a heteroepitaxial growth on sapphire (0001), it is expected to obtain oriented particles with the pores aligned perpendicular to the substrate.

Fused silica, BN and the W wire were coated with an ethanolic solution of $Ni(NO_3)_2$ to catalyze the growing of GaN since no growth of GaN was observed on the bare substrates, sapphire (0001) substrate was used without catalyst.

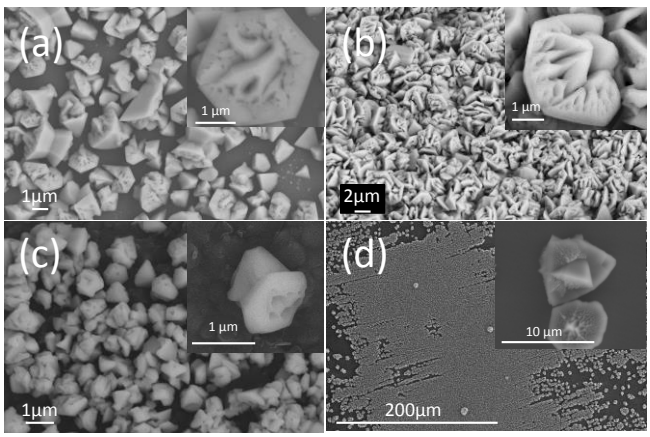

Figure 3.24. SEM images of the porous GaN particles grown on different substrates: (a) SiO_2-fused silica, (b) W wire, (c) pyrolitic BN and (d) (0001) sapphire.

SEM pictures of the porous GaN particles grown on these substrates reveal in all cases that GaN appears in the form of hexagonal micron-sized porous particles (see Figure 3.24). When fused silica was used, the level of porosity in the particles appears to be low, with the pores more concentrated at the central part of the particles, and with an elongated shape towards the external parts of the particles, as can be seen in Figure 3.24 (a).

On the W wire, the density of particles is very high, which might induce to think that GaN particles grow with a plate shape as can be seen in

Figure 3.24 (b). However, in the inset included in this figure, it can be clearly seen that the individual particles have the pyramid morphology obtained up to now.

In the case of p-BN, a certain degree of alignment of the GaN particles can be observed since a bigger number of pores perpendicular to the surface can be seen (see Figure 3.24 (c)). However, and due to the misalignment of the BN flakes that form p-BN, particles with different crystallographic orientations can be seen. Also, the porosity degree in these particles is lower than in the other cases, as can be seen in the inset of this figure.

However, structural characterization by XRD analysis (Figure 3.25 (a-c)) did not reveal any preferential growth in any of these samples. For W wire and p-BN, the diffraction corresponding to the substrate appears as intense and uniform Debye ring, indicating that they are polycrystalline. Fused silica is seen as a broad band at low 2θ angles, due to the amorphous nature of the material. In the X-ray pattern of the porous GaN particles grown on a tungsten wire, the presence of another crystalline phase corresponding to NiO is also observed. Even so, the intensity of this crystalline phase is very low.

Porous GaN particles grown on sapphire can be seen arranged in parallel lines (see Figure 3.24 (d)). Also, it can be seen in the SEM images that the coverage of the substrate is more uniform than in the other cases, although the substrate is not fully covered with GaN particles. A closer look to the images reveals that in some cases the particles show their (0001) plane parallel to the substrate, with the pores perpendicular to the substrate, as can be seen in the inset. However, a large portion of the particles are still tilted with their pores aligned parallel to the substrate, and consequently the (0001) plane lies perpendicular to the substrate. The XRD analysis (see Figure 3.25 (d)) corroborates these observations. The diffraction pattern indicates that the particles obtained are wurtzite GaN, but, the intensity ratio of the diffraction peaks of the sample does not match that of the reference pattern. The most

intense peak of the diffraction pattern of the sample is the $(11\bar{2}0)$ peak, in contrast with the reference one, which is the $(10\bar{1}1)$ peak. This seems to indicate that exists a preferential orientation of the layer of porous GaN particles deposited on sapphire, although it is not the one we expected, which would correspond to that with the (0001) plane parallel to the substrate.

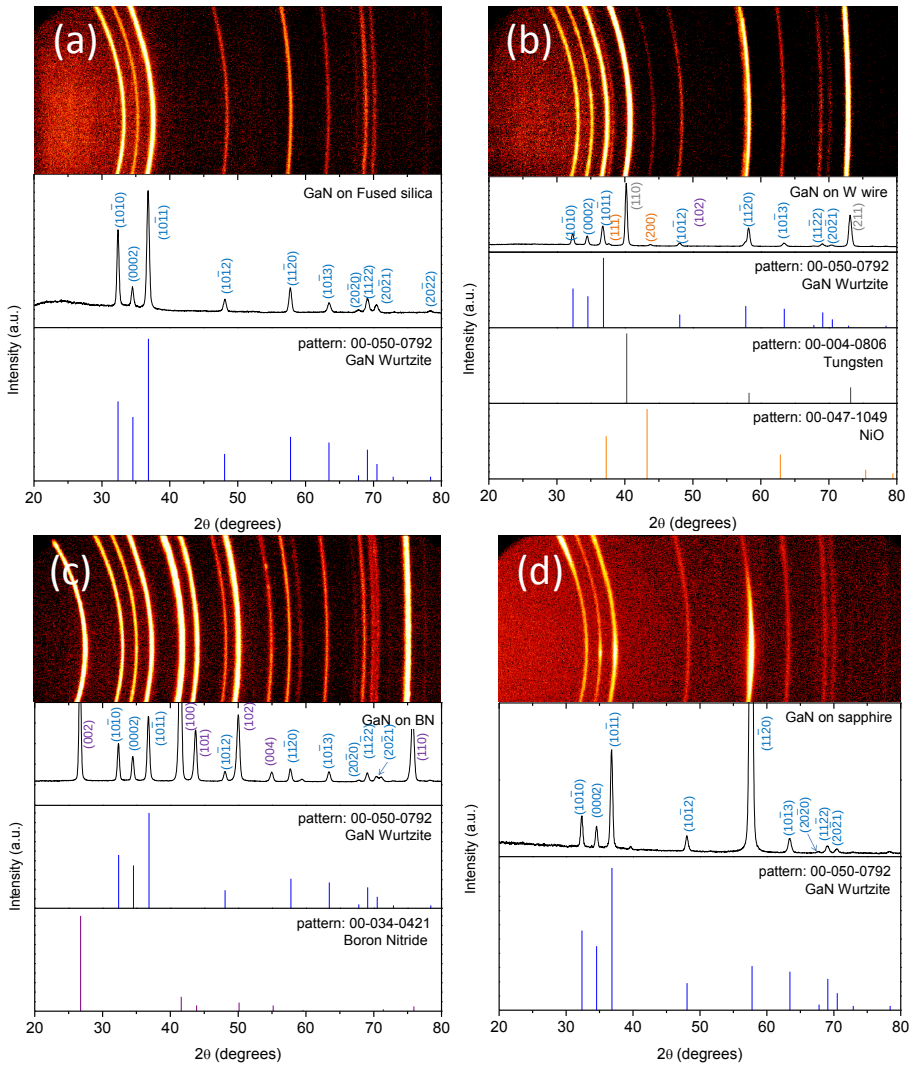

Figure 3.25. X-ray diffraction patterns with the corresponding Debye rings of porous GaN particles obtained on (a) fused silica, (b) W wire, (c) BN and (c) sapphire. The reference X-ray diffraction patterns of GaN, BN, W and NiO from the JCPDS database are included for comparison.

A closer analysis of the textures of the porous GaN particles grown on sapphire was done, analyzing the distribution of intensities in the 2D diffraction image and the γ angle. This is the angle defined by the imaginary line that cuts of the Debye rings from their centre of curvature in the horizontal plane and a line with the same origin but that ends at the desired point of the 2D diffraction image (see Figure 3.26). The sample can be moved in such a way that the maximum of intensity of the Debye ring appears in the centre of the 2D diffraction image (γ=0°) doing the appropiate χ-and φ-move as depicted in Chapter 2 Figure 2.16.

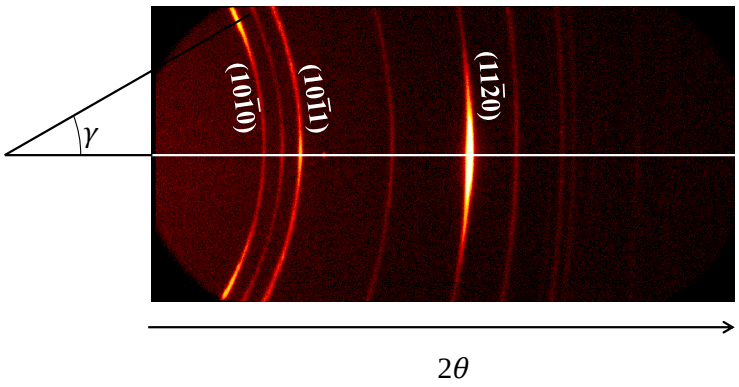

Figure 3.26. 2D diffraction image of the porous GaN particles grown on sapphire indicating the angle γ.

Figure 3.27 shows the distribution of intensity of the $(11\bar{2}0)$ and $(10\bar{1}0)$ peaks as a function of the γ angle. The expected γ angle between these two peaks is 30°, which corresponds to the angle between the $(11\bar{2}0)$ and $(10\bar{1}0)$ plane vectors, as indicated in Appendix 1. This would indicate that the particles are oriented in such a way that the $(11\bar{2}0)$ planes are parallel to the substrate and would be the responsible for the increase of the intensity of the $(10\bar{1}0)$ peak at γ=30°. Also the $(10\bar{1}1)$ peak has a non-uniform distribution of the intensity in the Debye ring with higher intensity at γ=0°, and it is expected that these oriented particles diffract at γ=40° in the $(11\bar{2}0)$ Debye ring, but it cannot be seen in the 2D diffraction image since it is out of the area detector.

However, the angle between the plane vectors of the $(10\bar{1}0)$ plane and $(10\bar{1}0)$ plane is γ=28°, thus the location of the intensity of the $(10\bar{1}0)$ diffraction peak at $\gamma \approx 30°$ may be a sum of the contribution of the particles oriented with the $(11\bar{2}0)$ and $(10\bar{1}1)$ planes parallel to the substrate as it fits with the broadening of the peak observed compared with the $(11\bar{2}0)$ diffraction peak in the γ-graph. Thus, the particles grown on sapphire have three different ways to orient: with the $(11\bar{2}0)$ face parallel to the substrate (see Figure 3.10 (d)), which is the predominant; with the $(10\bar{1}1)$ parallel to the substrate (see Figure 3.15), which is the second most important contribution; and randomly oriented which explains the continuity of the Debye ring.

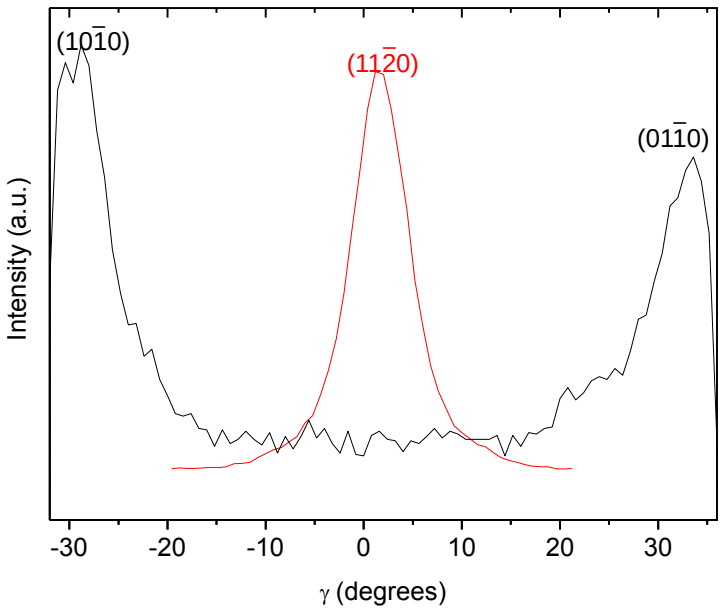

Figure 3.27. γ-graph of the $(11\bar{2}0)$ and $(10\bar{1}0)$ diffraction peaks.

References

[1] Xu, Q.; Oudalov, N.; Guo, Q.; Jaeger, H. M.; Brown, E., Effect of oxidation on the mechanical properties of liquid gallium and eutectic gallium-indium. *Phys. Fluids* **2012,** *24* (6), 063101.

[2] Wang, R.; Liu, D.; Zuo, Z.; Yu, Q.; Feng, Z.; Xu, X., Metal-assisted electroless fabrication of nanoporous p-GaN for increasing the light extraction efficiency of light emitting diodes. *AIP Advances* **2012,** *2* (1), 012109.

[3] Bilousov, O. V.; Carvajal, J. J.; Drouin, D.; Mateos, X.; Díaz, F.; Aguiló, M.; O'Dwyer, C., Reduced Workfunction Intermetallic Seed Layers Allow Growth of Porous n-GaN and Low Resistivity, Ohmic Electron Transport. *ACS Appl. Mater. Interfaces* **2012,** *4* (12), 6927-6934.

[4] Rizal, U.; Swain, B. S.; Swain, B. P., Correlation between the photoluminescence and chemical bonding in silicon nitride nanowires deposited by chemical vapour deposition. *J. Alloys Compd.* **2016,** *664*, 453-459.

[5] Saron, K. M. A.; Hashim, M. R.; Allam, N. K., Heteroepitaxial growth of GaN/Si (111) junctions in ammonia-free atmosphere: Charge transport, optoelectronic, and photovoltaic properties. *J. Appl. Phys.* **2013,** *113* (12), 124304.

[6] Tang, Y. B.; Chen, Z. H.; Song, H. S.; Lee, C. S.; Cong, H. T.; Cheng, H. M.; Zhang, W. J.; Bello, I.; Lee, S. T., Vertically Aligned p-Type Single-Crystalline GaN Nanorod Arrays on n-Type Si for Heterojunction Photovoltaic Cells. *Nano Lett.* **2008,** *8* (12), 4191-4195.

[7] Choi, J. H.; Zoulkarneev, A.; Kim, S. I.; Baik, C. W.; Yang, M. H.; Park, S. S.; Suh, H.; Kim, U. J.; Bin Son, H.; Lee, J. S.; Kim, M.; Kim, J. M.; Kim, K., Nearly single-crystalline GaN light-emitting diodes on amorphous glass substrates. *Nat Photon* **2011,** *5* (12), 763-769.

[8] Da Silva, J. L. F.; Stampfl, C.; Scheffler, M., Converged properties of clean metal surfaces by all-electron first-principles calculations. *Surf Sci.* **2006,** *600* (3), 703-715.

[9] Matysina, Z. A., The relative surface energy of hexagonal close-packed crystals. *Mater. Chem. Phys.* **1999,** *60* (1), 70-78.

[10] Zhu, T.; Oliver, R. A., Unintentional doping in GaN. *Phys. Chem. Chem. Phys.* **2012,** *14* (27), 9558-9573.

4

Crystal growth and characterization of Mg- and Si-doped GaN and InGaN ternary alloys

Controlling the electrical properties of semiconductors is a crucial step for the fabrication of *p*-*n* junction-based devices. For the fabrication of a *p*-*n* junction it is mandatory the doping of the semiconductor host with the appropriate dopant. In the case of GaN, a III-V semiconductor, it is very common to use an element of the II group, such as Mg [1], to produce a *p*-type semiconductor and an element of the IV group, such as Si [2], to produce an *n*-type semiconductor.

Also, it is very important for the development of the LED technology the fabrication of ternary allows of $In_xGa_{1-x}N$, either for the fabrication of MQWs within the *p* and *n* side of a *p*-*n* junction, as well as for the fabrication of a *p*-*n* junction itself producing an output wavelength ranging from 3.4 eV to 0.7 eV when tuning the In molar fraction in the material.

In all cases, the elements incorporated have to occupy the Ga site to obtain the desired effect, either doping in the case of Si and Mg, or ternary allow in the case of In.

The first part of this chapter is centered on continuing the previous study begun in our group by Dr. Oleksandr Bilousov on the incorporation of Mg to the porous GaN in order to obtain *p*-type doped GaN, using magnesium acetylacetonate ($Mg(acac)_2$) as the Mg precursor finalizing the cathodoluminescence study of the samples previously grown.

Then, the same doping was tried to obtain porous epitaxial films.

The second part of the chapter is also dedicated to the doping of porous GaN, but this time to obtaining *n*-type porous GaN doped with Si using silicon acetate ($Si(ac)_4$) as the Si precursor.

The third and last part of the chapter is devoted to the study of the incorporation of In to porous GaN in order to grow $In_xGa_{1-x}N$ ternary alloys. For this purpose two different approaches were used: the use of an In/Ga alloy of different concentrations of In, and a metalorganic approach using indium acetylacetonate ($In(acac)_3$).

4.1 Mg doping of porous GaN using $Mg(acac)_2$ as magnesium precursor

4.1.1 Determination of the correct location of the Mg precursor in the furnace

In this section, the first part is devoted to optimize the experimental parameters for the incorporation of magnesium into porous GaN particles grown on Si (100) substrates coated with an ethanolic solution of $Ni(NO_3)_2$ as catalyst using magnesium acetylacetonate.

The $Mg(acac)_2$ is presented as a white powder and was placed into the furnace on a crucible at a given distance, upstream, from the substrate.

In previous works performed in the group, it was synthesized a set of samples of GaN with different quantities of $Mg(acac)_2$ at different distances from the substrate which are listed in Table 4.1. These samples were characterized by SEM and CL at room temperature (RT). The morphogical analysis by SEM reveals in all cases nanoporous GaN particles with sizes around 2-4 μm. However, no evidences of the Mg incorporation on porous GaN particles were observed by CL. The absence of the DAP band in the CL spectra obtained at RT for the analyzed samples, is due to the quenching of the DAP band at RT. Thus, no information about the incorporation of magnesium could be obtained.

Table 4.1. Mg-doped GaN samples prepared with the $Mg(acac)_2$ precursor previously in the group.

Distance between the Ga and Mg sources (cm)	**Quantity of $Mg(acac)_2$** (g)
15	0.0507
20	0.0507
23	0.0507
24	0.0507
26	0.0507
30	0.0507
15	0.0844
20	0.0844
15	0.1688
20	0.1688
21	0.1688
23	0.1688
24	0.1688

In this case, we studied the samples grown using 0.1688 of Mg precursor located at 21, 23, and 24 cm from the substrate by CL at 80 K.

Figure 4.1 (a) shows the CL spectra recorded for the porous GaN particles grown on Si substrates using $Ni(NO_3)_2$ as a catalyst using 0.1688 g of $Mg(acac)_2$ as Mg precursor located at 24, 23 and 21 cm up-stream from the substrate. It can be seen that for samples grown placing the Mg precursor further away from the substrate, the CL spectra shows the presence of the NBE band and the YL band associated to *n*-type GaN, whereas the intensity of these peaks decrease as the precursor is located closer to the substrate, disappearing completely when the precursor is located at 21 cm away from the substrate.

In Figure 4.1 (b) we plotted the NBE/DAP ratio as a function of the distance at which the Mg precursor is located away from the substrate, as a measure of the incorporation of Mg into the porous GaN particles.

These results point out in the direction that the distance of 21 cm is the optimum distance for the doping of porous GaN particles with Mg using $Mg(acac)_2$.

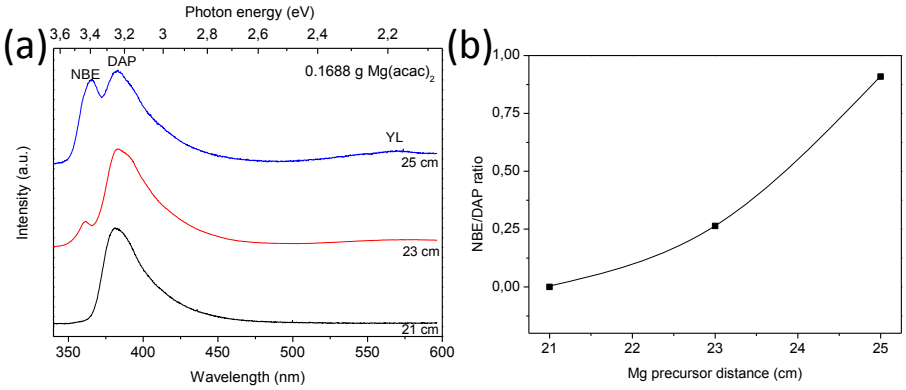

Figure 4.1. (a) CL spectra recorded for the porous GaN particles using 0.1688 g of $Mg(acac)_2$ as precursor placed at difference distances from the substrate. (b) NBE/DAP ratio extracted frin the CL spectra as a function of the distance of the Mg precursor from the substrate.

The distance at which the precursor is located can be correlated to temperature in that particular point of the horizontal tubular furnace, as it is depicted in Figure 2.3. Table 4.2 lists the temperatures for the different locations of the Mg precursor. Note that in all the positions where the precursor was placed, the associated temperature was above the decomposition temperature of the $Mg(acac)_2$ which is 538 K (265 °C). This ensures the maximum migration of Mg from the source to the substrate.

Table 4.2. Temperature of the furnace at the different distance locations of the Mg precursor, when the furnace temperature was set to 1203 K.

Distance (cm)	**Temperature** (K)	**Temperature** (°C)
15	1092	819
19	963	690
20	924	651
21	878	605
23	781	508
24	734	461
25	676	403
29	513	240

4.1.2 Crystal growth of Mg-doped porous GaN epitaxial layers

Using the same procedure, we tried to obtain epitaxial Mg-doped porous GaN layers grown on Si-doped GaN (0001)/sapphire (0001) substrates. The distance between the Mg precursor and the substrate was tuned from 15, 19, 21, to 25 cm corresponding to the temperatures listed in Table 4.2.

Figure 4.2 shows the SEM images of the GaN layers obtained. Figures 4.2 (a) and (b) show that when the $Mg(acac)_2$ precursor is located at a short distance from the substrate (15 and 19 cm) a porous GaN layer is obtained with isolated porous GaN particles on the top of it. In Figure 4.2 (c) it can be seen that a porous layer is beneath a dense layer of porous GaN particles. Finally, Figure 4.2 (d) shows that only porous GaN particles were obtained when the Mg precursor was located at 25 cm away from the substrate.

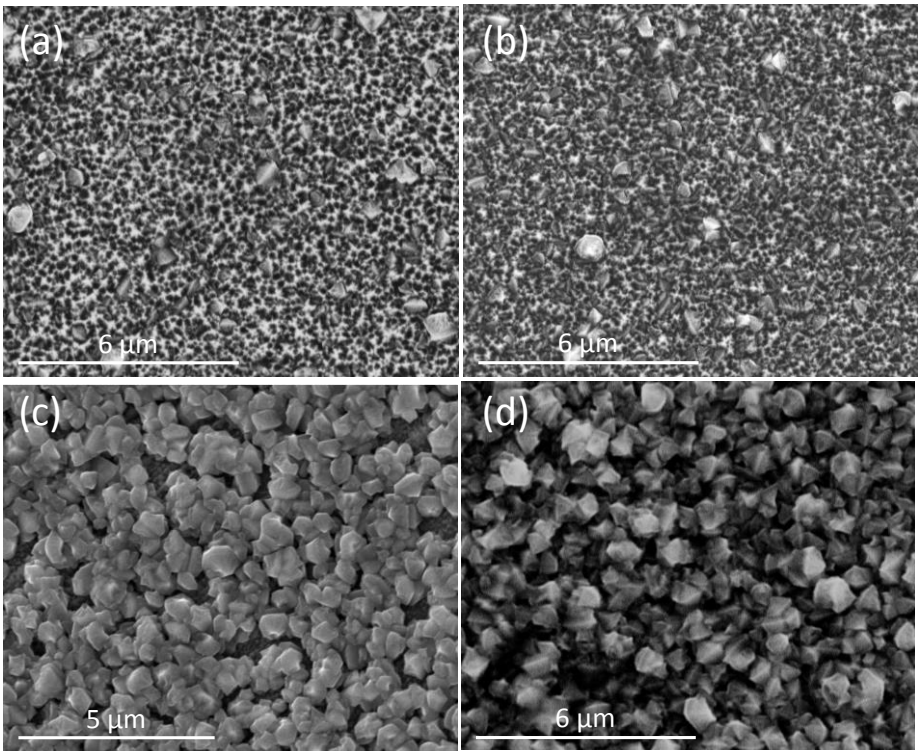

Figure 4.2. SEM images of the porous GaN samples synthesized using $Mg(acac)_2$ as the Mg precursor for Mg-doping placed at (a) 15, (b) 19, (c) 21, and (d) 25 cm from the substrate, on Si-doped GaN (0001)/Sapphire (0001) substrates.

In order to assess the concentration of Mg incorporated on porous GaN, electron probe micro-analysis (EPMA) was carried out. The results of this analysis are presented in Figure 4.3 that indicates that high concentrations of Mg are incorporated into GaN, of the order of 10^{20} cm^{-3}. The highest concentration of Mg incorporated into GaN was obtained for the sample in which the Mg precursor was placed 19 cm up-stream from the substrate. At longer distances a lower concentration of Mg was obtained, probably caused from a slow decomposition of the precursor and consequently a low flow rate towards the substrate. For shorter distances, the Mg concentration also decreases, probably due to a too fast decomposition of the $Mg(acac)_2$ which is at temperatures ~1090 K, much above its decomposition temperature, producing a rapid flow of Mg that avoids an optimum incorporation into GaN.

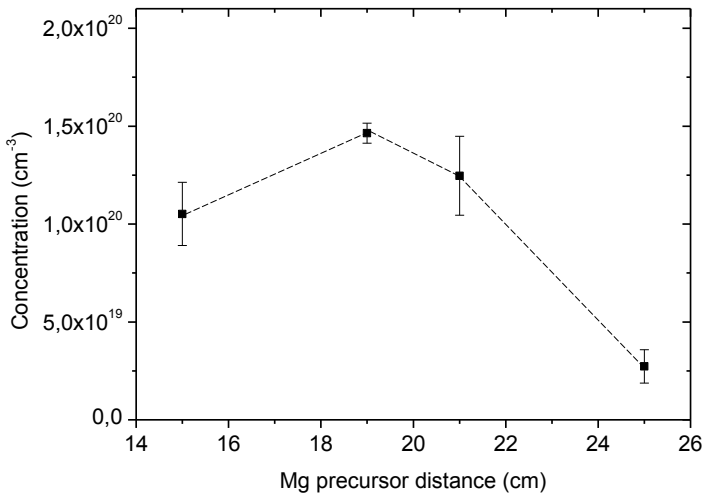

Figure 4.3. EPMA of the Mg-doped GaN samples using $Mg(acac)_2$ as the Mg precursor as a function of the distance from the Mg precursor to the substrate for porous GaN samples grown on Si-doped GaN (0001)/Sapphire (0001) substrates.

We observed that, after the deposition of porous GaN, a black powder remained on the $Mg(acac)_2$ crucible. We analyzed this powder by XRD, and the resulting pattern is presented in Figure 4.4. The only crystalline phase observed corresponds to MgO, formed as a byproduct of the $Mg(acac)_2$ decomposition. The peak at 9.7° and the broad band between 20-40° belong to the sample holder. The XRD results show that part of the Mg present in $Mg(acac)_2$ is diffused to the substrate when its decomposed, while the rest is calcinated and remained in the crucible as MgO.

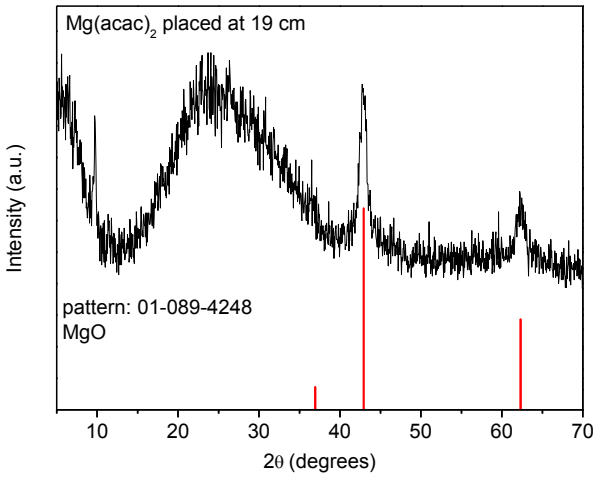

Figure 4.4. XRD of the remaining powder in the $Mg(acac)_2$ crucible extracted from the experiment in which the Mg precursor was located at 19 cm away from the substrate, corresponding to a temperature of 963 K (690 °C). The reference pattern for MgO (01-089-4248) is included for comparison.

4.2 Si doping of porous GaN using $Si(ac)_4$ as silicon precursor

4.2.1 Study of the incorporation of Si on porous GaN

Attempts have been done to dope porous GaN particles with Si in a CVD furnace using a solid precursor of Si. For this purpose, an organic salt of Si, silicone acetate, was chosen. $Si(ac)_4$ has a low boiling point of 421 K (148 °C) at low pressures (5 torr) [3], like the ones used during the experiment. The $Si(ac)_4$ was placed at different distances from the substrate in order to evaluate its effect on the doping concentration into GaN. Porous GaN particles were grown on Si (100) substrates using $Ni(NO_3)_2$ as catalyst. 0.021 g of $Si(ac)_4$ were placed on a crucible at 30, 25, and 20 cm upstream from the substrate.

Figure 4.5 shows the SEM pictures of the porous GaN particles using $Si(ac)_4$ as the Si precursor. In the three cases, porous particles with rough lateral walls rather than smooth surfaces were observed. Their size was quite uniform among all the samples, with particles sizes ranging from 1 to 3 μm.

When the porous GaN particles were grown placing the $Si(ac)_4$ precursor 20 cm away from the substrate, some GaN nanowires were observed nucleating from the edges of the particles (see Figure 4.5 (b)). The presence of nanowires is anecdotally observed also in the sample grown when $Si(ac)_4$ was placed at 25 cm away from the substrate, as it can be observed in Figure 4.5 (d). Finally, in the sample grown when $Si(ac)_4$ was placed 30 cm away from the substrate, no nanowires were observed (see Figure 4.5 (f)).

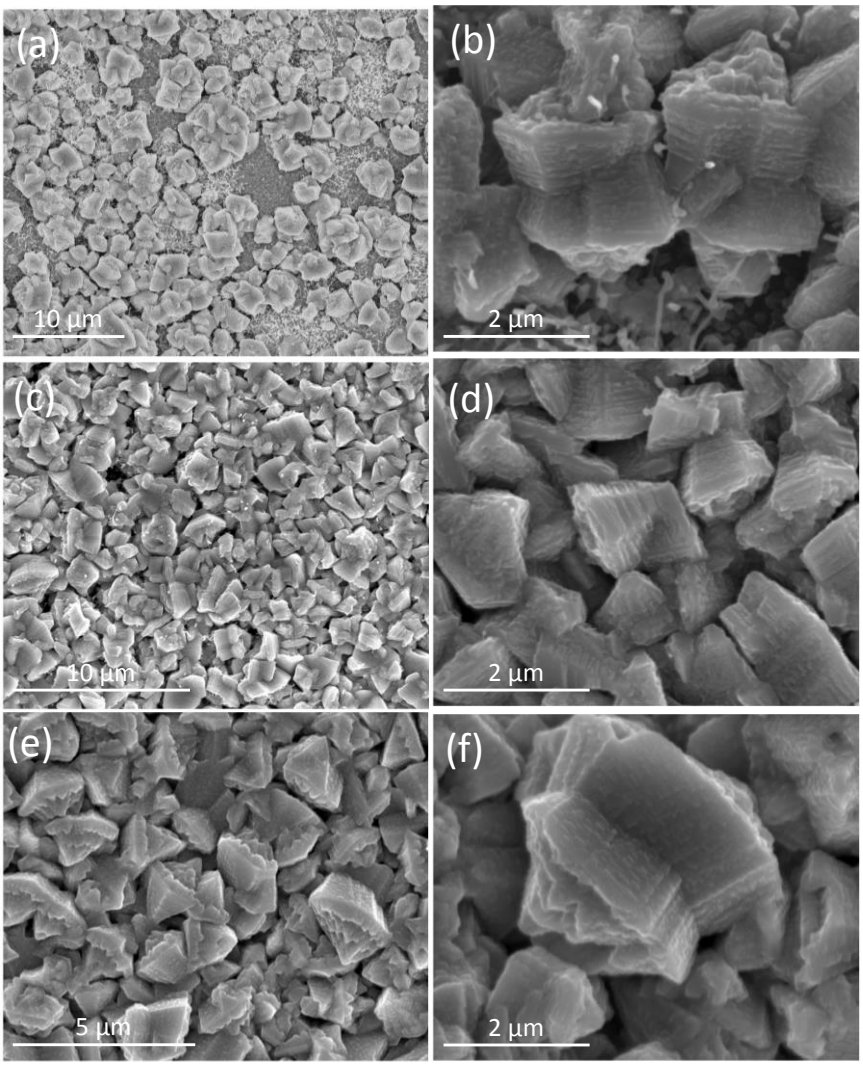

Figure 4.5. Low (left) and high (right) magnifiication SEM images of the porous GaN particles synthesized using $Si(ac)_4$ as the Si precursor for Si-doping placed at (a-b) 20, (c-d) 25, and (e-f) 30 cm from the Si (100) substrate coated with $Ni(NO3)_2$ as catalyst.

Figure 4.6 (a) shows the CL spectra recorded for the porous GaN particles synthesized using $Si(ac)_4$ as Si precursor for Si-doping. In these spectra we observed that the linewidth of the NBE peak broadens as the Si precursor is located closer to the substrate, while the NBE peak position is red-shifted. Figure 4.6 (b) depicts the NBE peak position and its FWHM as a function of the Si-source distance to the substrate.

The position of the NBE peak shifts from 3.408, 3.411, to 3.457 eV for the porous GaN particles grown with the Si precursor placed at 20, 25, and 30 cm away from the substrate, respectively.

The broadening of the NBE peak with Si doping was first reported by Schubert *et al.* in 1997 [4]. They proposed that the broadening of the peak was attributed to potential fluctuations caused by the random distribution of the doping impurities. Such, fluctuations in the Si distribution are caused by the unavoidable random distribution of the dopants during growth. These fluctuations of microscopic concentration of dopants cause a macroscopic potential fluctuation. Thus, if the concentration is sufficiently high, this potential fluctuation can be observed. This potential fluctuation is reported to be proportional to $(N_D+N_A)^{1/2}$ where N_D is the concentration of donors and N_A is the concentration of compensating acceptors. In our case the N_D is the concentration of Si dopants incorporated in the GaN structure, whereas the N_A is the concentration of self-compensating defects.

This red-shift of the NBE peak might be interpreted in terms of a band gap narrowing (BGN), according to Zhang *et al*. this band-gap renormalization, which is a shift in energy of the bands states due to the presence of impurities, increase with the dopant concentration. They treated this problem in terms of many-body theory, in which the band-gap shrinkage (ΔE_g) is proportional to the cubic root of the sum of the *n*-type and *p*-type carrier concentration [5]:

$$\Delta E_g = E_g - E_0 = -K(n^{1/3} + p^{1/3}) \qquad \textbf{Eq. 4.1}$$

where E_0 is the intrinsic energy band-gap, whereas E_g is the energy band-gap in the presence of excess of carriers, and K is the band-gap renormalization coefficient. Since all the samples were grown using the same conditions, except for the quantity of $Si(ac)_4$ used, the parameter p is considered as a constant independent of the Si-doping level.

In our case the concentration of free carriers n cannot be calculated using Eq. 4.1, since the K parameter is highly dependent on the growth method [6]. And, as well as in the case of the Mg-doped porous GaN Hall measurements have to be carried out in order to evaluate the concentration of free carriers in each case.

According to Yang et al. the YL is found to decrease as the doping concentration increases. This is due to the substitution of Si dopants on gallium lattices sites, thus decreasing the number of V_{Ga} and consequently the YL intensity, which is associated to V_{Ga}-O_N, decreases.

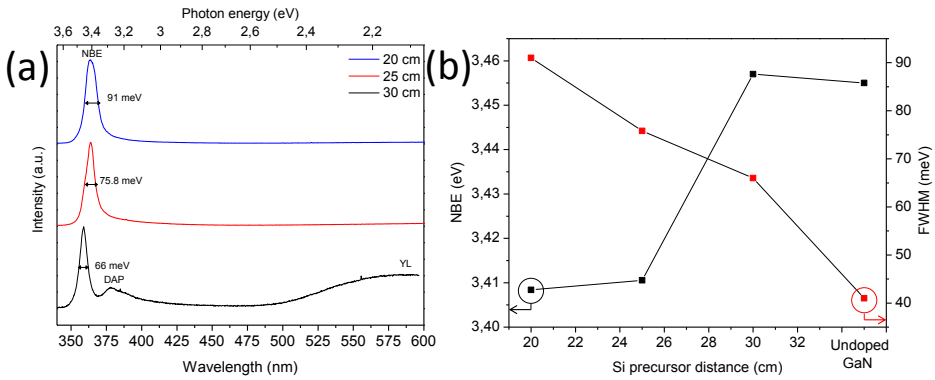

Figure 4.6. (a) CL spectra recorded for the porous GaN particles grown using $Si(ac)_4$ as the Si precursor located at different distances from the substrate. (b) NBE peak position and FWHM as a function of the distance of the Si precursor to the substrate.

Thus, the results obtained by CL, points out in the direction that there is an incorporation of Si into the porous GaN particles, inasmuch as when the si precursor is placed close to the substrate the band-gap narrowing is higher, the FWHM increases due to the potential fluctuations of the incorporated Si-dopants and the YL intensity tends to disappear. The incorporation of Si

reaches its higher value, for the studied samples, when the $Si(ac)_4$ was placed at 20 cm upstream from the substrate.

4.3 Attempts on obtaining porous InGaN structures

We analysed the possibilities of developing a strategy to obtain nanoporous $In_xGa_{1-x}N$ in a CVD system by the direct reaction of metallic Ga and ammonia (NH_3). For the purpose of doping porous GaN with In, we followed two different strategies. The first one is the use of metallic In, and the second is the use of a metalorganic precursor of In such as indium acetatylacetonate $In(acac)_3$. For this purpose we performed a set of experiments using different concentrations of In in a metallic alloy between In and Ga at different growing temperatures. The melting point of the Ga/In alloy is lower than that of pure metallic Ga in the range between 0-18 % of In atomic percentage, reaching its minimum at the eutectic point, which is found when the atomic percentage of In is ~15%, having a melting point of 288 K [7] (see Figure 4.7).

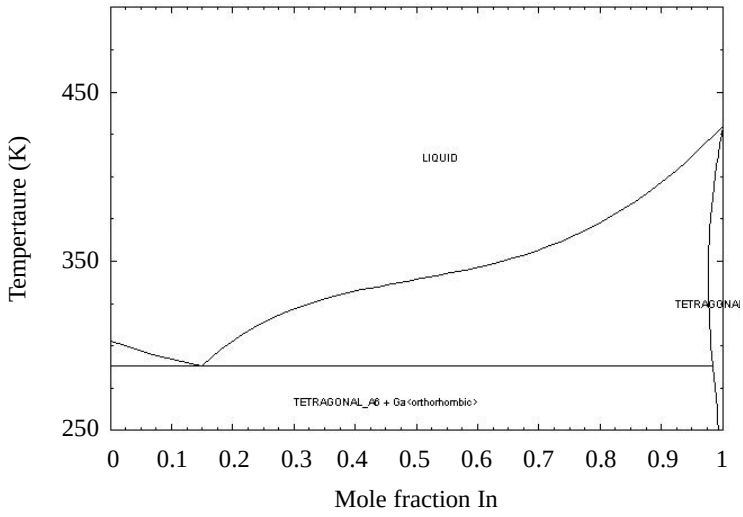

Figure 4.7. In-Ga alloy Phase diagram (image adapted from [7]).

For the first set of experiments we kept the concentration of In at 5% in weight and tuned the growth temperature of the reactor. The reactor temperatures used were 1143 (870 °C), 1173 (900 °C), and 1203 K (930 °C). The growth time, the ammonia flow, the pressure, the substrate and the catalyst were kept constant at 60 min, 75 sccm, 15 torr, Si (100) and an ethanolic solution of $Ni(NO_3)_2$ 0.01 M, respectively.

Figure 4.8 shows the SEM images of the samples grown at different furnace temperatures using 5% of In. In the SEM images we can observe, when the deposition temperature was set at 1143 K, the formation of thick nanowires (NWs) and not too long in length, concentrated in isolated islands along the substrate (see Figure 4.8 (a)). When the temperature was increased up to 1173 K, the formation of a dense layer of NWs was observed by SEM, longer in length and much thinner, when compared to those obtained at 1143 K (see Figure 4.8 (b)). Finally, when the deposition temperature was set at 1203 K the formation of particles was observed, together with a reduced number of NWs (see Figure 4.8(c)). However, these particles have not a well defined shape and the intraparticle porosity is not observed in them.

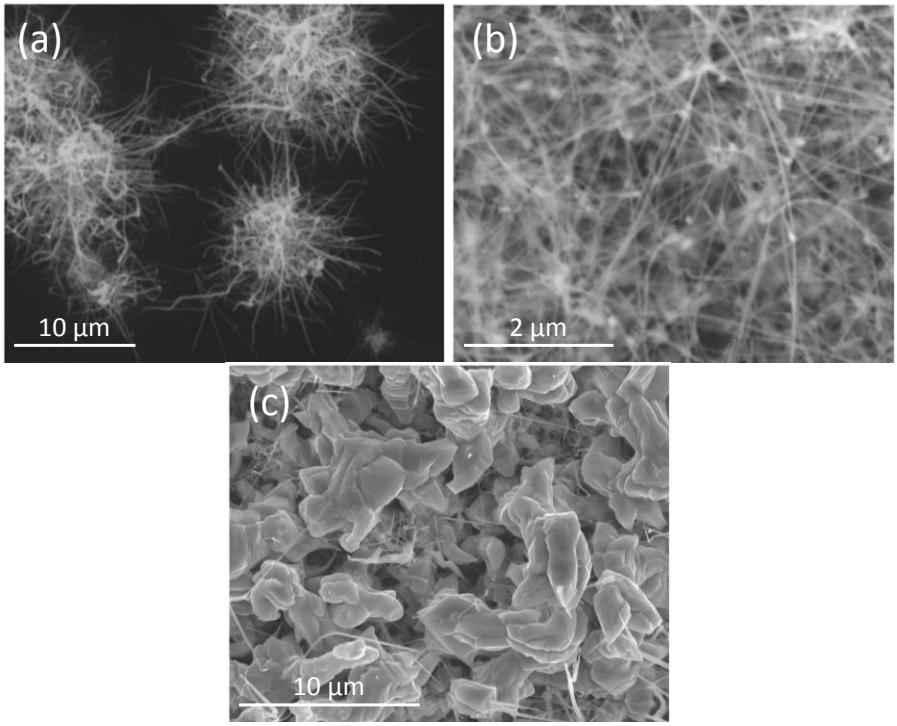

Figure 4.8. SEM images of the InGaN sample obtained when 5% in weight of In to respect Ga was used and the furnace was heated to (a) 1143, (b) 1173, and (c) 1203 K.

Another set of experiments were performed using the same experimental conditions but increasing the percentage of Indium in the In/Ga alloy to 10%. In Figure 4.9 we can see the SEM images of the samples obtained. When the deposition temperature was set at 1143 K, only disperse grains of irregular shape were observed along the substrate (see Figure 4.9 (a)). For the sample deposited at 1173 K only NWs were observed, similar to the sample grown using 5% of In (see Figure 4.9 (b)). Finally, irregular particles, surrounded by NWs, were observed for the sample deposited at 1203 K.

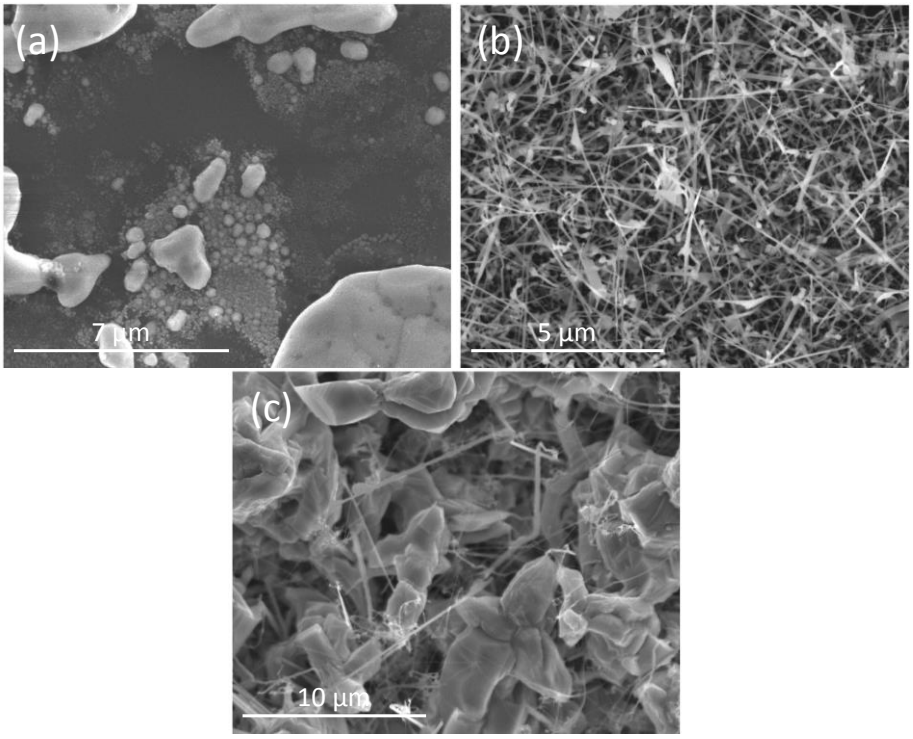

Figure 4.9. SEM images of the InGaN samples obtained when 10% in weight of In to respect Ga was used and the furnace was heated to (a) 1143, (b) 1173, and (c) 1203 K.

All these samples were analysed by XRD, to identify the crystalline structure of the deposited material. In all the cases, the XRD patterns obtained confirmed the presence of GaN and Ga_2O_3 (see Figure 4.10). Furthermore, the positions of the peaks corresponding to GaN are located at the exact position of the reference pattern, indicating that In was not incorporated in the GaN structure. We do not have an explanation for the formation of Ga_2O_3.

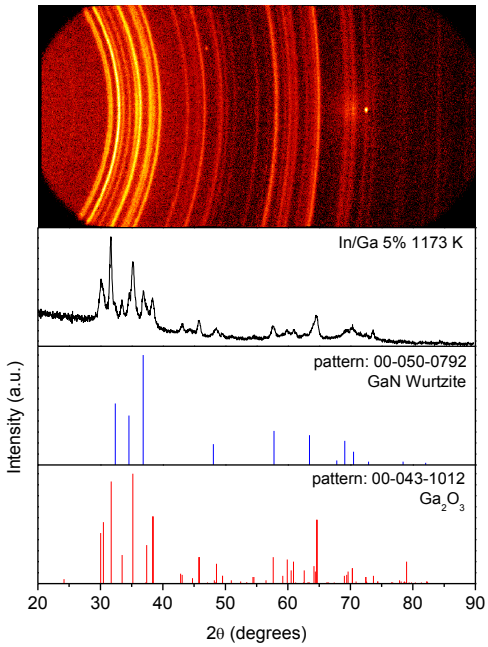

Figure 4.10. X-ray diffraction pattern with the corresponding 2D diffraction image of the sample grown using 5% of In and a deposition temperature of 1173 K. The lines in blue and red correspond to the reference patterns of GaN and Ga_2O_3, respectively.

The unmistakable evidence that indium was not incorporated when the approach of the In/Ga alloy was used, made us to follow a different strategy for the incorporation of In into the GaN structure, by using a metalorganic precursor. In this case we used indium acetylacetonate, $In(acac)_3$, a solid powder at room temperature with a melting point of 460-462 K (187-189 °C). Since the In precursor is solid at room temperature it is easy to manipulate and place it at different distances from the substrate, as we did previously for the precursors of Mg and Si. In this case we used 0.028 g of $In(acac)_3$ placed at upstream distances from the substrate of 30, 25, 23, and 20 cm. The distance between the In source and the substrate is associated to an specific value of temperature. Also, the furnace temperature was set at two different temperatures: 1173, and 1203 K.

For the first set of experiments the furnace was set at 1203 K. When the $In(acac)_3$ powder was placed at 30 cm (473 K) from the substrate almost

no significant evaporation of $In(acac)_3$ powder was observed during the experiment. When the $In(acac)_3$ powder was further approached at 25 cm (676 K), a decrease of the powder quantity in the crucible was observed. By decreasing the distance between the $In(acac)_3$ powder and the substrate to 23 cm (781 K aprox), almost all the $In(acac)_3$ powder was evaporated during the reaction. Finally, no $In(acac)_3$ powder was observed in the crucible after the reaction when the In precursor was placed at 20 cm (924 K) from the substrate.

Figure 4.11 shows the SEM images of the porous particles grown at 1203 K placing the In precursor at different distances from the substrate. In all cases, micron-sized porous particles were obtained similar to those grown using the same experimental condition without the presence of $In(acac)_3$.

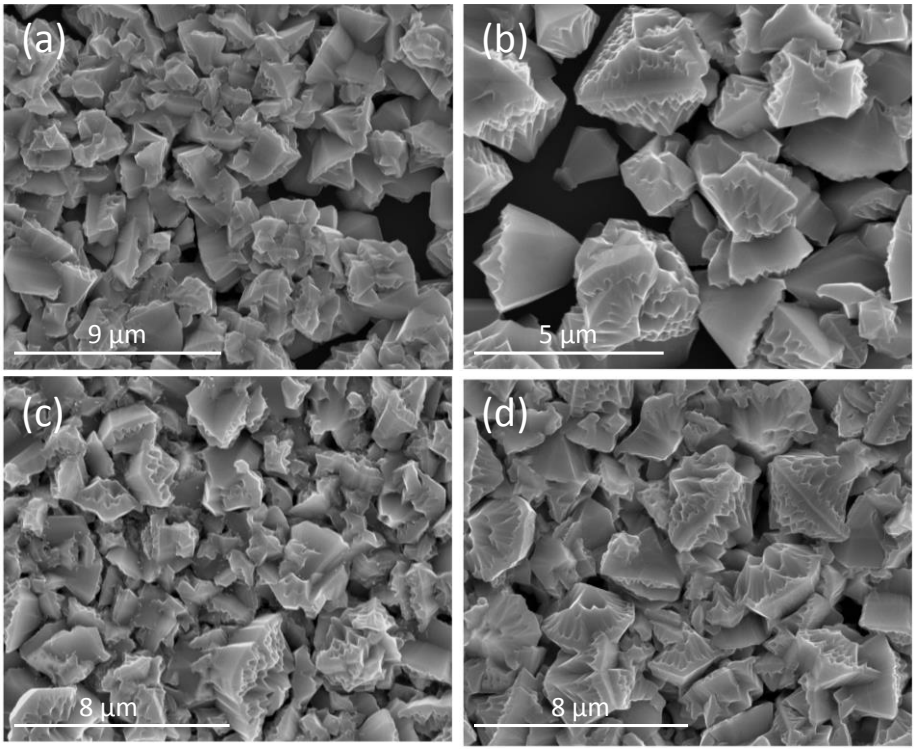

Figure 4.11. SEM images of the porous GaN samples synthesized using $In(acac)_3$ as the In precursor for the deposition of InGaN, placed at (a) 30, (b) 25, (c) 23, and (d) 20 cm from the substrate when the furnace was heated at 1203 K.

The luminescence properties of these samples were analyzed by taking cathodoluminescence measurements. Figure 4.12 shows the CL spectra of the different porous particles recorded at 80 K. In all cases, the NBE peak appears at 3.419 eV, except for the sample in which the In precursor was placed at 20 cm away from the substrate, for which it has been shifted to 3.430 eV. The difference in broadening and peak position of the different samples can be attributed to differences in strain [8]. However, no significant red-shift was observed for any of the samples, indicating that In has not been incorporated in the samples.

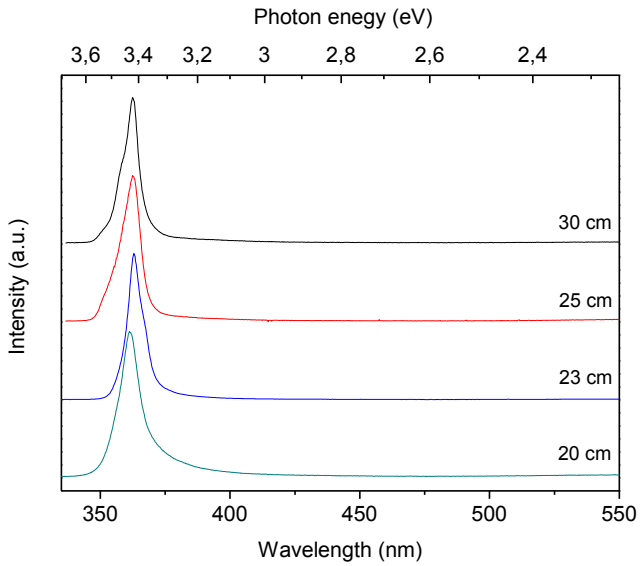

Figure 4.12. CL spectra recorded at 80 K for the porous GaN particles obtained using $In(acac)_3$ as the In precursor located at different distances from the substrate when the furnace was heated at 1203 K.

Another set of experiments was performed by decreasing the furnace temperature at 1173 K.

Figure 4.13 shows the SEM images of the particles obtained at 1173 K placing the In precursor at different distances from the substrate. When the In precursor was placed at 20 cm from the substrate only particles are observed along the substrate with an incipient porosity (see Figure 4.13

(d)). However, for the rest of the samples, particles together with NWs were observed (see Figures 4.12 (a-c)). It seems that the presence of nanowires is favored when the temperature of the furnace drops below 1203 K.

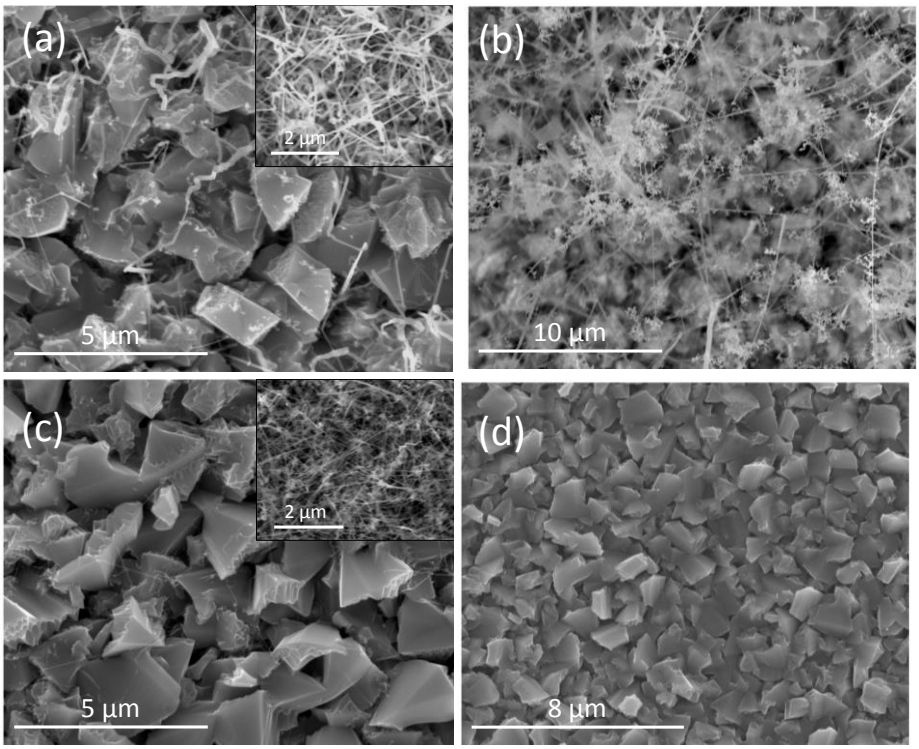

Figure 4.13. SEM images of the porous GaN samples synthesized using $In(acac)_3$ as the In precursor for the deposition of InGaN placed at (a) 30, (b) 25, (c) 23, and (d) 20 cm from the substrate when the furnace was heated at 1173 K.

Figure 4.14 shows the results of the CL measurements for the sample grown at 1173 K when the In precursor was placed at 23 cm from the substrate. When the CL was recorded for the NWs we observed the presence of two broad bands centered at ~3.3 eV and ~3.0 eV that are overlapped. This spectrum is similar to the one observed for the β-Ga_2O_3 reported in ref [9]. However, when the CL was recorded on the particles the typical GaN NBE is observed at ~3.41 eV. This behavior was observed for all the samples grown at 1173 K. Thus, from the CL measurements, we can conclude that there are no evidences of In incorporation into the nanoporous GaN particles,

since the incorporation of In decreases the NBE energy nearly linearly for low mole indium fractions [10], and this NBE red-shift is not observed for any of the samples. However, in contrast to the samples grown at 1203 K, we observe the luminescence corresponding to the β-Ga_2O_3.

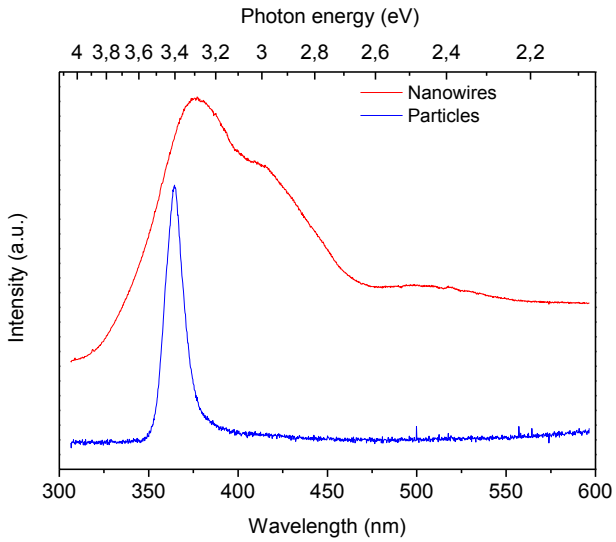

Figure 4.14. CL spectra recorded at 80 K for the porous GaN particles obtained using $In(acac)_3$ as the In precursor located at different distances from the substrate when the furnace was heated at 1173 K.

In order to confirm the presence of β-Ga_2O_3, the samples were characterized by XRD. Indeed, Figure 4.15 shows the X-ray pattern that confirms the presence of the β-Ga_2O_3 phase, together with wurtzite GaN.

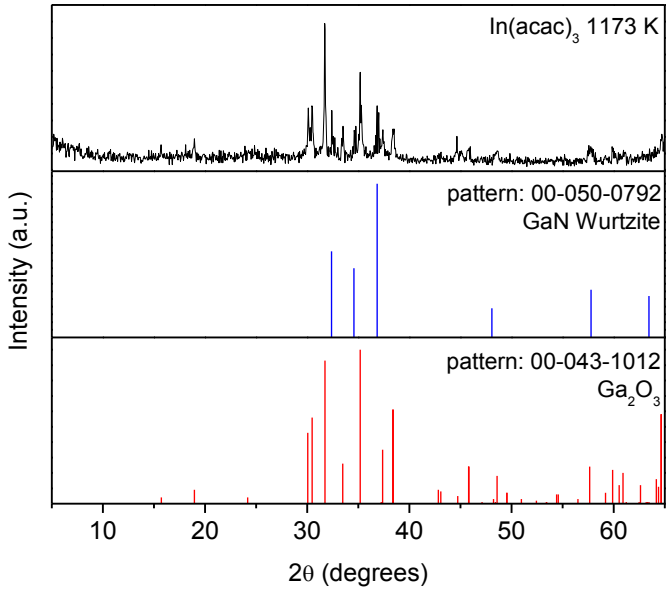

Figure 4.15. X-ray diffraction pattern of the sample grown using $In(acac)_3$ as the In precursor and a deposition temperature of 1203 K. The lines in blue and red correspond to the reference pattern of GaN and Ga_2O_3, respectively.

References

[1] Lieten, R. R.; Motsnyi, V.; Zhang, L.; Cheng, K.; Leys, M.; Degroote, S.; Buchowicz, G.; Dubon, O.; Borghs, G., Mg doping of GaN by molecular beam epitaxy. *J. Phys. D: Appl. Phys.* **2011,** *44* (13), 135406.

[2] Richter, E.; Stoica, T.; Zeimer, U.; Netzel, C.; Weyers, M.; Tränkle, G., Si Doping of GaN in Hydride Vapor-Phase Epitaxy. *J. Electron. Mater.* **2013,** *42* (5), 820-825.

[3] http://www.sigmaaldrich.com/catalog/product/aldrich/345156?lang=es&region=ES (accessed 27/27/2017).

[4] Lee, I. H.; Lee, J. J.; Kung, P.; Sanchez, F. J.; Razeghi, M., Band-gap narrowing and potential fluctuation in Si-doped GaN. *Appl. Phys. Lett.* **1999,** *74*.

[5] Schubert, E. F.; Goepfert, I. D.; Grieshaber, W.; Redwing, J. M., Optical properties of Si-doped GaN. *Appl. Phys. Lett.* **1997,** *71* (7), 921-923.

[6] http://www.factsage.cn/fact/documentation/binary/binary_figs.htm (accessed 24/07/2017).

[7] Vladimir, M. K.; Bernd, J.; Manfred, R.; Uwe, J.; Christian, H.; Frank, G.; Sergio, F.-G.; Oliver, B., Quantitative evaluation of the broadening of x-ray diffraction, Raman, and photoluminescence lines by dislocation-induced strain in heteroepitaxial GaN films. *J. Phys. D: Appl. Phys.* **2015,** *48* (38), 385105.

[8] Ho, C.-H.; Tseng, C.-Y.; Tien, L.-C., Thermoreflectance characterization of β-Ga2O3 thin-film nanostrips. *Opt. Express* **2010,** *18* (16), 16360-16369.

[9] Nakamura, S.; Pearton, S.; Fasol, G., *The Blue Laser Diode. The Complete Story*. 2 ed.; Springer-Verlag Berlin Heidelberg: 2000.

UNIVERSITAT ROVIRA I VIRGILI
POROUS GAN PRODUCED BY CVD: PROGRESS IN DEVELOPMENT AND CHARACTERIZATION
Josué Mena Gómez

5

Influence of the deposition time on the porosity degree, wetting, optical and structural properties of epitaxial porous GaN layers

In this chapter we analyze the porosity degree and porous mean diameter of the unintentionally doped *n*-type porous GaN epitaxial layers grown by CVD on *p*-type non-porous GaN substrates grown at different deposition times, trough an image processing method of the previously taken SEM images, also the porous and walls width was analyze trough AFM.

In this chapter we studied the residual strain of unintentionally doped *n*-type porous GaN epitaxial layers grown by CVD on *p*-type non-porous GaN substrates grown at different deposition times, using photoluminescence, cathodoluminescence, and resonant Raman scattering methods.

We also analyzed how the porous morphology and extension of the porous GaN epitaxial layers affect to the wetting properties of the material by measuring the apparent contact angle of a water droplet resting on the surface.

5.1 Analysis of the porosity of porous GaN produced by CVD

5.1.1 Morphological characterization

Porous GaN epitaxial layers were grown at different deposition times on *p*-type GaN (0001) coated sapphire (0001) substrates (see Figure 5.1) For these experiments, the Ga quantity used was 0.4 g, and the Ga container used was a half cylindrical tube, the rest of parameters were kept constant as discussed in Chapter 2. The morphology of the samples was analyzed here by SEM and AFM.

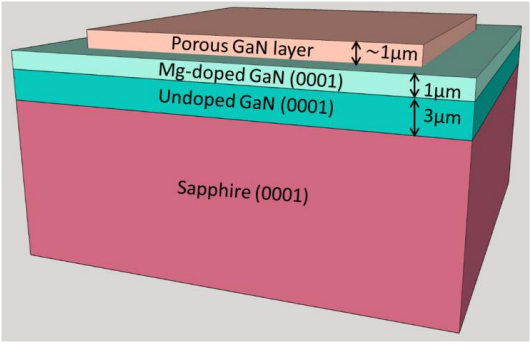

Figure 5.1. Scheme of the composition of the samples studied. The thickness of the porous GaN layer varies with the deposition time.

As it has been discussed previously in Chapter 3, the epitaxial layers are aligned along the [0001] crystallographic direction, thus, in we expect to observe the pores perpendicular to the substrate. Figure 5.2 shows the top view SEM images of the epitaxial porous GaN layers grown for different deposition times. In all cases, we observe a continuous porous layer with the pores aligned perpendicular to the substrate, as expected. The sample grown for 15 min shows a higher degree of porosity, with some small particles deposited along the porous layer as can be seen in Figure 5.2 (a). For a deposition time of 30 min, the diameter of the pores apparently increases, and the porosity degree seems to be quite similar to that of the sample grown for 15 min. It can be seen in Figure 5.2(b) that the circularity of the pores is maintained. For the samples grown for higher deposition times the circularity

of the pores fades away, especially for the sample grown for 45 and 60 min (see Figure 5.2 (c-d)). This is due to the coalescence of the walls between pores, as the thickness of the layer increases [1], producing more elongate pores rather than circular ones. In the sample grown for 45 min can be seen the presence of some particles grown along the porous layer as can be seen in Figure 5.2 (c). However, this is a common effect observed in all the samples, despite are not seen in Figures 5.2 (a), (b) and (d).

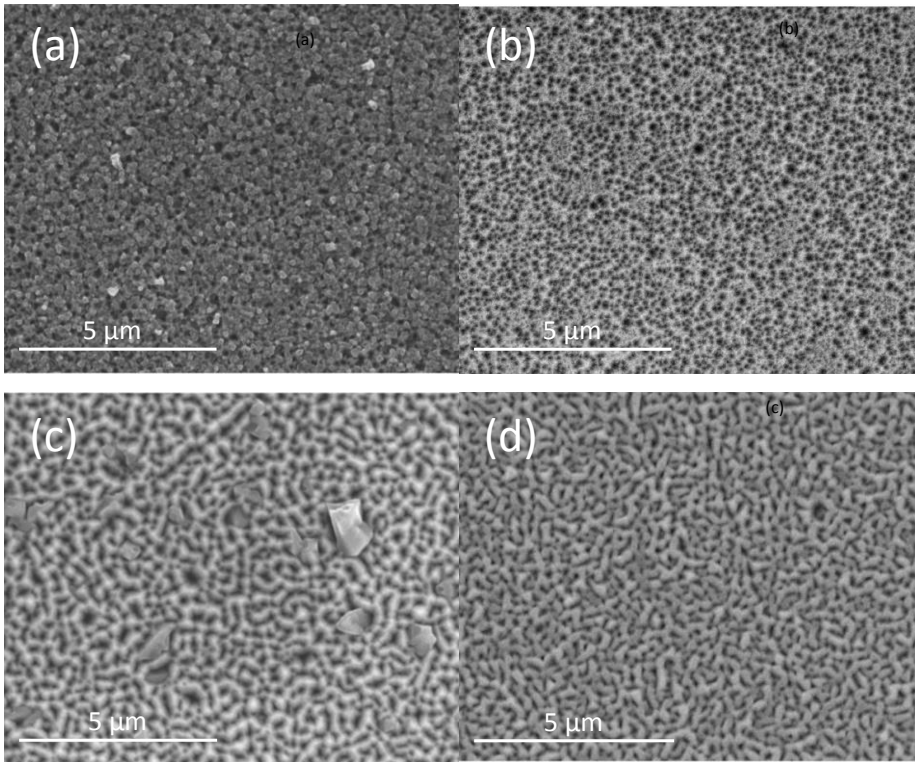

Figure 5.2. Top view SEM images of the porous GaN epitaxial layers grown on *p*-type GaN (0001) substrates grown on sapphire (0001) substrates produced by CVD during (a) 15, (b) 30, (c) 45, and (d) 60 min.

Figure 5.3 shows the 60° tilted SEM images of the epitaxial porous GaN layer grown for different deposition times. An image of the substrate obtained under the same conditions is included for comparison. From these images it can be seen that the surface of the samples is very rough.

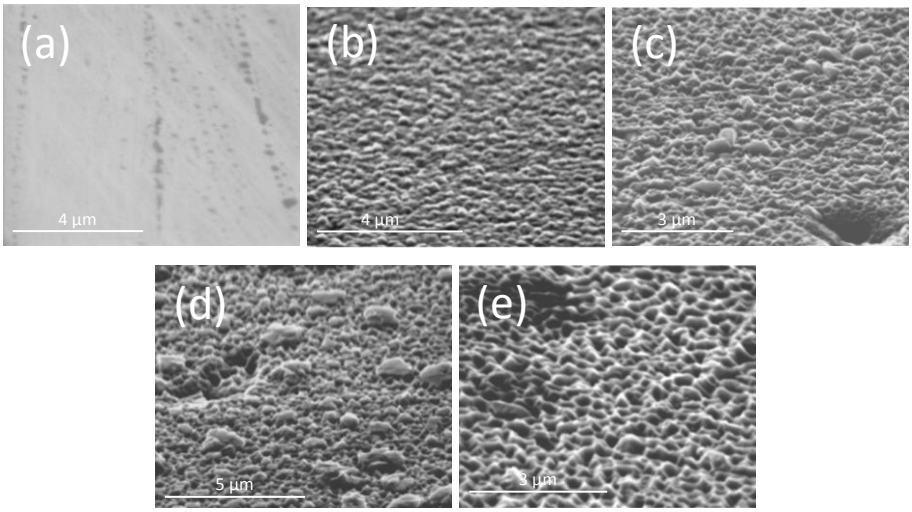

Figure 5.3. Tilted SEM images at 60° of the (a) *p*-type GaN (0001) thin film coated sapphire (0001) substrates and porous GaN epitaxial layers produced by CVD for (b) 15, (c) 30, (d) 45, and (e) 60 min.

To complete the morphological analysis by SEM, a cross-section SEM image of the sample grown for 30 min is shown in Figure 5.4. From the cross-section SEM image we can identify two different layers by different grey intensity. The change of color observed in the image reveals the change of the density of the sample due to the porosity induced on the sample. The grown layer has a thickness of approximately 1.17 µm, and the measured sample roughness is around 200 nm as shown in the image. Despite the change in color due to the different density induced by the porosity, the pores cannot by clearly defined, probably due to the cutting procedure that does not produce a clean cut, thus, preventing a clear observation of the pores.

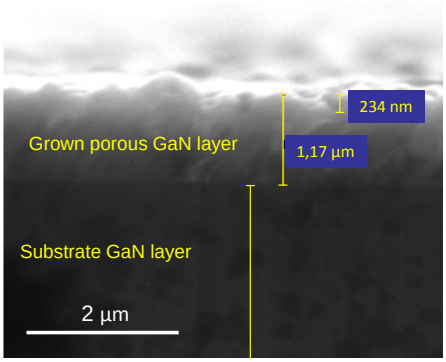

Figure 5.4. Cross-section SEM image of the porous GaN sample grown by CVD for 30 min indicating the thickness and roughness of the porous layer.

5.1.2 Topographical characterization

AFM in tapping mode was also used to characterize more in detail the topography of the porous GaN layers gown for different deposition times (see Figure 5.5). The porosity is also evident in the images, and different pores diameter as well as wall widths between pores were observed for the different deposition times. In the AFM image of the sample grown for 45 min (see Figure 5.5 (d)) it can be seen also the presence of big particles along the substrate, as it was previously observed by SEM (see Figure 5.2 (c)). In Figure 5.5 (a) an AFM image of a substrate is included for comparison.

AFM provides information about the roughness average (R_a) of the sample. The R_a value for the substrate is 0.437 nm, which confirms the flatness of the substrate and the absence of roughness in the substrate before the epitaxial growth proces of the porous GaN layer. Also, this AFM image reveals the presence of steps about 200 nm wide. Despite the AFM tip could not reach the bottom of the pores by steric effects, limiting the determination of an exact value of the pore height, an average roughness valey height was obtained using the *Roughness analysis* tool of the WSxM analysis software [2]. The values of roughness valleys height obtained for the samples grown for 15, 30, 45, and 60 min, are 70 ± 5, 235 ± 40, 260 ± 15, and 210 ± 10 nm respectively. The roughness valleys height obtained by AFM are not far from the observed in the cross-section SEM images.

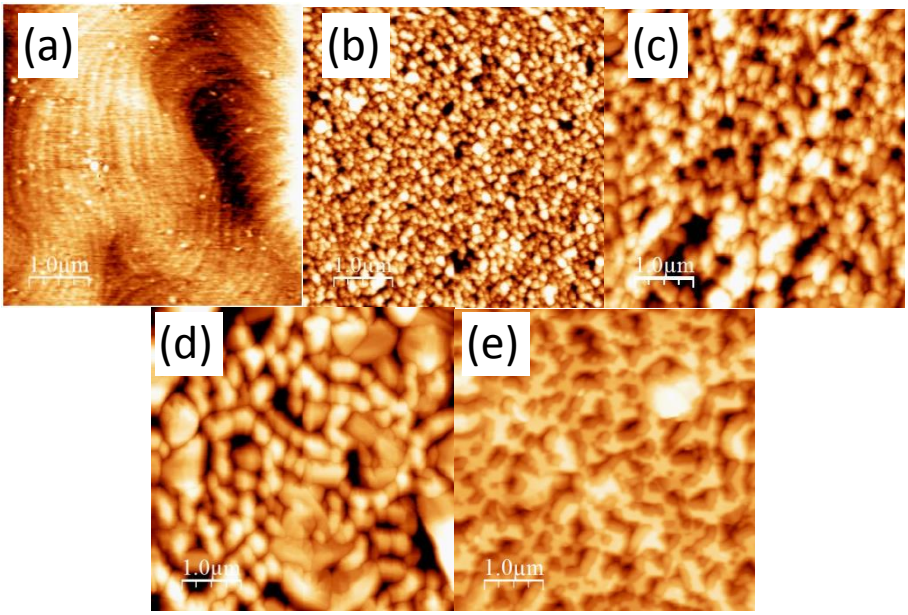

Figure 5.5. AFM images of the (a) *p*-type GaN (0001) thin film coated sapphire (0001) substrates and porous GaN epitaxial layers grown by CVD for (b) 15, (c) 30, (d) 45, and (e) 60 min.

5.1.3 Determination of the porosity characteristics of the samples by an image processing method

For this purpose we used in a first step a non-destructive method based on the analysis of SEM images using the software ImageJ [3] and the analysis of the AFM images with WSxM. From the SEM and AFM images shown in previous sections we determinate the porosity characteristics of the samples, including porosity degree, pores density, diameter of the pores and widths of the walls separating them.

The SEM images were recorded following the pattern shown in Figure 5.6 for a particular sample, in order to have a statistical representative value of the porosity for each sample, taking into account the fluctuations of porosity in the different parts of the sample.

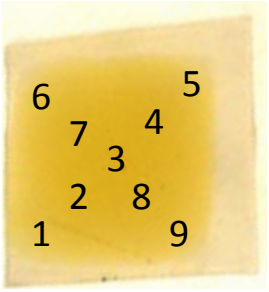

Figure 5.6. Scheme of the pattern followed to take enough statistical SEM images of the porous GaN layers grown by CVD on doped GaN (0001) coated sapphire (0001) substrates.

The SEM images were first converted from a RGB Color image into a 8-bit grayscale image, where the value of 255 is assigned to the white pixels whereas the 0 is assigned to the black pixels, and values in between are given for the scale of grays. The white pixels were associated to GaN, while the black pixels were associated to the pores. Each image was then adjusted using the *threshold* option and the gray colors with values between 0 and 255 that belong to the GaN are selected and converted into 255, whereas the rest are assigned to a value of 0. Finally, the outlines of the pores were defined using the process option *watershed* of the ImageJ software.

For the determination of the porosity degree and the average diameter of the pores of each sample we used the tool *Analyze particles*. When the tool is open it allows us to select the minimum and maximum areas of that program will define as pores. This option is crucial for a good determination of the porosity degree as well as for the determination of the mean pore size, since a bad exclusion of spots that the program recognize as pores will produce a downside value of the mean pore diameter and a higher porosity degree. To have more accurate results, the analysis of the porosity and the mean pore diameter was done separately. The reason for this procedure was that the software allowed excluding or including the pores at the edges. The pores at the edge of the image had to be included when the porosity degree was analyzed. However, when we analyzed the average diameter of the pores, those at the edge of the image had to be excluded, in order to avoid systematic

downward values of the average pore diameter, since the pores at the edge are always a fraction of the entire pore. Figure 5.7 shows the process followed and the images resulting from each step in the analysis process for a particular SEM image.

The *Analyze particles* tool only give us information of the mean porous area. Thus, in order to obtain de porous diameter the pores were assumed to be circles with a diameter (*d*) using the following equation:

$$d = \sqrt{\frac{4A}{\pi}} \qquad \textbf{Eq. 5.1}$$

where *A* is the area of the pore. However, this approximation is far away from ideality, since as the deposition time increases the circularity of the pores fades away. Nonetheless, this approximation provides qualitative information of the tendency followed for the pore sizes as the deposition time increases.

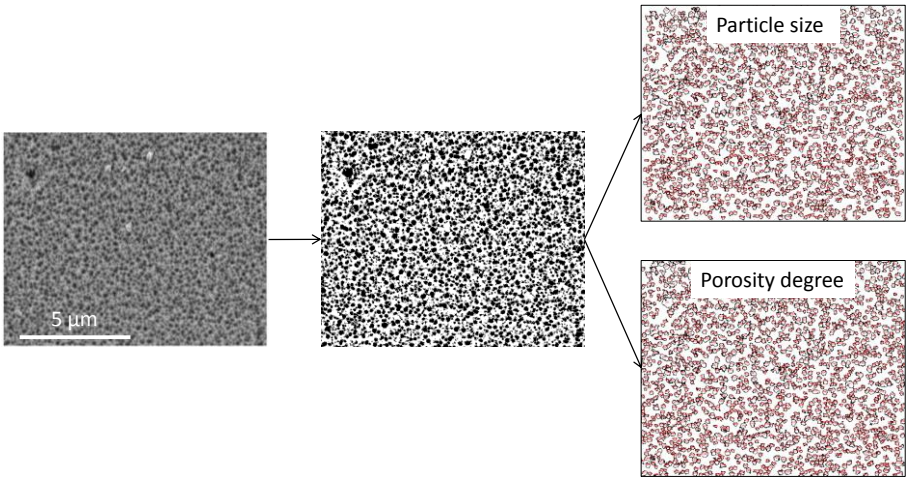

Figure 5.7. Scheme of the flow diagram followed for the determination of the porosity degree and the average pore diameter using SEM images. The first image correspons to a SEM image, followed by the SEM image converted to a 8-bit grayscale image and with the outline of the pores defined with the *watershed* option. The two images at the end correspond to the image with the pores at the edge excluded (top), and the pores at the edge included (bottom).

The mean pore diameters, porous area and pore density values obtained from the image analysis and their standard deviations are listed in Table 5.1.

Table 5.1. Pore mean size diameters, porosity degree and pore density in epitaxial porous GaN samples produced by CVD grown at different deposition times.

Deposition time (min)	**Mean pore diameter** (nm)	**Porous area** (%)	**Pore density** (pores/μm^2)
15	146 ± 3	40 ± 7	19 ± 3
30	181 ± 14	39 ± 4	13 ± 2
45	238 ± 20	41 ± 7	10 ± 1
60	195 ± 34	35 ± 3	10 ± 1

The data obtained reveals an increase of the mean pore diameter up to a deposition times of 45 min, upon which the mean porous size seams to decrease. The decrease on the porous diameter for times higher than 45 min may be due to an increase of the wall width as can be seen in the SEM images in Figure 5.2 (c) and (d). However, as it was discussed in Chapter 3, no further evaporation of Ga to the substrate occurs above a deposition time of ~45 min, since the Ga layer spread along the crucible tends to react with the incoming ammonia forming a GaN layer that stops the reaction. Even though, there is not a precise time for the formation of that GaN layer, and small fluctuations around the mean value (45 min) might be present in every experiment. Also, when the Ga evaporation is stopped, and consequently the GaN growth, the decomposition of GaN and further deposition into the substrate was observed and discussed in Chapter 3, for long times at high temperatures and low pressures. Thus, the variation of the wall widths can come from two sources: a further deposition of GaN onto the substrate, leading to thicker walls between pores or to the decomposition of GaN of the outer layers and redeposition onto the lateral walls.

The values of the porosity degree, however, are quite similar among all the samples. This behaviour can be explained by the increase of the wall thickness between pores with the deposition time, maintaining the porosity degree.

From this analysis another interesting parameter can be obtained, and is the density of pores, which is a concept that summarizes better the observed values of mean pore diameter and porous area in one concept. When the *Analyze particles* tool of the ImageJ software is used, provides a list with the pores enumerated with its corresponding value of area, from here we can extract the number of pores per unit area. The values of pore density are listed also in Table 5.1. The decrease in the pores density observed as the deposition time increases might be the consequence of the maintenance of the porosity degree, together with an increase of the pore diameters and the wall widths between pores.

5.1.4 Determination of the porosity characteristics of the samples by a topological study

Another method to measure the mean porous diameter is through the analysis of the data obtained in the AFM images. The profile of the porous GaN samples obtained from the AFM images give us a measure of the pore diameter and also the wall width between porous (see Figure 5.8). However, the value of R_a does not give us real information of the sample since the tip does not reach the bottom of the pore due to steric effects. For this purpose, we have analyzed the profile at different points in the same sample. Table 5.2 summarizes the values and their standard deviation of the pore diameters and wall widths obtained using the AFM profiles. The values of pore diameters obtained through the AFM profiles are similar to those obtained using the image processing method used with the SEM images, but with a higher standard deviation. Observing the AFM images in Figure 5.5 and the values of the pore diameters and wall widths in Table 5.2 one can observe that the

sample grown for 15 min has the lower value of pore diameters and wall widths among the samples. For higher deposition times the mean value of pore diameters increases reaching its maximum for the sample grown for 30 min, upon which decreases. However, the wall width reaches its maximum for the sample grown for 45 min. Also, the presence of particles deposited on the top the sample can be seen in the AFM image of the sample grown during 45 min, which introduces a high standard deviation in the pore diameter values, compared with the other samples.

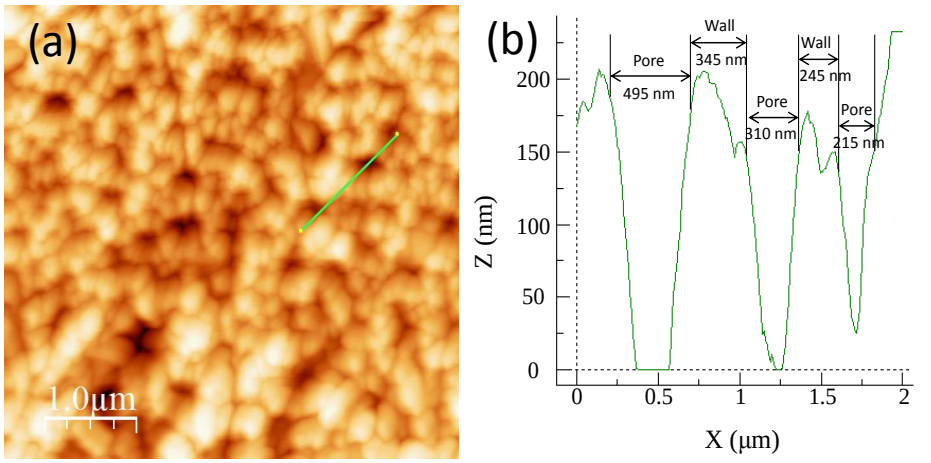

Figure 5.8. (a) AFM image and (b) profile of the porous GaN epitaxial layer grown on *p*-type GaN film coated sapphire (0001) substrates for 30 min showing the criteria used to determine the mean pore sizes and wall width from the AFM images. The profile corresponds to the green line depicted in the AFM image.

Table 5.2 Mean pore sizes and wall widths with their standard deviations for the porous GaN samples grown for different deposition times.

Deposition time (min)	**Mean pore size** (nm)	**Mean wall width** (nm)
15	140 ± 55	115 ± 30
30	250 ± 70	215 ± 65
45	240 ± 110	280 ± 65
60	225 ± 65	245 ± 70

5.2 Analysis of the hydrophobicity of the porous GaN layers

As it has been discussed in Chapter 1, GaN has attracted the attention for sensing applications due to its electronic and optoelectronic properties. However, GaN is an hydrophilic material, with a Young contact angle $\theta_Y<90°$, and this can become a drawback when GaN wants to be used as a biodetector and it is in direct contact with biological samples, which are always aqueous solutions, since the analytes of the samples may be attached to the hydrophilic GaN surface, thus, preventing reproducible results. A simple way to turn a hydrophilic material into a hydrophobic one is by increasing the real surface area of the macroscopic projected area [4]. When the surface of the detector is hydrophobic we have a self-cleaning surface, which is inspired in the so called "lotus effect", and this prevents the surface to be contaminated with impurities of previous analysis [5].

Thus, as indicated before, surface roughness affects the macroscopic wetting properties of the material, transforming a hydrophilic material into a hydrophobic one or into a more hydrophilic one, depending on the wetting of the liquid in the microstructure (see Figure 5.9). When the liquid of a droplet is in full contact with all the material's surface, the apparent contact angle (ACA) of the droplet is described by the Wenzel's model [6]:

$$\cos\theta_W = r\cos\theta_y \qquad \textbf{Eq. 5.2}$$

were θ_W and θ_Y are the apparent and intrinsic contact angles, respectively, and r is the roughness parameter, which is the ratio of the real surface area to the projected flat surface area, and it is invariably always greater than 1. Note that using this equation, hydrophobic materials become more hydrophobic by roughening ($\theta_W < \theta_Y$), while hydrophilic materials become more hydrophilic ($\theta_W > \theta_Y$). This model predicts that the microstructure always amplifies the hydrophilicity of the hydrophilic substrate and thus, it only holds when no air is trapped beneath the droplet and on the material.

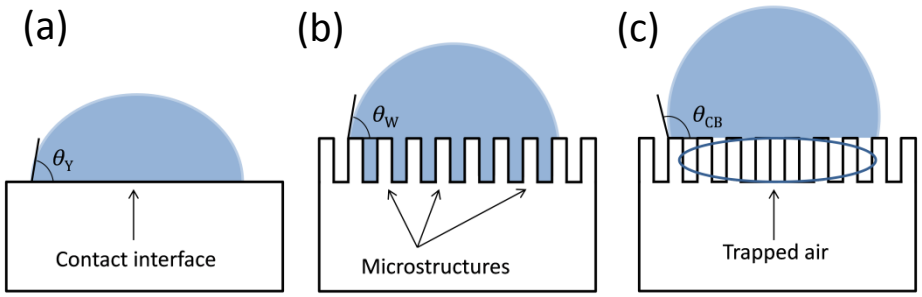

Figure 5.9. Scheme of the contact angle of a droplet in contact with a (a) flat, (b) wetted, and (c) composite surface.

When a hydrophilic material becomes hydrophobic after roughening, it can only be explained trough the formation of a composite interface by the material and trapped air within the microstructure and the liquid, in which the liquid is totally suspended in the air filling the voids. At equilibrium, in this composite material, the ACA is describe by the Cassie and Baxter model [7]:

$$\cos\theta_{CB} = f_1 \cos\theta_1 + f_2 \cos\theta_2 \qquad \textbf{Eq. 5.3}$$

where f_1 and f_2 is the fraction of area of the solid and vapor in contact with the liquid droplet, respectively, the sum of f_1 and f_2 invariable equals 1, and θ_1 and θ_2 are the contact angle between the material and water and air and water, respectively. This equation can be redefined only as a function of f_1 and θ_1, since θ_2 =180° [8]:

$$\cos\theta_{CB} = f_1 \cos\theta_Y + f_1 - 1 \qquad \textbf{Eq. 5.4}$$

The value of θ_2 =180° is derived from the Young-Depuré equation, for measuring contact angles for water deposited upon a layer of air. The resulting Young-Depuré equation for this concrete case is equal to zero [9]:

$$(1 + \cos\theta_2)\gamma = 0 \qquad \textbf{Eq. 5.5}$$

This model is valid when air is trapped between the substrate and the liquid, becoming isolated from the atmosphere. This would mean also, that the pores are not interconnected and are open to the atmosphere. Another point to take into account is that these two models, are only valid when the dimensions of the microstructures are much smaller than the dimensions of the liquid drop [10].

One may expect that the f_1 value in an ideal porous material may be close to the porosity degree of each sample if we assume a flat porous surface, and the liquid only wets the outer part of the surface. However, f_1 will be always greater than the porosity degree, since the liquid partially penetrates the pores in order to satisfy the geometrical limitations.

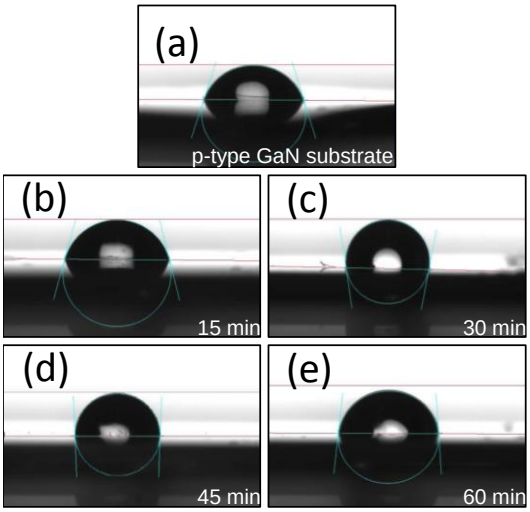

Figure 5.10. Optical images of the static contact angle of water on (a) *p*-type GaN substrate, and porous GaN layers grown for (b) 15 min, (c) 30 min, (d) 45 min, and (e) 60 min.

The images of water sessile droplets on the porous GaN samples grown for different deposition times, as well as a non-porous substrate are shown in Figure 5.10. For obtaining of the ACA, 5 measurements were taken for each sample. The values of the ACA as a function of the deposition time are shown in Figure 5.11. The mean values of the ACA measured for the samples grown for 15, 30, 45 and 60 min and their standard deviations are 75.5 ± 3.8°, 95.5 ± 6.9°, 95.6 ± 9.8°, and 90.8 ± 7.9°, respectively. The measured value of the contact angle for the substrate is 7.1 ± 2.6° which is taken as the θ_Y.

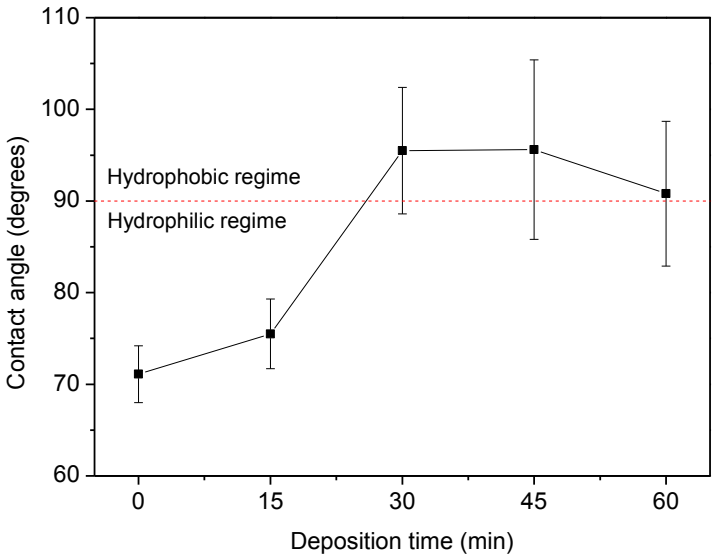

Figure 5.11. Evolution of the ACA with the deposition time.

Using Eq. 5.4 the predicted fraction of surface in contact with the water droplet is 0.94, 0.68, 0.68, and 0.75 for the samples grown for 15, 30, 45, and 60 min respectively. These predicted values for the wetted surface are not in agreement with the measured porosity degree [11] by taking in consideration the Cassie-Baxter model. In fact, if the droplet were completely suspended in a pure Cassie-Baxter state, an ACA of 101° would be obtained for the sample grown for 15 min with a porosity degree of 40%. Thus the results obtained indicate that the water partially penetrates the pores, leading to an intermediate state between the Wenzel state and the Cassie-Baxter state (see Figure 5.12).

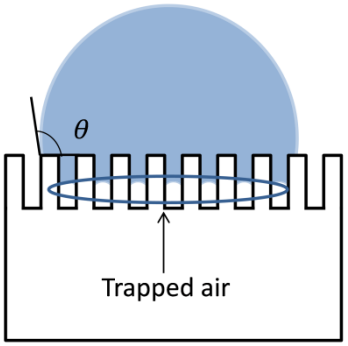

Figure 5.12. Schematic representation of a suspended droplet into a porous structure in an intermediate state between the Wenzel and the Cassie-Baxter state.

The water penetration on an ideal porous structure is explained using the capillary-pressure balance mechanism [12]. This mechanism assumes that when water reaches the pore, the air is compressed rather than expelled. Thus, there is a balance between the capillary force, which governs the penetration of the water into the pore, and the pressure of the trapped air, which acts against the penetration of the water into the pore. Water penetration into the pore (h) depends on geometrical parameters such as the: pore diameter (d) and the pore depth (L), as well as the intrinsic hydrophilic or hydrophilic nature of the material given by the Young contact angle (θ_Y). The mathematical relation between them is shown in Eq. 5.6:

$$h = \frac{4L\gamma \cos\theta_Y}{P_0 d + 4\gamma \cos\theta_Y} \qquad \textbf{Eq. 5.6}$$

where γ and P_0 are the surface tension of water and the atmospheric pressure, respectively.

For samples with similar pore depths, the ratio of the liquid penetrating the pore and the pore depth (h/L) can be used a tendency to predict the wetting state [13]. The obtained values of h/L for our porous the samples grown for 15, 30, 45, and 60 min are 0.69, 0.61, 0.62, and 0.63, respectively. Note that the h/L ratio depends only on the geometrical parameter d, and apparently does not depend on the depth of the pore L. However, L is reported in the literature to play a role in the wetting mechanism [12]. Nevertheless,

the penetration of water into the pore predicted from the geometrical parameters of our samples is in good agreement with the obtained values of the ACA, since a deeper penetration of water into the pores means higher fraction of water in contact with GaN, which would make the value of the ACA to decrease.

In our case, where the surface is also very rough, and has an approximately sinusoidal structure, it can also play a role in the observed ACA, where the position of the triple contact point is also a key factor [4]. Using the model to describe the Cassie-Baxter state in sinusoidal structures proposed by J.-L. Liu (see Fiugre 5.13), when the triple contact point x_0 (the point where the water meets the GaN and the air) is away from the valley of the sinusoidal profile, the ACA becomes bigger, whereas when the liquid penetrates into the structure and is close to the valley, the ACA drops to a minimum value. Thus, a deeper penetration of water into the pore will lead to lower value of x_0 and therefore to lower values of ACA.

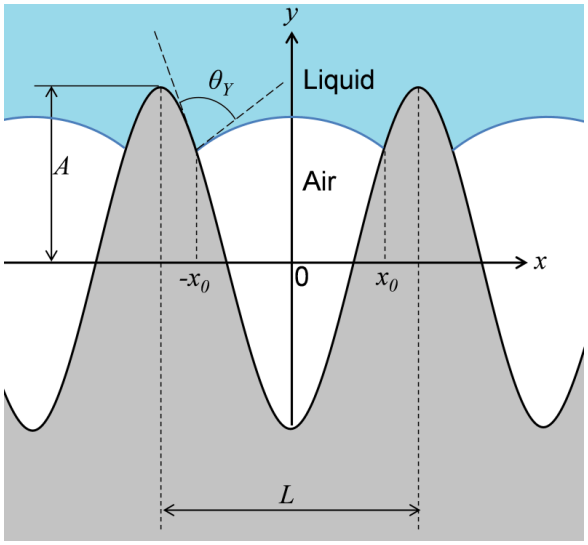

Figure 5.13. Scheme of the wetting mechanism inside the sinusoidal micro-structure.

However, the ratio does not allows us to determine to which wetting model is closer our system, since different pore depths give the same h/L value, while the wetting model might change from a quasi-Wenzel to a quasi-

Cassie-Baxter state [12]. Nonetheless, for similar pore depths, not only the pore size determines the ACA, but also the wall thickness between pores, contributes to drop the value of the ACA as the wall thickness between pores increases [14]. Thus, anytime the pore size and the wall thickness change the value of the ACA will change.

5.3 Analysis of the residual structural strain on porous GaN layers determined by optical means

Generally, GaN structures are grown on foreign substrates, e.g., *c*-oriented sapphire and 6H-SiC [15]. However, the lattice parameters of the substrates used, do not match with the lattice parameters of GaN, and this tends to produce either compressive, if the lattice mismatch is negative, or tensile, if the lattice mismatch is positive, biaxial strain in the heteroepitaxial layers [16]. The values for lattice mismatch of *c*-oriented sapphire and 6H-SiC with GaN are -13% and 4% respectively [17], resulting in a high density of threading dislocations ($\sim 10^{8}$-10^{10} cm^{-2}), micro cracks and other extended defects such as stacking faults, voids, inversion domains, plus a significant amount of point defects [18].

As a consequence of the strain, the band structure, and thus the band gap of the GaN, is modified, being the emission of the NBE red-shifted when the structure is expanded *x*-*y* plane, suffering from tensile strain, or blue-shifted when the structure is contracted in the *x*-*y* plane, thus, suffering from compressive strain [16]. The strain is altered by the presence of extended defects like dislocations, which are produced to accommodate the strain [19]. However, with the increase of the layer thickness the density of dislocations decreases through the dislocation annihilation process [20]. Not only the in-plane biaxial strain plays a role in the resulting strain of the epitaxial layers, but also the hydrostatic strain, which is caused by point defects or impurities. The hydrostatic strain can be compressive or expansive depending on the size of the impurity or point defect involved [16]. When the growth is

homoepitaxial, the main source of strain is due to the presence of point defects [21]. Therefore, the analysis of the strain in a sample is crucial to understand the emission properties of GaN. Also the analysis of the strain, and its origin, which is at the end a measure of the crystal quality it is crucial for its durability in applications in electronics and optoelectronics.

Luminescence techniques such as PL and CL can be used as a way to measure the strain in the GaN layers by means of the energy shift of the near band edge (NBE) emission [16]. As a consequence of the different strain contributions, the band structure, and thus the band gap of GaN is modified, inducing a red-shift of the band-edge luminescence emission for tensile strain and a blue-shift when compressive strain prevails [22]. In this section we analyze the luminescence properties of the porous GaN layers grown for different deposition times, and through this we can obtain information of the strain of the sample.

Figure 5.14 (a) shows the PL spectra of the nanoporous GaN films recorded at 80 K under excitation with the 325 nm line of a He-Cd laser. The probe depth of the 325 nm light in GaN is ~40 nm [23], which is smaller than the thickness of our epitaxial films [1]. However, due to the porosity of the samples, light might also reach the substrate through the pores, and thus the PL spectra could also contain a contribution from the substrate.

The PL spectra show the NBE emission at around 3.45 eV (360 nm), a donor-acceptor pair (DAP) transition band at 3.28 eV (378 nm) and the DAP-LO phonon replicas separated by the LO phonon energy ~90 meV. The first and the second DAP-LO phonon replicas are seen in the spectra shown in Figure 5.14 (a). Also, in some cases the typical yellow luminescence (YL) band arising from the *n*-type GaN can be observed; this band is mainly associated with Ga vacancies (V_{Ga}) and related complexes [24]. Their presence in the spectra seems to be influenced by the excitation conditions used, especially the penetration depth of the excitation beam, which is particularly difficult to define in porous materials. Thus, their absence in the spectra of some of the samples cannot be considered a probe of the quality of

the material, and for that, we did not consider this YL band in our analysis. The NBE emission band in *n*-type GaN is the emission due to neutral donor bound exciton and free exciton transitions, D^0X and FX_A, respectively [25]. At the measurement temperature of 80 K, FX_A is more intense than D^0X, since D^0X is thermally quenched due to the ionization of the neutral donor [26]. Thus, we can assume that the peak labelled as the NBE emission is mainly contributed by the FX_A transition.

The intensity of the NBE band increases with respect to the DAP emission intensity for increasing deposition time. The DAP emission arises from the *p*-type non-porous GaN substrate doped with Mg. The NBE emission, instead, should arise from the unintentionally doped *n*-type nanoporous GaN layer, since the *p*-type substrate does not present the NBE emission, as can be seen in the spectrum obtained for the bare substrate, also included in Figure 5.14 (a). In fact, the NBE band in Mg-doped GaN is usually quenched [27]. As the thickness of the nanoporous layer increases with the deposition time [1] one observes the NBE band to be enhanced, while the DAP emission and its phonon replicas are simultaneously quenched due to the reduced contribution of the substrate in thicker porous layers. However, it is difficult to analyse how the intensity of the NBE band is affected by the structural factors. From one side the porosity present in our samples makes difficult to determine exactly the probed volumes in the sample. From another side, the deposition temperatures used might allow Mg acceptors diffuse during growth towards the growing porous layers [28] [29] creating a transition layer at the interface. Despite in previous studies of deposition of Mg-doped porous GaN layers on already porous undoped GaN samples [18] we did not observe such dopant diffusion, we cannot rule out this hypothesis.

The peak energy of the NBE band as a function of the deposition time is plotted in Figure 5.14 (b). As the deposition time increases, the NBE band shifts towards the high energy side, from 3.432 eV (361 nm) for a deposition time of 15 min, to 3.467 eV (357 nm) for a deposition time of 60 min. As previously discussed, the energy gap of a semiconductor is affected by the

residual strain [16]. When GaN is under tensile strain, the NBE emission is shifted towards lower energies, while compressive strain leads to a blue-shift of the NBE. Compared to the position of the NBE emission in a strain free ideal GaN sample, which the FX_A emission at 80 K peaks at 3.47 eV [30], one can argue that our samples are under tensile strain. However, when the thickness of the nanoporous layer is increased, the NBE peak energy approaches the strain free value accounting for strain relaxation for the samples grown for long deposition times. One could consider that the blue shift observed with increasing layer thickness might be associated with the presence of free carriers in the top part of the thick nanoporous layers, due to the Burstein-Moss effect [31]. However, this effect must be negligible here, since we have shown previously that the carrier concentration of an unintentionally doped *n*-type nanoporous GaN grown by CVD was $\sim 10^{16}$ cm^{-3} [1]. At this concentration the Burstein-Moss shift is almost negligible. Thus, these results indicate a reduction in the structural strain in the samples as the deposition time increases.

The shape of the observed DAP related peaks changes between the different samples. The lineshape of this band depends on the concentration of Mg, as a consequence of the complexity of the Mg acceptor configuration in the GaN lattice [32], and the difficulty to set up the conditions for the optimum Mg doping. Recently, different DAP transitions associated with three different Mg-related acceptor levels have been reported [33]. Thus, the shape of the DAP band depends on the relative intensity of these three DAP transitions and it can substantially differ from the shape of a standard DAP peak with its corresponding phonon replicas. This band can even appear energetically shifted depending on the Mg concentration and the dominant DAP transition. Additionally, long-range potential fluctuations have been reported in Mg-doped GaN, which can also contribute to change the shape of the DAP band [32, 34]. This can explain the differences of the DAP band for the different samples studied. The differences in the DAP band shape observed between ours porous GaN layers and the p-type substrate seems to

suggest the incorporation of Mg acceptors in the lower part of the porous layer that would diffuse from the substrate as a consequence of the deposition temperature used as pointed out before [28-29].

The shape of this band greatly depends on the amount of Mg incorporated. The DAP band and its phonon replicas present a complex structure. The lineshape depends on the concentration of Mg, as a consequence of the complexity of the Mg acceptor configuration in the GaN lattice [32], and the difficulty to set up the conditions for the optimum Mg doping. Recently, different DAP transitions associated with three Mg-related acceptor levels have been reported [33]. The shape of the DAP band depends on the relative intensity of these three DAP transitions and it can substantially differ from a standard DAP peak with its corresponding phonon replicas. This band can appear even energetically shifted depending on the Mg concentration and the dominant DAP transition. Additionally, long-range potential fluctuations have been reported in Mg-doped GaN, which can also contribute to change the shape of the DAP band [32, 34]. This can explain the differences of the DAP band for the different samples studied. The NBE band in Mg doped GaN is usually quenched; see the PL spectrum of the reference p-type sample in Figure 5.14 (a).

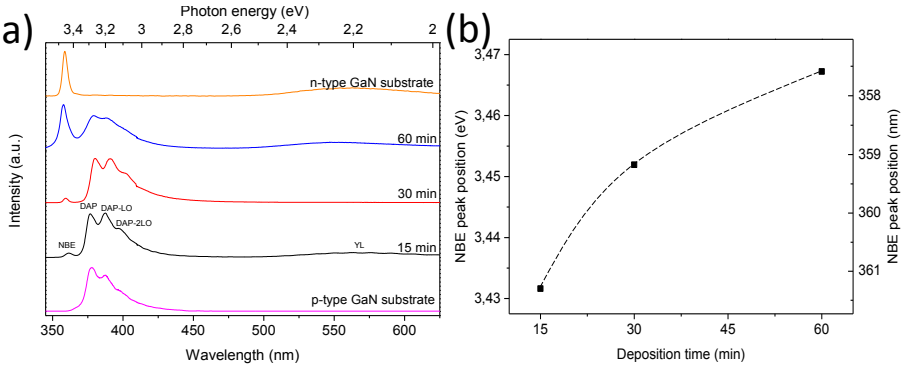

Figure 5.14. (a) PL spectra recorded at 80 K for porous GaN samples grown at 15, 30 and 60 min. The spectrum of the non-porous *p*-type substrate on which the porous layer are grown is also included. (b) Evolution of the position of the NBE band against the deposition time.

Figure 5.15(a) shows the PL spectra recorded at room temperature. The characteristic red-shift of the position of the NBE band due to the increase of the temperature at which the spectra are collected is attributed to a reduction of the band gap energy due to the lattice expansion of the GaN and to the electron-phonon interactions [26]. Despite the broadening and red-shift of the NBE band, its behaviour with the deposition time is consistent with the conclusions extracted from the parameters of the PL spectra recorded at 80 K. In that case, only the NBE emission is shown since the DAP emission quenches at room temperature due to the ionization of acceptors and donors [26].

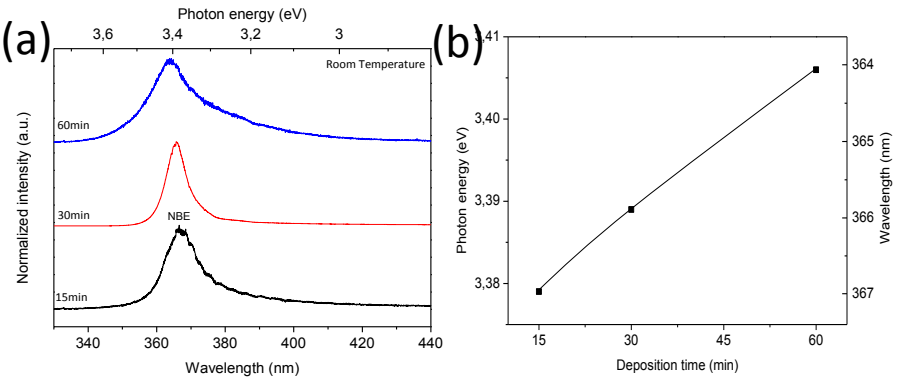

Figure 5.15. (a) PL spectra recorded at RT (300 K) for porous GaN samples grown at 15, 30 and 60 min and (b) the evolution of the position of the NBE band against the deposition time.

Panchromatic CL (pan-CL) images the nanoporous GaN samples were recorded. Figure 5.16 shows a superposition of the SEM image and the corresponding pan-CL image of the sample grown at 30 min. recorded for the same area, in which we changed the degree of transparency of the pan-CL image from 100% transparent to fully opaque to show the correspondence between the pores and the brightest light emission spots. For a better clarity in this sequence, we inverted the contrast of the pan-CL image, i.e., the darkest parts correspond to the regions in which the emission of light is more intense, while the bright parts correspond to regions where the emission of light is poor. In order to guide the reader allowing an easier visualization of the

correspondence between the pores and the bright emission spots, some of them have been marked with arrows. By comparing Figure 5.16 (a), corresponding to the SEM image, to Figure 5.16 (f), corresponding to the pan-CL image, one can appreciate circularly shaped forms corresponding to the pores. This would mean that the more intense light emission arises from the pores; one can argue that more light can escape the material due to multiple reflections of light on the lateral walls of the pores, accounting for a better light extraction in the presence of pores. In the intermediate sequence of images between Figures 5.17 (a) and (f), one can see that while the shape of a particular pore is blurred as the % of opacity of the pan-CL image increases, it is replaced by a dark spot, associated with the bright emission of light arising from this spot.

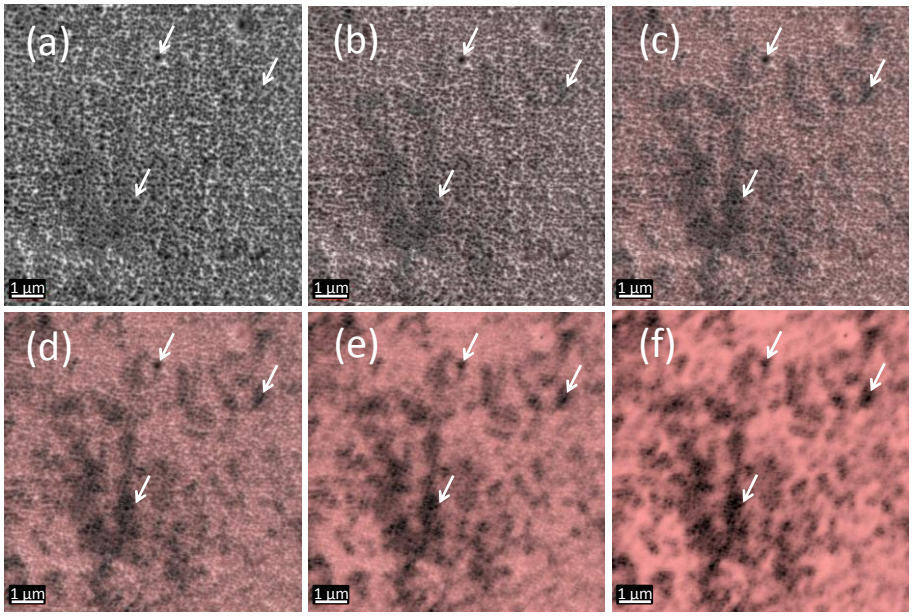

Figure 5.16. Superposition of SEM and pan-CL images in a sequence going from (a) pure SEM image and adding (b) 20%, (c) 40%, (d) 60%, (e) 80% and (f) 100% of the inverted pan-CL image, where black pixels represent the bright emission light spots of the sample.

The analysis of the CL spectra of the nanoporous GaN samples also confirms the shift of the NBE peak position towards the low energies for decreasing deposition time, corroborating the previous observations done by

PL (see Figure 5.17 (a)). This tendency was observed for 5 kV acceleration voltage, for which the CL probe depth in GaN is ~100 nm, probing the top porous layer. For increasing acceleration voltages, e.g. 10kV, the probe depth is estimated at ~370 nm. Note that those depths are calculated for bulk GaN; therefore, they must be handled with care when translated to porous layers. The peak energies were 3.398 eV (365 nm), 3.413 eV (363 nm) and 3.435 eV (361 nm) for 15, 30 and 60 min of deposition times, respectively. The differences with the PL energies can be related to the different generation volume in both experiments, and/or to a slight heating by the e-beam; nevertheless, the energy difference shifts between the different samples is preserved for both measurements.

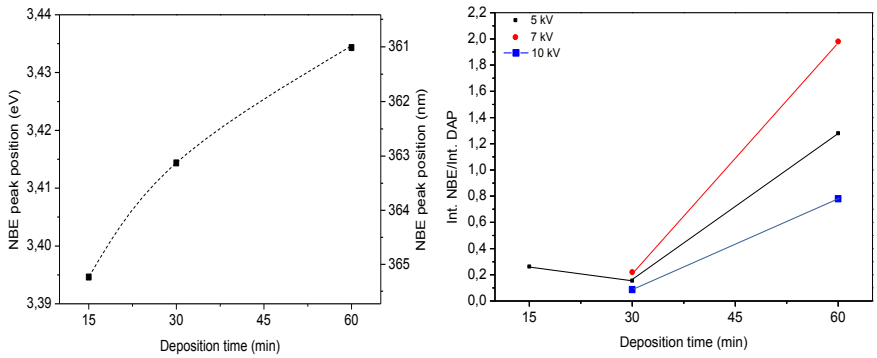

Figure 5.17. (a) Evolution of the NBE peak position with the deposition time, recorded for an acceleration voltage of 5 kV. (b) Evolution of the intensity ratio between the NBE and DAP emissions with the deposition time at three different acceleration voltages: 5, 7 and 10 kV.

The CL signal arises from the excited generation volume, which depends on the e-beam energy [35]. The higher the acceleration voltage of the electron beam used, the higher the penetration depth in the material, as the Grün approximation predicts [36]. Based on this, we tried to carry out a qualitative analysis of the nanoporous GaN layer density by CL. This was done by means of the relative intensity of the NBE peak with respect to that of the DAP peak. As discussed above the NBE peak arises from the unintentionally doped *n*-type nanoporous GaN layer, while the DAP peak and

its LO phonon replicas arise from the *p*-type substrate. In fact, Mg doped GaN (*p*-type) typically exhibits the DAP band with the phonon replicas, and a very weak, almost unappreciable NBE emission. The DAP band structure is determined by the Mg concentration and its electrical activation [27]. According to this, we would expect a decrease of the NBE/DAP intensity ratio as we increase the acceleration voltage, because the emission should mainly arise from the *p*-type substrate for high e-beam energies. Figure 5.17 (b) plots the NBE/DAP intensity ratio at different acceleration voltages for the different samples analysed. The NBE/DAP intensity ratio increases from 5 kV to 7 kV electron beam voltages; subsequently it decreases for 10 kV. This behaviour appears more obvious for the thicker porous layers corresponding to 60 min. deposition time. This behaviour evidences a complex electron beam penetration across the nanoporous layer, because of the non-homogeneous effective density of the porous layer.

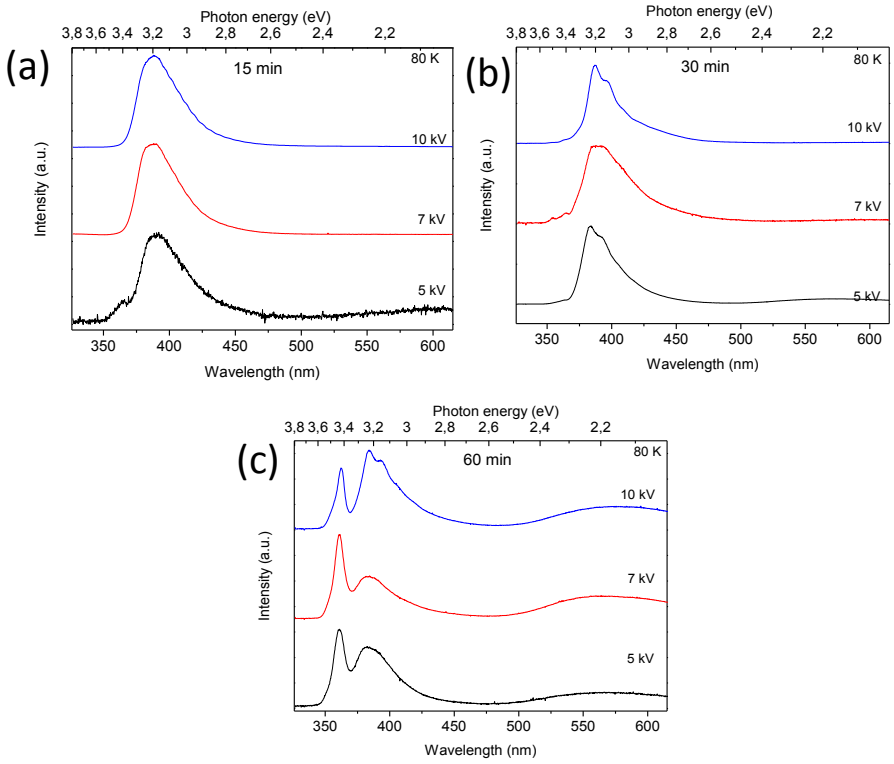

Figure 5.18. CL spectra recorded at three different acceleration voltages for the samples grown for (a) 15, (b) 30, and (c) 60 min.

Nevertheless, the CL data obtained at different acceleration voltages can provide an idea of the relative density of the nanoporous samples if one compares the results obtained in the different samples. In previous works [1], an approximate value of the thickness of the nanoporous layer was measured using cross section SEM images, obtaining values of 0.5, 1 and 1.7 μm for samples grown during 15, 30 and 60 min, respectively. Using the Grün equation [36], we obtain values of the electron beam penetration for bulk GaN of 110, 200 and 370 nm for acceleration voltages of 5, 7 and 10 kV, respectively. Figure 5.18 (a) plots the CL spectra of the sample grown during 15 min at different acceleration voltages. It can be seen the presence of the NBE peak only for the lowest acceleration voltage. For the sample grown during 30 min, the NBE peak can be observed for the three acceleration voltages used, but with low intensity, as can be seen in Figure 5.18 (b). Only for the sample grown at 60 min (see Figure 5.18 (c)) the NBE peak could be observed for all the accelerating voltages analysed with a high intensity, but its relative intensity with respect to the DAP band decreases for increasing electron energy. This shows that the upper part of the porous layer of this sample is free of acceptors. The presence of the DAP band even for the lowest electron energy (5keV) is the consequence of the porosity of the layer, which results in an effective density lower than that of the bulk material. Therefore, the probe depth is substantially higher than the thickness of the porous layer. Note that the nominal thickness of this porous layer is 1.7 μm: taking into account that the Grün electron range in bulk GaN is 370 nm for 10 keV, and that the bare p-type substrate emission is observed for 10 keV excitation, one can assume that the effective density of these nanoporous GaN layers is substantially reduced with respect to the bulk density by a factor around 5.

5.4 Analysis of the residual strain on porous GaN layers determined by resonant Raman scattering (RRS).

The results of the resonant Raman scattering under excitation with 325 nm (3.815 eV), above the band gap of GaN, are shown in Figure 5.19 (a) once the background luminescence emission has been subtracted. A strong first order A_1(LO) peak and a second order $2A_1$(LO) peak with lower intensity can be easily identified in the spectra recorded for the samples grown at different deposition times. The E_2(high) mode can be observed also with a very low intensity, since the non-polar phonons are not resonantly enhanced [37], and the scattering volume for UV in the porous layers is very small.

First, we studied the E_2(high) peak. The peak frequencies of 570, 572, and 574 cm^{-1} were obtained for the samples grown during 15, 30 and 60 min, respectively. These values are always above the frequency reported for the strain-free GaN (568 cm^{-1}) [38]. Thus, this would indicate a contradiction with the data obtained by PL and CL. However, as it can be seen in Figure 5.19 (a), the E_2(high) peak appears as a broad and not well defined peak overlapped by the low frequency broad spectral features associated with the A_1(LO) phonon band, especially for the samples deposited at shorter times, which makes difficult to reliably determine the peak frequency, and therefore, the structural strain. Note that the strain shift of the Raman bands is small, compared with the incertitude of the measurement.

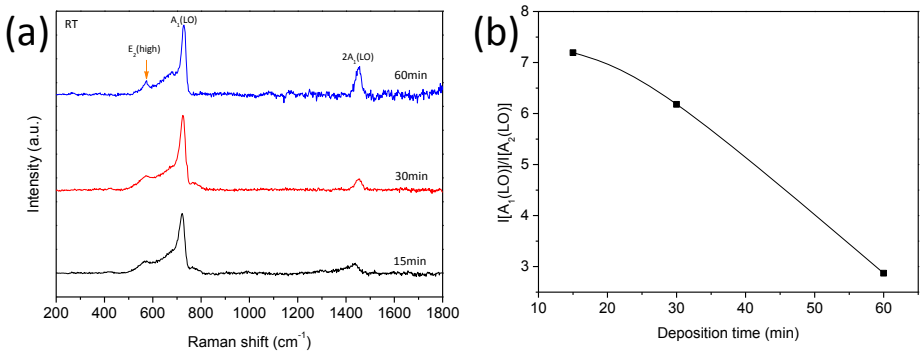

Figure 5.19. (a) Resonant Raman scattering spectra of porous GaN samples grown at 15, 30 and 60 min excited with a 325 nm laser. (b) Intensity ratio of the $A_1(LO)/2A_1(LO)$ peaks vs deposition time for porous GaN samples.

We focus the study in the much better defined polar $A_1(LO)$ phonon. Peak frequencies of 717, 721.3 and 724 cm^{-1} were obtained for the samples grown during 15, 30 and 60 min, respectively. All of them are below the frequency reported for strain-free GaN, which $A_1(LO)$ peak appears at 734 cm^{-1} [39]. However, the $A_1(LO)$ band under resonant conditions is redshifted because of the Martin's double resonance [40]; in fact, the $A_1(LO)$ band in the substrate reference under resonant excitation is observed at 729 cm^{-1}. The Raman shift of the nanoporous samples with respect to the reference cannot be accounted for by strain, because the experimental shift observed would lead to unreasonable strain values [39]. It should be noted that the double Martin's resonance is mediated by charged defects or impurity centres. Furthermore, broad spectral features are observed at both sides of the $A_1(LO)$ band (~660 cm^{-1} and 760 cm^{-1}), with decreasing intensity from 15 to 60 min deposition times; these broad bands can be associated with defect-activated modes. The FWHM of the $A_1(LO)$ band evolves from 21.5 cm^{-1} for the 15 min deposition sample to 16.7 cm^{-1} for the 60 min deposition sample, which roughly matches the FWHM of the reference substrate. All these data points to a significant improvement of the crystal order in the porous layers for increasing time deposition. Finally, Figure 5.19 (b) represents the $A_1(LO)/2A_1(LO)$ intensity ratio vs. deposition time. This intensity ratio

decreases as the deposition time increases, indicating the improvement of the crystalline and structural quality of the sample obtained at longer deposition times. This tendency is supported by the evolution of the FWHM of the A_1(LO) peak, indicating that effectively, the concentration of defects is substantially reduced when the deposition time is increased. The presence of those defects would be responsible for the strain deduced from the luminescence measurements in the initial growth stages of the nanoporous layers. The nature of the strain is tensile, which suggests the presence of vacancy complexes.

5.5 Structural characterization of the porous GaN layers by X-ray diffraction

XRD rocking cuves (RC) is a powerful characterization technique that allows obtaining information about crystal structure, such as cell parameters, presence of compressive or tensile strain, and distortions in the crystal. Figure 5.20 shows the X-ray powder diffraction pattern for a porous homoepitaxial GaN layer grown for 30 min using the Brag-Brentano geometry. Two RC analysis were done, one with the (0001) plane parallel to the floor (χ=0°) and another one with the $(10\bar{1}2)$ plane parallel to the floor (χ=43.19°) in order to quantify the screw and edge dislocations, respectively. Figure 5.20, recorded for χ=0°, shows the XRD pattern with the peaks corresponding to the (0002) and (0004) peaks of the GaN layer, and the (0006) peak corresponding to the underlying sapphire substrate. The fact that the peak corresponding to the underlying sapphire substrate is appearing constitutes a drawback if we want to do a more accurate analysis to obtain information about the screw and edge dislocation densities existing in the material, as well as a RC analysis, since the peaks appearing will not be only due to the porous layer but also from the underlying GaN layers of the substrate. However, this pattern reveals the homoepitaxial growth of the porous layer since only the peaks corresponding to the (000*l*) planes are observed.

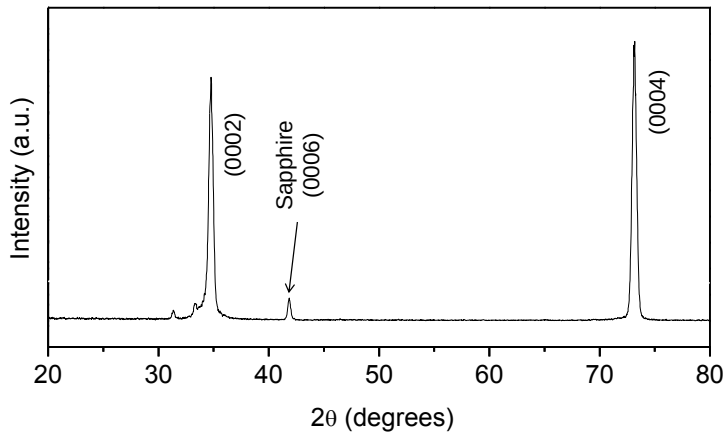

Figure 5.20. XRD of porous GaN grown for 30 min on GaN/sapphire substrate.

The RC of the $(10\bar{1}2)$ and (0004) diffraction peaks for the porous GaN layers grown for 15, 30, and 60 min, and the *p*-type GaN substrate, were recorded and are show in Figure 5.21. From the obtained RC we can observe that the obtained FWHM of the peak corresponding to the substrate used in all the samples grown for different deposition times varies from sample to sample, despite being from the same wafer. For that reason, we recorded the RC of a wafer of *p*-type GaN at different places, in order to see if the difference in the FWHM of the diffraction peaks arises from porous GaN layer and the *p*-type GaN substrate are significant or not. The determination of a precise value of the FWHM is determinant for the calculation of the dislocation densities [41]. The relation between the FWHM is given by Eq.5.7:

$$D = \frac{\beta^2}{4.36b^2} \qquad \textbf{Eq. 5.7}$$

where D is the dislocation density, β is the FWHM, and b is the Burgers vector module. The resulting RCs reveal dispersion in the values of FWHM and peak position between the RCs recorded for the same substrate as can be seen in Figure 5.21 (d).

This could be attributed to the fact that the incoming X-rays used are well focalized in the equatorial plane, being quasi-parallels with only 0.4° of divergence thanks to the use of the Goebel mirror, but they have higher divergence in the axial plane. This later point, does not affect the results obtained when χ=0°, but it does when χ has bigger values. Also, another common systematic error that may come from a non-perfect flat positioning of the sample, which affects mainly to the peak position from sample to sample. From another side, the penetration of the incident X-ray beam into the sample might have influence in not resolving only the porous layer in the RC analysis, but having a mixture of the signal coming from the signal arising from the porous layer and the substrate.

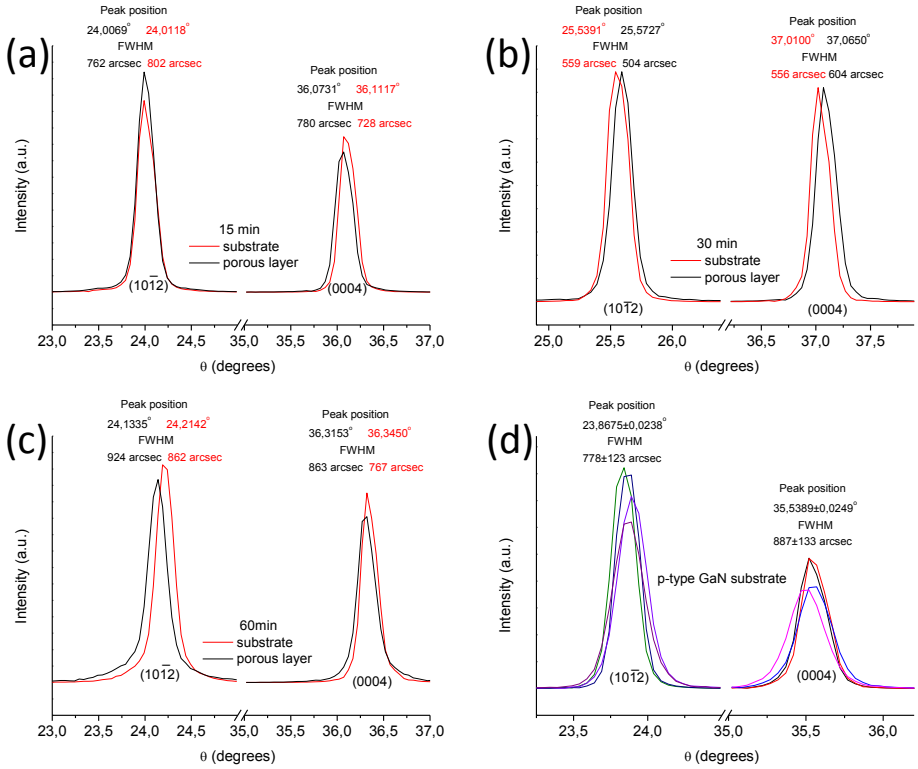

Figure 5.21. RC of the porous GaN samples grown at (a) 15 min, (b) 30 min, and (c) 60 min and (d) the *p*-type GaN substrate used for the deposition of the porous GaN layers.

This last point is corroborated by Figure 5.22 that shows the penetration depth of the X-ray incident beam in GaN as a function of 2θ The penetration depth of the X-rays in the Bragg-Brentano geometry depends on the X-ray wavelength (the lower the wavelength the deeper the penetration of the X-ray beam), the angle of incidence (θ) (the higher the angle of incidence the deeper the X-ray penetration), the density of the material (the lower the density the deeper the penetration of the X-ray beam), and the atomic composition (the lighter the atoms the deeper the penetration of the X-ray beam). The AbsorbDX software allows calculating the penetration depth of the incident beam as a function of the angle of incidence for a given material, a given X-ray wavelength and a given atomic composition. The parameters used were the X-ray wavelength: 1.5406 Å, the atomic composition: GaN, and the density of the material: 6.086 g/cm^3 (taken from the ICDD 01-073-7289). As can be seen in the figure, for the 2θ angles we used to record the RCs, the penetration depth of the X-ray beam is around 11-14 μm. Also, if we take into account that the density of a porous GaN layer is lower than bulk GaN, this would make the X-ray beam even more penetrable. Thus, these deep penetration values for the X-ray beams indicate that a reliable rocking curve analysis cannot be done in our case, since the porous layer thickness ranges from 0.5 - 2 μm and beneath there are two layers of GaN, one 1 μm thick of Mg-doped GaN and other 3 μm thick of undoped GaN grown of sapphire. Thus, the diffraction peaks we can observe would always be a sum of the information given by the three GaN layers, avoiding obtaining a reliable quantification of the screw and edge dislocations densities of the porous layers through the FWHM analysis of the (0002) and $(10\bar{1}2)$ rocking curves, respectively.

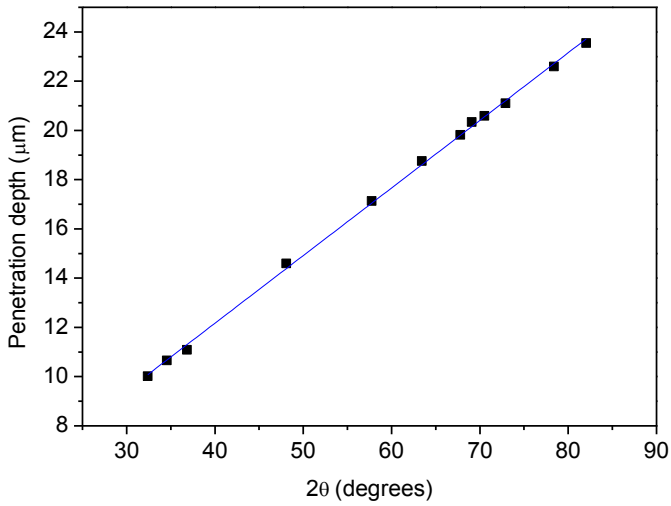

Figure 5.22. Calculated penetration depth of the X-ray incident bean in GaN as a function of 2θ.

Thus, due to the mentioned limitations of our system to measure the RC, we could not relay on these measurements to extract value information about the crystal structure of the porous layers, and we had to use the optical means presented in the previous sections.

References

[1] Bilousov, O. V.; Carvajal, J. J.; Mena, J.; Martínez, O.; Jiménez, J.; Geaney, H.; Díaz, F.; Aguiló, M.; O'Dwyer, C., Epitaxial growth of (0001) oriented porous GaN layers by chemical vapour deposition. *CrystEngComm* **2014,** *16* (44), 10255-10261.

[2] Horcas, I.; Fernández, R.; Gómez-Rodríguez, J. M.; Colchero, J.; Gómez-Herrero, J.; Baro, A. M., WSXM: A software for scanning probe microscopy and a tool for nanotechnology. *Rev. Sci. Instrum.* **2007,** *78* (1), 013705.

[3] Schneider, C. A.; Rasband, W. S.; Eliceiri, K. W., NIH Image to ImageJ: 25 years of image analysis. *Nat Meth* **2012,** *9* (7), 671-675.

[4] Jian-Lin, L.; Xi-Qiao, F.; Gangfeng, W.; Shou-Wen, Y., Mechanisms of superhydrophobicity on hydrophilic substrates. *J. Phys.: Condens. Matter* **2007,** *19* (35), 356002.

[5] Samiei, E.; Luka, G. S.; Najjaran, H.; Hoorfar, M., Integration of biosensors into digital microfluidics: Impact of hydrophilic surface of biosensors on droplet manipulation. *Biosens. Bioelectron.* **2016,** *81*, 480-486.

[6] Wenzel, R. N., Resistance of Solid Surfaces to Wetting by Water. *Ind. Eng. Chem.* **1936,** *28* (8), 988-994.

[7] Cassie, A. B. D.; Baxter, S., Wettability of porous surfaces. *Trans. Faraday Society* **1944,** *40* (0), 546-551.

[8] Miwa, M.; Nakajima, A.; Fujishima, A.; Hashimoto, K.; Watanabe, T., Effects of the Surface Roughness on Sliding Angles of Water Droplets on Superhydrophobic Surfaces. *Langmuir* **2000,** *16* (13), 5754-5760.

[9] Oss, C. J. v., *Interfacial Forces in Aqueous Media*. Second ed.; CRC Press: 2006; p 456.

[10] Liu, J.; Mei, Y.; Xia, R., A New Wetting Mechanism Based upon Triple Contact Line Pinning. *Langmuir* **2011,** *27* (1), 196-200.

[11] Josué, M.; Joan, J. C.; Oscar, M.; Juan, J.; Vitaly, Z. Z.; Peter, J. P.; Francesc, D.; Magdalena, A., Optical and structural characterisation of epitaxial nanoporous GaN grown by CVD. *Nanotechnology* **2017,** *28* (37), 375701.

[12] Ran, C.; Ding, G.; Liu, W.; Deng, Y.; Hou, W., Wetting on Nanoporous Alumina Surface: Transition between Wenzel and Cassie States Controlled by Surface Structure. *Langmuir* **2008,** *24* (18), 9952-9955.

[13] Rodrigues, S. P.; Alves, C. F. A.; Cavaleiro, A.; Carvalho, S., Water and oil wettability of anodized 6016 aluminum alloy surface. *Appl. Surf. Sci.* **2017,** *422*, 430-442.

[14] Norek, M.; Krasiński, A., Controlling of water wettability by structural and chemical modification of porous anodic alumina (PAA): Towards super-hydrophobic surfaces. *Surf. Coat. Technol.* **2015,** *276*, 464-470.

[15] Morkoç, H.; Strite, S.; Gao, G. B.; Lin, M. E.; Sverdlov, B.; Burns, M., Large-band-gap SiC, III-V nitride, and II-VI ZnSe-based semiconductor device technologies. *J. Appl. Phys.* **1994,** *76* (3), 1363-1398.

[16] Kisielowski, C.; Krüger, J.; Ruvimov, S.; Suski, T.; Ager, J. W.; Jones, E.; Liliental-Weber, Z.; Rubin, M.; Weber, E. R.; Bremser, M. D.; Davis, R. F., Strain-related phenomena in GaN thin films. *Phys. Rev. B* **1996,** *54* (24), 17745-17753.

[17] Ponce, F. A.; Bour, D. P.; Götz, W.; Johnson, N. M.; Helava, H. I.; Grzegory, I.; Jun, J.; Porowski, S., Homoepitaxy of GaN on polished bulk single crystals by metalorganic chemical vapor deposition. *Appl. Phys. Lett.* **1996,** *68* (7), 917-919.

[18] Park, B.-G.; Saravana Kumar, R.; Moon, M.-L.; Kim, M.-D.; Kang, T.-W.; Yang, W.-C.; Kim, S.-G., Comparison of stress states in GaN films grown on different substrates: Langasite, sapphire and silicon. *J. Cryst. Growth* **2015,** *425*, 149-153.

[19] Wei-Lin, W.; Jyh-Rong, G.; Cheng-Liang, W.; Wei-Tsai, L.; Ju-Liang, H.; Yuan-Chen, C.; Jen-Bin, S., Characteristics and Interactions of Threading Dislocations in GaN Films Grown on (0001) Sapphire Substrates With or Without Short-Period Superlattice Insertion. *Jpn. J. Appl. Phys.* **2006,** *45* (9R), 6888.

[20] Hijikuro, M.; Kuwano, N.; Takeuchi, M.; Aoyagi, Y., TEM analysis of annihilation process of threading dislocations in GaN thin films grown by MOVPE with anti-surfactant treatment. *physica status solidi (c)* **2006,** *3* (6), 1832-1835.

[21] Aggarwal, N.; Krishna, S. T. C.; Goswami, L.; Mishra, M.; Gupta, G.; Maurya, K. K.; Singh, S.; Dilawar, N.; Kaur, M., Extenuation of Stress and Defects in GaN Films Grown on a Metal–Organic Chemical Vapor Deposition-GaN/c-Sapphire Substrate by Plasma-Assisted Molecular Beam Epitaxy. *Crystal Growth & Design* **2015,** *15* (5), 2144-2150.

[22] Hsu, S. C.; Pong, B. J.; Li, W. H.; III, T. E. B.; Graham, S.; Liu, C. Y., Stress relaxation in GaN by transfer bonding on Si substrates. *Appl. Phys. Lett.* **2007,** *91* (25), 251114.

[23] Correia, M. R.; Pereira, S.; Pereira, E.; Frandon, J.; Alves, E., Raman study of the A1(LO) phonon in relaxed and pseudomorphic InGaN epilayers. *Appl. Phys. Lett.* **2003,** *83* (23), 4761-4763.

[24] Kamyczek, P.; Placzek-Popko, E.; Kolkovsky, V.; Grzanka, S.; Czernecki, R., A deep acceptor defect responsible for the yellow luminescence in GaN and AlGaN. *J. Appl. Phys.* **2012,** *111* (11), 113105.

[25] Cheng, K.; Degroote, S.; Leys, M.; Germain, M.; Borghs, G., Strain effects in GaN epilayers grown on different substrates by metal organic vapor phase epitaxy. *J. Appl. Phys.* **2010,** *108* (7), 073522.

[26] Luong Tien, T.; Lin, K. L.; Chang, E. Y.; Huang, W. C.; Hsiao, Y. L.; Chiang, C. H., Photoluminescence and Raman studies of GaN films grown by MOCVD. *J. Phys. Conf. Ser.* **2009,** *187* (1), 012021.

[27] Hortelano, V.; Martínez, O.; Cuscó, R.; Artús, L.; Jiménez, J., Cathodoluminescence study of Mg activation in non-polar and semi-polar faces of undoped/Mg-doped GaN core–shell nanorods. *Nanotechnology* **2016,** *27* (9), 095706.

[28] Köhler, K.; Gutt, R.; Wiegert, J.; Kirste, L., Diffusion of Mg dopant in metal-organic vapor-phase epitaxy grown GaN and AlxGa1−xN. *J. Appl. Phys.* **2013,** *113* (7), 073514.

[29] Benzarti, Z.; Halidou, I.; Bougrioua, Z.; Boufaden, T.; El Jani, B., Magnesium diffusion profile in GaN grown by MOVPE. *J. Cryst. Growth* **2008,** *310* (14), 3274-3277.

[30] Slimane, A. B.; Najar, A.; Elafandy, R.; San-Román-Alerigi, D. P.; Anjum, D.; Ng, T. K.; Ooi, B. S., On the phenomenon of large photoluminescence red shift in GaN nanoparticles. *Nanoscale Res. Lett.* **2013,** *8* (1), 342.

[31] Teisseyre, H.; Perlin, P.; Suski, T.; Grzegory, I.; Porowski, S.; Jun, J.; Pietraszko, A.; Moustakas, T. D., Temperature dependence of the energy gap in GaN bulk single crystals and epitaxial layer. *J. Appl. Phys.* **1994,** *76* (4), 2429-2434.

[32] Eckey, L.; Gfug, U. v.; Holst, J.; Hoffmann, A.; Kaschner, A.; Siegle, H.; Thomsen, C.; Schineller, B.; Heime, K.; Heuken, M.; Schön, O.; Beccard, R., Photoluminescence and Raman study of compensation effects in Mg-doped GaN epilayers. *J. Appl. Phys.* **1998,** *84* (10), 5828-5830.

[33] Callsen, G.; Wagner, M. R.; Kure, T.; Reparaz, J. S.; Bügler, M.; Brunnmeier, J.; Nenstiel, C.; Hoffmann, A.; Hoffmann, M.; Tweedie, J.; Bryan, Z.; Aygun, S.; Kirste, R.; Collazo, R.; Sitar, Z., Optical signature of Mg-doped GaN: Transfer processes. *Phys. Rev. B* **2012,** *86* (7), 075207.

[34] Reshchikov, M. A.; Xie, J.; He, L.; Gu, X.; Moon, Y. T.; Fu, Y.; Morkoç, H., Effect of potential fluctuations on photoluminescence in Mg-doped GaN. *Phys Stat Sol (C)* **2005,** *2*.

[35] Reimer, L., *Scanning Electron Microscopy. Physics of Image Formation and Microanalysis*. 2 ed.; Springer-Verlag Berlin Heidelberg: 1998; p 529.

[36] Everhart, T. E.; Hoff, P. H., Determination of Kilovolt Electron Energy Dissipation vs Penetration Distance in Solid Materials. *J. Appl. Phys.* **1971,** *42* (13), 5837-5846.

[37] Dhara, S.; Chandra, S.; Mangamma, G.; Kalavathi, S.; Shankar, P.; Nair, K. G. M.; Tyagi, A. K.; Hsu, C. W.; Kuo, C. C.; Chen, L. C.; Chen, K. H.; Sriram, K. K., Multiphonon Raman scattering in GaN nanowires. *Appl. Phys. Lett.* **2007,** *90* (21), 213104.

[38] Wieser, N.; Klose, M.; Dassow, R.; Scholz, F.; Off, J., Raman studies of longitudinal optical phonon–plasmon coupling in GaN layers. *J. Cryst. Growth* **1998,** *189–190*, 661-665.

[39] Demangeot, F.; Frandon, J.; Renucci, M. A.; Briot, O.; Gil, B.; Aulombard, R. L., Raman determination of phonon deformation potentials in α-GaN. *Solid State Commun.* **1996,** *100* (4), 207-210.

[40] Davydov, V. Y.; Klochikhin, A. A.; Smirnov, A. N.; Strashkova, I. Y.; Krylov, A. S.; Lu, H.; Schaff, W. J.; Lee, H. M.; Hong, Y. L.; Gwo, S., Selective excitation of E1(LO) and A1(LO) phonons with large wave vectors in the Raman spectra of hexagonal InN. *Phys. Rev. B* **2009,** *80* (8), 081204.

[41] Ayers, J. E., The measurement of threading dislocation densities in semiconductor crystals by X-ray diffraction. *J. Cryst. Growth* **1994,** *135* (1), 71-77.

6

Chemical functionalization of the GaN surface

Among the different approaches for the chemical functionalization of the surface of GaN, we focused our effort on two of them: (i) the use of silane molecules, in this case (3-aminopropyl)trimethoxysilane (APTMS), previously explored in the literature for the chemical functionalization of GaN [1-2], and (ii) the use of diazonium salts, used for the chemical functionalization of the surface of diamond nanoparticles [3] and SWCNT [4] among others, but never explore for the functionalization of GaN. The diazonium salts synthesized can be classified in two groups: (a) non-conjugated molecules and (b) conjugated molecules, where the electrons are free to move along the molecule through conjugated bonds.

6.1 Chemical functionalization of the GaN surface with APTMS

6.1.1 Experimental procedure for the silanization of GaN surfaces with APTMS

The first strategy explored for the functionalization of the surface of GaN films was the use of silane molecules. In particular, we used 3-aminopropyl trimethoxysilane (APTMS), since the amino terminal group present in this molecule can be transformed easily in a N_3 group to use later the molecule for click-chemistry reactions.

Prior to chemical functionalization, Mg-doped GaN (*p*-type) and Si-doped GaN (*n*-type) non-porous substrates were cleaned for 5 min with boiling dichloromethane, 5 min with boiling acetone and 5 min with boiling methanol, in all cases under reflux conditions. Then, the surface of GaN was oxidized using a *piranha* solution (3 volumes of concentrated H_2SO_4 and 1 volume of 30% H_2O_2), using 20 ml of solution at 353 K (80 °C) for 50 min. After cleaning the samples with deionized water to eliminate the rests of *piranha* solution, they were dried under vacuum in a desiccator.

For the silanization, a 20 mM APTMS solution in dry toluene was prepared. The silanization was conducted using 10 ml of this solution. Two different strategies were followed for the silanization reaction. In the first strategy, the silanization was done in an ultrasound bath, and the reaction was performed under 3 different conditions: (i) 1.5 h at 323 K (50 °C), (ii) 1.5 h at RT, and (iii) 10 h at RT. The second strategy was performed at RT under stirring for 1.5 h on Mg-doped GaN (*p*-type) and Si-doped GaN (*n*-type) non-porous substrates and unintentionally doped (*n*-type) and Mg-doped (*p*-type) porous GaN samples. In all cases the reaction was conducted under a nitrogen atmosphere.

This approach is different than those reported in the literature [1-2] in terms of exploring the possibility of using a lower temperature (RT), and reducing the probability of polymerization of silane molecules by conducting

the reaction under a nitrogen atmosphere, avoiding, thus, the presence of oxygen.

After the reaction, the samples were cleaned for 5 min in dry toluene and 5 min in isopropanol in the ultrasound bath in order to remove all the unreacted silane molecules.

6.1.2 Characterization of the silanized GaN surfaces

6.1.2.1 Optical microscope analysis

Figure 6.1 shows optical microscope pictures of the GaN samples after the cleaning process, after the oxidation process and after the first strategy followed for the silanization process, respectively. It can be seen that after the oxidation and removal of all organic contamination of the sample, the surface appears clean, and this is maintained after the silanization process.

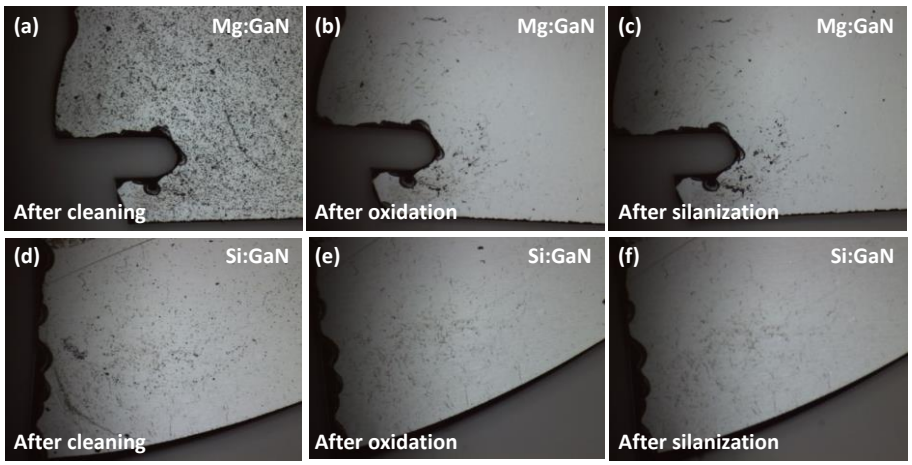

Figure 6.1. Optical microscope pictures of the non-porous GaN samples (a,d) after the cleaning process, (b,e) after the oxidation process and (c,f) after the silanization process, respectively. (a-c) Mg-doped GaN, (d-f) Si-doped GaN.

6.1.2.2 Diffuse reflectance infrared Fourier transform spectroscopy and Raman scattering

The samples silanized using the first strategy were characterized by diffuse reflectance infrared Fourier transform spectroscopy (DRIFTS) spectroscopy and Raman scattering. No changes were observed in the DRIFTS spectra after silanization of the samples, despite the different reaction conditions used, as can be observed in Figure 6.2(a,b) for Mg-doped and Si-doped GaN, respectively. This might be due to the fact, that the portion of surface in these samples, and thus, the concentration of APTMS on the surface is too low, to respect the volume of the sample. So, the vibrational bands corresponding to GaN dominate over the possible vibration bands of the APTMS molecules attached to the surface of the samples. DRIFTS spectroscopy is a valid technique when the functionalization is performed on nanoparticles where the surface to volume ratio is very high.

In the case of Raman scattering, some changes in intensity, broadening and shifting of the position of the A_1 (LO) and E_1 (LO) bands of GaN can be observed after the oxidation process as can be seen in Figure 6.2 (c,d) for Mg-doped and Si-doped GaN, respectively. However, the reasons that drive towards these small changes are unknown, and further investigation would be required to understand them.

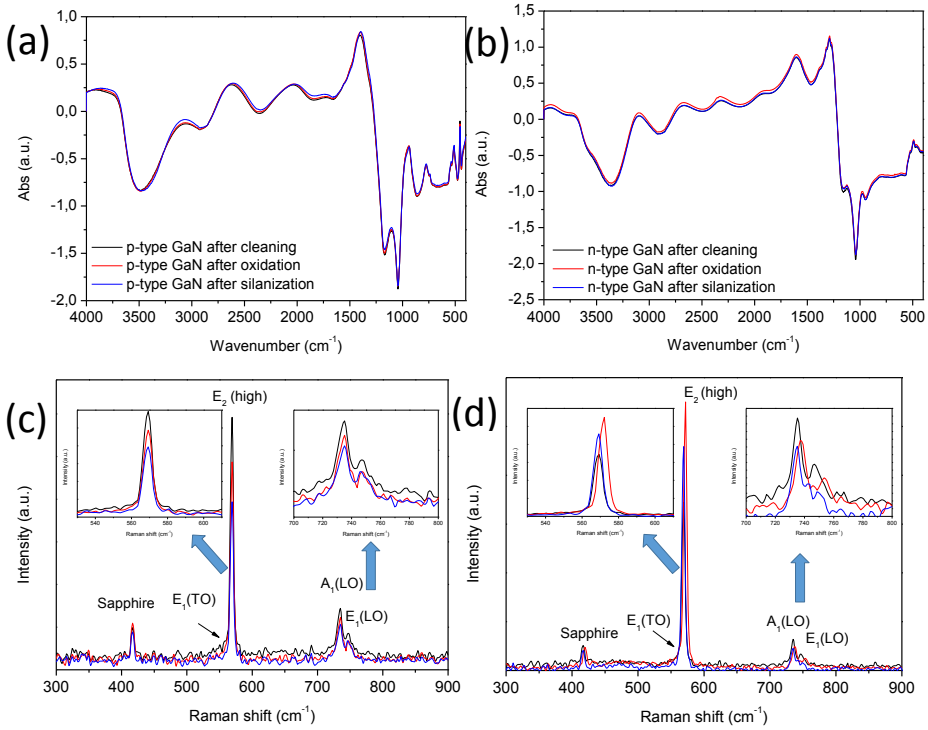

Figure 6.2. DRIFTS spectra of (a) Mg-doped and (b) Si-doped GaN samples after cleaning (black), after oxidation (red) and after silanization (blue). Raman scattering spectra of (c) Mg-doped and (d) Si-doped GaN after cleaning (black), after oxidation (red) and after silanization (blue).

Non-porous silanized samples following the second strategy were also characterized by DRIFTS (Figure 6.3). However, the same result was observed as with the silanized non-porous samples following the first strategy. The absence of signal change is due to the same fact as discussed above.

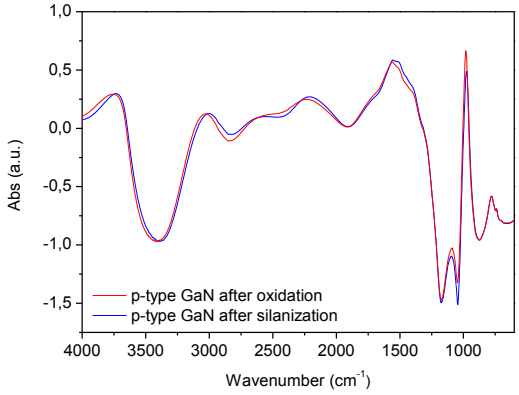

Figure 6.3. DRIFTS spectra of Mg-doped (*p*-type) GaN sample after oxidation (red) and after silanization (blue).

Porous GaN silanized samples following the second strategy were also characterized by DRIFTS (Figure 6.4). The same behavior is observed as for the other GaN substrates silanized, despite that porous GaN has a greater surface to volume ratio, but it is not enough to reveal any change in the spectra.

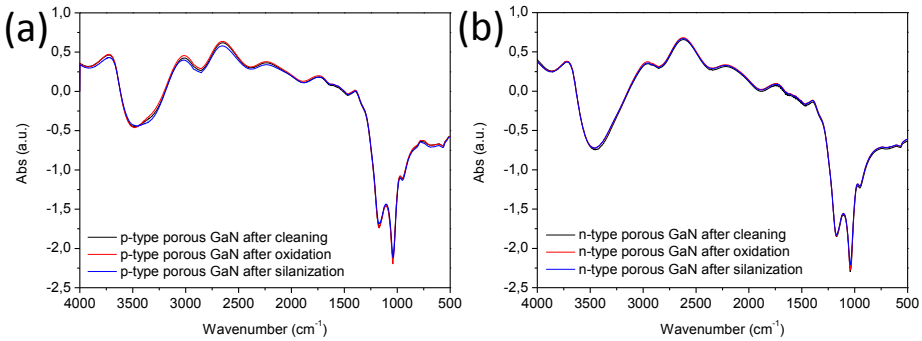

Figure 6.4. DRIFTS spectra of (a) Mg-doped (*p*-type) porous GaN and (b) unintentionally doped (*n*-type) porous GaN samples after oxidation (red) and after silanization (blue).

6.1.2.3 Kaiser test

Since FTIR spectroscopy and Raman scattering characterization could not confirm the chemical functionalization of the surface of GaN by APTMS molecules, we decided to use the Kaiser test, through which, ninhydrin reacts

with a primary amine group giving as final product a Schiff base chromophore which produces a deep blue or purple color known as Ruhemann's purple. The reaction between the ninhydrin and a primary amine group is shown in Scheme 6.1.

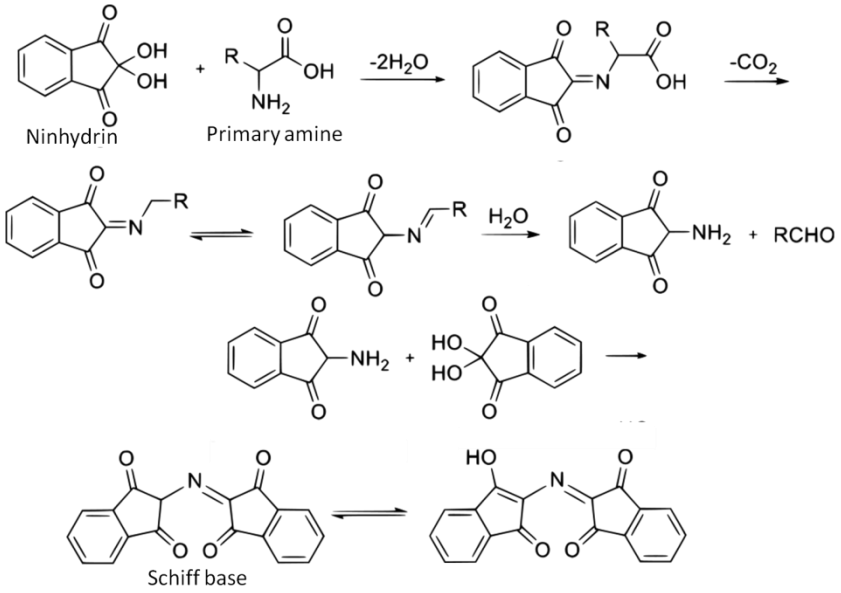

Scheme 6.1. Scheme of the Kaiser test reaction

Thus, bare GaN should not give a positive color in the Kaiser test, whereas the chemically functionalized GaN with APTMS molecules should do as these molecules contain a primary amine group. If the test results positive, when analyzed with a UV-vis spectrometer, this would indicate that APTMS molecules were attached to the surface of GaN. The results obtained for the silanized samples are presented in Figure 6.5. The Kaiser tests of the silanized GaN samples in an ultrasonic bath are shown in Figure 6.5 (a) where we can see that in all cases a broad absorption band centered at 560 nm was recorded, indicating that the Kaiser test was positive for the three reaction conditions used in our experiments. In contrast, the Kaiser test for the GaN samples silanized at RT under stirring was negative as can be seen in Figure 6.5 (b), which may indicate that the silanization did not occur under these conditions. Thus, according to these results it seems that performing the

reaction in an ultrasonic bath is important to get the silane molecules attached to the surface of GaN. The Kaiser test was not performed on silanized porous GaN samples, since this reaction cuts the amine group from the silane molecules, which would prevent the possibility of carrying out further characterization of these samples.

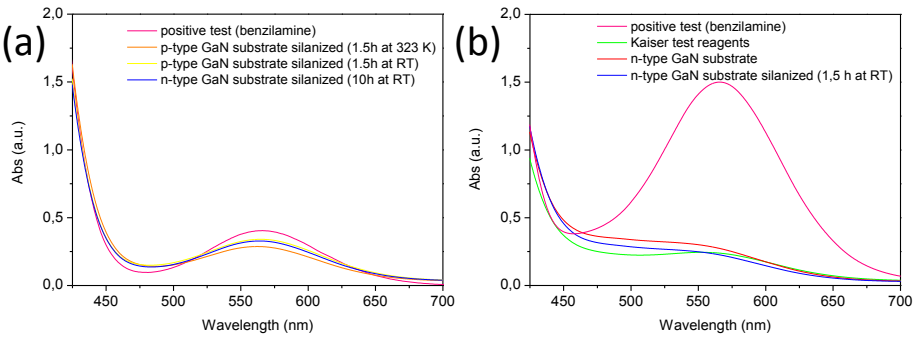

Figure 6.5. UV-vis absorption spectra of the solution obtained after the Kaiser test performed on the GaN samples functionalized with APTMS (a) *p*-type GaN silanized at RT (red line); *p*-type GaN silanized at 323 K (50 °C) (yellow line); and *n*-type GaN silanized at 323 K (50 °C) (blue line) using an ultrasonic bath in the three cases. The spectra of benzilamine (pink line) used as a reference positive test is included in the graph; (b) *n*-type GaN silanized at RT (blue line) under magnetic stirring, *n*-type GaN substrate in which no silanization was performed, (red line). Kaiser test reagents (green line) and benzilamine as the reference positive test (pink line).

Although these results would need to be confirmed by X-ray photoelectron spectroscopy (XPS) characterization, this would indicate that the functionalization of the surface of non-porous GaN samples with APTMS was successful using the ultrasonic bath. This would represent for the first time that silanization can be achieved on GaN at RT, reported here for the first time, probably induced by the avoidance of the presence of oxygen in the reaction medium that would promote the polymerization of silane molecules rather that linking them to the oxidized surface of GaN.

Despite the results obtained, a recent report [5] indicates that silane self-assembled monolayers on GaN surfaces attached to a thin passivating layer of Ga_2O_3 are not stable in aqueous media, and completely desorbs after

24 h of immersion in water and common biological buffers, apparently because of the dissolution of the oxide layer. Thus, despite the success of our approach, since this chemical functionalization strategy shows a low stability in water-based media, this represents a serious limitation to employ GaN functionalized in this way for biosensing applications in which the environment is an aqueous solution. So, we decided not explore further this functionalization methodology and focus our effort on the second approach presented below.

6.2 Chemical functionalization of the GaN surface with non-conjugated diazonium salts

We proposed a new strategy to graft organic moieties to GaN surfaces. The second strategy we explored for the chemical functionalization of the surface of non-porous and porous GaN samples was the use of diazonium salts. In a first step we used non-conjugated diazonium salts. In particular, three different diazonium salts were used for this purpose: 4-(2-azidoethyl)phenylamine (**1**), 4-(2-chloroethyl)benzoldiazonium tetrafluoroborate (**3**) and 4-cyanobenzoldiazonium tetrafluorobotate (**4**). The three different diazonium salts synthesized were chosen with the purpose to facilitate the detection of the functional groups once grafted to GaN. In the case of 4-(2-azidoethyl)phenylamine (**1**) and 4-cyanobenzoldiazonium tetrafluorobotate (**4**) they show a characteristic IR peak at 2096 and 2242 cm^{-1} respectively, in a region where no other peaks are expended for these molecules, thus it would be easy to identify them if they are attached to the surface of GaN. In the case of 4-(2-choroethyl)benzoldiazonium tetrafluoroborate (**3**) it may give an unequivocal signal in XPS related with the chlorine atom that could confirm the arylation of GaN with this molecule.

6.2.1 Experimental procedure for the synthesis of the non-conjugated diazonium salts and the arylation of GaN surfaces with the non-conjugate diazonium salts

Scheme 6.2 shows the reactions followed for the preparation of these diazonium salts.

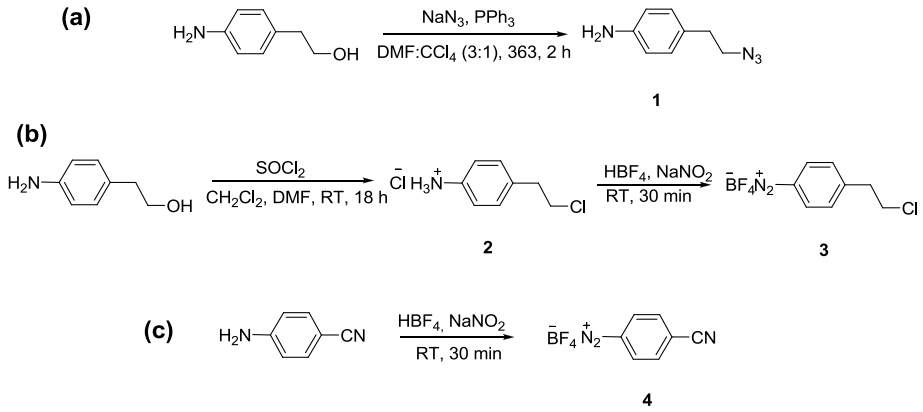

Scheme 6.2. Chemical reactions followed for the preparation of the diazonium salts used in this work. (a) 4-(2-azidoethyl)phenylamine (**1**), (b) 4-(2-choroethyl)benzoldiazonium tetrafluoroborate (**3**) and (c) 4-cyanobensoldiazonium tetrafluoroborate (**4**).

The first approach of arylation of GaN was preparing the diazionium salt *in situ* using 4-(2-azidoethyl)phenylamine (**1**). A second approach consisted in isolating the diazonium salt and then arylate the GaN with the isolated salt. This method was used for 4-(2-chloroethyl)benzoldiazonium tetrafluoroborate (**3**) and 4-cyanobenzoldiazonium tetrafluorobotate (**4**).

A more detailed description of the most important synthesis steps and the corresponding characterization procedures to ensure the attaching of the desired product is shown in Appendix 2.

6.2.2 Experimental procedure for the arylation of GaN surfaces with the non-conjugate diazonium salts

The GaN substrates were cleaned with boiling dichloromethane, acetone and methanol, successively, for 5 min each, under reflux with the thermocouple set at 353 K (80 °C), prior to functionalization. Then the substrate was immersed in a fresh piranha solution to remove organic solvents and oxidize the surface under reflux at 353 K (80 °C) for 50 min. Finally, the substrate was rinsed with deionized water and kept in the desiccator until use.

For the arylation of GaN with diazonium salts prepared *in situ* 1 eq of 4-(2-azidoethyl)phenylamine (**1**) and 1 eq of isoamyl nitrite were added to 9,6 ml of water with the GaN substrate inside. Another procedure was followed for the functionalization of GaN using HCl 1 M instead of water as the reaction media. The flask was heated up to 353 K (80 °C) under stirring for 18 h. After cooling down to RT the GaN substrate was cleaned with dimethyl sulfoxide (DMSO), water, acetone and dichloromethane in consecutive washing-ultrasound cycles, in order to get rid of all the unreacted reagents and byproducts adsorbed to the GaN substrate.

Another strategy we followed for the arylation of GaN substrates was using isolated diazonium salts. The first step was immersing the GaN substrate in 6 ml of water and the diazonium salt 4-(2-chloroethyl)benzoldiazonium tetrafluoroborate (**3**) and 4-cyanobenzoldiazonium tetrafluoroborate (**4**). The solution was kept in an ultrasonic horn (Branson sonifier 450) for 2.5 h at RT at an output power of 1 and with a cool water bath to avoid the excess of heat produced by the ultrasonic horn. The GaN substrates were cleaned with DMSO in consecutive washing-ultrasounds cycles after the functionalization process, in order to get rid of all the unreacted reagents and byproducts adsorbed to the GaN substrate. Scheme 6.3 shows the process followed for the arylation of GaN using the different diazonium salts prepared in this work.

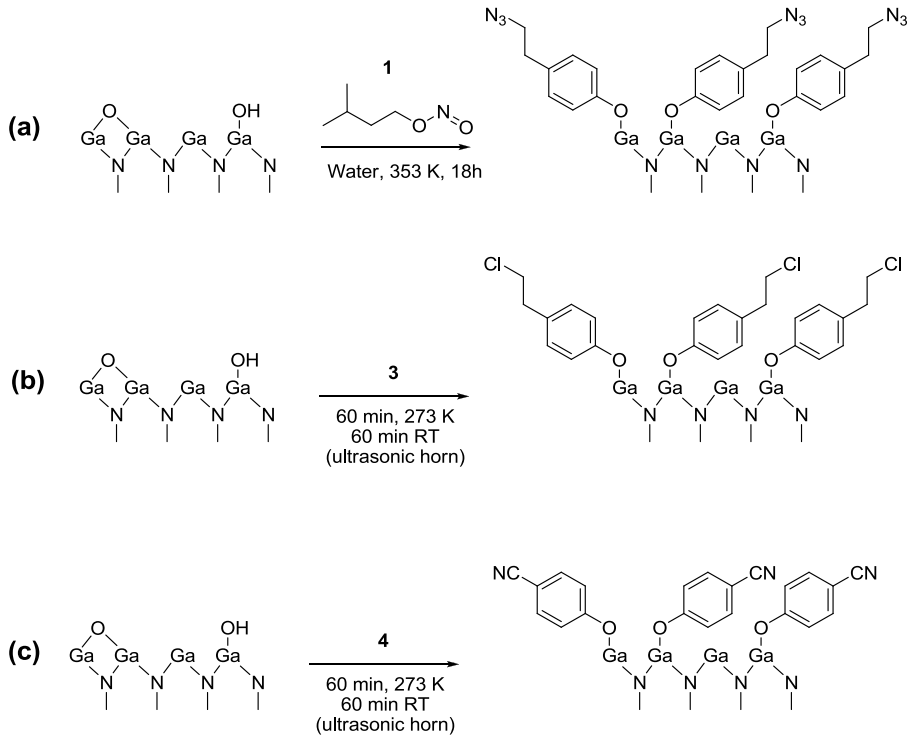

Scheme 6.3. Arylation processes followed for the chemical functionalization of GaN using (a) 4-(2-azidoethyl)phenylamine **(1)**, (b) 4-(2-choroethyl)benzoldiazonium tetrafluoroborate **(3)** and (c) 4-cyanobensoldiazonium tetrafluoroborate **(4)**.

Since we could not prove by DRIFTS spectroscopy that the arylation process was successful (as could be seen in section 6.2.2.3), and DRIFTS was the only analytical tool available in the synthesis laboratory to characterize the functionalized surfaces, we decided to link a fluorescent dye, 5-TAMRA modified with an azide terminal group, on the surface of a porous aryl-functionalized GaN. For this purpose we decided to synthesize a diazonium salt with an alkyne terminal group to be able to react with the azide terminal group of the dye via click chemistry. Thus, we decided to synthesize the 4-(prop-2-yn-1-yloxy)benzenediazonium tetrafluoroborate (**7**). In this way, by using a fluorescent microscope we would be able to confirm the chemical functionalization of GaN.

6.2.3 Experimental procedure for the synthesis of the non-conjugated diazonium salt with an alkyne moiety for click chemistry

The 4-(prop-2-yn-1-yloxy)benzenediazonium tetrafluoroborate (**7**) was used to functionalize a porous GaN sample. The synthesis path is shown in Scheme 6.4.

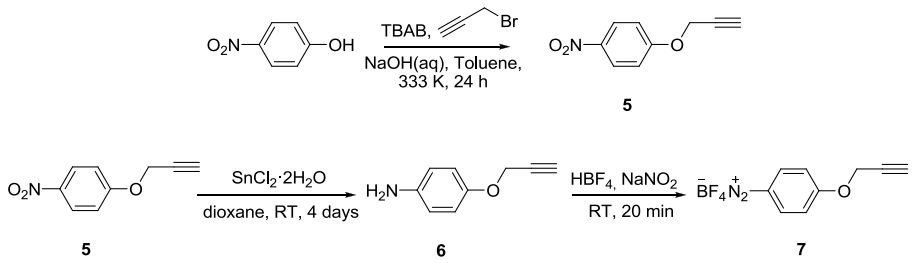

Scheme 6.4. Chemical reactions followed for the preparation of the 4-(prop-2-yn-1-yloxy)benzenediazonium tetrafluoroborate.

The description of the processes to obtain the reaction intermediates, until getting the desired 4-(prop-2-yn-1-yloxy)benzenediazonium tetrafluoroborate is in Appendix 2.

6.2.4 Experimental procedure for the arylation of GaN surfaces with the non-conjugated diazonium salt with an alkyne moiety for click chemistry

Prior to the functionalization of porous GaN, the substrate was cleaned following the same procedure as the followed for the GaN substrates described above. The arylation of porous GaN samples started by immersing the porous GaN substrate in 6ml of water and the 4-(prop-2-yn-1-yloxy)benzenediazonium tetrafluoroborate (**7**). The solution was ultrasonicated with an ultrasonic horn for 2.5 h at RT under cool water bath to avoid the excess of heat produced by the ultrasonic horn. The porous GaN substrate was cleaned with DMSO in consecutive washing-ultrasound cycles after the functionalization process. Scheme 6.5 shows the proposed process followed for the arylation of GaN using this diazonium salt.

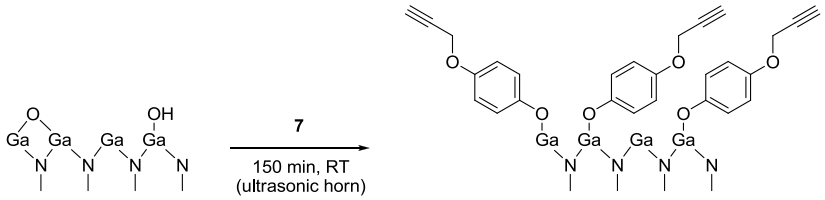

Scheme 6.5. Arylation process followed for the chemical functionalization of porous GaN using 4-(prop-2-yn-1-yloxy)benzenediazonium tetrafluoroborate (**7**).

The following step was the linkage of the 5-TAMRA fluorescent dye to the 4-(prop-2-yn-1-yloxy)benzenediazonium tetrafluoroborate (**7**), used to functionalize the surface of the porous GaN sample, using click-chemistry. The reaction followed is described in Scheme 6.6.

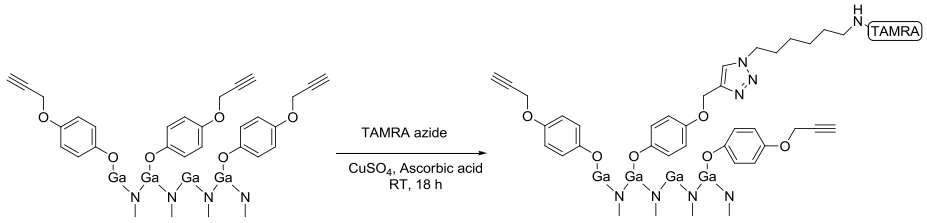

Scheme 6.6. Click-chemistry reaction followed for the attachment of 5-TAMRA fluorescent dye on the arylated porous GaN.

In order to compare the results of fluorescence, a blank, consisting on a non-functionalized porous GaN sample, was immersed also in the solution containing the 5-TAMRA and the reagents needed for the click-chemistry.

Click reaction of alkyne-functionalized porous GaN to 5-TAMRA fluorescent dye

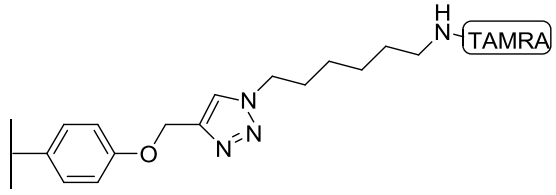

For that, the alkyne-functionalized porous GaN substrate was placed in a covered assay tube for with 0.25 mg of 5-TAMRA-azide (Invitrogen ™),

2 ml of DMSO, 0.06 mg (0.3 µmol) of sodium ascorbate and 0.02 mg (0.125 µmol) of $CuSO_4$. The reaction mixture was stirred under the absence of light for 18 h. The porous GaN substrate was cleaned with DMF:H_2O (3:1) in consecutive washing-ultrasounds cycles.

6.2.5 Characterization of the arylated GaN surfaces with non-conjugated diazonium salts

The arylated porous GaN surface grafted to 5-TAMRA fluorescent dye was characterized by fluorescence microscopy since it is a straight forward method to identify if the fluorescent dye is present or not, as GaN do not present any fluorescence in that region.

PL and CL measurements were performed in order to identify the 5-TAMRA emission in the case of the sample with the dye linked to the functionalized molecule.

The arylated non-porous GaN surfaces were analyze by XPS, since this is the more powerful technique to characterize functionalized surfaces.

Also DRIFTS spectroscopy was performed in order to follow a systematic study of the silanized samples, despite no signal of the anchored molecules was observed.

Also reflectance measurements were performed in order to see any macroscopic change in the reflectance of the arylated GaN samples.

Finally, electrical characterization was performed, recording the I-V curves using two probes measurements, in order to asses if any change in the electrical conductivity after the functionalization of the GaN surface could be observed.

6.2.5.1 Fluorescence microscopy of the porous GaN surface grafted to 5-TAMRA fluorescent dye

In order to confirm the successful attachment of the 5-TAMRA fluorescent dye on the previously arylated porous GaN sample, the sample was characterized under a fluorescent confocal microscope. For comparison, a blank non-functionalized porous GaN sample was prepared following the same reaction procedure as the functionalized one, with the exception of the prior arylation step, so that, 5-TAMRA could only be adsorbed on the surface of GaN, but not covalently attached. Fluorescent confocal images are shown in Figure 6.6, after illumination with green light (525-540 nm) and recording the fluorescence in the red channel (605-655 nm) with an acquisition time of 900 ms.

5-TAMRA grafted to GaN shows a brighter fluorescent image (see Figure 6.6 (b)) compared to the blank sample (see Figure 6.6 (a)), indicating that 5-TAMRA was successfully attached to the aryl-functionalized porous GaN sample, since the fluorescence coincides with the fluorescence band of the 5-TAMRA fluorescent dye (see Figure 6.6(c)). Furthermore, the homogeneity in the brightness of the image, would indicate a good homogeneity in the distribution of 5-TAMRA on the sample, attributed to a good dispersion of 4-(prop-2-yn-1-yloxy)benzene molecules linked on GaN. The bright spots observed in the sample might correspond to accumulation of 5-TAMRA molecules on larger pores, although this hypothesis has to be corroborated in the future. From another side, the fluorescence observed in the blank sample is attributed to 5-TAMRA residues adsorbed on the surface of the pores due to the polarity of GaN.

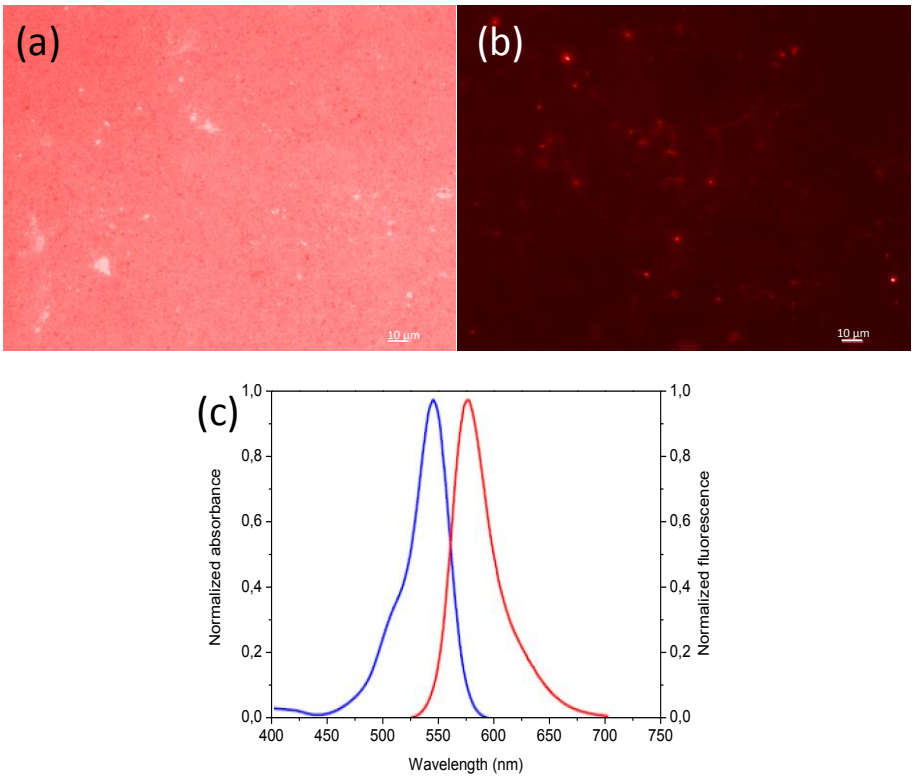

Figure 6.6. Confocal fluorescence microscope images of (a) blank and (b) 5-TAMRA functionalized porous GaN samples, and (c) absorbance (in blue) and fluorescence (in red) spectrum of 5-TAMRA fluorescent dye. (image adapted from [6])

6.2.5.2 Photoluminescence of the porous GaN surface grafted to 5-TAMRA fluorescent dye

This sample was also characterized by recording photoluminescence spectrum. The photoluminescence measurements were first carried out at RT using a He–Cd laser operating at 325 nm as an excitation source (see Figure 6.7 (a)). PL is a non-destructive method to study the surface of semiconductors. In direct-band gap semiconductors such as GaN, above-bandgap excitation as the case presented here, has a penetration depth of the order of 40 nm, thus, it allows studying the surface effects in samples. Figure 6.7(a) shows the PL spectrum of the arylated porous GaN sample with the

5-TAMRA fluorescent dye linked, with a peak centered at 362 nm corresponding to the near band edge (NBE) emission and a broad band at lower energies attributed to the yellow luminescence band (YL), which is related with defects and vacancies. Despite it is a method widely used to study the surface of semiconductors, the penetration depth of the laser light gets deep enough to mask the emission light of the 5-TAMRA by exciting GaN.

Photoluminescence spectrum was also recorded pumping the sample with a Nd:YAG laser operating at 532 nm, since the 5-TAMRA fluorescent dye has a maximum of absorbance at 557 nm, as indicated in the Figure. Figure 6.7(b) shows the PL spectrum of the arylated porous GaN sample with the dye. A broad band centered at 553 nm (2.23 eV) dominates the spectrum. Despite using a laser of energies below the band gap and close to the dye maximum of the absorption peak we cannot clearly distinguish the emission from the GaN attributed to the YL and the emission of the dye.

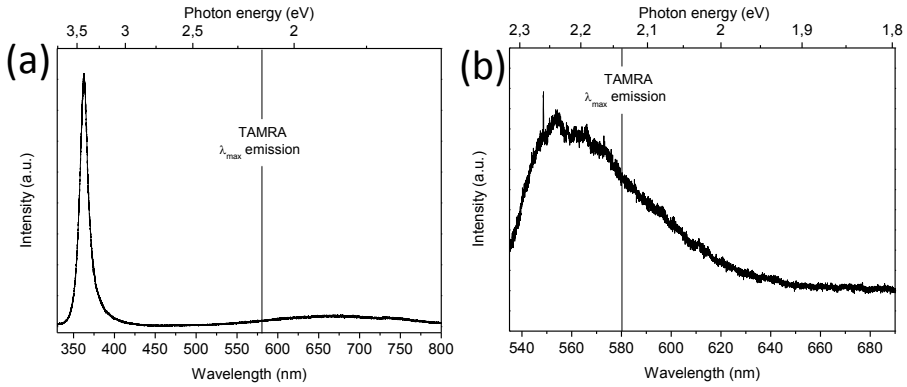

Figure 6.7. Photoluminescence measurements of arylated porous GaN linked with 5-TAMRA using (a) a He–Cd laser operating at 325 nm and (b) a Nd:YAG laser operating at 532 nm.

6.2.5.3 Cathodoluminescence of the porous GaN surface grafted to 5-TAMRA fluorescent dye

The sample was also characterized by means of cathodoluminescence. In Figure 6.8 we can clearly see again a broad band centered at 2.2 eV corresponding to the YL band that could mask the emission of the 5-TAMRA

fluorescent dye. Since there are no studies of 5-TAMRA fluorescence emission at low temperatures by CL we cannot conclude if the 5-TAMRA fluorescent dye is emitting light in the same wavelength range coinciding with the YL band of GaN, or due to the low temperatures (80 K) the emission is shifted to lower fluorescence wavelengths and the band observed is a summation of the YL band and the 5-TAMRA fluorescence emission.

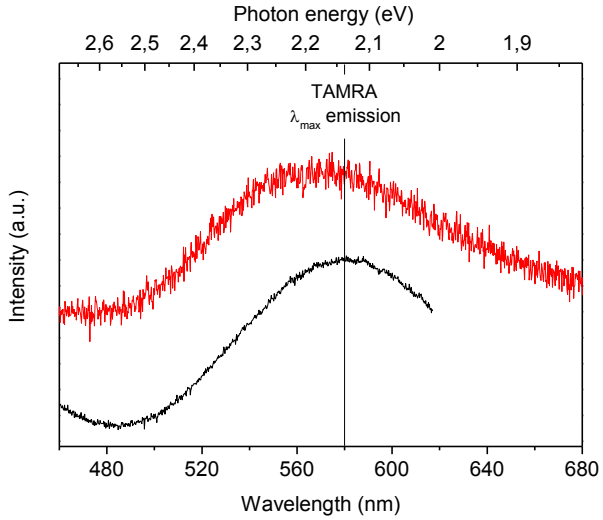

Figure 6.8. Cathodoluminescence spectra of functionalized porous GaN sample linked with 5-TAMRA fluorescent dye (red line) and porous GaN sample for comparison (black line).

6.2.5.4 X-ray photoelectron spectroscopy

After proving the successful attachment of diazonium salts on GaN surfaces by linking a fluorescent dye to them, X-ray photoelectron spectroscopy (XPS) measurements were carried out on the GaN samples functionalized with 4-(2-azidoethyl)phenylamine (**1**) and 4-(2-chloroethyl)bensoldiazonium tetrafluoroborate (**3**). Also, XPS measurements were undertaken in a non-functionalized GaN sample for comparison.

The measurements were carried out in a hemispherical analyzer PHOIBOS 150 (SPECS) with a 2D-DLD detector, an energy resolution of

0.1 eV, and an acceptance area (field of view on the sample) of ~2 mm. A non monochromated Mg Kα (hν = 1253.6 eV) and Al (hν = 1486.61 eV) X-ray sources were used, operating at 200 W and 12 kV. For XPS spectra quantification the CasaXPS software was used, performing the peak fitting by using a Shirly type backgroung and mixed Gaussian/Lorenzian peak shapes. The samples were mounted to the sample plate using Ta wire, 125 µm in diameter.

Figure 6.9 shows the XPS survey spectra recorded for these samples. Ga, N, O and C were detected on the samples, but no Cl was detected in the sample functionalized with 4-(2-chloroethyl)bensoldiazonium tetrafluoroborate (**3**).

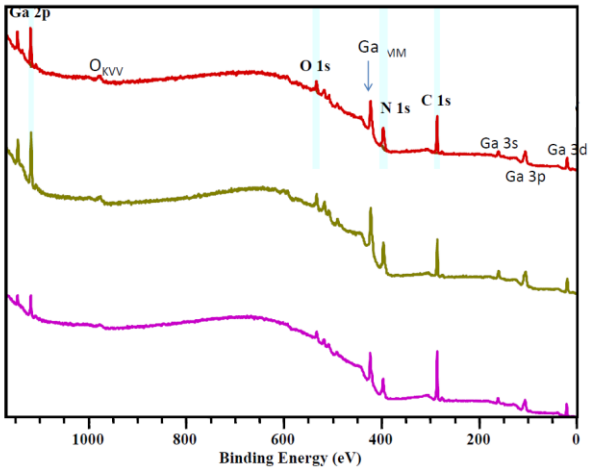

Figure 6.9. XPS survey spectra of GaN samples functionalized with 4-(2-azidoethyl)phenylamine (**1**) (red) , 4-(2-chloroethyl)bensoldiazonium tetrafluoroborate (**3**) (olive) and bare GaN sample (purple).

Figure 6.10 depicts the high resolution XPS spectra for the GaN samples functionalized with 4-(2-azidoethyl)phenylamine (**1**) and 4-(2-chloroethyl)bensoldiazonium tetrafluoroborate (**3**), as well as for the GaN bare sample.

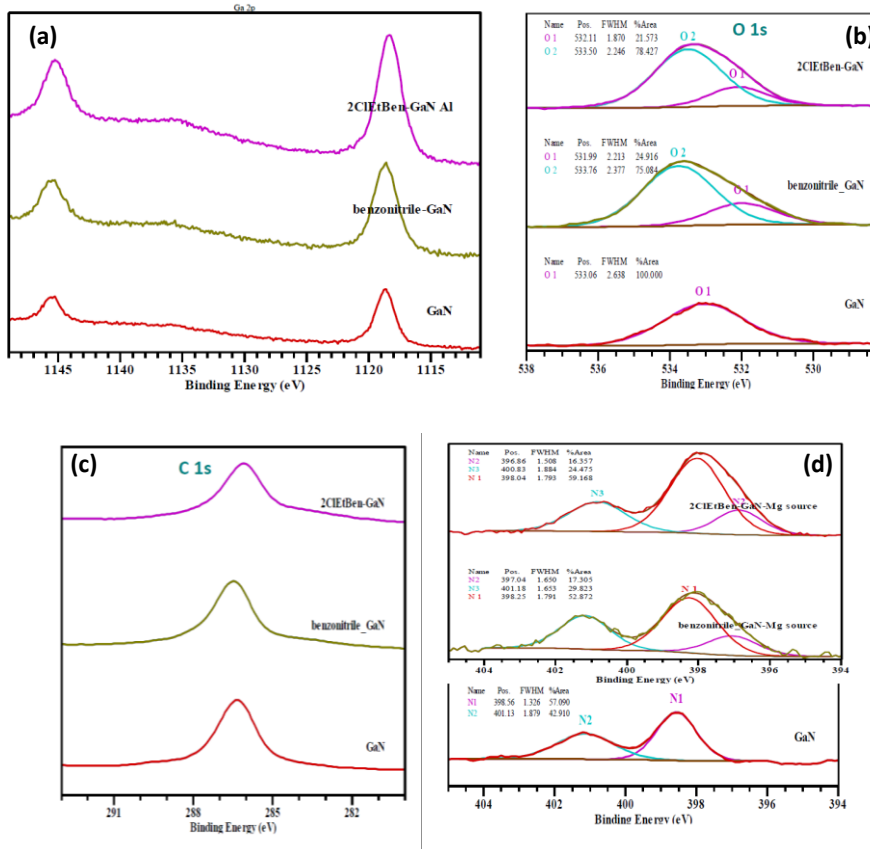

Figure 6.10. XPS high resolution spectra of GaN samples functionalized with 4-(2-azidoethyl)phenylamine (**1**) (green line) , 4-(2-chloroethyl)bensoldiazonium tetrafluoroborate (**3**) (purple line) and bare GaN sample (red line) corresponding to (a) Ga 2p, (b) O 1s, (c) C 1s and (d) N 1s.

The analysis of these spectra confirm that only one oxidation state of Ga is present in the samples, while 2 different kind of oxygen atoms could be detected in the functionalized samples. Also, despite the similarity of the peaks corresponding to carbon in all the samples, the shape and the position changed slightly in the functionalized samples. Finally, an additional N state could be detected in the functionalized samples. These results seem to confirm that diazonium salts were linked to the surface of GaN samples.

6.2.5.5 DRIFT spectroscopy

Aryl-functionalized GaN samples were characterized by DRIFT spectroscopy after the functionalization in the same laboratory. However, no evidence of the presence of the aryl molecules was observed on the spectra, as can be seen in Figure 6.11, probably due to the low concentration of these molecules to respect the volume of GaN, whose vibration bands dominate the spectra, as it happened before with the silanization approach.

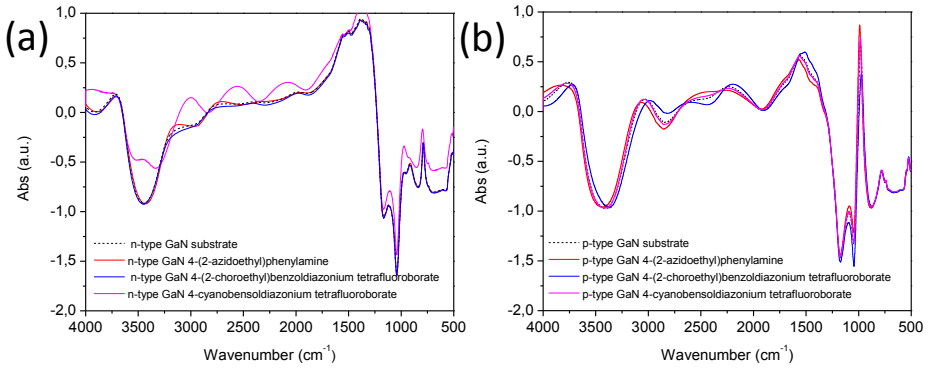

Figure 6.11. DRIFTS spectra of (a) Mg-doped and (b) Si-doped GaN functionalized with 4-(2-azidoethyl)phenylamine (**1**) (red line), 4-(2-choroethyl)benzoldiazonium tetrafluoroborate (**3**) (blue line) and 4-cyanobensoldiazonium tetrafluoroborate (**4**) (magenta line).

6.2.5.6 Reflectance measurements

Reflectance measurements of the functionalized GaN substrates with the different diazonium salts were performed. The scan rate was 6nm/min and four measurements were carried out in each sample in order to have statistical dispersion.

Figure 6.12 shows the reflectance measurements of *n*-type GaN functionalized substrates. In all the cases the given signal above the band gap is characteristic of the interference pattern due to the flatness and good parallelism of the two faces of the substrate. Also, a small decrease of the reflectance of the sample occurs at ~400 nm which corresponds to the DAP transition. The biggest drop in the signal occurs at ~365 nm which belongs to

the NBE of the GaN. In Figure 6.12 we included also the spectrum of a non functionalized substrate. As can be seen, no significant changes can be observed between the spectrum of the bare substrate and those of the samples functionalized with diazonium salts.

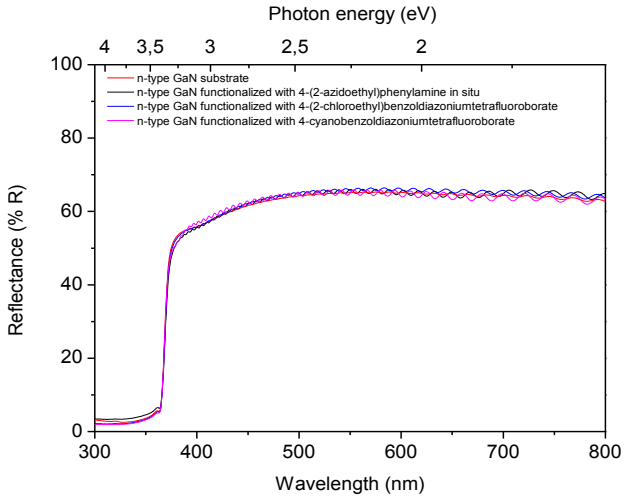

Figure 6.12. Reflectance spectra of *n*-type GaN substrate (black dotted line) and *n*-type GaN funcionalized samples with 4-(2-azidoethyl)phenylamine (**1**) (red line), 4-(2-choroethyl)benzoldiazonium tetrafluoroborate (**3**) (blue line) and 4-cyanobensoldiazonium tetrafluoroborate (**4**) (magenta line).

Reflectance measurements of the functionalized porous GaN sample linked with the 5-TAMRA fluorescent dye were also performed. A comparison between a bare porous GaN sample and the functionalized GaN linked with 5-TAMRA fluorescent dye is shown in Figure 6.13. The black curve indicates de mean value of reflectance of the arylated porous GaN sample linked with 5-TAMRA fluorescent dye and the red curve indicates the mean value of reflectance of the non-functionalized porous GaN sample. It can be seen in that the reflectance values of the arylated porous GaN linked with 5-TAMRA fluorescent dye are quite similar to the reflectance values of the standard porous non-functionalized GaN sample. Despite there is a depletion of reflectance in the wavelengths above the band gap (~360 nm) there is no significant variation of the sample reflectance that could prove the

presence of 5-TAMRA in the sample since there is no change of the reflectance pattern in the absorption wavelength of the 5-TAMRA fluorescent dye.

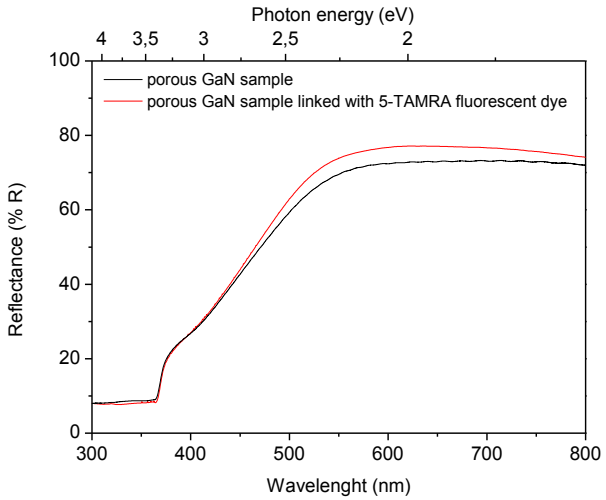

Figure 6.13. Reflectance spectra of bare porous GaN sample (black line) and functionalized porous GaN sample linked with 5-TAMRA fluorescent dye (red line).

6.2.5.7 Electrical characterization

Charge transport measurements on the surface of the aryl-functionalized *n*-type GaN samples were conducted using two-probe measurements. Linear voltage sweeps were obtained between the ranges of -5 V to 5 V.

In all cases, for the aryl-functionalized GaN samples we observed an ohmic behavior as it was expected for *n*-type GaN samples [7] and the contacts used as can be seen in Figure 6.14.

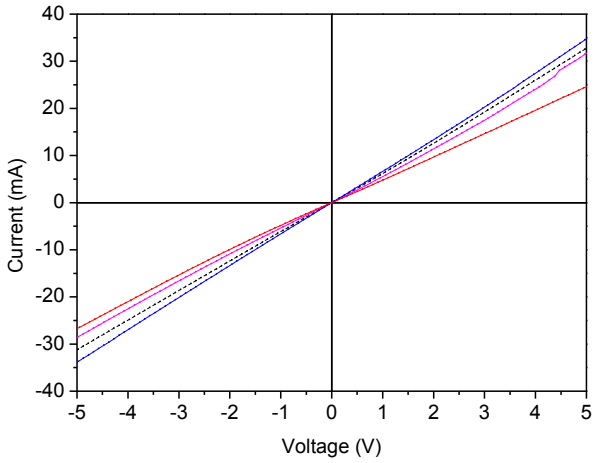

Figure 6.14. I-V curves of the bare (black dotted line) and functionalized *n*-type GaN substrates samples with 4-(2-azidoethyl)phenylamine (**1**) (red line), 4-(2-choroethyl)benzoldiazonium tetrafluoroborate (**3**) (blue line) and 4-cyanobensoldiazonium tetrafluoroborate (**4**) (magenta line).

6.3 Chemical functionalization of the GaN surface with conjugated diazonium salts

Diazonium salts containing conjugated bonds were synthesized to facilitate the energy transfer from the semiconductor to the dye that we have chosen to be attached to them, promoting a potential sensing mechanism.

Two different strategies were explored, that allowed to perform the deprotection of the terminal amine group either in acidic and basic conditions, respectively, which is needed for the further reaction with the fluorescent dye, and exploring at the same time how these conditions would affect to the surface of GaN.

6.3.1 Experimental procedure for the synthesis of the conjugated diazonium salts

The first synthetic strategy consisted on the use of 4-((4-(2,2,2-trifluoroacetamido)phenyl)ethynyl)benzenediazonium

tetraborofluorate **(12)**. Scheme 6.7 shows the synthesis reactions required to synthesize 4-((4-(2,2,2-trifluoroacetamido)phenyl)ethynyl)benzenediazonium tetraborofluorate:

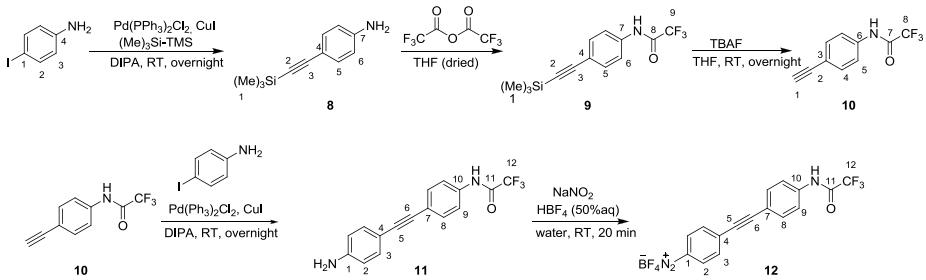

Scheme 6.7. Chemical reactions followed for the preparation of the 4-((4-(2,2,2-trifluoroacetamido)phenyl)ethynyl)benzenediazonium tetraborofluorate.

The second synthetic strategy consisted on the use of 4-((4-(*tert*-butoxycarbonylamino)phenyl)ethynyl)benzenediazonium tetrafluoroborate **(16)**. Scheme 6.8 shows the synthesis procedures required to obtain 4-((4-(*tert*-butoxycarbonylamino)phenyl)ethynyl)benzenediazonium tetrafluoroborate:

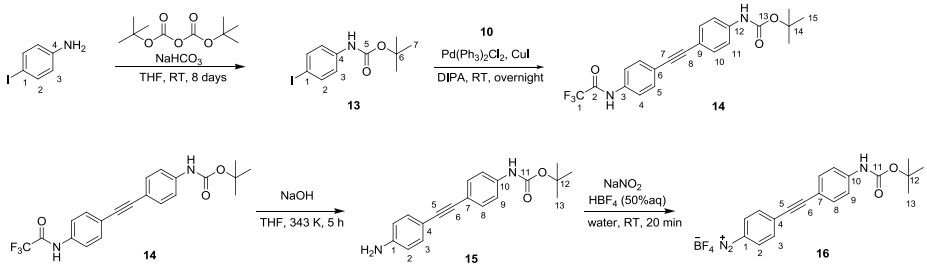

Scheme 6.8. Chemical reactions followed for the preparation of the 4-((4-(*tert*-butoxycarbonylamino)phenyl)ethynyl)benzenediazonium tetrafluoroborate.

A more detailed description of the different synthesis steps and the corresponding characterization procedures to ensure the obtaining of the desired product is explained in Appendix 2.

6.3.2 Experimental procedure for the arylation of porous GaN surfaces with the conjugate diazonium salts

GaN substrates were cleaned with boiling dichloromethane, acetone and methanol, successively, under reflux at 353 K (80 °C) for 5 min prior to functionalization. Then, the substrate was immerse in a fresh piranha solution to remove organic solvents and oxidize the surface under reflux at 353 K (80 °C) for 50 min. Finally, the substrate was rinsed with deionized water and kept in a desiccator until use.

Once the diazonium salts were prepared, the arylation of porous GaN proceeded by immersing the porous GaN sample in 6 ml of water and 100.3 mg (0.25 mmol) of 4-((4-(2,2,2-trifluoroacetamido)phenyl)ethynyl)benzenediazonium tetraborofluorate (**12**). The solution was ultrasonicated using an ultrasonic horn for 2.5 h at rom temperature, under cool water bath to avoid the excess of heat produced by the ultrasonic horn. The porous GaN substrates were then cleaned with DMSO in consecutive washing-ultrasounds cycles. The same protocol was followed for 4-((4-(*tert*-butoxycarbonylamino)phenyl)ethynyl)benzenediazonium tetrafluoroborate (**16**), using 108.4 mg (0.27 mmol).

Deprotection of 4-((4-(2,2,2-trifluoroacetamido)phenyl)ethynyl)benzene linked to oxidized porous GaN

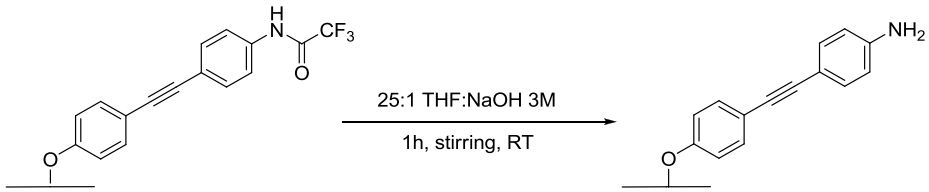

Scheme 6.9. Deprotection of the TFA group of the of 4-((4-(2,2,2-trifluoroacetamido)phenyl)ethynyl)benzene.

The GaN functionalized sample with 4-((4-(2,2,2-trifluoroacetamido)phenyl)ethynyl)benzenediazonium tetraborofluorate (**12**) was immersed in a solution of 25 ml of THF and 1 ml of NaOH 3 M, and the solution was stirred for 1 h at RT, as indicated in scheme 6.9. After 1 h, the sample was picked up from the solution and cleaned with deionized water and placed in a desiccator until dryness.

Deprotection of 4-((4-(tert-butoxycarbonylamino)phenyl)ethynyl)benzene linked to oxidized porous GaN

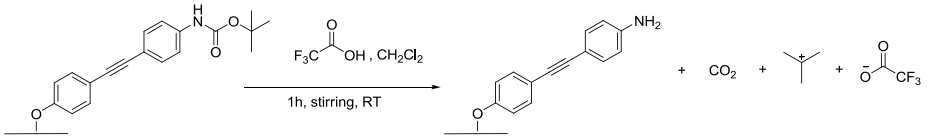

Scheme 6.10. Deprotection of the Boc group of the of 4-((4-(2,2,2-trifluoroacetamido)phenyl)ethynyl)benzene.

The GaN functionalized sample with 4-((4-(*tert*-butoxycarbonylamino)phenyl)ethynyl)benzenediazonium tetraborofluorate (**16**) was immersed in a solution of 20 ml of CH_2Cl_2 and 20 ml of TFA, and the solution was stirred for 1 h at RT as shown in scheme 6.10. After 1 h the sample was picked up from the solution and cleaned with deionized water and placed in a desiccator until dryness.

6.3.3 Experimental procedure for the binding of the ATTO465-NHS dye with the arylated porous GaN with conjugated diazonium salts

ATTO465-NHS fluorescent dye was selected among other fluorescent dyes commercially available due to its absorption band located near the near band-edge (NBE) emission of GaN. Thus, it would be able to absorb the emission generated by a GaN-based LED. Furthermore, its emission band is located far from other GaN luminescence peaks (NBE, DAP, or YL), thus, allowing unequivocally obtaining a fingerprint signature of the presence of the dye (see Figure 6.15).

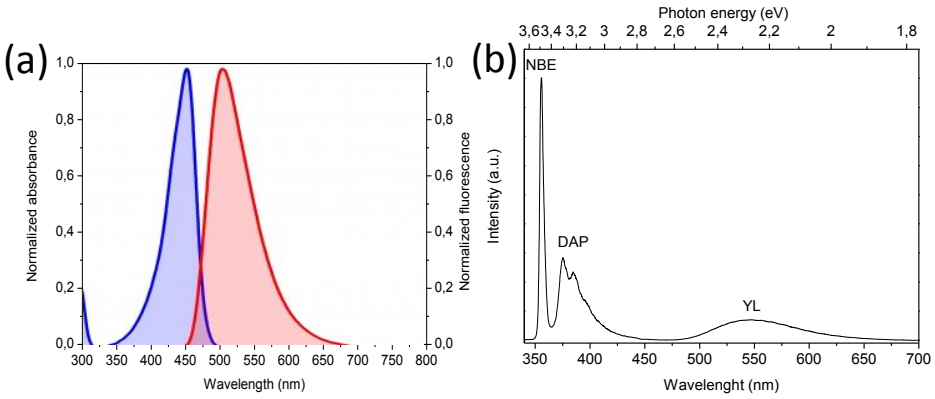

Figure 6.15. (a) Absorbance (in blue) and fluorescence (in red) spectra of ATTO 465 dye (image adapted from [6]), and (b) PL spectra of GaN.

The reaction to link the ATTO465-NHS fluorescent dye to the amine-functionalized porous GaN is summarized in Scheme 6.11. As well as in the case of the porous GaN sample grafted with 5-TAMRA fluorescent dye, a blank sample, consisting on a non-functionalized porous GaN sample, was immersed also in the solution containing the ATTO465-NHS fluorescent dye and the reagents needed for the coupling reaction, in order to compare the results of fluorescence.

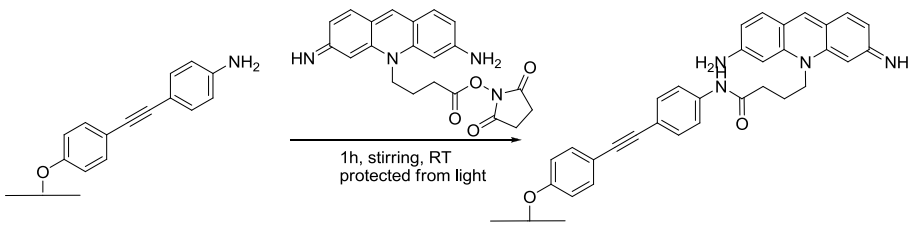

Scheme 6.11. Chemical reaction followed for the attachment of ATTO465-NHS fluorescent dye on the NH_2-temrminal arylated porous GaN.

Reaction of amine-functionalized porous GaN to ATTO465-NHS fluorescent dye

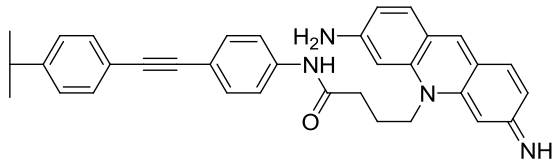

1 mg of ATTO465-NHS fluorescent dye was dissolved in DMSO. Amine functionalized porous GaN was placed in a covered flask with 10 ml of DMSO. The ATTO465-NHS fluorescence dye was added to the solution and stirred for 1 h at RT in the absence of light. Finally, the samples were cleaned with DMSO in consecutive washing-ultrasound cycles, in order to get rid of all the unreacted dye adsorbed to the GaN substrates.

6.3.4 Characterization of the arylated GaN surfaces with conjugated diazonium salts by fluorescence microscopy

Fluorescent microscope measurements were also performed in amine-functionalized porous GaN with attached ATTO465-NHS fluorescent dye to bear out if the functionalization was successfully achieved, supposing the dye reacted with the free amine of the linker system. In order to excite the ATTO465 fluorescent dye, an excitation source with emission in the range of 465-495 nm was used and the fluorescence recorded was in the range of 515-555 nm. Results are presented in Figure 6.16. No fluorescence information on the functionalized sample and the blank were obtained, while a saturated fluorescence image was obtained in a drop of ATTO465 dye dissolved in DMSO. An image of the ATTO465 dye dissolved in DMS droplet under 465-495 nm light excitation is shown in Figure 6.16 (d), showing an intense green fluorescence.

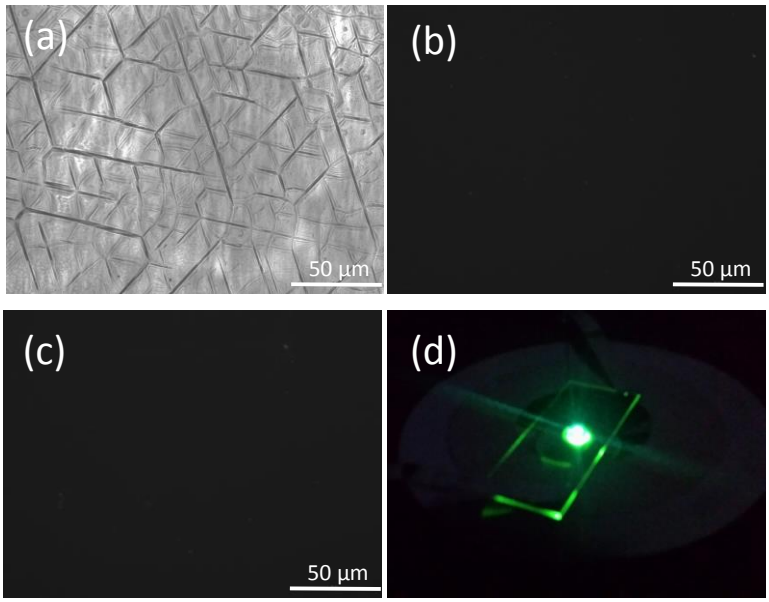

Figure 6.16. Confocal microscope pictures of (a) porous GaN functionalized with with 4-((4-(2,2,2-trifluoroacetamido)phenyl)ethynyl)benzenediazonium tetraborofluorate **(12)** and fluorescence microscope pictures of (b) porous GaN functionalized with 4-((4-(2,2,2-trifluoroacetamido)phenyl)ethynyl)benzenediazonium tetraborofluorate linked with ATTO 465 dye **(12)** (c) porous GaN functionalized with 4-((4-(*tert*-butoxycarbonylamino)phenyl)ethynyl)benzenediazonium tetrafluoroborate linked with ATTO 465 dye **(16)** illuminated with blue light (465-495 nm) and recording the green light at 515-555 nm.

The absence of fluorescence signal can be attributed to three facts: (i) a bad coupling between the dye and the free amine. However, since the reaction between NHS esters and primary amines is very favorable yielding a stable amide, this assumption might be wrong. (ii) Since the deprotection of the amine was performed in strong acid and basic conditions, the GaN surface might be etched [8], destroying the bond between GaN and the linker. The (ii) assumption is true for the porous GaN sample functionalized 4-((4-(2,2,2-trifluoroacetamido)phenyl)ethynyl)benzenediazonium tetraborofluorate (**12**) in which the deprotection of the amine is in basic conditions (NaOH solution), since GaN gets etched under basic conditions.

(iii) The functionalization of GaN with diazonium salts of the conjugated linker was unsuccessful.

References

[1] Baur, B.; Steinhoff, G.; Hernando, J.; Purrucker, O.; Tanaka, M.; Nickel, B.; Stutzmann, M.; Eickhoff, M., Chemical functionalization of GaN and AlN surfaces. *Appl. Phys. Lett.* **2005,** *87* (26), 263901.

[2] Ismail, M. N.; Goodrich, T. L.; Ji, Z.; Ziemer, K. S.; Warzywoda, J.; Sacco, A., Assembly of titanosilicate ETS-10 crystals on organosilane-functionalized gallium nitride surfaces. *Microporous Mesoporous Mater.* **2009,** *118* (1), 245-250.

[3] Meinhardt, T.; Lang, D.; Dill, H.; Krueger, A., Pushing the Functionality of Diamond Nanoparticles to New Horizons: Orthogonally Functionalized Nanodiamond Using Click Chemistry. *Adv. Funct. Mater.* **2011,** *21* (3), 494-500.

[4] Powell, L. R.; Piao, Y.; Wang, Y., Optical Excitation of Carbon Nanotubes Drives Localized Diazonium Reactions. *The Journal of Physical Chemistry Letters* **2016,** *7* (18), 3690-3694.

[5] Arisio, C.; Cassou, C. A.; Lieberman, M., Loss of Siloxane Monolayers from GaN Surfaces in Water. *Langmuir* **2013,** *29* (17), 5145-5149.

[6] https://www.thermofisher.com/order/catalog/product/C6121 =126 (accessed 2017/07/24).

[7] Abdalla, S.; Marzouki, F.; Al-ameer, S.; Turkestani, S., Electric Properties of n-GaN: Effect of Different Contacts on the Electronic Conduction. *International Journal of Physics* **2013,** *1* (2), 41-48.

[8] Stocker, D. A.; Schubert, E. F.; Redwing, J. M., Crystallographic wet chemical etching of GaN. *Appl. Phys. Lett.* **1998,** *73* (18), 2654-2656.

7

Conclusions

Porous GaN particles and layers were obtained in a single step by the direct reaction of gallium and ammonia in a CVD furnace at high temperature (1203 K) and relatively low pressure (15 torr). This technique supposes a reduction of time, and costs in the production of porous GaN, being that no post-treatment is needed for the production of porosity, since the porosity is induced during the crystal growth process.

We have studied the influence of various reaction parameters on the morphology and porosity of the porous GaN particles grown by the direct reaction of gallium and ammonia. The reaction parameters studied in this thesis were: (i) the gallium container shape, (ii) the gallium quantity, (iii) the deposition time, (iv) the catalyst, and (v) the substrate. All of them seem to influence the final morphology of the porous GaN particles. The gallium container shape modifies the gallium evaporation rate and subsequently the deposition rate on the substrate. The flat gallium container allows the gallium to spread along the container without any limitation, whereas in the half cylindrical tube the gallium is more restricted in the lateral direction, and the concave container traps the gallium in the bottom on the container, and the only way to escape the container is by climbing the walls against gravity. The fastest evaporation of gallium occurs when the flat container is used whereas the slower but constant evaporation of gallium occurs when the concave container is used. The half cylindrical tube produces an intermediate

evaporation rate. This clearly affects the earlier consumption of metallic gallium for the synthesis of porous GaN particles. The GaN particles obtained when using a flat plate or a half cylindrical tube as gallium holders were similar, with sizes between 2-3 μm, and a similar degree of porosity, whereas the particles obtained using the concave container show bigger sizes ~4 μm, and the pores seem to be smaller in diameter. The gallium quantity affects to the substrate coating with porous GaN particles. It has been observed that above a certain gallium quantity (0.4 g) no further deposition is observed, thus, identifying the optimal gallium quantity. The deposition time of the porous particles grown on silicon substrates has an effect on the substrate coating, but not an obvious effect on the particles sizes for the deposition times analyzed. It has been observed that for long deposition times (above 60 min) the particles seem to decompose, since the reactor is at a relatively high temperature and low pressure, and the gallium evaporation is prevented by the formation of a GaN layer on the surface of the metallic source. Despite the slightly texturation of the porous GaN particles grown using thin films of metallic Ni, Pt and Au, only when the porous GaN particles where grown using a thin film of metallic Ti a clear orientation of the particles was observed. The substrate may play a role on the orientation of the metallic catalyst needed for the growth of porous GaN, which acts as an intermediate layer between the GaN and the substrate.

The results obtained by CL and EPMA points in the right direction to confirm the incorporation of Mg in GaN when $Mg(acac)_2$ was used as magnesium source for the *p*-type doping of porous GaN. Also, the results obtained by CL confirm the incorporation of Si when using $Si(ac)_4$ as silicon source for the *n*-type doping of porous GaN. However, in order to confirm the *p*-type and *n*-type conductivity, and thus, the successful doping, Hall measurements are required to be performed in the futre.

Despite the results obtained for the Mg- and Si-doping of GaN, the results obtained for the formation of porous InGaN ternary alloys using either In/Ga alloy and $In(acac)_3$ are not promising. The results obtained by CL do

not indicate any evidence of the incorporation of In in the porous GaN structure. Moreover, the formation of Ga_2O_3 is observed by both XRD and CL.

Porous layers of GaN were successfully grown on GaN/sapphire substrates. We studied the influence of the deposition time on the morphology, the porosity degree, and the wetting properties. We also characterized structurally the layers by optical means. The deposition time has a clear influence on the mean pore diameter as it was confirmed by the image processing method of the SEM images and by the AFM measurements. The mean pore diameter tends to increase with the deposition time until a certain limit which was found to be 45 min, above that time the pore diameter does not increase further but decreases. The porous area is more or less constant independently of the deposition time; however, this effect is compensated by the pore density which decreases with the increase of the deposition time, again, until the limit of 45 min of deposition time. The resulting morphology of the porous GaN layer for the different deposition times affects the wetting properties of the porous GaN layers, getting to switch from a hydrophilic material into a hydrophobic one by tuning parameters such as the pore diameter, the wall distance between pores and the pore height. The structural properties of the porous GaN layers were studied by PL at 80 K and RT, CL and resonant Raman scattering. The results obtained by these three techniques are consistent and show a tensile strain at low deposition times which tends to relax with the increase of the deposition time, as the thickness of the layer increases. The cause of this strain is the existence of structural defects that need to be further investigated in the future to assess its origin.

Finally, the chemical functionalization of GaN surface with silane molecules and diaznonium salts, and later characterization was carried out. The results obtained on the functionalization of the GaN surface with silane molecules, in our case APTMS, point out that the chemical functionalization is successful when it occurs under sonication at 323 K (50 °C), whereas seems not to work when the functionalization occurs under stirring at RT. GaN

surfaces chemically functionalized with diazonium salts where confirmed by XPS for the samples functionalized with 4 (2 azidoethyl)phenylamine and 4 (2 choroethyl)benzoldiazonium tetrafluoroborate. The functionalization of the GaN surface with 4-(prop-2-yn-1-yloxy)benzenediazonium tetrafluoroborate was confirmed by fluorescent microscopy, since the alkyl moiety on the 4-(prop-2-yn-1-yloxy)benzenediazonium tetrafluoroborate is used to react with the azide group of the fluorescent dye TAMRA-azide using click-chemistry. The comparison of the functionalized GaN surface with 4-(prop-2-yn-1-yloxy)benzenediazonium tetrafluoroborate and further reacted with TAMRA dye, with a blank sample, confirms the functionalization of the GaN surface with 4-(prop-2-yn-1-yloxy)benzenediazonium tetrafluoroborate. Despite the evidences obtained in the previous cases that point out to a successful functionalization of GaN surfaces, it was not the case when GaN surfaces were functionalized with conjugated diazonium salts 4 ((4 (2,2,2-trifluoroacetamido)phenyl)ethynyl)benzenediazonium tetraborofluorate and 4-((4-(*tert*-butoxycarbonylamino)phenyl)ethynyl)benzenediazonium tetrafluoroborate. No fluorescence was observed on the fluorescence microscope after the linking of ATTO-465 to the amine moiety of the attached diazonium salt, revealing that no functionalization was achieved.

Despite all the progress made during this thesis, further characterization of the doped samples and the functionalized samples has to be done. In the case of doped porous GaN samples with magnesium and silicon Hall measurements are needed to properly characterize the carrier concentration, and thus, confirm its applications for electronics and optoelectronics. To properly study the functionalization of GaN surfaces with diazonium salts an interesting proposition would be the functionalization *in situ* right before the XPS analysis, in order to avoid contamination of the sample. Once this would be confirmed, the next step is to develop a complete sensing system linking the desired antibody to the molecule attached to the GaN surface, which is used as an intermediate.

Appendix 1: Calculation of the angle between vectors perpendicular to different crystallographic planes

In wurtzite GaN:

$$\alpha = \beta = 90° \qquad a = b = 3.18940\ \text{Å}$$

$$\gamma = 120° \qquad c = 5.18614\ \text{Å}$$

$$|\vec{a^*}| = |\vec{b^*}| = \frac{1}{|\vec{a}|\cos 30} = 0.362\ \text{Å}^{-1}$$

$$|\vec{c^*}| = \frac{1}{|\vec{c}|\cos 0} = 0.193\ \text{Å}^{-1}$$

$$\alpha^* = 90°;\ \beta^* = 90°;\ \gamma^* = 60°$$

▪ Angle between the vectors perpendicular to the $(11\bar{2}0)$ and $(10\bar{1}1)$ planes:

$$(\vec{a^*} + \vec{b^*})(\vec{a^*} + \vec{c^*}) = |(\vec{a^*} + \vec{c^*})||(\vec{a^*} + \vec{b^*})|\cos\delta_1$$

$$(\vec{a^*} + \vec{b^*})(\vec{a^*} + \vec{c^*}) = |\vec{a^*}|^2 + |\vec{a^*}||\vec{c^*}|\cos\beta^* + |\vec{b^*}||\vec{a^*}|\cos\gamma^* + |\vec{b^*}||\vec{c^*}|\cos\alpha^*$$
$$= |\vec{a^*}|^2 + |\vec{b^*}||\vec{a^*}|\cos\gamma^* = |\vec{a^*}|^2 + |\vec{a^*}|^2\cos\gamma^* = \frac{3}{2}|\vec{a^*}|^2$$

$$|(\vec{a^*} + \vec{c^*})| = \sqrt{(\vec{a^*} + \vec{c^*})(\vec{a^*} + \vec{c^*})} = \sqrt{|\vec{a^*}|^2 + |\vec{a^*}||\vec{c^*}|\cos\beta^* + |\vec{c^*}|^2}$$
$$= \sqrt{|\vec{a^*}|^2 + |\vec{c^*}|^2}$$

$$|(\vec{a^*} + \vec{b^*})| = \sqrt{(\vec{a^*} + \vec{b^*})(\vec{a^*} + \vec{b^*})} = \sqrt{|\vec{a^*}|^2 + 2|\vec{a^*}||\vec{b^*}|\cos\gamma^* + |\vec{b^*}|^2}$$
$$= \sqrt{2|\vec{a^*}|^2 + 2|\vec{a^*}|^2\cos\gamma^*}$$

$$\cos\delta_1 = \frac{(\vec{a^*} + \vec{b^*})(\vec{a^*} + \vec{c^*})}{|(\vec{a^*} + \vec{c^*})||(\vec{a^*} + \vec{b^*})|} = \frac{|\vec{a^*}|^2 + |\vec{a^*}|^2\cos\gamma^*}{\sqrt{|\vec{a^*}|^2 + |\vec{c^*}|^2}\sqrt{2|\vec{a^*}|^2 + 2|\vec{a^*}|^2\cos\gamma^*}}$$

$$\delta_1 = 40.15°$$

▪ Angle between the vectors perpendicular to the $(10\bar{1}1)$ and $(10\bar{1}0)$ planes:

$$(\vec{a^*})(\vec{a^*}+\vec{c^*}) = |(\vec{a^*})||(\vec{a^*}+\vec{c^*})|\cos\delta_2$$

$$(\vec{a^*})(\vec{a^*}+\vec{c^*}) = |\vec{a^*}|^2 + |\vec{a^*}||\vec{c^*}|\cos\beta^* = |\vec{a^*}|^2$$

$$|(\vec{a^*}+\vec{c^*})| = \sqrt{(\vec{a^*}+\vec{c^*})(\vec{a^*}+\vec{c^*})} = \sqrt{|\vec{a^*}|^2 + 2|\vec{a^*}||\vec{c^*}|\cos\beta^* + |\vec{c^*}|^2}$$
$$= \sqrt{|\vec{a^*}|^2 + |\vec{c^*}|^2}$$

$$\cos\delta_2 = \frac{(\vec{a^*})(\vec{a^*}+\vec{c^*})}{|(\vec{a^*})||(\vec{a^*}+\vec{c^*})|} = \frac{|\vec{a^*}|^2}{\vec{a^*}\sqrt{|\vec{a^*}|^2 + |\vec{c^*}|^2}}$$

$$\delta_2 = 28.04°$$

▪ Angle between the vectors perpendicular to the $(11\bar{2}0)$ and $(10\bar{1}0)$ planes:

$$(\vec{a^*})(\vec{a^*}+\vec{b^*}) = |(\vec{a^*})||(\vec{a^*}+\vec{b^*})|\cos\delta_3$$

$$(\vec{a^*})(\vec{a^*}+\vec{b^*}) = |\vec{a^*}|^2 + |\vec{a^*}||\vec{b^*}|\cos\gamma^* = |\vec{a^*}|^2 + |\vec{a^*}|^2\cos\gamma^*$$
$$= |\vec{a^*}|^2(1+\cos\gamma^*)$$

$$|(\vec{a^*}+\vec{b^*})| = \sqrt{(\vec{a^*}+\vec{b^*})(\vec{a^*}+\vec{b^*})} = \sqrt{|\vec{a^*}|^2 + 2|\vec{a^*}||\vec{b^*}|\cos\gamma^* + |\vec{b^*}|^2}$$
$$= \sqrt{|\vec{a^*}|^2 + 2|\vec{a^*}|^2\cos\gamma^* + |\vec{a^*}|^2} = \sqrt{2|\vec{a^*}|^2 + 2|\vec{a^*}|^2\cos\gamma^*}$$
$$= \sqrt{2|\vec{a^*}|^2(1+\cos\gamma^*)} = |\vec{a^*}|\sqrt{2(1+\cos\gamma^*)}$$

$$\cos\delta_3 = \frac{(\vec{a^*})(\vec{a^*}+\vec{b^*})}{|(\vec{a^*})||(\vec{a^*}+\vec{b^*})|} = \frac{|\vec{a^*}|^2(1+\cos\gamma^*)}{|\vec{a^*}||\vec{a^*}|\sqrt{2(1+\cos\gamma^*)}} = \frac{1+\cos\gamma^*}{\sqrt{2(1+\cos\gamma^*)}}$$

$$\delta_3 = 30.00°$$

Appendix 2: Synthesis and characterization of the organic molecules and its intermediates for the functionalization of GaN surfaces

*Synthesis of 4-(2-azidoethyl)phenylamine (**1**)*

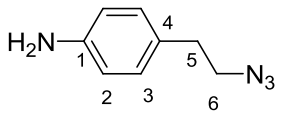

1.5 g (11 mmol) of 4-aminophenethyl alcohol was dissolved in a mixture of 8 ml (20%) of carbon tetrachloride and 32 ml (80%) of DMF. After, 2.9 g (11 mmol) of triphenylphosphine were added to the solution, and finally 0.84 g (13 mmol) of sodium azide were added to the solution. The mixture was heated up to 363 K (90 °C) for 2h under reflux. After cooling to RT, 30 ml of water were added to the mixture and stirred for another 10 min. Subsequently, the mixture was extracted twice with 50 ml of diethyleter and the organic phase was washed three times with 30 ml of water. The organic phase was then dried over sodium sulphate. The mixture was then placed in the rotavap to evaporate the solvent. After evaporation a yellow viscous liquid remained in the flask.

The yield of the reaction was 1.3628 g of 4-(2-azidoethyl)phenylamine (8.4 mmol, 77%).

Figure A2.1 shows the FT-IR spectrum of 4-(2-azidoethyl)phenylamine. The spectrum confirms the presence of N_3 through the peak located at 2096 cm^{-1}. No broad band was observed at ~3400 cm^{-1} corresponding to the –OH group indicating that the –OH group has been substituted for the azide group. The main vibrations identified in this spectrum together with their relative intensity in the spectrum and the assignations to the corresponding vibration are listed below Figure A2.1.

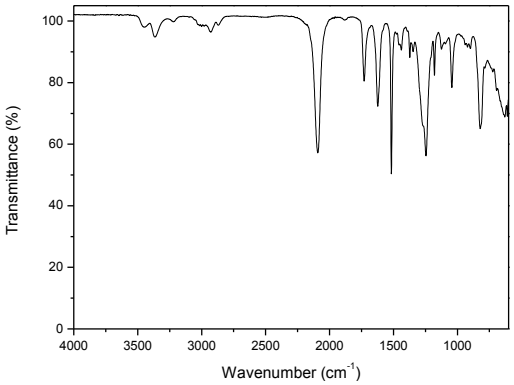

Figure A2.1. FR-IR spectrum of 4-(2-azidoethyl)phenylamine synthesis (**1**).

FT-IR (ATR): $\tilde{\nu}$ = 3361 (br, ν(N-H)), 3222 (m, ν(Ar-H)), 2925 (m, ν(C-H)), 2868 (w), 2096 (s, ν(N≡N)), 1729 (m), 1621 (m), 1520 (s), 1432 (w), 1369 (w), 1350 (w), 1242 (s, br), 1179 (m), 1122 (w), 104 0(s), 913 (w), 825 (s, δ(C-H_{arom})) cm^{-1}.

Figure A2.2 shows the ^{1}H-NMR spectrum recorded for the 4-(2-azidoethyl)phenylamine that confirms the presence of two different protons in the aromatic's region, two different protons in the alkene's region al low ppm and a broad peak corresponding to the amine protons at δ = 3.6 ppm. The chemical shift and the coupling constants for each proton are listed below Figure A2.2.

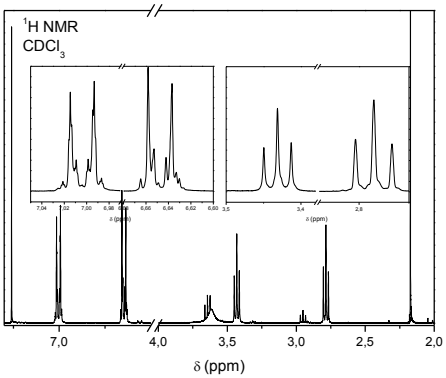

Figure A2.2. NMR spectrum of 4-(2-azidoethyl)phenylamine (**1**) in the inset are magnified the peaks corresponding to the compound.

^{1}H-NMR (400MHz, $CDCl_3$): δ = 7.00 (m, 2H; 3-H), 6.65 (m, 2H; 2-H), 3.62 (br s 2H; N-H_2), 3.43 (t, ^{3}J = 7.26Hz, 2H; 5-H), 2.79 (t, ^{3}J = 7.26Hz, 2H; 6-H) ppm.

*Synthesis of 4-(2-chloroethyl)benzoldiazoniumtetrafluoroborat (**3**)*

The first step to synthesize 4-(2-chloroethyl)benzoldiazoniumtetrafluoroborat (**3**) is the synthesis of 1-amino-4-(2-cloroethyl)benzol-hydroclorid (**2**) as an intermediate product starting from 2-(4-aminophenyl)ethanol.

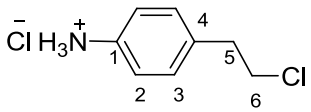

2.00 g (14.58 mmol) of 2-(4-aminophenyl)ethanol were dissolved in 30 ml of dried CH_2Cl_2 and 0.4 ml of DMF in an ice-bath at 273 K (0 °C). After, 2 ml of $SOCl_2$ (28 mmol) were added and the reaction was kept under stirring for 18 h at RT. Afterwards the reaction, the mixture was heated up under reflux at 328-333 K (55-60 °C) for 2 h. After reflux, the solvent was removed in the rotavap. 5 ml of concentrated HCl were added drop by drop to the solid under ice-bath at 273 K (0 °C) and a solid is formed. This solid was washed with 20 ml of concentrated HCl and 20 ml of acetone. The raw product was placed in a flask with 3 ml of acetone and heated up under refux for 5 min. The product was then filtered off with 10 ml of acetone. The solid was dried in a desiccator.

The yield of the reaction was 643.7 mg of 1-amino-4-(2-cloroethyl)benzol-hydroclorid (3.35 mmol, 23%).

Figure A2.3 shows the FT-IR spectrum of 1-amino-4-(2-cloroethyl)benzol-hydroclorid. The spectrum confirms the presence of a broad band at 2818 cm^{-1} assigned to the protonated amine. No broad band was observed at ∼3400 cm^{-1} corresponding to the –OH group indicating that the –OH group has been substituted for the chloride group.

Also, strong peaks between 800-600 cm^{-1} are assigned to C-Cl bonds. The main vibrations identified in this spectrum together with their relative intensity in the spectrum and the assignations to the corresponding vibration are listed below Figure A2.3.

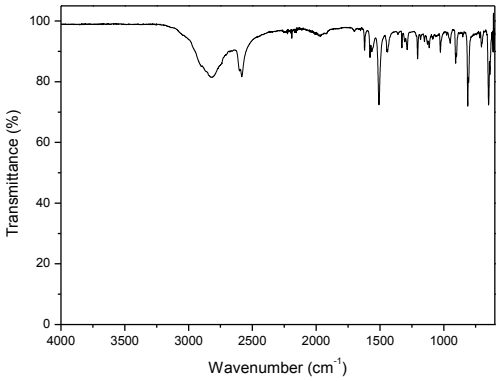

Figure A2.3. FT-IR spectrum of 1-amino-4-(2-cloroethyl)benzol-hydroclorid (**2**).

FT-IR (ATR): $\tilde{\nu}$ = 2818 (s,br), 2582 (s), 1969 (w), 1620 (m), 1568 (m), 1507 (s), 1438 (m), 1358 (w), 1329 (w), 1288 (m), 1204 (m), 1150 (w), 1116 (w), 1026 (w), 951 (w), 908 (m), 810 (s), 703 (w), 650 (s) cm^{-1}.

^{1}H-NMR (400MHz, D_2O): δ = 7.44 (m, 2H; 2-H), 7.34 (m, 2H; 3-H), 3.84 (t, ^3J = 6.8 Hz, 2H; 5-H), 3.12 (t, ^3J = 6.8Hz, 2H; 6-H) ppm.

For the synthesis of 4-(2-chloroethyl)benzoldiazonium tetrafluoroborat

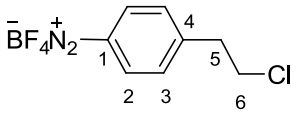

553 mg (2.88 mmol) of 1-amino-4-(2-chlorethyl)benzol-hydrochlorid (**2**) were dissolved in 4.8 ml of water and 4 ml of a solution of 50% HBF_4 were added. The mixture was on an ice bath and a solution formed by 220 mg (3.2 mmol) of $NaNO_2$ and 0.65 ml of water was added dropwise to the solution. Then, the ice bath was removed and the solution was left under stirring at RT for 30 min. After, the mixture was cooled down again in the ice bath and the precipitated solid was filtered and washed with 3 ml of a mixture of cool

HBF_4 solution:water in a proportion 1:1 (v:v) and 20 ml of diethylether. The solid obtained was dried in a dessicator under vacuum.

The yield of the reaction was 147.9 mg of 4-(2-chloroethyl)benzoldiazonium tetrafluoroborat (0.58 mmol, 20%).

Figure A2.4 shows the FT-IR spectrum of 4-(2-chloroethyl)benzoldiazonium tetrafluoroborat. The spectrum confirms that the broad band corresponding to the protonated amine at 2818 cm^{-1} has disappear and a peak at 2288 cm^{-1} corresponding to diazonium is observed. The main vibrations identified in this spectrum together with their relative intensity in the spectrum and the assignations to the corresponding vibration are listed below Figure A2.4.

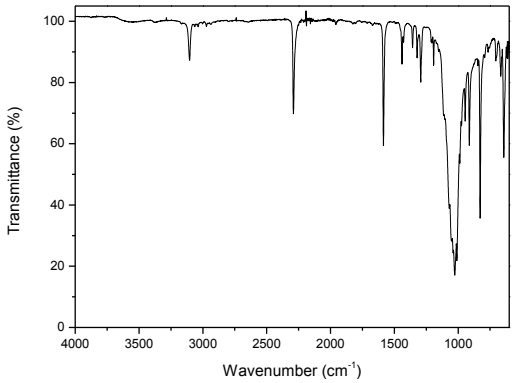

Figure A2.4. FT-IR spectrum of Synthesis of 4-(2-chloroethyl)benzoldiazonium tetrafluoroborat (**3**).

FT-IR (ATR): $\tilde{\nu}$ = 3104 (w), 2288 (s), 1586 (s), 1439 (w), 1356 (w), 1320 (w), 1290 (w), 1191 (w), 1029 (s), 945 (m), 912 (m), 827 (s), 665 (w), 642 (s) cm^{-1}.

Figure A2.5 shows the ^{1}H-NMR spectrum recorded for the 4-(2-chloroethyl)benzoldiazonium tetrafluoroborat that confirms the presence of two different protons in the aromatic's region and two different protons in the alkene's region al low ppm. The chemical shift and the coupling constants for each proton are listed below Figure A2.5.

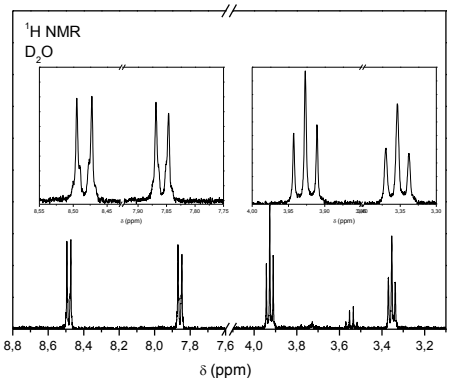

Figure A2.5. NMR spectrum of 4-(2-chloroethyl)benzoldiazonium tetrafluoroborat (**3**).

in the inset are magnified the peaks corresponding to the compound.

^{1}H-NMR (400MHz, D_2O): δ = 8.48 (m, 2H; 2-H), 8.86 (m, 2H; 3-H), 3.84 (t, ^{3}J = 3.93.8 Hz, 2H; 5-H), 3.353 (t, ^{3}J = 6.8Hz, 2H; 6-H) ppm.

*Synthesis of 4-cyanobenzoldiazonium tetrafluoroborat (**4**)*

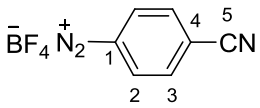

1.25 g (10.6 mmol) of 4-aminobenzonitrile were dissolved in 8.5 ml of an aqueous solution HBF_4 (25%) and cooled down with an ice bath. Then 686.5 mg (10 mmol) of $NaNO_2$ dissolved in 2.1 ml of water were added to the cooled mixture. The mixture was stirred on the ice bath for 15 min, then the ice bath is removed and we left the solution under stirring for 20 more minutes. After that, the mixture was cooled down again in an ice bath. The precipitated solid was cleaned and filtered with 20 ml of chilled diethyl ether.

The yield of the reaction was 1.9045 g of 4-cyanobenzoldiazonium tetrafluoroborat (16 mmol, 83%).

Figure A2.6 shows the FT-IR spectrum of 4-cyanobenzoldiazonium tetrafluoroborat. The spectrum confirms that no broad band corresponding to the amine is present and a peak at 2289 cm^{-1} corresponding to diazonium is observed. The main vibrations identified in this spectrum together with their

relative intensity in the spectrum and the assignations to the corresponding vibration are listed below Figure A2.6.

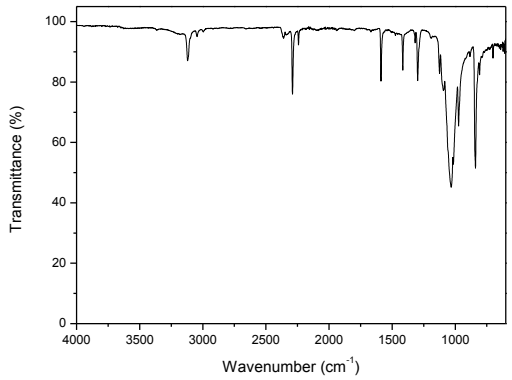

Figure A2.6. FT-IR spectrum of Synthesis of 4-cyanobenzoldiazoniumtetrafluoroborat (**4**).

FT-IR (ATR): $\tilde{\nu}$ = 3119 (m), 3046 (w), 2994 (w), 2358 (w), 2289 (s), 2242 (m), 1588 (s), 1416 (s), 1035 (s), 974 (m), 841 (s) cm^{-1}.

Figure A2.7 shows the ^{1}H-NMR spectrum recorded for the 4-cyanobenzoldiazonium tetrafluoroborat that confirms the presence of only two different protons in the aromatic's region and the protons of DMSO at δ = 2.5 ppm. The chemical shift and the coupling constants for each proton are listed below Figure A2.7.

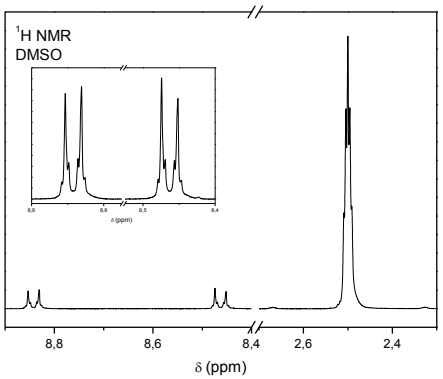

Figure A2.7. NMR spectrum of 4-cyanobenzoldiazoniumtetrafluoroborat (**4**) in the inset are magnified the peaks corresponding to the compound.

^{1}H-NMR (DMSO, 400MHz): δ = 8.86-8,83 (m, 2H, Aryl-2,6-H, ^{3}J = 8.9 Hz), 8.48-8.44 (m, 2H, 3,5-H, ^{3}J = 8.9 Hz) ppm.

*Synthesis of 4-nitrophenyl-propargylether (**5**)*

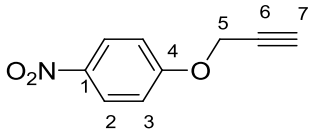

5.6 g (40 mmol) of 4-nitrophenol were dissolved in 50 ml of 0.8 N NaOH and heated at 333 K (60 °C). After a clear solution had formed, 1.3 g (4.0 mmol) of tetrabutylammonium bromide was added. Subsequently, 4.5 ml (42 mmol) of propargyl bromide (80 wt. % solution in toluene) were further diluted with 16 ml of toluene and added portionwise. The reaction mixture was stirred at 333 K (60 °C) for 24 h. After cooling to RT, the formed yellow precipitate was filtered off. Additionally, the toluene layer was separated and washed three times with 20 ml of water. Evaporation of the solvent afforded a yellowish solid. The combined crude products were dissolved in 50 ml of dioxane and poured into 80 ml of water. The precipitate was filtered off, washed with 400 ml of water and recrystallized from ethanol. Drying in vacuum yielded the product as colorless crystals.

The yield of the reaction was 78% for the synthesis of 4-nitrophenyl-propargylether.

FT-IR (ATR): $\tilde{\nu}$ = 3257 (s), 2125 (w), 1594 (s), 1498 (s), 1325 (s), 1245 (s), 1020 (s), 1015 (s), 836 (s) cm^{-1}.

^{1}H-NMR (250 MHz, CDCl3): δ = 8.21 (d, ^{3}J = 9.3 Hz, 2 H; 3-H), 7.04 (d, ^{3}J = 9.3 Hz, 2 H; 2-H), 4.79 (d, ^{3}J = 2.4 Hz, 2 H; 5-H), 2.58 (t, ^{3}J = 2.4 Hz, 1 H; 7-H) ppm.

*Synthesis of 4-aminophenyl-propargylether (**6**)*

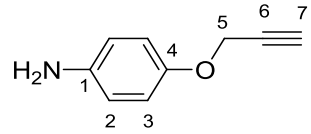

4.0 g (23 mmol) of 4-nitrophenyl propargylether were dissolved in 90 ml of dioxane. A cooled solution of 20 g (89 mmol) of $SnCl_2 \cdot 2H_2O$ in 45 ml of concentrated hydrochloric acid were added portionwise while keeping the temperature at 283 K (10 °C) using an ice bath. The reaction mixture was stirred at RT for 4 days, afterwards neutralized with sodium hydroxide and extracted twice with 100 ml of dichloromethane. The organic layer was dried over magnesium sulfate. Evaporation of the solvent afforded a brown viscous liquid. The crude product was purified by distillation (338 K (65 °C) at 0.1 mbar) and the product was obtained as a colorless highly viscous liquid which crystallized upon cooling.

The yield of the reaction was 82% for the synthesis of 4-aminophenyl-propargylether.

FT-IR (ATR): $\tilde{\nu}$ = 3431 (s), 3352 (s), 3262 (s), 2116 (w), 1622 (m), 1503 (s), 1201 (s), 1015 (s), 826 (s) cm^{-1}.

^{1}H-NMR (250 MHz, $CDCl_3$): δ = 6.83 (d, ^3J = 9.0 Hz, 2 H; 2-H), 6.65 (d, ^3J = 9.0 Hz, 2 H; 3-H), 4.61 (d, ^3J = 2.4 Hz, 2 H; 5-H), 3.49 (br. s, 2 H; NH2), 2.50 (t, ^3J = 2.4 Hz, 1 H; 7-H) ppm.

*Synthesis of 4-(prop-2-yn-1-yloxy)benzenediazonium tetrafluoroborate (**7**)*

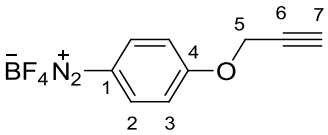

500 mg (3.4 mmol) of 4-aminophenyl-propargylether was dissolved in 3ml of water and 2.5 ml (20 mmol) of a 50% tetrafluoroboric acid solution. The solution was chilled with an ice bath and 0.7 ml (3.8 mmol) of 5.43 molar solution of sodium nitrite were added dropwise. The ice-bath was removed

and the reaction mixture was stirred for 20 min at RT. After stirring for 20 min the suspension was brought again to the ice bath and the precipitated solid was then filtered. The product was washed with 3 ml of a cooled mixture of tetrafluoroboric acid and water (1:1) and 20 ml of diethyl ether. The solid was dried in a desiccator *in vacuo* yielding a pale solid.

The yield of the reaction was 97% for the synthesis of 4-(prop-2-yn-1-yloxy)benzenediazonium tetrafluoroborate.

FT-IR (ATR): $\tilde{\nu}$ = 3253 (m) 3109 (m), 2262 (s), 2122 (w), 1579 (s), 1487 (m), 1275 (s), 1038 (s), 999 (s), 841 (s), 744 (m) cm^{-1}.

^{1}H-NMR (250 MHz, DMSO-d6): δ = 8.64 (d, ^3J = 9.4 Hz, 2 H; 2-H), 7.52 (d, ^3J = 9.4 Hz, 2 H; 3-H), 5.16 (d, ^3J = 2.4 Hz, 2 H; 5-H), 3.83 (t, ^3J = 2.4 Hz, 1 H; 7-H) ppm.

*Synthesis of 4-[(trimethylsilyl)ethynyl]aniline (**8**)*

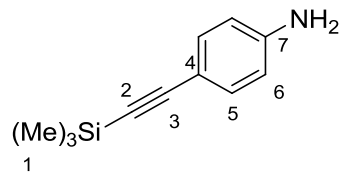

6.64 g (30 mmol) of 4-iodoaniline were dissolved in 150 ml of Di-isopropylamine (DIPA) with 0.21 g (0.3 mmol) of $Pd(PPh_3)_2Cl_2$ and 0.03 g (0.15 mmol) of CuI. The oxygen dissolved in the solution was removed by means of 3 cycles of freeze pump. After 3 cycles of freeze pump ~4.55 ml (31.5 mmol) of trimethylsilylacetylene under positive nitrogen pressure were added. The reaction mixture was stirred overnight under nitrogen atmosphere. The reaction mixture was rotavap to get rid of the DIPA solvent. 20 ml of water was added to the solid and the aqueous phase cleaned with 20 ml of diethyl ether for three times. The organic phase was dried with $MgSO_4$ and filtered. The dried organic phase was rotavap until the dryness of the solid. Column chromatography was performed to purify 4-[(Trimethylsilyl)ethynyl]aniline (**8**) with an eluent composition of 5:1 Cyclohexane/Ethyl acetate.

The yield of the reaction was 4.5508 g of 4-[(trimethylsilyl)ethynyl]aniline (24 mmol, 80%).

Figure A2.8 shows the FT-IR spectrum of 4-[(trimethylsilyl)ethynyl]aniline. The spectrum confirms that there is a band centered at 3289 cm^{-1} which corresponds to the amine and a sharp peak at 2163 cm^{-1} corresponding to the alkyne. The main vibrations identified in this spectrum together with their relative intensity in the spectrum and the assignations to the corresponding vibration are listed below Figure A2.8.

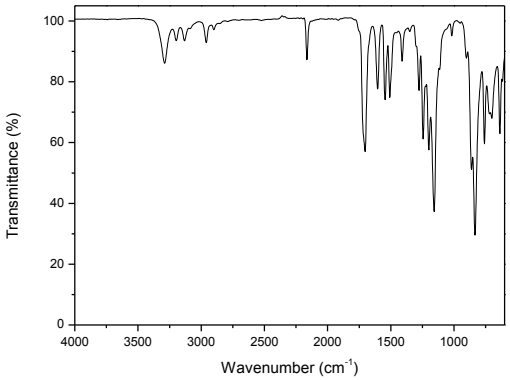

Figure A2.8. FT-IR spectrum of Synthesis of 4-[(Trimethylsilyl)ethynyl]aniline (**8**).

FT-IR (ATR): 3289 (s, ν(N-H)), 3195 (m), 3131 (m), 2960 (m, ν(C-Harom)), 2900 (m, ν(C-H)), 2163 (s, ν(C≡C)), 1544 (m), 1508 (m, ν(C=C)), 1411 (m), 1276 (w), 1243 (s), 1199 (m), 1157 (s, ν (Ar-N)) 1016 (w), 902 (2), 862(s), 835 (vs, δ(C-Harom)), 759 (s), 719 (m), 700 (m), 636 (s) cm^{-1}.

Figure A2.9 shows the ^{1}H-NMR spectrum recorded for the 4-[(trimethylsilyl)ethynyl]aniline that shows a broad band at high ppm attributed to protons from the amine, the presence of two different protons in the aromatic's region and protons in the alkene's region al low ppm from the TMS group. The chemical shift and the coupling constants for each proton are listed below Figure A2.9.

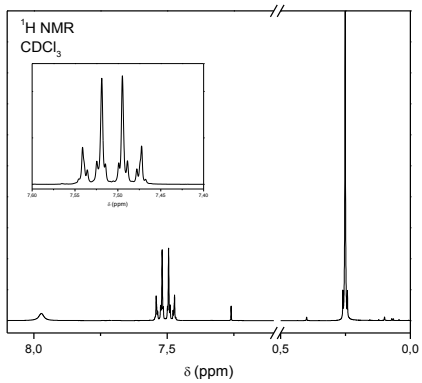

Figure A2.9. ^{1}H-NMR spectrum of 4-[(Trimethylsilyl)ethynyl]aniline (**8**) in the inset are magnified the peaks corresponding to the aromatic ring.

^{1}H-NMR (400 MHz, $CDCl_3$): δ = 7.97 (br. S, 1H; NH2), 7.53 (m, J = 8.99 Hz, 2H; 5-H), 7.48 (m, J = 8.99 Hz, 2H; 6-H), 0.25 (s, 9H; 1-H) ppm.

Figure A2.10 shows the composite pulse decoupling (CPD) and distortionless enhancement by polarization transfer (DEPT) ^{13}C-NMR spectrum recorded for the 4-[(trimethylsilyl)ethynyl]aniline. The DEPT ^{13}C-NMR allows us to distinguish the primary and tertiary carbons from the secondary and quaternary carbons, since the last do not appear in the spectra. The chemical shift and the corresponding assignation to the corresponding carbon are listed below Figure A2.9.

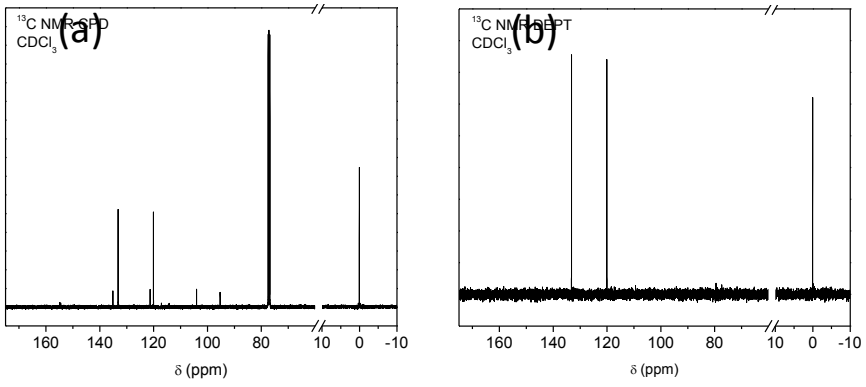

Figure A2.10. (a) CPD and (b) DEPT ^{13}C-NMR spectrum of 4-[(Trimethylsilyl)ethynyl]aniline (**8**).

^{13}C-NMR (400 MHz, $CDCl_3$): δ = 135.15 (C_q, C-7) 133.17 (C_t, C-5), 121.33 (C_q, C-4) 120.14(C_t, C-6), 104.08 (C_q, C-3), 95.31 (C_q,C-2) 0.03 (C_p, C-1) ppm.

*Synthesis of 2,2,2-trifluoro-N-[4-[2-(trimethylsilyl)ethynyl]phenyl]-acetamide (**9**)*

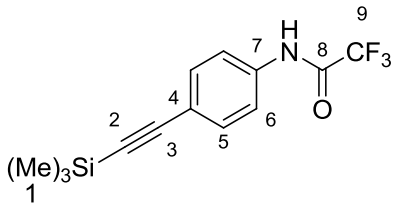

4.55 g (24 mmol) of 4-[(Trimethylsilyl)ethynyl]aniline (**8**) were added to 50 ml of dried THF under positive nitrogen atmosphere. 6.72 ml (48 mmol) of trifluoroacetic anhydride were added dropwise during 15 min to the solution immersed in an ice-bath in order to prevent the overheating of the solution. The solution was further stirred for 40 min at RT. Then, the reaction mixture was rotavaporated until dryness and the resulting crystalline solid was washed twice with milipore water in order to remove the excess of trifluoroacetic anhydride. The resulting solid was filtered under vacuum, yielding a white solid.

The yield of the reaction was 5.6836 g of 2,2,2-trifluoro-N-[4-[2-(trimethylsilyl)ethynyl]phenyl]-acetamide (19.9 mmol, 83%).

FT-IR (ATR): $\tilde{\nu}$ = 3291 (s, ν(N-H)), 3198 (m), 3131 (m), 2958 (m, ν(C-H_{arom})), 2897 (w, ν(C-H)), 2163 (s, ν(C≡C)), 1702 (s, ν(C=O)=, 1605 (s), 1545 (s), 1507 (s), 1409 (s), 1348 (w), 1275 (s), 1243 (s), 1196 (s), 1157 (s), 1112 (m), 1017 (w), 901 (m), 862 (s), 835 (vs, δ(C-H_{arom})), 758 (s), 721 (s), 698 (s), 634 (s) cm^{-1}.

Figure A2.11 shows the ^{1}H-NMR spectrum recorded for the 2,2,2-trifluoro-*N*-[4-[2-(trimethylsilyl)ethynyl]phenyl]-acetamide that confirms the presence of only one proton adjacent to a nitrogen corresponding to the amine. The chemical shift and the coupling constants for each proton are listed below Figure A2.11.

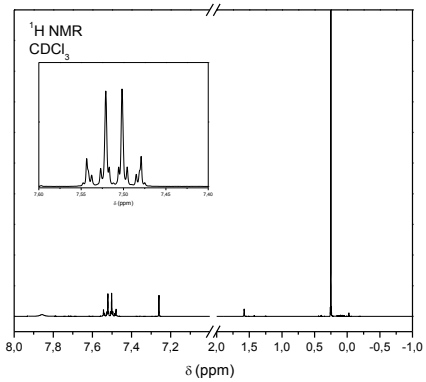

Figure A2.11. ^{1}H-NMR spectrum of 2,2,2-trifluoro-N-[4-[2-(trimethylsilyl)ethynyl]phenyl]-acetamide (**9**). The inset shows a magnification of the peaks corresponding to the aromatic ring.

^{1}H-NMR (400 MHz, $CDCl_3$): δ = 7.86 (br. S, 1H; NH), 7.53 (m, J = Hz, 2H; 5-H), 7.49 (m, J = Hz, 2H; 6-H), 0.25 (s, 9H; 1-H) ppm.

Figure A2.12 shows the composite pulse decoupling (CPD) and distortionless enhancement by polarization transfer (DEPT) ^{13}C-NMR spectrum recorded for the 2,2,2-trifluoro-*N*-[4-[2-(trimethylsilyl)ethynyl]phenyl]-acetamide. A signal in the CPD at 154 ppm confirms the presence of a carbonyl group from the TFA and a doublet centered at 115 ppm confirms the presence of a carbon surrounde by electronegative atoms like the fluorine of TFA. The chemical shift and the corresponding assignation to the corresponding carbon are listed below Figure A2.12.

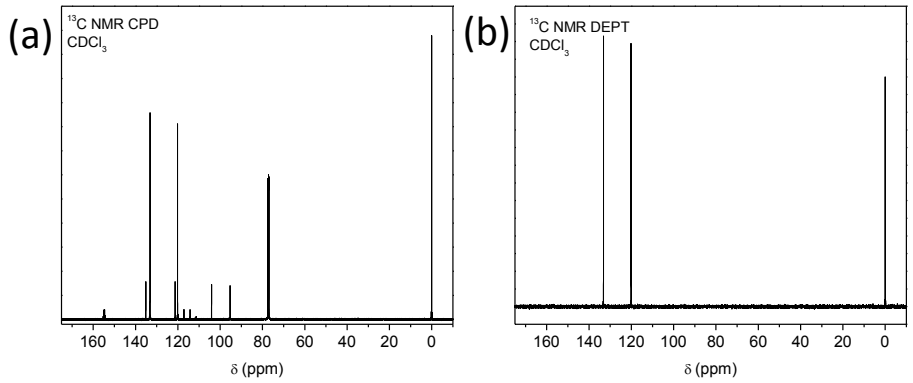

Figure A2.12. (a) CPD and (b) DEPT ^{13}C-NMR spectrum of 2,2,2-trifluoro-*N*-[4-[2-(trimethylsilyl)ethynyl] phenyl]-acetamide (**9**).

^{13}C-NMR (400 MHz, $CDCl_3$): δ = 154.17 (q, C_s, C-8) 135.14 (C_t, C-7), 133.20 (Cs,C-5), 121.33 (C_q, C-4) 120.14(C_t, C-6), 115.69 (q, C_p, C-9), 104.07 (C_q, C-3), 95.31 (C_q,C-2) 0.03 (C_p, C-1) ppm.

*Synthesis of N-(4-ethynylphenyl)-2,2,2-trifluoroacetamide (**10**)*

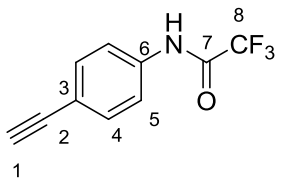

4.95 g (17 mmol) of *N*-(4-ethynylphenyl)-2,2,2-trifluoroacetamide (**9**) were dissolved in THF, then 4 ml of tetra-n-butylammonium fluoride (TBAF) solution 1 M in THF was added portionwise to the solution. The solution was stirred overnight at RT. The reaction mixture was dried in the rotavapor. In order to separate the compounds and to avoid the reaction of the free alkyne with the column, cold column chromatography was performed at 278 K (5 °C). The column was constantly refrigerated with isopropanol at 278 K (5 °C). The eluent choosen was a mixture 4:1 volume ratio (v:v) of cyclohexane/ethyl acetate. Due to solubility problems of the solid, it was solved in cyclohexane/ethyl acetate 1:1 (v:v).

The yield of the reaction was 3.3048 g of *N*-(4-ethynylphenyl)-2,2,2-trifluoroacetamide (15.5 mmol, 81%).

Figure A2.13 shows the FT-IR spectrum of *N*-(4-ethynylphenyl)-2,2,2-trifluoroacetamide. The spectrum confirms the deprotection of the TMS group with the presence of a peak at 3276 cm^{-1} corresponding to the H-C≡ stretching. The main vibrations identified in this spectrum together with their relative intensity in the spectrum and the assignations to the corresponding vibration are listed below Figure A2.13.

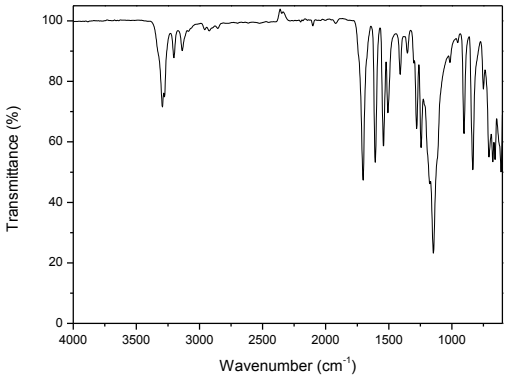

Figure A2.13. FT-IR spectrum of Synthesis *N*-(4-ethynylphenyl)-2,2,2-trifluoroacetamide (**10**).

FT-IR (ATR): $\tilde{\nu}$ = 3294 (s, ν(N-H)), 3276 (s ν(≡C-H)), 3203 (m), 3135 (m), 2957 (w), 2929 (w), 2851 (w), 2101 (w, ν(C≡C)), 1921(w), 1703 (s, ν(C=O)), 1608, 1541 (s), 1507 (m), 1408 (m), 1352 (w), 1301 (w), 1279 (m), 1243 (s), 1175 (s) 1146 (s), 1014 (w), 953 (w), 905 (m), 832 (s, δ(C-H_{arom})), 750 (m), 707(s), 675 (m), 656 (m), 609 (m) cm^{-1}.

Figure A2.14 shows the ^{1}H-NMR spectrum recorded for the *N*-(4-ethynylphenyl)-2,2,2-trifluoroacetamide that confirms the presence of one proton at ~3.1 ppm from the alkyne group. The chemical shift and the coupling constants for each proton are listed below Figure A2.14.

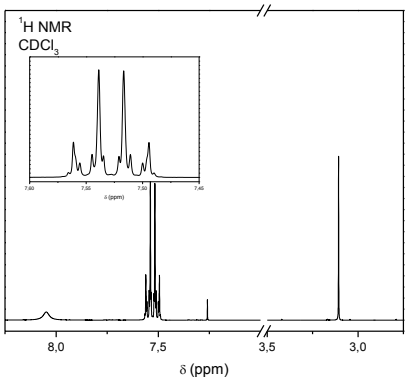

Figure A2.14. ^{1}H-NMR spectrum of *N*-(4-ethynylphenyl)-2,2,2-trifluoroacetamide (**10**). The inset shows a magnification of the peaks corresponding to the aromatic ring.

^{1}H-NMR (400 MHz, $CDCl_3$): δ = 8.05 (br. S, 1H; NH), 7.55 (m, J = 8.99 Hz, 2H; 4-H), 7.50 (m, J = 8.99 Hz, 2H; 5-H), 3.11 (s, 1H; 1-H) ppm.

Figure A2.15 shows the composite pulse decoupling (CPD) and distortionless enhancement by polarization transfer (DEPT) ^{13}C-NMR spectrum recorded for the *N*-(4-ethynylphenyl)-2,2,2-trifluoroacetamide that confirms the absence of the carbon peak corresponding to the TMS group at 0 ppm. The chemical shift and the corresponding assignation to the corresponding carbon are listed below Figure A2.15.

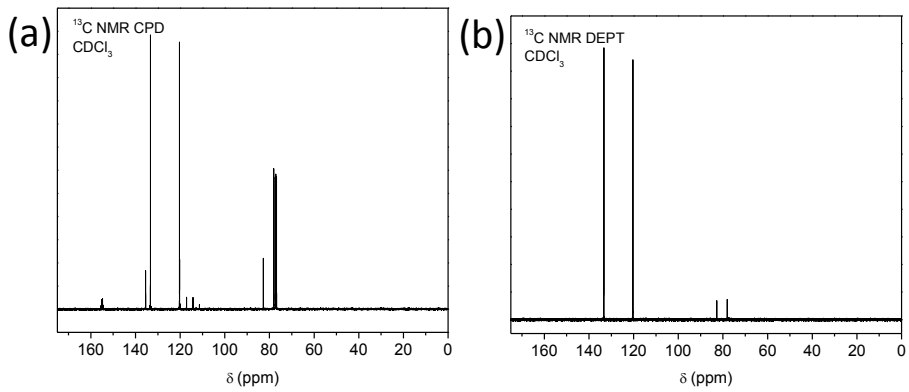

Figure A2.15. (a) CPD and (b) DEPT ^{13}C-NMR spectra of *N*-(4-ethynylphenyl)-2,2,2-trifluoroacetamide (**10**).

^{13}C-NMR (400 MHz, $CDCl_3$): δ = 154.94 (q, C_s, C-7) 135.46 (C_t, C-6), 133.33 (C_s,C-4), 120.32 (C_q, C-3) 120.14(C_t, C-5), 115.69 (q, C_p, C-8), 82.75 (C_q, C-2), 78.11 (C_q,C-1) 0.03 (C_p, C-1) ppm.

*Synthesis of N-(4-((4-aminophenyl)ethynyl)phenyl)-2,2,2-trifluoroacetamide (**11**)*

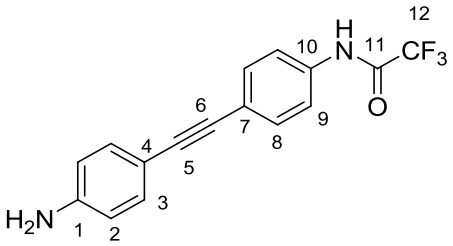

N-(4-((4-aminophenyl)ethynyl)phenyl)-2,2,2-trifluoroacetamide (**11**) was obtained by Sonogashira coupling between *N*-(4-ethynylphenyl)-2,2,2-trifluoroacetamide (**10**) and 4-iodoaniline. 1.09 g (4.7 mmol) of 4-iodoaniline were dissolved in 150ml of DIPA with 0.017 g (0.023 mmol) of $Pd(PPh_3)_2Cl_2$ and 2.4 mg (0.012 mmol) of CuI. 3 cycles of pump freeze were performed in order to remove the oxygen of the solution. Once the cycles were finished the flask was let under positive nitrogen pressure and 1 g (4.7 mmol) of *N*-(4-((4-aminophenyl)ethynyl)phenyl)-2,2,2-trifluoroacetamide (**10**) was added to the solution. The solution was under stirring overnight at RT protecting from the entrance of oxygen with a bubbler. DIPA solvent was removed in the rotavap. The solid obtained was dissolved in 100 ml of dichloromethane for the decantation. The organic phase was cleaned firstly with 100 ml and 10 ml of saturated NH_4Cl solution and subsequently cleaned 3 times with 30 ml of water. The organic phase was dried with $MgSO_4$ and filtered. The dichloromethane was removed in the rotavap. For column chromatography a 2:1 (v:v) cyclohexane:ethyl acetate eluent was chosen. The desired fraction was collected and rotavap until dryness.

The yield of the reaction was 1.2522 g of *N*-(4-((4-aminophenyl)ethynyl)phenyl)-2,2,2-trifluoroacetamide (4.1 mmol, 88%).

Figure A2.16 shows the FT-IR spectrum of *N*-(4-((4-aminophenyl)ethynyl)phenyl)-2,2,2-trifluoroacetamide. The spectrum shows a broader band at ~3450 cm^{-1} corresponding to the primary and secondary amine of the molecule. The main vibrations identified in this spectrum together with their relative intensity in the spectrum and the assignations to the corresponding vibration are listed below Figure A2.16.

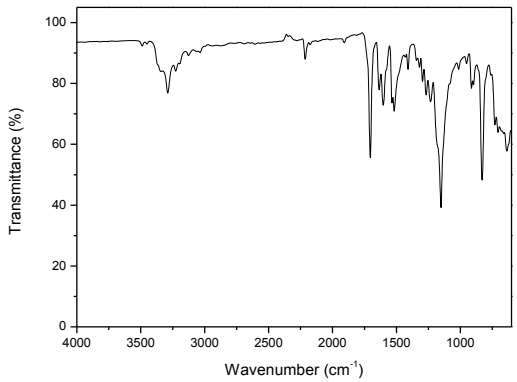

Figure A2.16. FT-IR spectrum of *N*-(4-((4-aminophenyl)ethynyl)phenyl)-2,2,2-trifluoroacetamide (**11**).

FT-IR (ATR): $\tilde{\nu}$ = 3489 (w, ν(N-H)), 3449 (w, ν(N-H)), 3343 (w), 3288 (s, ν(N-H)), 3226 (m), 3190 (w), 3125 (w), 3035 (w), 2213 (m, ν(C≡C)), 2173 (w), 1907 (w), 1703 (s, ν(C=O)), 1635 (m), 1602 (m), 1534 (m), 1516 (m), 1408 (w), 1295 (w), 1268 (m), 1233 (m), 1181 (m), 1151 (s), 1012 (w), 951 (w), 914 (w), 897 (w), 830 (s, δ(C-H_{arom})), 729 (m), 704 (m), 635 (m) cm^{-1}.

Figure A2.17 shows the ^{1}H-NMR spectrum recorded for the *N*-(4-((4-aminophenyl)ethynyl)phenyl)-2,2,2-trifluoroacetamide that confirms the presence of one proton adjacent to a nitrogen form the amide at ~11.3 ppm and two protons adjacent to a nitrogen atom from the amine at ~5.6 ppm.

Also four different protons in the aromatic region are observed. The chemical shift and the coupling constants for each proton are listed below Figure A2.17.

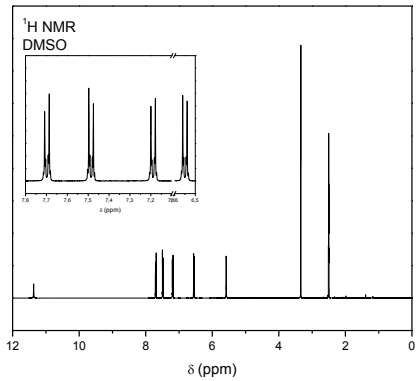

Figure A2.17. ^{1}H-NMR spectrum of *N*-(4-((4-aminophenyl)ethynyl)phenyl)-2,2,2-trifluoroacetamide (**11**). The inset shows a magnification of the peaks corresponding to the aromatic rings.

^{1}H-NMR (400 MHz, DMSO-d_6): δ = 11.37 (s, 1H; NH), 7.70 (m, J = 8.90 Hz, 2H; 9-H), 7.48 (m, J = 8.90 Hz, 2H; 8-H), 7.19 (m, J=8.65, 2H; 3-H), 6.55 (m, J=8.65, 2H; 2-H), 5.58 (s, 2H; NH_2) ppm.

Figure A2.18 shows the composite pulse decoupling (CPD) and distortionless enhancement by polarization transfer (DEPT) ^{13}C-NMR spectrum recorded for the *N*-(4-((4-aminophenyl)ethynyl)phenyl)-2,2,2-trifluoroacetamide. The DEPT ^{13}C-NMR spectra confirms the presence of two new tertiary peaks corresponding to the carbons of the aromatic ring coming from the 4-iodoaniline. The chemical shift and the corresponding assignation to the corresponding carbon are listed below Figure A2.18.

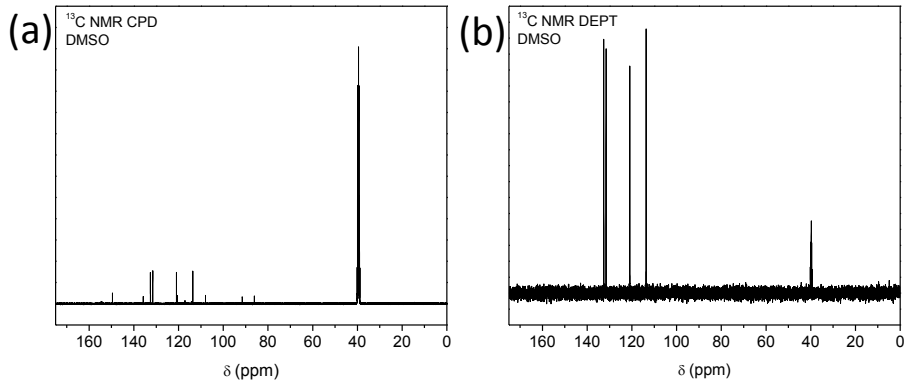

Figure A2.18. (a) CPD and (b) DEPT ^{13}C-NMR spectra of *N*-(4-((4-aminophenyl)ethynyl)phenyl)-2,2,2-trifluoroacetamide (**11**).

^{13}C-NMR (400 MHz, DMSO-d_6): δ = 154.43 (q, C_s, C-11) 149.59 (C_q, C-1), 135.58 (C_s,C-10), 132.58 (C_t, C-3),131.56 (C_t, C-8), 120.93(C_t, C-9), 120.50 (C_q, C-7), 115.72 (q, C_p, C-8), 113.64.75 (C_t, C-2), 107.97 (C_q,C-4), 91.51 (C_q,C-5) 86.11 (C_q, C-6) ppm.

*Synthesis of 4-((4-(2,2,2-trifluoroacetamido)phenyl)ethynyl)benzenediazonium tetraborofluorate (**12**)*

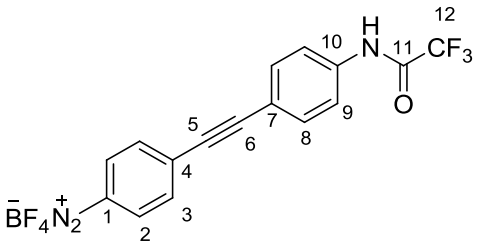

200 mg (0.657 mmol) of *N*-(4-((4-aminophenyl)ethynyl)phenyl)-2,2,2-trifluoroacetamide (**11**) were suspended in 2.5 ml of water and 0.5 ml of HBF_4 50%. Then the suspension was chilled in an ice-bath. 54.5 mg (1.97 mmol) of $NaNO_2$ were dissolved in 0.3 ml of water and were added dropwise to the cooled suspension. When the addition of $NaNO_2$ solution was finished, the solution was stirred for 20 min at RT. After 20 min under stirring, the solution was chilled with an ice-bath

again and the precipitate was filtered under vacuum with 3 ml of a cool mixture of HBF_4 (50%) and water (1:1) (v:v) and 20 ml of cool diethyl ether. Finally, an orange solid was obtained.

The yield of the reaction was 264.5 mg of 4-((4-(2,2,2-trifluoroacetamido)phenyl)ethynyl)benzenediazonium tetraborofluorate (0.65 mmol, 91%).

Figure A2.19 shows the FT-IR spectrum of 4-((4-(2,2,2-trifluoroacetamido)phenyl)ethynyl)benzenediazonium tetraborofluorate. The spectrum shows the characteristic of the diazonium group at 2265 cm^{-1}. The main vibrations identified in this spectrum together with their relative intensity in the spectrum and the assignations to the corresponding vibration are listed below Figure A2.19.

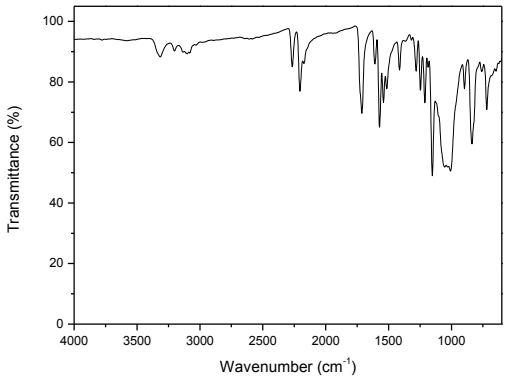

Figure A2.19. FT-IR spectrum of 4-((4-(2,2,2-trifluoroacetamido)phenyl)ethynyl)benzenediazonium tetraborofluorate (**12**).

FT-IR (ATR): $\tilde{\nu}$ = 3314 (m), 3201 (w), 3134 (m), 3099 (m), 3078 (m), 3028 (w), 2265 (m, ν(-N≡N)), 2205 (s, ν(C≡C)), 2172 (m), 1713 (s, ν(C=O)), 1607 (s), 1571 (s), 1539 (m), 1512 (m), 1411 (m), 1281 (m), 1245 (m), 1209 (m), 1152 (s), 1028 (s, ν(B-F)), 896 (w), 836 (m), 754 (w), 719 (m) cm^{-1}.

^{1}H-NMR (400 MHz, DMSO): Confusing information due to decomposition in the solvent.

^{13}C-NMR (400 MHz, DMSO): Confusing information due to decomposition in the solvent.

*Synthesis of tert-butyl 4-iodophenylcarbamate (**13**)*

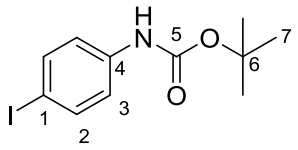

9.96 g (45 mmol) of 4-iodoaniline were dissolved in 125 ml of THF with 7.56 g (90 mmol) of $NaHCO_3$ and 16 ml (67.5 mmol) of di-*tert*-butyl dicarbonate (Boc anhydride). The reaction was stirred for 8 days at RT protected with a bubbler. The $NaHCO_3$ salts were removed by filtration. The solution was rotavaporated until 40 ml of solution was left. To the remaining solution 100 ml of ethyl acetate and 100 ml of water were added for extraction. The organic phase was subsequently washed for 3 times with water in order to remove the anhydride excess. Later on, the organic phase was dried with $MgSO_4$ and filtered. The solution was then rotavaporated until dryness. For column chromatography a ratio of 6:1 (v:v) cyclohexane/ethyl acetate was used as eluent. The desired fraction was collected and rotavap until the obtaining of a dry solid. The solid was finally recrystalized. For this purpose it was dissolved in 63 ml of cyclohexane and stirred. The solution was heated under reflux with the heat gun until the entire product was dissolved. Then, the solution was kept under constant heating for 5 minutes. After heating, the flask was cooled down to RT and finally stored in the fridge overnight. The solid was then filtered under vacuum and cleaned with chilled cyclohexane.

The yield of the reaction was 12.4996 g of *tert*-butyl 4-iodophenylcarbamate (39.2 mmol, 87%).

Figure A2.20 shows the FT-IR spectrum of *tert*-butyl 4-iodophenylcarbamate. The spectrum shows the peak at 1700 cm^{-1} corresponding to the carbonil group of the carbamate. The main vibrations identified in this spectrum together with their relative intensity in the

spectrum and the assignations to the corresponding vibration are listed below Figure A2.20.

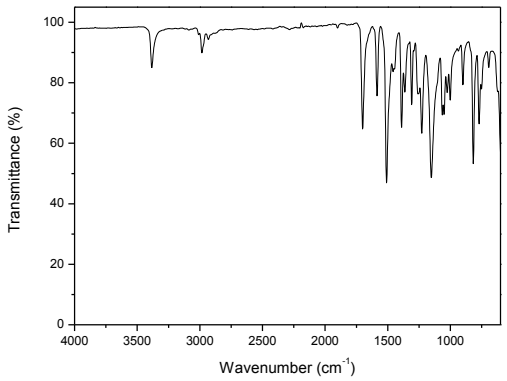

Figure A2.20. FT-IR spectrum of *tert*-butyl 4-iodophenylcarbamate (**13**).

FT-IR (ATR): $\tilde{\nu}$ = 3382 (s, ν(N-H)), 3009 (w), 2982 (m, ν(C-H)) 2931 (w), 2870 (w), 1901 (w), 1700 (s, (C=O)), 1583 (m), 1508 (s), 1457 (m), 1441 (m), 1390 (s), 1362 (m), 1308 (m), 1227 (s), 1152 (s), 1065 (m), 1049 (m), 1022 (m), 1000 (M), 936 (w), 898 (m), 816 (s, δ(C-H_{arom})), 768 (m), 751 (m), 690 (w) cm^{-1}.

Figure A2.21 shows the ^{1}H-NMR spectrum recorded for the *tert*-butyl 4-iodophenylcarbamate confirms the presence of two protons in the aromatic region, a proton adjacent to a nitrogen atom from the amide and protons from the *tert*-butyl group at ~1.5 ppm. The chemical shift and the coupling constants for each proton are listed below Figure A2.11.

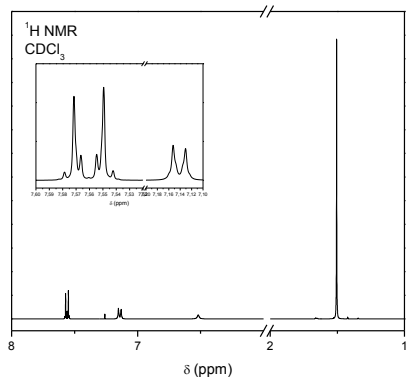

Figure A2.21. ^{1}H-NMR spectrum of *tert*-butyl 4-iodophenylcarbamate (**13**). The inset shows a magnification of the peaks corresponding to the aromatic ring.

^{1}H-NMR (400 MHz, $CDCl_3$): δ = 7.56 (m, J = 8.90 Hz, 2H; 1-H), 7.14 (m, J = Hz, 2H; 2-H), 6.52 (s, 1H; NH), 1.51 (s, 9H; 7-H) ppm.

Figure A2.22 shows the composite pulse decoupling (CPD) and distortionless enhancement by polarization transfer (DEPT) ^{13}C-NMR spectrum recorded for the *tert*-butyl 4-iodophenylcarbamate. The DEPT ^{13}C-NMR spectra confirms the presence of a primary carbon at low ppm corresponding to the alkane of the Boc group. The chemical shift and the corresponding assignation to the corresponding carbon are listed below Figure A2.22.

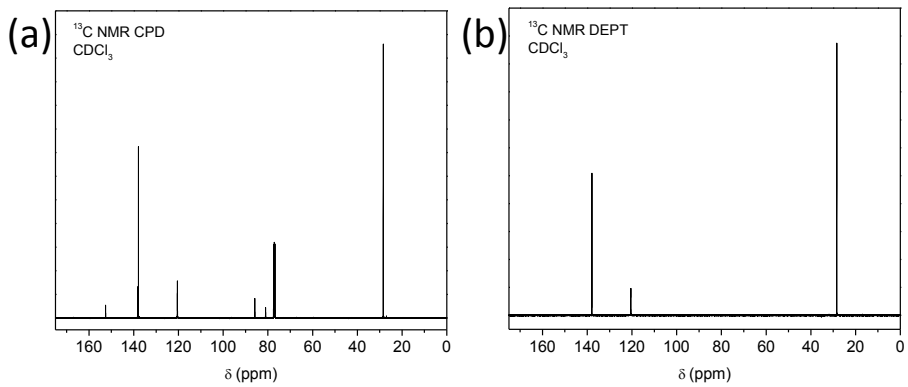

Figure A2.22. (a) CPD and (b) DEPT ^{13}C-NMR spectra of *tert*-butyl 4-iodophenylcarbamate (**13**).

^{13}C-NMR (400 MHz, $CDCl_3$): δ = 152.58 (C_s, C-5) 138.30 (C_q, C-4), 137.91 (C_t, C-2), 120.50 (C_t, C-3), 85.84 (C_q, C-1), 81.03(C_q, C-6), 28.42 (C_p, C-7) ppm.

*Synthesis of tert-butyl 4-((4-(2,2,2-trifluoroacetamido)phenyl)ethynyl)phenylcarbamate (**14**)*

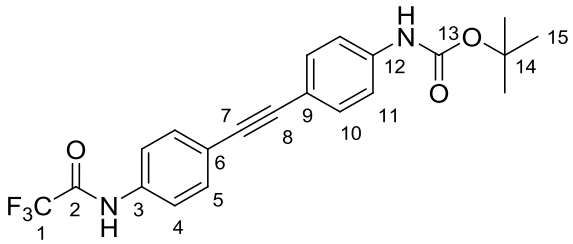

3.14 g (9.8 mmol) of *tert*-butyl 4-iodophenylcarbamate (**13**) were dissolved in 150 ml of DIPA, together with 34 mg (0.047 mmol) of $Pd(PPh_3)_2Cl_2$ and 0.0046 g (0.023 mmol) of CuI. Before the Sonogashira coupling reaction, 3 cycles of freeze pump were performed to remove the oxygen. After the 3 cycles of freeze pump, 2.00 g (9.4 mmol) of *N*-(4-ethynylphenyl)-2,2,2-trifluoroacetamide (**10**) were added to the solution under positive pressure of nitrogen. The solution was stirred overnight at RT and the flask was protected from the entrance of oxygen with a bubbler. When the coupling was complete, the flask was rotavaporated to remove the DIPA. The obtained solid was dissolved in 20 ml of diethyl ether for decantation. Then, 50 ml of water were added to the organic phase, and it was cleaned 3 times with 20 ml of diethyl ether. The organic phase was dried with $MgSO_4$ and filtered. For column chromatography a mixture of 5:1 (v:v) cyclohexane/ethyl acetate was used as eluent. The desired fraction was collected and rotavaporated until dryness.

The yield of the reaction was 2.7242 g of *tert*-butyl 4-((4-(2,2,2-trifluoroacetamido)phenyl)ethynyl)phenylcarbamate (6.74 mmol, 71.8%).

Figure A2.23 shows the FT-IR spectrum of *tert*-butyl 4-((4-(2,2,2-trifluoroacetamido)phenyl)ethynyl)phenylcarbamate. The spectrum shows a weak peak at 2213 cm^{-1} corresponding to the alkyne bond. The main vibrations identified in this spectrum together with their relative intensity in the spectrum and the assignations to the corresponding vibration are listed below Figure A2.23.

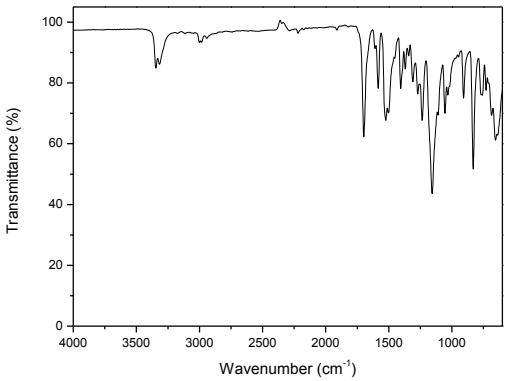

Figure A2.23. FT-IR spectrum of *tert*-butyl 4-((4-(2,2,2-trifluoroacetamido)phenyl)ethynyl)phenylcarbamate (**14**).

FT-IR (ATR): $\tilde{\nu}$ = 3291 (s, ν(N-H)), 3198 (m), 3131 (m), 2958 (m, ν(C-H_{arom})), 2897 (w, ν(C-H)), 2213 (w, ν(C≡C)), 1702 (s, ν(C=O)=, 1605 (s), 1545 (s), 1507 (s), 1409 (s), 1348 (w), 1275 (s), 1243 (s), 1196 (s), 1157 (s), 1112 (m), 1017 (w), 901 (m), 862 (s), 835 (vs, δ(C-H_{arom})), 758 (s), 721 (s), 698 (s), 634 (s) cm^{-1}.

Figure A2.24 shows the ^{1}H-NMR spectrum recorded for the *tert*-butyl 4-((4-(2,2,2-trifluoroacetamido)phenyl)ethynyl)phenylcarbamate that confirms the presence four different protons in the aromatic region and protons in the alkenes region from the *tert*-butyl group. Also the presence of protons adjacent to nitrogen are observed, one at higher ppm than the other due to the deshield produced from the presence of 3 electronegative fluorine atoms adjacent to the amide. The chemical shift and the coupling constants for each proton are listed below Figure A2.24.

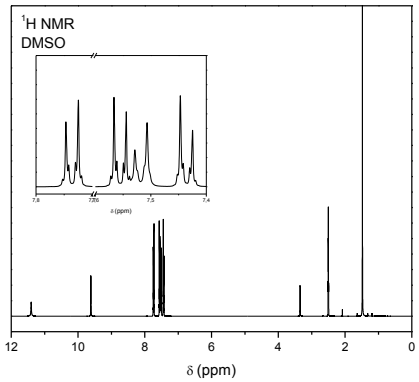

Figure A2.24. ^{1}H-NMR spectrum of *tert*-butyl 4-((4-(2,2,2-trifluoroacetamido)phenyl)ethynyl)phenylcarbamate (**14**). The inset shows a magnification of the peaks corresponding to the aromatic rings.

^{1}H-NMR (400 MHz, DMSO): δ = 11.40 (s, 1H, NH-TFA), 9.61 (s, 1H; NH-BoC), 7.73 (m, J = 8.8 Hz, 2H; 9-H), 7.55 (m, J = 8.8 Hz, 2H; 8-H), 7.52 (m, J = 8.8 Hz, 2H; 3-H), 7.44 (m, J = 8.8 Hz, 2H; 2-H), 1.48 (s, 9H; 15-H) ppm.

Figure A2.25 shows the composite pulse decoupling (CPD) and distortionless enhancement by polarization transfer (DEPT) ^{13}C-NMR spectrum recorded for the *tert*-butyl 4-((4-(2,2,2-trifluoroacetamido)phenyl)ethynyl)phenylcarbamate. The DEPT ^{13}C-NMR spectra confirms the presence of two new tertiary carbons in the region of the aromatic carbons, confirming the success in the Sonogashira coupling reaction.. The chemical shift and the corresponding assignation to the corresponding carbon are listed below Figure A2.25.

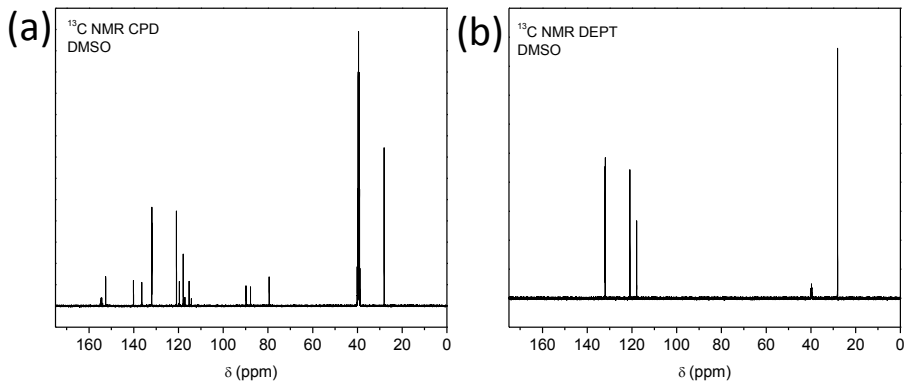

Figure A2.25. (a) CPD and (b) DEPT ^{13}C-NMR spectra of *tert*-butyl 4-((4-(2,2,2-trifluoroacetamido)phenyl)ethynyl)phenylcarbamate (**14**).

^{13}C-NMR (400 MHz, DMSO): δ = 154.47 (C_q, C-2) 152.56 (C_q, C-13), 140.13 (C_q, C-3), 136.40 (C_q, C-12), 132.02 (C_t, C-5), 131.94 (C_t, C-10), 120.92 (C_t, C-11), 117.91 (C_t, C-4), 117.43 (C_q, C-1), 117.11 (C_q, C-9), 114.24 (C_q, C-6), 89.81 (C_q, C-7), 87.79(C_q, C-8), 79.46(C_q, C-14), 20.06(C_p, C-15) ppm.

*Synthesis of tert-butyl 4-((4-aminophenyl)ethynyl)phenylcarbamate (**15**)*

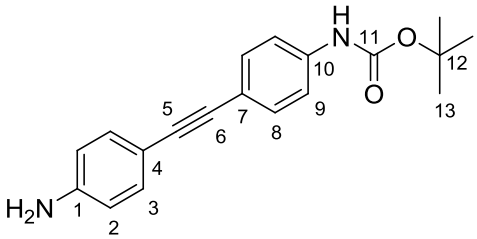

For the deprotection of the TFA protection group, 2.4 g (5.9 mmol) of 4-((4-(2,2,2-trifluoroacetamido)phenyl)ethynyl)phenylcarbamate (**14**) were dissolved in THF and 20ml (60 mmol) of NaOH 3 M were also added to the solution. The reaction mixture was stirred for 5 h at 343 K (70 °C). The solution was then rotavaporated yielding a humid solid due to the difficulty to remove the water. For column chromatography a ratio of 3:12 (v:v) cyclohexane/ethyl acetate was used as eluent. Due to solubility problems the

solid placed on the top of the sand layer of the column chromatography was covered with another sand layer. Then, the eluent was shifted to pure ethyl acetate. The desired fraction was collected and rotavaporated until dryness.

The yield of the reaction was 1.7712 g of *tert*-butyl 4-((4-aminophenyl)ethynyl)phenylcarbamate (5.74 mmol, 96%).

Figure A2.26 shows the FT-IR spectrum of *tert*-butyl 4-((4-aminophenyl)ethynyl)phenylcarbamate. The spectrum shows a peak at 3472 cm^{-1} corresponding to the primary amine resulting from the deprotection. The main vibrations identified in this spectrum together with their relative intensity in the spectrum and the assignations to the corresponding vibration are listed below Figure A2.26.

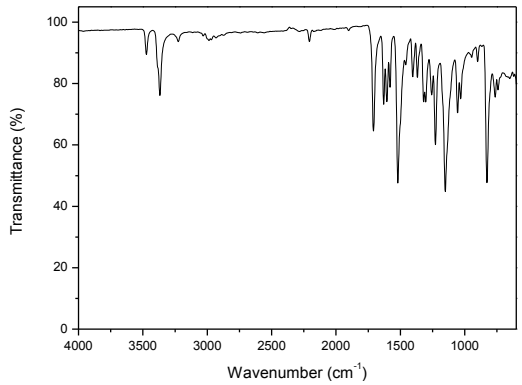

Figure A2.26. FT-IR spectrum of *tert*-butyl 4-((4-aminophenyl)ethynyl)phenylcarbamate (**15**).

FT-IR (ATR): $\tilde{\nu}$ = 3472 (m, ν(N-H)), 3366 (s ν(N-H)), 3225 (s ν(N-H)), 3031 (w, ν(C-H_{arom})), 2987 (w), 2967 (w, ν(C-H)), 2934 (w), 2874 (w, ν(C-H)), 2201 (m, ν(C≡C)), 1901 (w), 1709 (s, ν(C=O)), 1631 (m, δ (N-H)), 1604 (m), 1579 (m), 1520 (s), 1458 (w), 1405 (m), 1366 (m), 1319 (m), 1302 (m), 1256 (w), 1227 (m), 1150 (s), 1055 (m), 1030 (m), 900 (w), 825 (s, δ(C-H_{arom})), 764 (w, δ(N-H)), 740(w) cm^{-1}.

Figure A2.27 shows the ^{1}H-NMR spectrum recorded for the *tert*-butyl 4-((4-aminophenyl)ethynyl)phenylcarbamate that confirms the presence of two protons adjacent to a nitrogen group from the amine resulting from the

deprotection of the TFA group. The chemical shift and the coupling constants for each proton are listed below Figure A2.27.

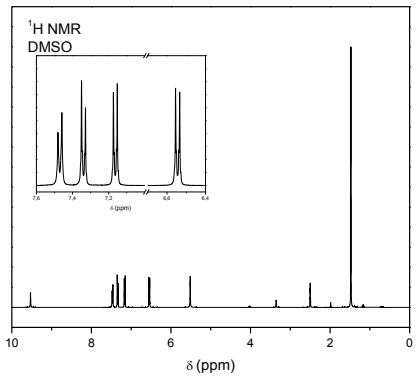

Figure A2.27. [1]H-NMR spectrum of *tert*-butyl 4-((4-aminophenyl)ethynyl)phenylcarbamate (**15**). The inset shows a magnification of the peaks corresponding to the aromatic rings.

^{1}H-NMR (400 MHz, DMSO): δ = 9.53 (s, H; NH), 7.47 (m, J = 8.7 Hz, 2H; 9-H), 7.34 (m, J = 8.7 Hz, 2H; 8-H), 7.16 (m, J = 8.6 Hz, 2H; 3-H), 6.54 (m, J = 8.6 Hz, 2H; 2-H), 5.52 (s, 2H; NH_2), 1.48 (s, 9H; 13-H) ppm.

Figure A2.28 shows the composite pulse decoupling (CPD) and distortionless enhancement by polarization transfer (DEPT) ^{13}C-NMR spectrum recorded for the *tert*-butyl 4-((4-aminophenyl)ethynyl)phenylcarbamate. The CPD ^{13}C-NMR spectra confirms the absence of the multiplet at 154 ppm from the TFA, confirming the success in the deprotection of the amine protected with TFA. The chemical shift and the corresponding assignation to the corresponding carbon are listed below Figure A2.28.

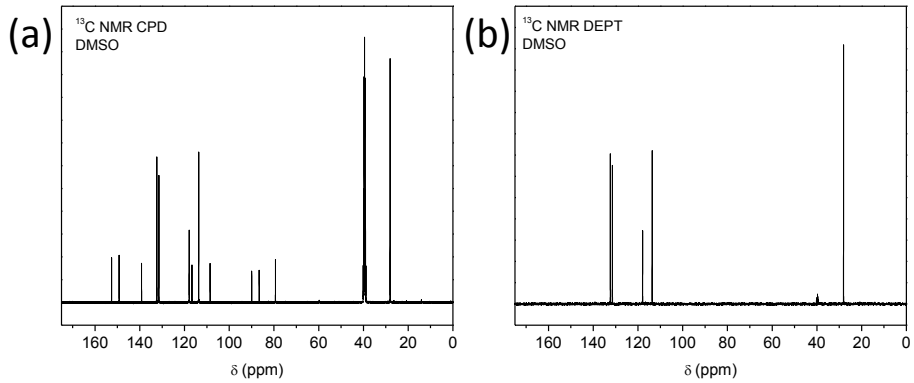

Figure A2.28. (a) CPD and (b) DEPT ^{13}C-NMR spectra of *tert*-butyl 4-((4-aminophenyl)ethynyl)phenylcarbamate (**15**).

^{13}C-NMR (400 MHz, DMSO): δ = 152.61 (C_q, C-11) 149.24 (C_q, C-1), 139.20 (C_q, C-10), 132.27 (C_t, C-3), 131.45 (C_t, C-8), 117.91 (C_t, C-9), 116.65 (C_q, C-7) 113.66 (C_t, C-2), 106.55 (C_q, C-4), 89.95 (C_q, C-6), 86.61 (C_q, C-5), 79.34 (C_q, C-12), 28.10 (C_p, C-13) ppm.

*Synthesis of 4-((4-(tert-butoxycarbonylamino)phenyl)ethynyl)benzenediazonium tetrafluoroborate (**16**)*

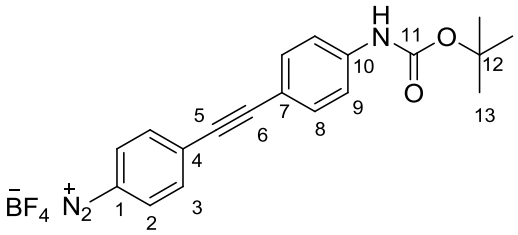

For the diazonium salt formation, 1 g (3.2 mmol) of *tert*-butyl 4-((4-aminophenyl)ethynyl)phenylcarbamate (**15**) was suspended in 2.5 ml of water and 0.5 ml of HBF_4 50%. The suspension of *tert*-butyl 4-((4-aminophenyl)ethynyl)phenylcarbamate (**15**) was chilled in an ice-bath. 0.27 g (3.9 mmol) of $NaNO_3$ dissolved in 0.6 ml of water were added to the suspension. Once all the reagents were added to the flask, it was removed from the ice-bath and stirred for 20 min at RT. After 20 min, the solution was

chilled in an ice-bath. The precipitate was filtered under vacuum with 3 ml of a cool mixture of HBF_4 (50%) and water 1:1 (v:v) and 20 ml of cool diethyl ether. An orange product was obtained.

The yield of the reation was 1.003 g of 4-((4-(*tert*-butoxycarbonylamino)phenyl)ethynyl)benzenediazonium tetrafluoroborate (2.46 mmol, 76%).

Figure A2.29 shows the FT-IR spectrum of 4-((4-(*tert*-butoxycarbonylamino)phenyl)ethynyl)benzenediazonium tetrafluoroborate. The spectrum shows a peak at 2276 cm^{-1} corresponding to the diazonium group. The main vibrations identified in this spectrum together with their relative intensity in the spectrum and the assignations to the corresponding vibration are listed below Figure A2.29.

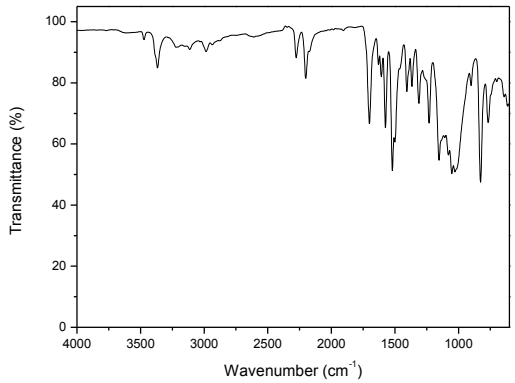

Figure A2.29. FT-IR spectrum of 4-((4-(*tert*-butoxycarbonylamino)phenyl)ethynyl)benzenediazonium tetrafluoroborate (**16**).

FT-IR (ATR): $\tilde{\nu}$ = 3472 (m), 3366 (s), 3225 (w), 3111 (w), 3987 (m), 2934 (w), 2874 (w), 2276 (m, ν(-N≡N)), 2201 (s, ν(C≡C)), 2172 (m), 1905 (w), 1700 (s, ν(C=O)), 1629 (w), 1606 (w), 1574 (s, ν(C=C)), 1520 (s), 1500 (m), 1460 (w), 1408 (m), 1306 (m), 1311 (m), 1230 (s), 1150 (w), 1080(s), 1028 (s, ν(B-F)), 901 (w), 825 (s, δ(C-H_{arom})), 765 (m), 740 (w) cm^{-1}.

^{1}H-NMR (400 MHz, DMSO): No information obtained due to decomposition in the solvent

^{13}C-NMR (400 MHz, DMSO): Confusing information due to decomposition in the solvent.

UNIVERSITAT ROVIRA I VIRGILI
POROUS GAN PRODUCED BY CVD: PROGRESS IN DEVELOPMENT AND CHARACTERIZATION
Josué Mena Gómez

UNIVERSITAT ROVIRA I VIRGILI
POROUS GAN PRODUCED BY CVD: PROGRESS IN DEVELOPMENT AND CHARACTERIZATION
Josué Mena Gómez

UNIVERSITAT ROVIRA I VIRGILI
POROUS GAN PRODUCED BY CVD: PROGRESS IN DEVELOPMENT AND CHARACTERIZATION
Josué Mena Gómez

UNIVERSITAT
ROVIRA i VIRGILI